sid.inpe.br/mtc-m21c/2021/05.10.18.03-TDI

MODELING DROPOUTS OF RADIATION BELT ELECTRONS DRIVEN BY COROTATING INTERACTION REGIONS DURING WEAK TO MODERATE GEOMAGNETIC STORMS

Graziela Belmira Dias da Silva

Doctorate Thesis of the Graduate Course in Space Geophysics, guided by Drs. Lívia Ribeiro Alves, Antonio Lopes Padilha, and Weichao Tu, approved in May 14, 2021.

URL of the original document:
<http://urlib.net/8JMKD3MGP3W34R/44LJNEL>

INPE
São José dos Campos
2021

PUBLISHED BY:

Instituto Nacional de Pesquisas Espaciais - INPE
Coordenação de Ensino, Pesquisa e Extensão (COEPE)
Divisão de Biblioteca (DIBIB)
CEP 12.227-010
São José dos Campos - SP - Brasil
Tel.:(012) 3208-6923/7348
E-mail: pubtc@inpe.br

BOARD OF PUBLISHING AND PRESERVATION OF INPE INTELLECTUAL PRODUCTION - CEPPII (PORTARIA Nº 176/2018/SEI-INPE):

Chairperson:

Dra. Marley Cavalcante de Lima Moscati - Coordenação-Geral de Ciências da Terra (CGCT)

Members:

Dra. Ieda Del Arco Sanches - Conselho de Pós-Graduação (CPG)

Dr. Evandro Marconi Rocco - Coordenação-Geral de Engenharia, Tecnologia e Ciência Espaciais (CGCE)

Dr. Rafael Duarte Coelho dos Santos - Coordenação-Geral de Infraestrutura e Pesquisas Aplicadas (CGIP)

Simone Angélica Del Ducca Barbedo - Divisão de Biblioteca (DIBIB)

DIGITAL LIBRARY:

Dr. Gerald Jean Francis Banon

Clayton Martins Pereira - Divisão de Biblioteca (DIBIB)

DOCUMENT REVIEW:

Simone Angélica Del Ducca Barbedo - Divisão de Biblioteca (DIBIB)

André Luis Dias Fernandes - Divisão de Biblioteca (DIBIB)

ELECTRONIC EDITING:

Ivone Martins - Divisão de Biblioteca (DIBIB)

André Luis Dias Fernandes - Divisão de Biblioteca (DIBIB)

sid.inpe.br/mtc-m21c/2021/05.10.18.03-TDI

MODELING DROPOUTS OF RADIATION BELT ELECTRONS DRIVEN BY COROTATING INTERACTION REGIONS DURING WEAK TO MODERATE GEOMAGNETIC STORMS

Graziela Belmira Dias da Silva

Doctorate Thesis of the Graduate Course in Space Geophysics, guided by Drs. Lívia Ribeiro Alves, Antonio Lopes Padilha, and Weichao Tu, approved in May 14, 2021.

URL of the original document:
<http://urlib.net/8JMKD3MGP3W34R/44LJNEL>

INPE
São José dos Campos
2021

Cataloging in Publication Data

Silva, Graziela Belmira Dias da.

Si38m Modeling dropouts of radiation belt electrons driven by corotating interaction regions during weak to moderate geomagnetic storms / Graziela Belmira Dias da Silva. – São José dos Campos : INPE, 2021.

xxx + 190 p. ; (sid.inpe.br/mtc-m21c/2021/05.10.18.03-TDI)

Thesis (Doctorate in Space Geophysics) – Instituto Nacional de Pesquisas Espaciais, São José dos Campos, 2021.

Guiding : Drs. Lívia Ribeiro Alves, Antonio Lopes Padilha, and Weichao Tu.

1. Earth's radiation belts. 2. Relativistic electrons. 3. Flux dropouts. 4. Radial diffusion. 5. ULF waves. I.Title.

CDU 551.521.2:550.385.4

Esta obra foi licenciada sob uma Licença Creative Commons Atribuição-NãoComercial 3.0 Não Adaptada.

This work is licensed under a Creative Commons Attribution-NonCommercial 3.0 Unported License.

MINISTÉRIO DA CIÊNCIA, TECNOLOGIA E INOVAÇÕES

INSTITUTO NACIONAL DE PESQUISAS ESPACIAIS

DEFESA FINAL DE TESE DE GRAZIELA BELMIRA DIAS DA SILVA
BANCA Nº 096/2021 REG 133612/2017

No dia 14 de maio de 2021, as 14h00min, por teleconferência, o(a) aluno(a) mencionado(a) acima defendeu seu trabalho final (apresentação oral seguida de arguição) perante uma Banca Examinadora, cujos membros estão listados abaixo. O(A) aluno(a) foi APROVADO(A) pela Banca Examinadora, por unanimidade, em cumprimento ao requisito exigido para obtenção do Título de Doutora em Geofísica Espacial/Ciências do Ambiente Solar-Terrestre. O trabalho precisa da incorporação das correções sugeridas pela Banca Examinadora e revisão final pelo(s) orientador(es).

Título: "Modeling dropouts of radiation belt electrons driven by corotating interaction regions during weak to moderate geomagnetic storms"

Eu, Cristiano Max Wrasse, como Presidente da Banca Examinadora, assino esta ATA em nome de todos os membros, com o consentimento dos mesmos.

Dr. Cristiano Max Wrasse - Presidente - INPE

Dra. Lívia Ribeiro Alves - Orientador - INPE

Dr. Antonio Lopes Padilha - Orientador - INPE

Dra. Weichao Tu - Orientador - West Virginia University

Dr. Vitor Moura Cardoso e Silva Souza - Membro Interno – INPE

Dr. Rodrigo Andrés Miranda Cerda - Membro Externo – UNB

Dra. Flavia Reis Cardoso Rojas - Membro Externo - USP

Documento assinado eletronicamente por **Cristiano Max Wrasse**, **Pesquisador**, em 27/05/2021, às 10:29 (horário oficial de Brasília), com fundamento no art. 6º do Decreto nº 8.539, de 8 de outubro de 2015.

A autenticidade deste documento pode ser conferida no site http://sei.mctic.gov.br/verifica.html, informando o código verificador **7272175** e o código CRC **DF288994**.

"O Senhor é o pastor que me conduz, não me falta coisa alguma".
(Sl 23)

.

*A **Deus**, a minha querida mãe **Nildes**, a meu saudoso avô **Vinicius Dias** (in memoriam) e a meus amados irmãos **Isabela, Anne Karen e Pyerre***

ACKNOWLEDGEMENTS

I would like first to thank my advisors Dra. Lívia Ribeiro Alves and Dr. Antonio Lopes Padilha for all the guidance and assistance throughout the course of this program, and for the exciting Project they have provided me with to work on the Radiation belts topic.

I would like to thank the Brazilian government through CNPq for the Doctoral fellowship at INPE, and through CAPES-Print for the sponsorship of my stage abroad at the West Virginia University (USA).

I would like to thank the INPE's Postgraduate program in Space Geophysics for the efforts to make the Exchange program at the West Virginia University possible.

I would like to thank Dra. Weichao Tu to have kindly welcomed me at the West Virginia University, and guided my PhD Project since then, with the excellent help of her Postdoc/students Lifang Li, Xingzhi Lyu, and Mohammad Barani.

I would like to thank Drs. Vitor Souza and Marcelo Banik from INPE for their prompt assistance to deal with the MHD simulations and installation of the LGM library, respectively, which were of great importance for this Project.

I would like to thank Dra. Jasmine Sandhu from the Mullard Space Science Laboratory (UK) for the valuable suggestion of implementing radial diffusion coefficients from in-situ observations to validate the diffusion rates obtained with global MHD.

I thank each friend of mine that made my stay in São José dos Campos be so joyful. In the same way, to my colleagues in Morgantown (West Virginia) for the great moments we spent together during the time of my visit at WVU.

I give special thanks to all my English teachers from Fisk SJC (Tatiana, Janaína, and Taisa) and from the Literacy Volunteers of Monongalia and Preston Counties in Morgantown.

Finally, I thank my family for all support and prayers for me to achieve this graduation at INPE, and Jesus for everything!

ABSTRACT

The Earth's outer radiation belt hosts very dynamic populations of relativistic and ultrarelativistic electrons trapped by the geomagnetic field. Flux dropouts are common variations observed in these electron populations, which can occur after solar wind drivers hit the magnetosphere, such as corotating interaction regions (CIRs). Currently, observational evidence indicates that CIRs promote rapid dropouts produced by magnetopause shadowing and outward radial diffusion mechanisms. However, it is still necessary to investigate the role of these two dynamic mechanisms through modeling. To quantify the contribution of each of them to loss processes in the outer belt triggered by CIRs passages close to Earth, this work extensively investigated three cases that occurred during weak to moderate magnetic storms in 2017, at the end of NASA Van Allen Probes era. This period was concomitant with the declining phase of solar cycle 24 between 2016 and 2018. A catalog of CIRs that includes the chosen case studies was produced for this interval. Two of the selected events had solar wind parameters varying at similar values in the CIRs, such as the flow speed (400 to $\gtrsim$ 600 km/s), dynamic pressure ($\lesssim$ 15 nPa) and density ($\lesssim 40\ cm^{-3}$). As a result, the magnetopause was similarly compressed in both cases to $\sim 7R_E$ using the model of Shue et al. (1998), or to $\sim 8R_E$ as simulated with a global magnetohydrodynamic (MHD) model. However, the electron dropouts in the two events differed significantly in intensity and in the affected L shells. From the calculation of the analytical radial diffusion coefficients using MHD simulations, it was found that the strongest and deepest dropout was related to more intense diffusion rates inside the magnetopause during the storm time. This result was validated by comparisons of the calculated diffusion rates with observed radial diffusion coefficients obtained from in-situ measurements of ultra-low frequency waves. Also, the last closed drift shell (LCDS) calculated with the TS04 magnetosphere model showed that the effect of magnetopause compression reached $L^* = 5.5$ in the most intense dropout event, and $L^* = 6$ for the least intense dropout. Radial diffusion simulations of these events were run for relativistic populations, using as inputs the analytical diffusion coefficients (to simulate outward radial diffusion), a loss term defined outside the LCDS (to simulate magnetopause shadowing) and a variable condition at the outer boundary ($L^* = 6$), obtained from calibrated phase space densities measured by GOES-15. The simulated phase space densities are comparable to the phase space densities observed by the Van Allen Probes, so that the significant differences between the two dropouts were reproduced. Simulations of radial diffusion effects were also performed for the third case, although using only the radial diffusion coefficients estimated from empirical models. In this case, however, the simulations overestimated the phase space densities during the dropout by factors up to ~ 100. This significant error throughout $L^* < 6$ is attributed to an invalid approximation in L^* of the outer boundary condition during the shadowing losses and to substorm injections in this dynamic condition. The results obtained through the 1D diffusion modeling for the analyzed events show that magnetopause shadowing and outward radial diffusion are potential loss mechanisms for generating

dropouts during CIR-magnetosphere couplings, even in periods of weak to moderate storms.

Keywords: Earth's Radiation belts. Relativistic electrons. Flux dropouts. Radial diffusion. ULF waves.

MODELAGEM DE DROPOUTS DE ELÉTRONS DO CINTURÃO DE RADIAÇÃO EXTERNO IMPULSIONADOS POR REGIÕES CORROTANTES DE INTERAÇÃO DURANTE TEMPESTADES GEOMAGNÉTICAS FRACAS A MODERADAS

RESUMO

O cinturão de radiação externo da Terra hospeda populações muito dinâmicas de elétrons relativísticos e ultrarelativísticos aprisionados pelo campo geomagnético. Decréscimos de fluxo (*dropouts*) são variações comuns observadas nessas populações de elétrons, as quais podem ocorrer após a passagem pela magnetosfera de estruturas do vento solar, tais como regiões corrotantes de interação (CIRs). Atualmente, evidências observacionais indicam que as CIRs promovem rápidos *dropouts* pela magnetopausa, por meio dos mecanismos de compressão da magnetopausa e difusão radial para fora do cinturão. No entanto, ainda é necessário investigar o papel desses dois mecanismos dinâmicos por meio de modelagem. Para quantificar a contribuição de cada um deles em processos de perda no cinturão externo desencadeados por passagens de CIRs próximas da Terra, este trabalho investigou extensivamente três casos ocorridos durante tempestades magnéticas fracas a moderadas em 2017, no final da era das sondas Van Allen da NASA. Este período foi concomitante com a fase de declínio do ciclo solar 24 entre 2016 e 2018. Um catálogo de CIRs que inclui os estudos de caso abordados foi produzido para este intervalo. Dois desses eventos escolhidos tiveram parâmetros do vento solar variando em valores semelhantes nas CIRs, tais como a velocidade de prótons (400 a $>$ 600 km/s), pressão dinâmica ($\lesssim$ 15 nPa) e densidade ($\lesssim$ 40 cm^{-3}). Como resultado, a magnetopausa foi comprimida de forma semelhante nos dois casos para $\sim 7R_E$ usando o modelo de Shue et al. (1998), ou para $\sim 8R_E$ de acordo com estimativa de um modelo magnetohidrodinâmico global (MHD). No entanto, as perdas de elétrons nos dois eventos diferiram significativamente em intensidade e nas camadas L afetadas. A partir do cálculo dos coeficientes de difusão radial analíticos utilizando simulações MHD, constatou-se que o *dropout* mais forte e profundo esteve relacionado a taxas de difusão mais intensas na magnetosfera durante o período da tempestade magnética. Esse resultado foi validado por comparações dessas taxas de simulação com observações de taxas de difusão calculadas com medidas *in situ* de ondas de frequência ultra baixa. Também, o parâmetro que determina a última órbita fechada dos elétrons (LCDS, *last closed drift shell*), calculado com o modelo da magnetosfera TS04 mostrou que o efeito da compressão da magnetopausa atingiu $L^* = 5,5$ no evento de *dropout* mais intenso e $L^* = 6$ para o caso menos intenso. Simulações de difusão radial desses eventos foram feitas para populações relativísticas, usando como entradas os coeficientes de difusão analíticos (para simular perdas por difusão radial), um termo de perda externo ao LCDS (para simular perdas diretas pela magnetopausa) e uma condição variável no limite mais externo da simulação ($L^* = 6$), obtida por medidas calibradas da função de distribuição de elétrons feitas pelo GOES-15. As densidades no espaço de fase simuladas são comparáveis às densidades no espaço de fase observadas pelas Sondas Van Allen, de forma que as significativas diferenças dos dois *dropouts* foram reproduzidas. Simulações de efeitos por difusão radial também foram feitas para um terceiro caso, usando apenas os coeficientes de difusão radial estimados a partir de

modelos empíricos. Nesse caso, porém, as simulações superestimaram a função de distribuição durante o *dropout* por fatores de até 100. Esse erro significativo é atribuído a efeitos secundários observados na condição dinâmica utilizada em $L^* = 6$. Os resultados obtidos através da simulação 1D de difusão radial para os eventos analisados mostram que a compressão da magnetopausa e o mecanismo de difusão radial para fora da magnetosfera são processos potenciais para geração de *dropouts* durante acoplamentos CIR-magnetosfera, mesmo em períodos de tempestades fracas a moderadas.

Palavras-chave: Cinturões de radiação da Terra. Elétrons relativísticos. Decréscimos de fluxo. Difusão radial. Ondas ULF.

LIST OF FIGURES

Page

LIST OF TABLES

Page

LIST OF ABBREVIATIONS

ACE	–	Advanced Composition Explorer
AE	–	Auroral Electrojet (index)
AMPTE	–	Active Magnetospheric Particle Tracer Explorer
BATS-R-US	–	Block-Adaptive Tree Solar-wind Roe-type Upwind Scheme
CCMC	–	Community Coordinated Modeling Center
CIMI	–	Comprehensive Inner-Magnetosphere Ionosphere (model)
CIR	–	Corotating Interaction Region
CRRES	–	Combined Release and Radiation Effects Satellite
DSCOVR	–	Deep Space Climate Observatory
Dst	–	Disturbance Storm-Time (index)
ECT	–	Energetic Particle, Composition, and Thermal Plasma Suite (on RBSP)
EFI	–	Electric Field Instrument (on THEMIS)
EMFISIS	–	Electric and Magnetic Field Instrument Suite & Integrated Science (on RBSP)
EFW	–	Electric Field and Waves Instruments (on RBSP)
EMIC	–	Electromagnetic Ion Cyclotron (waves)
ELF	–	Extremely-low frequency
eV	–	electron-Volt
FAC	–	Field Aligned Coordinates
FFT	–	Fast Fourier Transform
FGM	–	Fluxgate Magnetometer (on THEMIS)
FLR	–	Field Line Resonances
FOV	–	Field-of-view
FTCS	–	Forward Time Centered Space (scheme)
GOES	–	Geostationary Operational Environmental Satellite
GPS	–	Global Positioning System
GSE	–	Geocentric Solar Ecliptic
GSM	–	Geocentric Solar Magnetospheric
HEO	–	Highly Elliptical Orbit
HOPE	–	Helium-Oxygen-Proton-Electron (mass spectrometers on RBSP)
HSS	–	High-Speed Streams
Hz	–	Hertz
ICME	–	Interplanetary Coronal Mass Ejection
IGRF	–	International Geomagnetic Reference Field
IMF	–	Interplanetary Magnetic Field
IMP	–	Interplanetary Monitoring Platform
IRBEM-LIB	–	International Radiation Belt Environment Modeling Library
ISEE	–	International Sun-Earth Explorer
K−H	–	Kelvin-Helmholtz (instability)
Kp	–	Planetary K-index
LANL	–	Los Alamos National Laboratory

LCDS	–	Last Closed Drift Shell
LGM	–	LanlGeoMag (library)
MAGED	–	Magnetospheric Electron Detector (on GOES)
MagEIS	–	Magnetic Electron Ion Spectrometer Instruments (on RBSP)
MF	–	Matching factor (in phase space density)
MHD	–	Magnetohydrodynamics
MLT	–	Magnetic Local Time
NOAA	–	National Oceanic and Atmospheric Administration
Pc (1-5)	–	Magnetic continuous pulsations (from 1.67 mHz to 5 Hz)
PDE	–	Partial Differential Equation
POES	–	Polar-orbiting Operational Environmental Satellites
PhSD	–	Phase Space Density
PSD	–	Power Spectral Density
RBSP	–	Van Allen Probes (formerly Radiation Belt Storm Probes)
RBSP-A	–	Van Allen Probe A
RBSP-B	–	Van Allen Probe B
REPT	–	Relativistic Electron-Proton Telescope (on RBSP)
SYM-H	–	Symmetric Horizontal (component disturbances index)
SOHO	–	Solar and Heliospheric Observatory
TS04	–	Tsyganenko & Sitnov (2005) (magnetosphere model)
THEMIS	–	Time History of Events and Macroscale Interactions during Substorms
TH (-A, -D, or -E)	–	THEMIS (probes)
TPSD	–	Total Power Spectral Density
ULF	–	Ultra-Low Frequency
UT	–	Universal Time
VLF	–	Very-Low Frequency

LIST OF SYMBOLS

α, α'	–	local pitch angle
α_{eq}	–	pitch angle at the magnetic equator
$\mathbf{B}$	–	magnetic field vector
B	–	magnitude of the local magnetic field vector
B_{mes}, B_{mod}	–	magnitude of the local magnetic field measured, modeled
B_E	–	magnitude of the Earth's magnetic field on the surface, at the equator
B_m, B_{min}	–	magnetic field strength at the mirror point and at the Earth's equator
B	–	magnitude of the interplanetary magnetic field
B_z(GSM) or IMF-B_z	–	B_z component of the interplanetary magnetic field
$\mathbf{B_0}$, B_0	–	uniform and constant magnetic field vector of the plasma and magnitude
$\vec{B}, \vec{B_0}$	–	local geomagnetic field vector, background geomagnetic field vector
$B_\mu, B_\parallel, B_z$(SM)	–	compressional magnetic field component in the magnetosphere
B_ϕ	–	toroidal magnetic field component in the magnetosphere
B_ν	–	poloidal magnetic field component in the magnetosphere
$\vec{B_{FAC}}$	–	(B_μ,B_ϕ,B_ν) local geomagnetic field vector in FAC coordinates
$\vec{b_{FAC}}$	–	(b_μ,b_ϕ,b_ν) local magnetic field fluctuation vector in FAC
c	–	speed of light in vacuum
D_{ij}, D_{33}	–	Fokker-Planck diffusion coefficients
D_{LL}	–	radial diffusion coefficient
$D_{LL}(L^*, t)$	–	radial diffusion coefficient model
D_{LL}^E	–	D_{LL} due to electric (induced and electrostatic) fluctuations
D_{LL}^B	–	D_{LL} due to magnetic fluctuations
D_{LL}^{MHD}	–	total D_{LL} from MHD simulations
D_{LL}^{OBS}	–	total D_{LL} from observations using RBSP-B and THEMIS data
D_p	–	Dynamic solar wind pressure
$\mathbf{E}$	–	electric field vector
$\vec{E}$	–	local electric field vector near Earth
E, E_i	–	particle kinetic energy
E_ϕ (FAC or SM)	–	azimuthal-electric field component in the magnetosphere
E_ν	–	radial electric field component in the magnetosphere
ε	–	electric permittivity of free space
F	–	unperturbed fast wind
F'	–	compressed and decelerated fast wind
f	–	drift-averaged PhSD corresponding to $f(L^*, t)$ in the radial diffusion equation
f_d	–	particle drift frequency ($= \omega_d/2\pi$)
Φ	–	J_3: invariant magnetic flux through a particle drift shell
$\hat{\phi}$ (FAC or SM)	–	unit vector in the direction azimuthal to $\vec{B_0}$
G	–	gauss ($1G = 10^5$ nanotesla (nT))

γ	–	Lorentz factor
γ'	–	ratio of specific heats at constant pressure and at constant volume
ΔL	–	guiding center deviation of drift shell due to radial diffusion
I	–	geometric integral ($= J/2p$)
J_1, J_2, J_3	–	action-integral invariants associated with the gyro, bounce, and drift motions
J	–	second adiabatic invariant
j	–	particle differential-directional flux ($= j(E, \alpha, \vec{r})$)
K	–	J_2: second adiabatic invariant independent of p ($= I\sqrt{B_m}$)
Kp_{max}	–	maximum Kp index
L	–	normalized equatorial radial distance
L_{PP}	–	L location of the plasmapause
L^*	–	Roederer's L (invariant) parameter proportional to $1/\Phi$
LCDS	–	maximum L^*, depends on $K(\alpha)$
L^*_A, L^*_B	–	L^* of RBSP-A and RBSP-B
m	–	azimuthal wavenumber or mode number
m_0	–	particle rest mass
μ	–	J_1: first adiabatic invariant
$\hat{\mu}$ (FAC)	–	unit vector in the direction parallel to $\vec{B_0}$
μ_0	–	magnetic permeability of free space
N	–	bulk density in the solar wind
$\hat{\nu}$ (FAC)	–	unit vector in the direction radial to $\vec{B_0}$
P	–	plasma pressure
P^E_m, P^B_m	–	ULF wave power spectral densities at frequencies ($\omega = m\omega_d$) in E_ϕ and $B_\parallel$
$\mathbf{p}, p$	–	particle momentum vector and magnitude
$p_\parallel, p_\perp$	–	component of particle momentum parallel and perpendicular to $\mathbf{B}$
ρ_c	–	gyroradius
R_E	–	Earth equatorial radius
R_{MP}	–	standoff equatorial distance to the subsolar point on the magnetopause
R^2	–	coefficient of determination (= correlation coefficient squared)
$R(t)$	–	rotation matrix from geocentric to FAC system
r	–	geocentric radial distance
r_e	–	geocentric radial distance to the field line in the magnetic equatorial plane
R	–	normalized geocentric radial distance
$\mathbf{r}, \vec{r}$	–	position vector
S	–	source term in the Fokker-Planck equation
S	–	unperturbed slow wind
S'	–	compressed and accelerated slow wind
T	–	bulk temperature in the solar wind
τ_c, τ_b, τ_d	–	gyro, bounce, and drift periods

τ_{CH}, τ_{HI}	–	electron lifetimes due to pitch angle scattering by chorus and hiss
V	–	flow speed of the solar wind
V_ϕ	–	transverse flow velocity of the solar wind
Ω	–	gyrofrequency of the electron
ω_d	–	bounce-averaged angular drift frequency

CONTENTS

1 INTRODUCTION

The Earth's electron radiation belt consists of trapped relativistic electrons of highly dynamic fluxes that populates the outer belt region ($L = 3 - 7$). They execute the quasi-periodic motions of gyro (bounce) around (along) the geomagnetic field lines, in addition to drift around the Earth, so as to conserve three adiabatic invariants, i.e., constants of motion (NORTHROP; TELLER, 1960). The first invariant μ describes the conservation of the magnetic moment of an electron within a gyro motion, and the second invariant K is the longitudinal invariant preserved within a bounce motion. The third invariant Φ is defined as the magnetic flux enclosed by an electron's drift shell, L. The L parameter that takes into account the conservation of Φ is called L^* (ROEDERER, 1970).

Dropouts are sudden depletions of the electron fluxes often associated with geomagnetic storms (REEVES et al., 2003). During geomagnetically active times, electrons are lost both to the atmosphere or across the magnetopause because of a breakdown of their adiabatic invariants (SHULZ; LANZEROTTI, 1974; TURNER et al., 2012a). This occurs due to a diffusive transport of the electrons caused by various types of wave-particle interactions with high-frequency waves (Hz to 10s of kHz) (e.g., Turner et al. (2014)) or due to the combined effect of drift loss and outward radial diffusion (e.g., Brautigam and Albert (2000), Ozeke et al. (2014b), Hudson et al. (2014), Alves et al. (2016)). As illustrated in Figure 1.1, the primary condition for the drift loss (or "magnetopause shadowing") is the compression of the magnetopause towards the inner magnetosphere, so as to remove trapped electrons from their nearly stable closed drift orbits at higher L shells. The outward radial diffusion is a subsequent process that produces flux dropouts in a few hours ($\lesssim$ 5h) as a result of the sharp radial gradient left in the phase space density (LOTO'ANIU et al., 2010; TURNER et al., 2012b). Consequently, storm main phase flux dropouts may reach electron populations from lower L shells, which are further lost to the magnetopause or by deceleration. Inward or outward radial diffusion is mainly mediated by drift-resonant interactions with ultra-low frequency (ULF) waves in the Pc5 band ($\sim 2 - 7$ mHz) excited through storm time (ELKINGTON, 2006).

As indicated in Figure 1.1, the size and shape of the magnetopause strongly depends on the control exercised by the solar wind dynamic pressure and also on the southward interplanetary magnetic field component (SHUE et al., 1998). In this regard, corotating interaction regions (CIRs) that propagate in the solar wind ahead of high speed streams (HSSs) are common interplanetary structures that lead to in-

creased dynamic pressure of $\sim$ 10s of nPa near Earth (e.g., Richardson (2018)). Morley et al. (2010) conducted a superposed epoch analysis of 67 CIR-driven dropouts ($2005 - 2008$) using electron counts measured at the Global Positioning System (GPS) altitudes ($L^* \gtrsim 4$). The main find was that gradual dropouts observed at higher L^*, as the magnetopause from Shue et al. (1998) compressed, were consistent with magnetopause shadowing and outward radial diffusion. This result is important because previous studies have primarily attempted to associate enhanced parameters within CIRs/HSSs with flux enhancements only (e.g., Tsurutani et al. (2006), McPherron et al. (2009)). A more recent superposed epoch analysis concerning dropouts driven by CIRs was performed by Yuan et al. (2015). The study containing a set of 223 CIR events during $1994 - 2003$ compared flux dropouts of $1.5 - 6.0$ MeV electrons throughout the outer belt associated with low and high dynamic pressure regimes. It was observed that dropouts are commonly generated in both cases, although they become more intense under higher dynamic pressure.

Figure 1.1 - Diagrams showing evolution of outer belt losses by magnetopause shadowing added to outward radial diffusion over storm time.

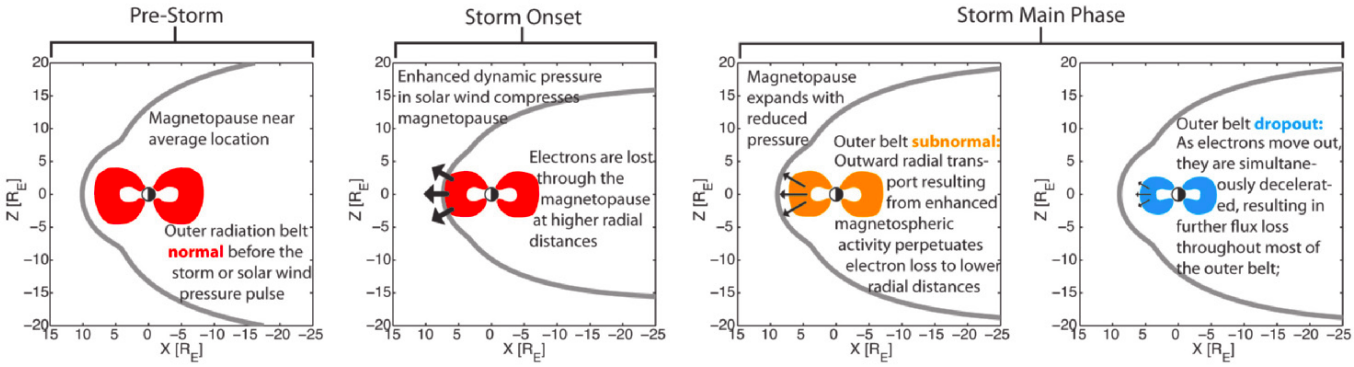

SOURCE: Adapted from Turner et al. (2012b).

Other observational evidence for ULF wave radial diffusion driving electron flux dropouts during CIRs was provided by Loto'Aniu et al. (2010). In this study, radial diffusion rates (D_{LL}) were quantified from ULF wave power observed by the Time History of Events and Macroscale Interactions during Substorms (THEMIS) satellites. It was found that the corresponding time scale of radial diffusion computed at $L = 6.6$ as $\tau_{LL} = 1/D_{LL}$ reproduced an estimate in the range of $1 - 4$h, inferred from the GOES-12's measured fluxes of the relativistic electron dropout. Turner et al. (2012b) also demonstrated that losses to the magnetopause through

magnetopause shadowing added to outward radial diffusion would be the most viable explanation for the CIR-related outer belt dropout on January 6, 2011. These authors used NOAA-POES flux measurements of trapped and precipitating electrons to show that there were no observations of relativistic electron precipitation during the main phase dropout. Such precipitation activity took place rather around a day later when the trapped relativistic population recovered to higher levels than the prestorm levels. The role of dropouts with ultimate loss to the magnetopause had already been demonstrated through modeling by Shprits et al. (2006). They performed radial diffusion simulations using the Kp-based D_{LL} model of Brautigam and Albert (2000) and compared the results of 1 MeV electron fluxes adopting a variable or constant outer boundary condition, with observations provided by Highly Elliptical Orbit (HEO), SAMPEX, and CRRES satellites. A good agreement was found from the use of the variable condition at the outer boundary, which resolved main phase fast losses down to $L^* = 4 - 5$.

Unlike the magnetopause standoff distance, the last closed drift shell (LCDS) represents the magnetopause boundary for trapped populations based on the conservation of Φ, which is the third invariant (ROEDERER, 1970). Fei et al. (2006) used analytical D_{LL} rates from ULF waves obtained with global MHD modeling as input for radial diffusion simulation of the $24 - 26$ September 1998 intense magnetic storm. The outer boundary condition was made dynamic both in time and in L^* by setting this time-varying condition at the LCDS. Comparisons with test-particle simulation from MHD showed that the radial diffusion model reproduced the storm-time peak in phase space density at $L^* \sim 4.2$ as the LCDS decreased to $L^* \sim 4.5$, concurrent with enhanced inward radial diffusion within the same region. More recently, results of event-specific LCDS have been used in radial diffusion modeling of the outer belt to primarily assess the contribution of magnetopause shadowing losses to the relativistic electron dropout on 22 June 2015, which was driven by one of the largest storms in the Van Allen Probes era ($2012 - 2019$) (TU et al., 2019).

The above discussion shows that there is systematic evidence that the outer belt electrons are lost across the magnetopause following CIR events, through the mutual mechanisms of magnetopause shadowing and outward radial diffusion. However, despite all the knowledge such studies have produced, there is still a need for further efforts to model dropouts under this common type of solar wind driver to quantify the contribution of both mechanisms. As an example, none of the aforementioned modeling studies (Fei et al. (2006), Shprits et al. (2006), and Tu et al. (2019)) dealt with relativistic electron dropouts driven by CIRs. In addition, there is still a

great window of opportunity to investigate the viability of D_{LL} models run in radial diffusion codes to reproduce storm-time observed rates, as well as more accurate particle distributions.

For this study, 46 CIRs of the $2016 - 2018$ biennium were identified and tabulated, comprising the descending phase of solar cycle 24. During this time interval, NASA's Van Allen Probes provided continuous measurements of electron flux at a wide range of energies, angular distributions and L shells, which allowed to observe dropouts related to the set of cataloged CIRs. Three dropout events were selected and are studied here extensively, using global MHD simulation for two of them. These two simulated events had CIR passages with very similar ranges in the solar wind bulk speed, density, and dynamic pressure, but produced significantly different dropout dynamics both in L shell and intensity. Briefly, the main goal of this study is to use these events to evaluate the contribution of magnetopause shadowing and outward radial diffusion through the physical modeling of such outer belt dropouts, which are related to small and moderate storms driven by CIRs. The numerical simulations of this thesis complement the statistical and observational studies on CIRs previously mentioned. The new findings are that: (1) the LCDS at $L^* < 6$ along with an enhanced storm-time ULF wave radial diffusion played a role in the major dropout, and (2) the use of modeled D_{LL} comparable to in-situ D_{LL} rates increases the agreement between radial diffusion simulation results and particle observations.

Following in this text, Chapter 2 presents the theoretical background of the study, while Chapter 3 presents the data sets and tools used. Chapter 4 shows the results of the radial diffusion coefficients, specific for the two cases studies on 27 March 2017 and on 21 November 2017, to be analyzed in more detail. Following the propositions of Fei et al. (2006), Tu et al. (2012), Li et al. (2017), and Li et al. (2020), the analytical radial diffusion coefficients were quantified for each case using ULF waves simulated with a global MHD code (D_{LL}^{MHD}). Also, following Loto'Aniu et al. (2010) and Olifer et al. (2019), D_{LL}^{MHD} results were validated with D_{LL} rates derived from in situ observations, i.e., D_{LL}^{OBS}, using Van Allen Probe B and three THEMIS satellites. The magnetopause standoff distance obtained by MHD is compared with the result of Shue et al. (1998) for both cases. Moreover, the simulated ULF wave power used to derive D_{LL}^{MHD} is validated with observations from Van Allen Probe B, GOES and THEMIS satellites. In Chapter 5, a separate analysis involving the results of D_{LL}^{OBS} from the three CIR studies and an additional event (not included in the catalog) is provided to emphasize the accuracy of the D_{LL} empirical models in events with lesser or greater activity of ULF waves. In Chapter 6, the radial diffusion simulations

of the two special cases are discussed, calculated using the respective D_{LL}^{MHD} and empirical D_{LL} estimated from Brautigam and Albert (2000), Liu et al. (2016), and Ali et al. (2016). Following Shprits et al. (2006), a variable outer boundary condition is set at $Lmax = 6$ in all runs, along with a loss term defined above the event-specific LCDS, as in Tu et al. (2019). The simulation results in all runs are compared with the particle observations from the Van Allen Probes. These simulation results are discussed based on the results obtained in Chapters 4 and 5, from the comparisons of D_{LL}^{MHD} and empirical rates with in-situ D_{LL}^{OBS}. Finally, the conclusions are presented in Chapter 7.

2 BACKGROUND OF THE STUDY

In this chapter, basic concepts related to this work are presented, including some properties of the magnetosphere and the Van Allen radiation belts.

2.1 The Magnetosphere

The Earth's dipole-like (internal) magnetic field constantly interacts with the solar wind, which is a supersonic plasma flow resulting from the expansion of the Sun's outer atmosphere radially towards the interplanetary medium. This solar wind is composed of ions, mostly protons (H^+) and alpha particles (He^{2+}), and an equal number of electrons. As a consequence of the ideal MHD fluid theory, the solar wind can be treated as a highly conducting fluid, in which magnetic fields of solar origin are frozen and transported out with it, forming the interplanetary magnetic field (IMF) (PARKS, 2004, p. 5).

In the vicinity of the Earth, a cavity is formed due to the interaction of the solar wind with the geomagnetic field, which prevents the direct interaction of the solar wind plasma with the terrestrial atmosphere at low and mid latitudes. This cavity is called *magnetosphere* and the geomagnetic field predominates within it. As an effect of the dynamic pressure of the solar wind on the Earth's dayside, the shape of the magnetosphere is of compressed magnetic field lines on the dayside and elongated field lines on the nightside, as shown in Figure 2.1.

As also shown in this Figure, a shock region develops in front of the magnetosphere known as *bow shock*, which is due to the super-magnetosonic speeds of $\sim 300 - 800$ km/s reached by the solar wind close to Earth. Note that the typical speed exceeds that of plasma waves that are about $50 - 100$ km/s (GANUSHKINA et al., 2018). This is the explanation of why the solar wind is considered super-magnetosonic. In the bow shock, however, the solar wind plasma becomes sub-magnetosonic, although increases its velocity as it travels around the magnetosphere from the subsolar region to the flanks. This crossing region is called *magnetosheath* and is located between the bow shock and the magnetosphere.

Figure 2.1 - "Noon-midnight" meridional representation of the formation of the magnetosphere and its basic boundaries for an inclined IMF-B_z configuration.

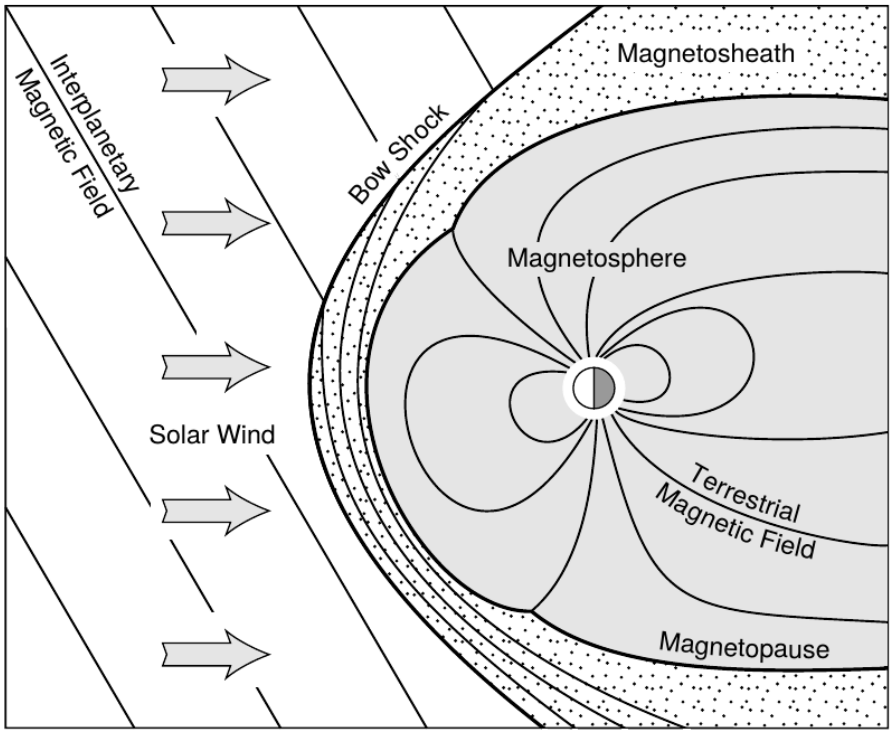

The Earth's tilted dipole represented has the S-pole close to the geographic north pole and the N-pole close to the geographic south pole, so that near the equator the geomagnetic field points northward.

SOURCE: Baumjohann and Treumann (1996, p. 6).

Not only the shape, but also the size of the magnetosphere is largely determined by pressure balance between the solar wind ($P_{sw} = \rho_{sw} u_{sw}^2$) and the geomagnetic field ($P_B = \frac{B^2}{2\mu_0}$), where μ_0 is the permeability of free space, and ρ_{sw} and u_{sw} are the solar wind's bulk density and flow speed, respectively. The local $\mathbf{B}$ strength is assumed to be twice that of a dipole, from which $B(r) = B_E(\frac{R_E}{r})^3$ (KAMIDE; CHIAN, 2007; GANUSHKINA et al., 2018), where B_E is the equatorial magnitude of the Earth's magnetic field on the surface ($\sim$ 30,000 nT) and R_E is the Earth radius (1 R_E = 6371.2 km). The ultimate boundary of the magnetosphere, represented in Figure 2.1 as the thick black line surrounding it, is called *magnetopause*. The pressure gradient ∇P produced by the different plasma populations on both sides of the magnetopause (on the magnetosheath and from the magnetosphere) makes this boundary a thin current layer that is responsible for the distortion of the dipole mag-

netic field. Assuming static conditions and local isotropic pressure P, the equation below provides a simplified definition for the magnetopause current density, also recognized as Chapman-Ferraro current (Ganushkina et al. (2018) and references therein):

$$\mathbf{J}_{\perp} = \frac{\mathbf{B} \times \nabla P}{B^2}. \tag{2.1}$$

In addition, by making $P_{sw} = P_B$, the magnetopause nose location (R_{MP}, in units of R_E) is obtained as given by (GANUSHKINA et al., 2018):

$$R_{MP} = 2^{1/3} \left(\frac{B_E^2}{2\mu_0 \rho_{sw} u_{sw}^2} \right)^{1/6}. \tag{2.2}$$

The subsolar point at which the magnetopause is typically determined is located along the Sun-Earth line, while its nose changes its location depending on the seasonal dipole tilt angle defined in the plane containing this line and the magnetic dipole. The geocentric solar magnetospheric (GSM) system is actually based on these definitions, with the x-axis along the Sun-Earth line, positive towards the Sun, the y-axis perpendicular to the dipole axis, so that this axis is found in the $x - z$ plane, and the z-axis pointing towards the northern magnetic pole. These definitions form a right-handed system (KIVELSON; RUSSELL, 1995).

The IMF also plays a major role in the dynamics of the magnetosphere, especially if it carries a significant southward-B_z component (GONZALEZ et al., 1994). Since the geomagnetic field points northward near the magnetic equator, the anti-parallel magnetic field condition found in the case of an intense ($\lesssim -10$ nT) and prolonged ($\gtrsim 3$ hours) southward IMF component of solar wind transients (e.g., Richardson (2018)) causes the geomagnetic field lines to reconnect with the IMF field lines on both the dayside and nightside. The described process is known as magnetic reconnection, and occurs through a localized breakdown of the ideal-MHD frozen-in condition (ALFVÉN, 1958). For southward IMF, it first takes place at an X-line across the equatorial dayside magnetopause, in a 3D representation (LAVRAUD et al., 2011). The connected or "open" field lines are dragged anti-sunward with the solar wind and reconnects again on the nightside, leading to the formation of the *magnetotail* (KAMIDE; CHIAN, 2007). The magnetotail has a basic structure that extends at least $240R_E$ away from the Earth, according to downtail spacecraft observations (e.g., Eastwood et al. (2015)).

Figure 2.2, adapted from Gonzalez et al. (1994), summarizes the complex magnetospheric dynamics that follows the solar wind-magnetosphere coupling discussed so far. The overall concept behind this was first formulated by Dungey (1961). In this meridional view from noon to midnight of the magnetosphere, it is possible to localize the two reconnection sites marked by "x", over which each of the X-lines stands. It is seen that the solar wind plasma moves on the flanks of the magnetosphere, perhaps with a certain velocity $\mathbf{u}$ and magnetic field $\mathbf{B}$. In this movement, it induces the convection electric field $\mathbf{E} = \mathbf{-u} \times \mathbf{B}$ and the magnetopause current $\mathbf{J}$ of Equation 2.1, in addition to dragging tailward the open field line from the dayside magnetic reconnection region to be reconnected on the nightside, in the distant magnetotail.

Figure 2.2 - Sketch showing the magnetospheric dynamo triggered by anti-parallel reconnection with the IMF and the mechanical work of the solar wind plasma.

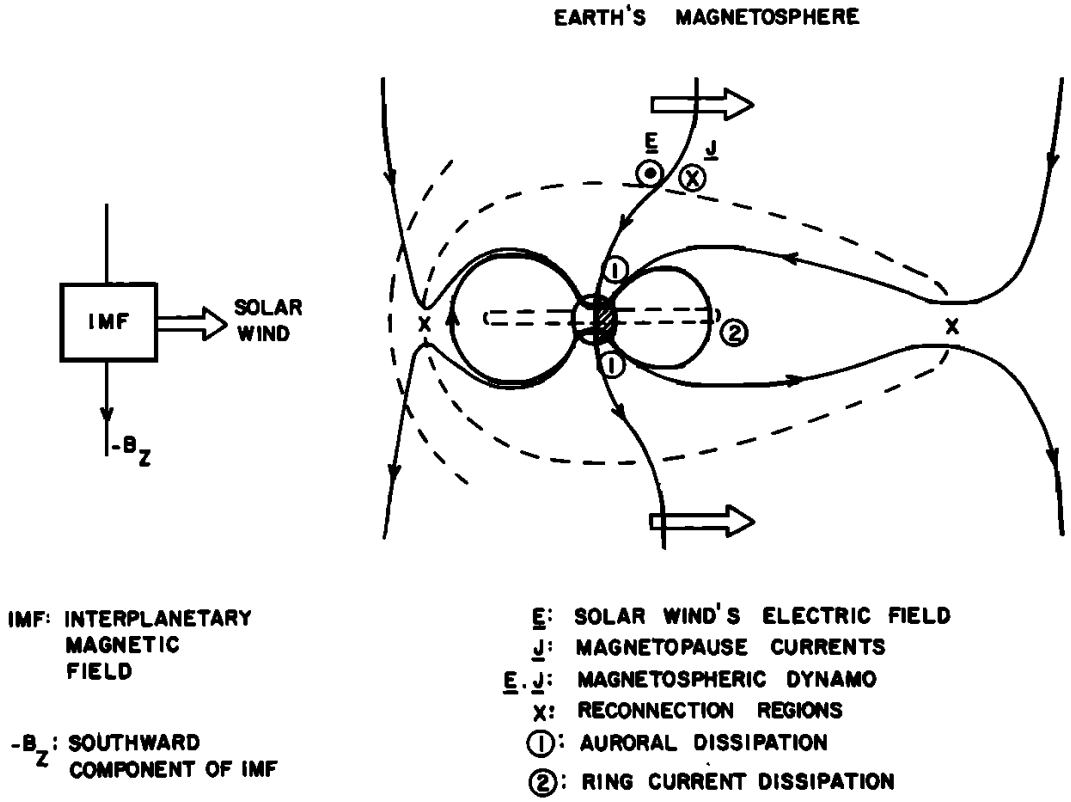

See text for detail.

SOURCE: Modified from Gonzalez et al. (1994).

The direct consequence of reconnection is the transfer of energy, momentum and plasma into the magnetosphere-ionosphere system (e.g., Kamide and Chian (2007)). In the magnetotail, the drastic release of magnetic energy converted to plasma energy allows the hot plasma from the magnetosheath to fill a low-latitude region called *plasma sheet*. When the latter process also occurs closer to Earth, a magnetospheric substorm develops (EASTWOOD et al., 2015).

Under the extreme conditions discussed previously for the transient southward IMF, the just explained "magnetospheric dynamo" in Figure 2.2 can lead to the occurrence of so-called geomagnetic storms (GONZALEZ et al., 1994). Geomagnetic storms are recognized as the result of a strong and prolonged plasma convection into the magnetosphere (EASTWOOD et al., 2015). As a consequence, there is the buildup of the storm-time *ring current*, which can drastically reduce the magnitude of the geomagnetic field near the magnetic equator, because its westward-toroidal sense of flow induces a southward field (which is why it is a diamagnetic current). The diamagnetic effect of the ring current on the horizontal component magnetic field near the equator is quantified by the hourly Disturbance Storm-Time (Dst) index, or its equivalent SYM-H index, with a 1-minute time resolution (WANLISS; SHOWALTER, 2006). In turn, the Auroral Electrojet (AE) index has historically been used to monitor auroral activity, often linked to substorms.

Gonzalez et al. (1994) pointed out that the buildup of the storm-time ring current and auroral activity are the main mechanisms for dissipating the energy released in the magnetosphere, as shown in Figure 2.2. It should be mentioned that the connection between storms and substorms is not yet fully understood (e.g., Eastwood et al. (2015)).

Besides the ring current particles, the inner magnetosphere also hosts relativistic and ultrarelativistic charged particles from the *radiation belts*. Basically, these two populations differ in the energy regime, which in the case of electrons spans 10s to a few 100s of keV for the ring current and from $\sim$ 500 keV to 10s of MeV for the radiation belts. This difference in energy causes both trapped populations to exhibit different dynamics, mainly in terms of the mechanisms governing their net source and loss. For instance, the gradual decay of the ring current (ions) is mainly due to charge exchange with neutral atoms existing in various Earth radii (JORDANOVA et al., 2020, p. 82).

Another particle population that we are concerned with in the inner magnetosphere is the dense, cold plasma ($\lesssim$ 10 eV) confined to the *plasmasphere*. This region typi-

cally extends from the ionosphere to its variable outer boundary, known as *plasmapause* (BAKER et al., 2018). The three aforementioned magnetospheric charged particle populations (ring current, radiation belts and from the plasmasphere) coexist spatially in nearly closed field lines since they are trapped by the geomagnetic field (KAMIDE; CHIAN, 2007, p. 8). The magnetopause is the usual outermost boundary considered for ring current and radiation belts.

Baker et al. (2018) outlined the means by which the plasma of the ring current and the plasmasphere can be coupled to the radiation belts to explain the dynamics of the latter under extreme effects of the so-called space weather, such as magnetic storms. It is known that these couplings have a strong relationship with the excitation of plasma waves across the inner magnetosphere. Following this paradigm of wave-particle interactions, radiation belt electrons (focus of this study) can be affected by (Hudson et al. (2014), Baker et al. (2018), and references therein): i) Electromagnetic ion-cyclotron (EMIC) waves driven by unstable ring current proton distributions on the dusk side; ii) Very-low frequency (VLF) chorus waves driven by temperature anisotropies in ring current electrons, particularly on the dawn side; and (iii) VLF hiss waves driven by the cold plasma of the plasmasphere and by dayside plasmaspheric plumes. In modeling radiation belt losses (our focus problem), the plasmapause location has been widely recognized to constrain the regions of predominance of interactions with chorus waves (external) and hiss waves (internal) (e.g., Tu et al. (2009), Thorne (2010), Li et al. (2014b), Ozeke et al. (2014b), Drozdov et al. (2015)).

2.1.1 Empirical models of the magnetosphere

In this section, empirical models of the magnetosphere used in this study are described, that is, the plasmapause location given by O'Brien and Moldwin (2003), the magnetopause subsolar location from Shue et al. (1998), and the TS04 magnetosphere model from Tsyganenko and Sitnov (2005).

2.1.1.1 Plasmapause location model

The plasmapause is the time- and activity-dependent outer boundary of the plasmasphere. The model for the plasmapause location in L shell space (L_{pp}), taken from O'Brien and Moldwin (2003), is built on the Dst index minima. The connection between this index and the plasmapause is that during magnetically disturbed periods, the dynamics of the plasmapause is largely dominated by magnetospheric convection (CARPENTER; ANDERSON, 1992), and so does the storm-time Dst index.

Consequently, the plasmapause is eroded to geocentric distances closer to the Earth during those times.

As the plasmapause is expected to respond several hours later to the actual time of change in convection, the minimum Dst value considered is that of the preceding state of the plasmaspause calculated from the interval of the previous 24 hours. The model consists of a best-fit linear function for L_{pp} in relation to the running minima of Dst, which is defined between $t_1 = -24h$ and $t_2 = 0h$ (current instant) as $Q = log_{10}|min_{-24,0}Dst|$. The observational database used in the fitting is from over 900 plasmapause crossings taken in $1990 - 1991$. The model for L_{pp} in units of R_E then reads (O'BRIEN; MOLDWIN, 2003):

$$L_{pp} = -1.57Q + 6.3. \tag{2.3}$$

2.1.1.2 Magnetopause subsolar location model

The model of Shue et al. (1998) is widely recognized for reporting the location of the subsolar magnetopause under quiet to extreme solar wind conditions. It was improved from a previous model (SHUE et al., 1997), using the same database of magnetopause crossings obtained with ISEE 1 and 2, AMPTE and IMP 8 satellites. The main adjustment was to provide a single expression for the magnetopause stand-off distance R_{MP}, as a function of the solar wind dynamic pressure D_p and IMF-B_z, so that this model is valid for both northward and southward B_z components.

In this empirical approach, the observed locations of the magnetopause were first fit to the following functional form:

$$r = R_{MP}\left(\frac{2}{1+\cos\theta}\right)^{\alpha_{TF}}, \tag{2.4}$$

where r is the radial distance to the locus of the measurements, that is, the point represented by coordinates $(X_{GSM}, Y_{GSM}, Z_{GSM})$, R_{MP} is the desired day-side magnetopause location along the Sun-Earth line, the angle θ is defined from $X_{GSM} = r\cos\theta$, and α_{TF} describes the shape (closed or open) of the tail magnetopause, depending also on D_p and B_z as follows:

$$\alpha_{TF} = (0.58 - 0.007B_z)[1 + 0.024\ln(D_p)]. \tag{2.5}$$

Finally, the nonlinear function derived to represent R_{MP} is given by:

$$R_{MP} = \{10.22 + 1.29\tanh[0.184(B_z + 8.14)]\}(D_p)^{-1/6.6}. \tag{2.6}$$

2.1.1.3 The TS04 magnetosphere model

Throughout this thesis, we will often refer to the TS04 empirical model of the inner magnetosphere (TSYGANENKO; SITNOV, 2005) to discuss methods and results based on such a model. The TS04 model reports the magnetic field vector at given locations, for the upstream solar wind and IMF input conditions. The external model field is approximated as a sum of the induced fields from each of the seven major current systems acting in the magnetosphere, including the Chapman-Ferraro, ring current (axially symmetric and asymmetric) and a cross-tail current sheet. This tail current is defined as a nightside equatorial westward current outside 6.6 R_E, with closure at the magnetopause (GANUSHKINA et al., 2018). Given its sense of flow and intensity, it actually contributes, in most cases exceeding the symmetric ring current's southward field, to the decrease in the equatorial strength of the geomagnetic field during geomagnetic storms, as shown by Tsyganenko and Sitnov (2005).

The Chapman-Ferraro field is modeled to confine the Earth's internal field within the magnetopause, taking into account the strength and tilt angle of the dipole. The internal field is defined from the International Geomagnetic Reference Field (IGRF), while the surface defining the magnetopause is fitted to the boundary location as modeled by Shue et al. (1998), although only the control of the dynamic pressure is assumed. Thus, fields can be mapped from this boundary to the distant magnetotail at 70 R_E. Additionally, the Chapman-Ferraro component is defined from a combination of curl-free fields whose potentials yields an expansion of 18 longitudinal Fourier modes, which in turn are used to shield the other component fields (TSYGANENKO, 2002; TSYGANENKO; SITNOV, 2005).

It is assumed that each of the field sources (W_k) evolves in time according to:

$$\frac{\partial W_k}{\partial t} = S_k - L_k, \tag{2.7}$$

with S_k representing the feeding rate instantaneously driven by the solar wind parameters N, V and B_s (bulk density, speed and a function of the magnitude of

the southward IMF component, respectively) and L_k representing slower processes controlling the saturation or decay of the current system.

Short-lived phenomena, such as substorms, are left out of this approach. An improvement of this model over the previous ones is the definition of a decay rate (r_k: inverse of the characteristic relaxation time) for each component, which is multiplied by W_k subtracted by its quiet-time baseline $W_{k,0}$ to define L_k, i.e., $L_k = r_k(W_k - W_{k,0})$. Each source solution $W_k(t)$ is determined separately as a time integral of Equation 2.7, and "*multiplied by a scalar coefficient, representing the magnitude of each source as a function of the current state of the interplanetary medium and of the previous history of the external driving*" (TSYGANENKO; SITNOV, 2005). The saturation levels of the fields are included in these coefficients for the model to deal with extremely strong interplanetary driving (e.g., Huang et al. (2008)).

The iterative search is applied in an instant of time, so that the best fit values for the scalar coefficients are found from the solar wind and IMF parameters, resulting in dynamical $W_k(t)$ (the $W_1 - W_6$ parameters of the "*Qin-Denton*" files (QIN et al., 2007)). This is done in a totally optimized way in relation to magnetospheric data records covering the wide region of the model domain. It was achieved through the use of spacecraft magnetic field data, in which 90% were obtained from measurements at geosynchronous orbit with GOES 8-10, and beyond, during 37 storm events in $1996-2000$. Overall, TS04 is a storm-time dynamic model of the Earth's external magnetic field in the inner magnetosphere, which has also proved useful for predictions of the *Dst* index during the full cycle[1] of a magnetic storm (TSYGANENKO; SITNOV, 2005). The temporal resolution of the output magnetic field data derived from TS04 can be 1 minute, 5 minutes, or 1 hour.

2.1.2 ULF waves

So far, the dynamic magnetosphere has been described in terms of its formation from the direct drive of the solar wind, and the configuration change linked to several current systems flowing through this medium, defining its shape and size. Besides, ring current and plasmaspheric particles often present unstable distributions that provide free energy for the growth of many high-frequency waves ($\sim$ Hz to 10s of kHz)[2] in the inner magnetosphere. All of these processes are enhanced during

[1] On the basis of the *Dst* index, the full cycle of a magnetic storm comprises three phases: initial phase (sudden increase of *Dst* to positive values); main phase (the index falls off to very negative values until a minima); recovery phase (recovery of *Dst* to undisturbed conditions).

[2] e.g.: whistler-mode VLF chorus and hiss ($\sim 1 - 10$ kHz).

magnetic storms and can also be connected to give rise to global magnetic oscillations in the ultra-low frequency (ULF) regime, known as ULF waves.

In the cold-plasma MHD approximation of the magnetosphere, ULF electromagnetic waves appear at frequencies below the ion gyrofrequency, from the combined effect of mechanical and electromagnetic forces on this fluid (KAMIDE; CHIAN, 2007, p. 400). The MHD equations used to describe low frequency waves in space plasmas are three fluid equations, the four Maxwell's equations and the Ohm's law (BITTENCOURT, 2004):

Continuity, motion and state equations

$$\frac{\partial \rho_m}{\partial t} + \nabla \cdot (\rho_m \mathbf{u}) = 0, \tag{2.8}$$

$$\rho_m \frac{\partial \mathbf{u}}{\partial t} + \rho_m (\mathbf{u} \cdot \nabla)\mathbf{u} = -\nabla P + \mathbf{J} \times \mathbf{B}, \tag{2.9}$$

$$\frac{P}{\rho_m^{\gamma'}} = constant, \tag{2.10}$$

Modified Maxwell's equations

$$\nabla \cdot \mathbf{E} = 0, \tag{2.11}$$

$$\nabla \cdot \mathbf{B} = 0, \tag{2.12}$$

$$\nabla \times \mathbf{B} = \mu_0 \mathbf{J}, \tag{2.13}$$

$$\nabla \times \mathbf{E} = -\frac{\partial \mathbf{B}}{\partial t}, \tag{2.14}$$

Ohm's law

$$\mathbf{J} = \sigma(\mathbf{E} + \mathbf{u} \times \mathbf{B}). \tag{2.15}$$

The parameters presented in these equations are the plasma mass density (ρ_m), bulk velocity ($\mathbf{u}$), pressure (P), current density ($\mathbf{J}$), magnetic field ($\mathbf{B}$), a constant derived from the ratio of specific heats at constant pressure and constant volume (γ'), the electric field ($\mathbf{E}$) and the electric conductivity (σ). In Equation 2.11, zero charge density is assumed because of the quasi-neutrality condition of the plasma,

in Equation 2.13 the displacement current (i.e., $\varepsilon_0 \partial \mathbf{E}/\partial t$) is neglected since it only becomes important for high frequencies outside the MHD regime, and in Equation 2.15 other terms of the generalized form of the equation are omitted. In this equation, for finite σ, there is an associated resistivity and the MHD approach is treated as resistive. In the limit of $\sigma \to \infty$, there is no associated resistivity and the MHD approach is said to be ideal.

Using this set of equations and assuming a linear description of the small disturbances in $\mathbf{B}$, ρ_m, and $\mathbf{u}$ that can generate wave modes in the plasma, one defines:

$$\begin{aligned} \mathbf{B}(\mathbf{r}, t) &= \mathbf{B_0} + \mathbf{B_1}(\mathbf{r}, t), \\ \rho_m(\mathbf{r}, t) &= \rho_{m0} + \rho_{m1}(\mathbf{r}, t), \\ \mathbf{u}(\mathbf{r}, t) &= \mathbf{u_1}(\mathbf{r}, t), \end{aligned} \tag{2.16}$$

where $\mathbf{B_0}$ and ρ_{m0} are spatially uniform and constant values from the equilibrium state, in which the plasma has zero velocity ($\mathbf{u_0} = 0$). Each of the disturbance terms $\mathbf{B_1}$, $\rho_{\mathbf{m1}}$ and $\mathbf{u_1}$ can be described by plane waves, which for $\mathbf{u_1}$ is represented as:

$$\mathbf{u_1}(\mathbf{r}, t) = \mathbf{u_1} \exp\left(i\mathbf{k} \cdot \mathbf{r} - i\omega t\right), \tag{2.17}$$

where $\mathbf{k}$ is the wave vector.

After combining some of the MHD equations and replacing those from 2.16, as well as considering the equation for $\mathbf{u_1}$, two types of dispersion equations (3.1 and 4.1 in Bittencourt (2004, p. 382-383)) are found in relation to the direction of the ambient magnetic field $\mathbf{B_0}$. This leads to three possible solutions of wave modes in a homogeneous medium. When $\mathbf{k}$ is parallel to $\mathbf{B_0}$, ULF waves propagate with phase velocity equivalent to the Alfvén speed V_A, calculated as:

$$\frac{\omega}{k} = V_A; \; V_A = \left(\frac{B_0^2}{\mu_0 \rho_{m0}}\right)^{1/2}, \tag{2.18}$$

Note that k is the wavenumber and B_0 is the magnitude of $\mathbf{B_0}$. For the Alfvén mode waves, $\mathbf{u_1}$ is perpendicular to $\mathbf{k}$ and $\mathbf{B_0}$, and then they are classified as transverse waves. The resulting plasma motion and magnetic field perturbations occur perpendicular to the field lines, but without associated variations in density or pressure.

Pure sound waves can also propagate longitudinally through the plasma, transmitting pressure variations only (KAMIDE; CHIAN, 2007, p. 401). They are defined with $\mathbf{u_1}$ parallel to $\mathbf{k}$ and $\mathbf{B_0}$, and the corresponding sound speed V_S is given by:

$$\frac{\omega}{k} = V_S;\ V_S = \left(\frac{\gamma' P}{\rho_{m0}}\right)^{1/2}. \tag{2.19}$$

On the other hand, for the case of $\mathbf{k}$ perpendicular to $\mathbf{B_0}$, longitudinal waves in which $\mathbf{u_1}$ is parallel to $\mathbf{k}$ refer to ULF waves propagating in the fast mode, with phase velocity defined as:

$$\frac{\omega}{k} = (V_S^2 + V_A^2)^{1/2}. \tag{2.20}$$

This mode yields compressions and rarefactions of the field lines and the fluid, with associated disturbances in the magnetic field and density. In reality, the three modes above can be described in a more general way than shown in Equations 2.18 to 2.20, by considering the propagation of oblique waves so that the angle between $\mathbf{k}$ and $\mathbf{B_0}$ is not necessarily 0° or 90°.

However, the plasma in the magnetosphere is rather inhomogeneous, which means that the assumptions made for $\mathbf{B_0}$, ρ_{m0} and $\mathbf{u_0} = 0$ from the equilibrium state may not be valid. For example, Alfvén waves propagate in this medium with $V_A \approx 1,000$ km/s and corresponding wavelengths of $\approx 15 - 25 R_E$ for oscillations with periods of ~ 100 s. This illustrates the large-scale nature of ULF waves, which are responsible for producing quasi-sinusoidal signatures in magnetic field measurements reported in situ or on the ground, known as magnetic pulsations. Magnetic pulsations, in turn, are well explained when considering Alfvén and fast modes as being coupled, which arises naturally from the inhomogeneous condition of the plasma (KAMIDE; CHIAN, 2007, p. 401).

The propagation of ULF waves in the magnetosphere was first resolved by Dungey (1967). In the proposed model of field line resonances (FLR), the ambient magnetic field $\mathbf{B_0}$ is the Earth's dipole, and the waves are assumed to cause longitudinal variations in $\mathbf{B_0}$, ρ_{m0}, or in $\mathbf{u_0}$, in the form $\exp i(m\phi - \omega t)$, where m is the azimuthal wave (or mode) number, ϕ is the angle in the azimuth and ω the angular frequency of the wave. The field lines are considered to have footpoints fixed in the perfectly conducting ionosphere, which serves to define the boundary conditions for

the eigenperiods of the modeled system (ALVES et al., 2017; KAMIDE; CHIAN, 2007). The oscillations in this system are thought to correspond to standing Alfvén waves in those geomagnetic field lines.

Figure 2.3 - Representation of ULF wave modes, with respective direction of field perturbations and energy transport along a dipolar geomagnetic field line.

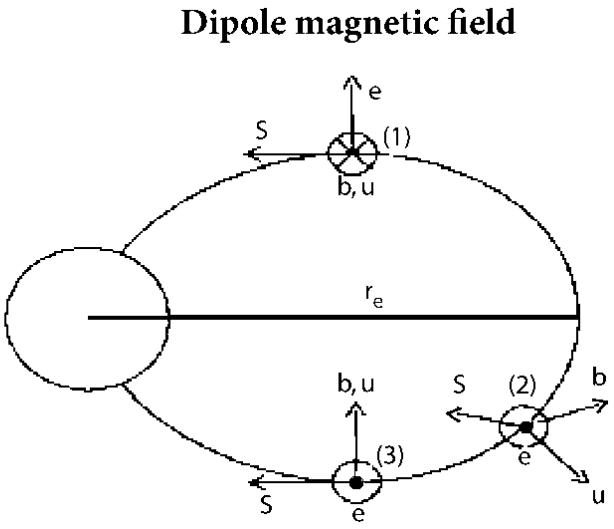

(1) Toroidal mode, (2) compressional mode, (3) poloidal mode; $\mathbf{b}, \mathbf{u}$ and $\mathbf{e}$ stand for the disturbed magnetic field, plasma velocity, and induced electric field. $\mathbf{S} = \mathbf{e} \times \mathbf{b}/\mu_0$ is the Poynting vector. Note that the geocentric distance to the field line in the magnetic equatorial plane indicated by the solid black line can be taken as a representation of the L shell parameter (L).

SOURCE: Adapted from Kamide and Chian (2007, p. 401).

Figure 2.3 shows the solutions for the ULF wave modes in a dipolar magnetic field. They are derived from limit cases of m and lead to three different oscillation modes. In the first case, $m \to 0$ is considered, which specifies the so-called "*toroidal mode*" in which the magnetospheric L shells oscillate independently, accompanied by global azimuthal perturbations in the magnetic field and the plasma velocity, as well as induced electric field in the radial direction. The schematic representation of this mode is seen in scheme (1) of that Figure, where $\mathbf{b}$, $\mathbf{u}$ and $\mathbf{e}$ correspond to the disturbed parameters previously mentioned. In the same Figure, the scheme (2) illustrates ULF waves in the "*compressional mode*" that also arises from the limit case $m \to 0$. In contrast to the previous mode, these waves are not guided along the field line, as indicated by the Pointing vector $\mathbf{S}$. The magnetic field perturbations

appear along the field line, inducing azimuthal **e** globally, in which both disturbances contribute to the entire oscillation of the cavity (KAMIDE; CHIAN, 2007, p. 401). On the other hand, in (3) is represented the "*poloidal mode*" that corresponds to the case of $m \to \infty$. Large values of mode number are immediately indicative of small-scale disturbances in the plasma and in the geomagnetic field, so that this mode leads to independent azimuthal oscillations of the field lines, constrained to the meridional plane (ELKINGTON, 2006). As represented in Figure 2.3, disturbed **b** and **u** appear in the radial direction, while inducing azimuthal **e**.

To summarize, the ULF waves in the magnetosphere of the toroidal and poloidal modes are recognized as MHD waves in the Alfvén mode, since the propagation occurs parallel to the background geomagnetic field. Conversely, the compressional modes are related to MHD waves in the fast mode due to the perpendicular propagation in relation to the ambient magnetic field.

All these modes are capable of transmitting plasma and electromagnetic disturbances throughout the magnetosphere, characterizing an important way by which the energy from the external impulse of the solar wind is transferred into the system. Indeed, it has been proposed that ULF waves originate externally through the direct transmission of dynamic pressure variations intrinsic to the solar wind, by upstream waves of the foreshock region and also from Kelvin-Helmholtz (K-H) instability in the magnetopause (Takahashi (2016, p. 60), and references therein). It follows that these mechanisms are in fact sources of fast/compressional modes near the dayside magnetopause and transmit energy to the inner magnetosphere by means of FLR, that is, involving wave propagation in the toroidal and poloidal modes. On the other hand, the common mechanism for internal generation of ULF waves mostly accounts for the source of poloidal modes, being credited to drift-bounce resonances with ring current ions.

Table 2.1 presents information about the main types of magnetic pulsations associated with the internal and external mechanisms of ULF wave excitation described previously, as originally classified by Jacobs et al. (1964). In addition, the range of typical amplitude values for each continuous pulsation type is also provided. It should be highlighted the two classes shown that can directly affect the motion of high-energy electrons and lead to losses in the outer radiation belt: EMIC waves, defined within the high-frequency bands given by Pc1 and Pc2, and Pc5 waves (LOTO'ANIU et al., 2010; THORNE, 2010).

As previously introduced, EMICs are driven by unstable ring current proton distri-

Table 2.1 - Wave properties of geomagnetic continuous pulsations. Typical ranges of amplitude are from ground-based measurements.

Name	**T(s)**	**Frequency**	**Amplitude * (nT)**
Pc1	$0.2 - 5$	$0.2 - 5$ Hz	$0.001 - 1$
Pc2	$5 - 10$	$0.1 - 0.2$ Hz	$0.1 - 1$
Pc3	$10 - 45$	$22 - 100$ mHz	≤ 10
Pc4	$45 - 150$	$7 - 22$ mHz	$5 - 20$
Pc5	$150 - 600$	$2 - 7$ mHz	$\leq 10 - 50$

(*)Volwerk (2016, p. 142) and reference therein.

butions in the magnetosphere, with this internal process being called ion-cyclotron instability (SAMSON, 1991). Pc5 waves are mainly associated with compressional and toroidal modes in the inner magnetosphere (ANDERSON, 1994). The compressional magnetic field perturbation is often accompanied by a comparable radial polarization, as illustrated in Figure 2.4. Even if the compressional mode arises in the FLR theory from the $m \to 0$ limiting case, compressional Pc5 waves with radial polarization can also be composed of high-finite m values (e.g., $50 - 100$). In this case, these waves are most probably originated from the mixing with the poloidal mode. Compressional Pc5s are also typically dominant close to geosynchronous, which favors the magnetotail as the source region of energy transmission rather than the dayside magnetopause. Conversely, toroidal Pc5s are global oscillations of the fundamental mode and observational evidence links these waves to a source region on the flanks of magnetopause, as a result of K-H instabilities.

As a final remark, it should be noted that many of the processes in the magnetosphere, discussed so far, can be reproduced by global MHD models, using upstream conditions of the solar wind as input. The MHD equations are solved throughout the extent of the inner magnetosphere and beyond, in a coupled manner, which make this modeling framework more robust than any other empirical model discussed (although all of them are necessary for analysis here). Global MHD codes can ultimately resolve the propagation of ULF waves, especially from the Pc5 range if limitations in the time-resolution of the MHD simulation is a concern. In Chapter 4, results and discussions of events in the magnetosphere investigated with MHD modeling will be presented. The goal of this analysis will be to quantify the diffusion coefficients from the resonance interactions involving these waves and outer radiation belt electrons.

Figure 2.4 - Observations of compressional Pc5 waves.

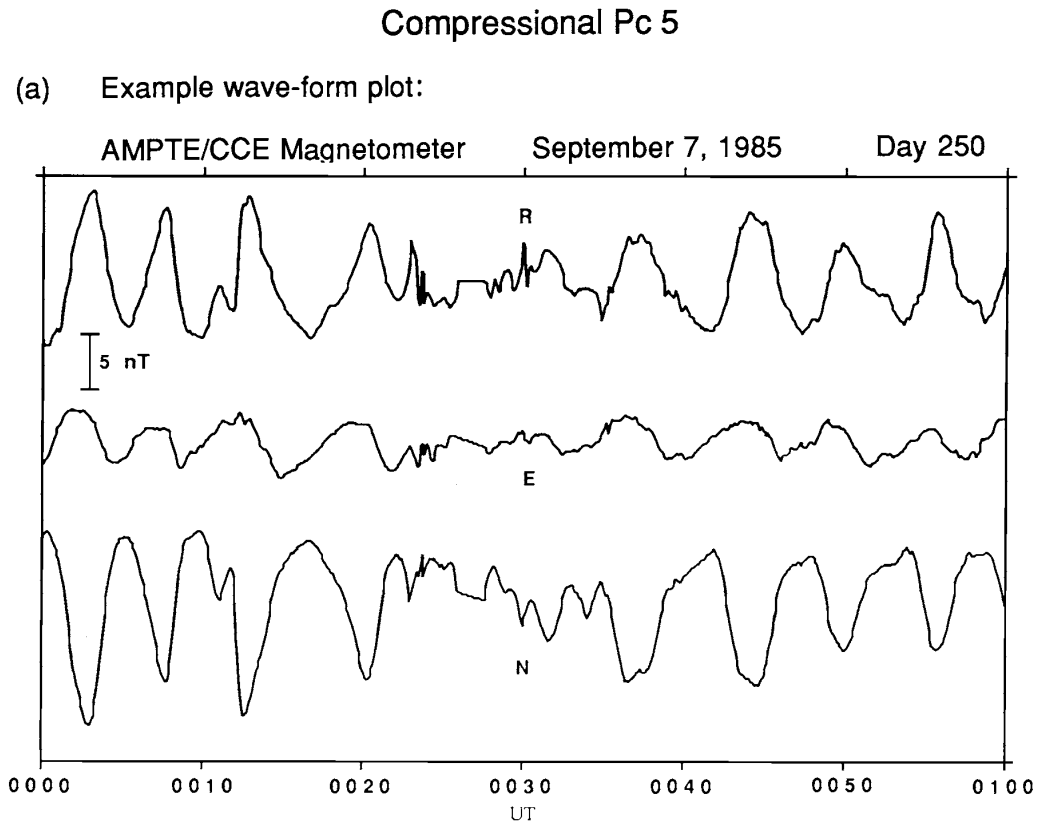

The magnetic field fluctuations are given in the field-aligned reference frame, with R, E and N indicating propagation in the radial, azimuthal-east and parallel direction with respect to that of the local geomagnetic field. A similar plot for toroidal Pc5 can be viewed in Anderson (1994, p. 41).

SOURCE: Adapted from Anderson (1994, p. 27).

2.2 The Van Allen radiation belts

The Earth's Radiation Belts consist of relativistic protons and electrons trapped by the geomagnetic field inside the magnetosphere. The structure of these doughnut-shaped populations is that of high-energy protons concentrated in the inner zone ($L < 2$), followed by the slot region within $2 \leq L \leq 3$, generally absent of very energetic particles, and beyond $L \sim 3$ to typically $L = 6.5$ where there is an outer zone populated by high-energy electrons, referred to as the outer radiation belt (VAN ALLEN, 1959; BAKER et al., 2018). The outer zone and the slot region become very dynamic under the occurrence of geomagnetic storms, so that the stated limits and particle flux conditions can change considerably during these periods. The in-

ner zone is commonly more stable to storm-time flux variations, except for intense geomagnetic storms (Turner et al. (2012a) and references therein).

It is known that the electron fluxes at $\sim$ MeV and multi-MeV levels of the outer belt undergo significant decreases, enhancements or even no considerable changes during the cycle of a magnetic storm (REEVES et al., 2003). The sudden depletion or even extinction of the belt, affecting several energy levels, is more likely to occur during the storm main phase and it is called flux *dropout* (OZEKE et al., 2017; OLIFER et al., 2018). As the recovery phase progresses, acceleration mechanisms dominate the dynamics of the electrons and flux enhancements can refill the outer zone of MeV particle populations. Nonetheless, less active periods (say $Dst > -50$ nT) can also have impact on the outer belt by generating dropouts, as long as there is an associated driver in the solar wind (e.g., the isolated pressure pulse that originated a dropout on 20 September 2007, studied by Albert (2014)).

To exemplify the behavior of the radiation belts during a magnetically active period, Figure 2.5 shows the time and spatial evolution of the 2.1 MeV electron flux acquired with Van Allen Probe A over a short period (21 days) of observations of the outer belt. The associated geomagnetic activity and other measured solar wind parameters are also shown for this time interval. The Dst index shows that this was an active period, but with only minor magnetic storms ($Dst > -50$ nT). Panel (a) presents the evolution of the 2.1 MeV electron flux and can be used to check several aspects previously mentioned about relativistic populations within the belt: (i) the outer belt with higher fluxes was concentrated above $L \sim 3.5$ throughout this time interval; (ii) the slot region with lower fluxes is clearly identified between $L \sim 2.5 - 3.5$; (iii) the outer belt is very dynamic even during this period of low magnetic activity. In this regard, panel (a) shows a large 2.1 MeV population dropout in the outer belt (from $L > 4$ to $L < 6$) from 11/04 onwards, which lasts until 11/16. In panel (b), cutoffs at $L \sim 5$ of electron fluxes obtained for $1.8-4.2$ MeV energies show depletion of the outer belt content throughout this period in $\sim$ 2 orders of magnitude, whose effect increases with increasing energy. These are typical signatures of flux dropouts, which for this interval mainly affected more external populations. After 11/16, the outer belt is refilled to previous flux levels, indicating that acceleration mechanisms were in progress (see panels (a) and (b)). The other panels (c-g) allow to relate the flux variations identified with the passage near Earth of solar wind transients and the associated geomagnetic activity.

Figure 2.5 - Overview of the outer belt flux at 2.1 MeV from Van Allen Probe A, solar wind and geomagnetic conditions during $1-21$ November 2014.

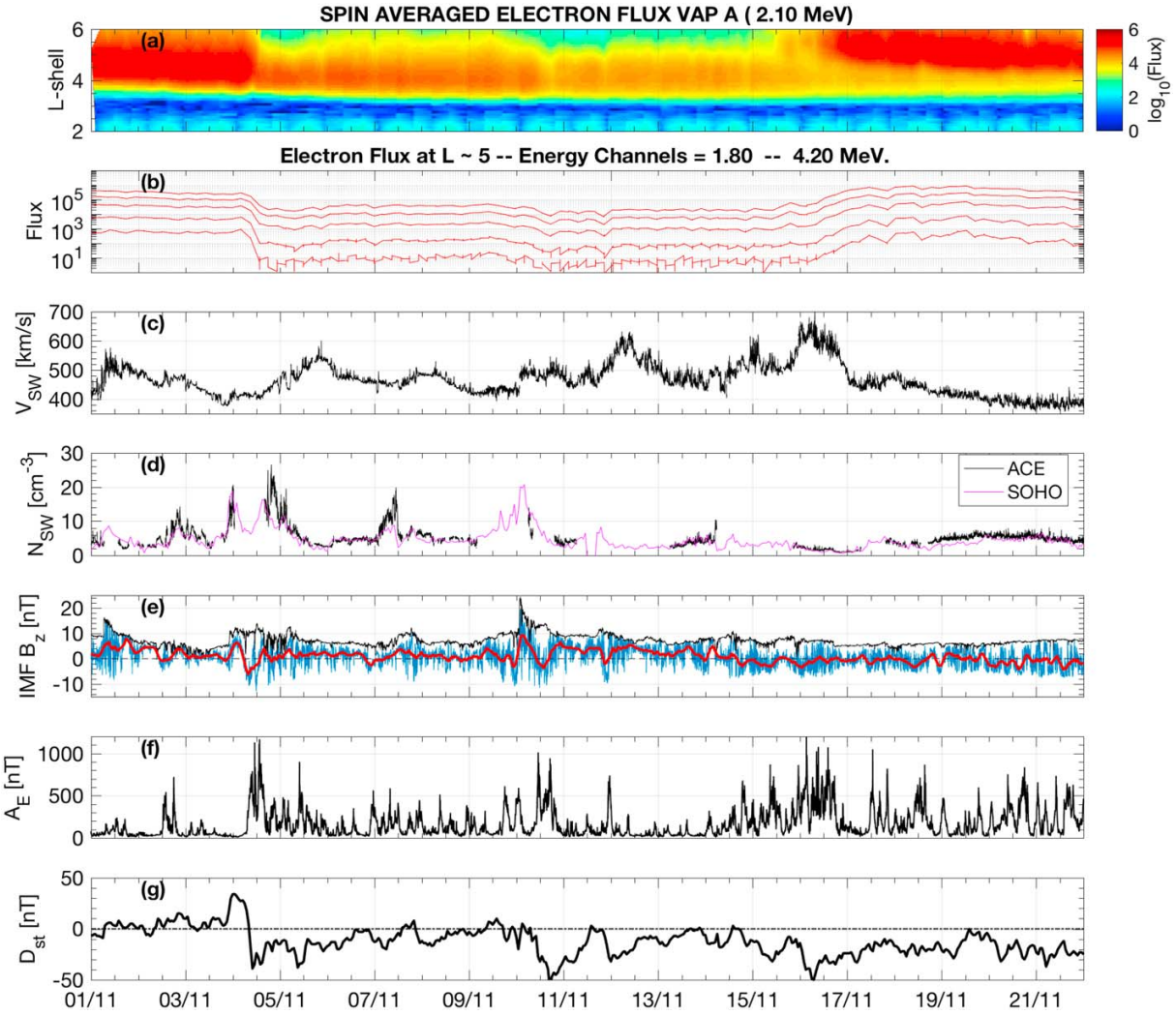

(a) Dynamic map of the electron flux (units of $[1/s.sr.cm^2.MeV]$) given in the time and L shell space; (b) Cutoffs of $1.8-4.20$ MeV electron fluxes at $L \sim 5$; (c-e) solar wind speed, density, and IMF-B_z acquired by both SOHO and ACE spacecraft. In panel (e), the black curve shows the magnitude of the IMF, the blue curve shows IMF-Bz with a 16 s time resolution, and in red is the 4h running average of IMF-B_z; (f-g) geomagnetic indices AE and Dst, respectively. Date format: dd/mm (plot); mm/dd (text).

SOURCE: Courtesy of Souza et al. (2017).

On the other hand, the formation of the outer radiation belt has long been associated with radial diffusion, which nowadays is known to act either to energize electrons from an external source or to transport those in previous stable orbits

outside the inner magnetosphere (GREEN; KIVELSON, 2004; SHPRITS et al., 2006; LEJOSNE; KOLLMANN, 2020). Hence, radial diffusion is a key mechanism to describe flux enhancements and losses in the outer belt on a daily basis. In addition, radial diffusion modeling has become a feasible way to evaluate the structure of the outer belt, especially during storm time (BRAUTIGAM; ALBERT, 2000). In the next section, the adiabatic motion and the main dynamics governing the acceleration, transport and loss of radiation belt electrons will be revised, with a final focus on radial diffusion driven by ULF waves and its relationship with dropouts.

2.2.1 Adiabatic motion in the Van Allen belts

The nearly dipolar configuration of the geomagnetic field in the inner magnetosphere allows charged particles to execute three quasi-periodic motions relative to the magnetic field lines: (i) cyclotron, (ii) bounce between mirror points to the north and to the south of the magnetic equator, and (iii) azimuthal drift around the Earth's magnetic dipole axis. The equation of motion for relativistic particles under the action of background fields $\mathbf{E}$ and $\mathbf{B}$ is given by (FOK, 2020, p. 232):

$$\begin{cases} d\mathbf{p}/dt = q(\mathbf{E} + \mathbf{v} \times \mathbf{B}) \\ d\mathbf{r}/dt = \mathbf{p}/m_{rel} \end{cases} \tag{2.21}$$

where $\mathbf{p}$, $\mathbf{v}$, $\mathbf{r}$, m_{rel} represents the particle's relativistic momentum vector (p denotes its magnitude), velocity, position, and mass, respectively, and q stands for the charge.

Thus, the perpendicular component of the Lorentz force (which solves $p_\perp$) explains the particle's gyration around the magnetic field line, while the parallel component (which solves $p_\parallel$) explains the cyclic motion along a field line presenting curvature. Note that $p_\perp = p \sin\alpha$ and $p_\parallel = p \cos\alpha$, in which α is from now on the local pitch angle defined between $\mathbf{v}$ and $\mathbf{B}$. The drift motion in relativistic particles is mostly a result of the magnetic drift velocity, due to the gradient and curvature characteristics of the geomagnetic field (LEJOSNE; KOLLMANN, 2020).

Each periodic motion sets up a very separate time scale, such that for 1 MeV electrons located at 6 R_E the gyration frequency will be $\sim$ 1 kHz, the bounce frequency $\sim$ 1 Hz and the drift frequency $\sim$ 1 mHz (KANEKAL; BAKER, 2016). In this condition, the Hamiltonian mechanics determines adiabatic invariants of the action integral over each of the cycles, valid as long as oscillations in $\mathbf{B}$ and/or $\mathbf{E}$ are negligible during one period of each motion (ROEDERER; LEJOSNE, 2018). Furthermore, the

length scale of these field fluctuations L_f must not approximate the gyroradius ρ_c, that is, $\rho_c \ll L_f$.

The adiabatic invariants relative to the gyration, bounce and drift are defined respectively as:

$$\mu = \frac{p_\perp^2}{2m_0 B}, \tag{2.22}$$

$$J = \oint p_\parallel ds, \tag{2.23}$$

$$\Phi = \oint \mathbf{B} \cdot d\mathbf{S}. \tag{2.24}$$

In Equation 2.22, B is the local magnetic strength and m_0 is the rest mass, while in Equation 2.23 ds is the element of the arc of the field line, and in Equation 2.24 Φ is the magnetic flux enclosed by the particle's drift shell through the area element $d\mathbf{S}$. The drift shell is the closed surface of the particle drift around an L shell. Figure 2.6 shows a representation for the case of a drift shell defined in a dipole. Based on the conservation of Φ, Roederer (1970) introduced an L parameter called L^* that is adiabatically conserved for time-dependent and asymmetric $\mathbf{B}$, which determines the drift shell as given by:

$$L^* = \frac{2\pi k_0}{\Phi R_E}, \tag{2.25}$$

in which L^* is also dependent on the Earth's dipole moment (k_0) and the Earth radius (R_E).

For constant p, it is possible to derive other constants from the conservation of invariants μ and J, such as the geometric integral $I = J/(2p)$ and the magnetic field strength at the mirror point $B_m = p^2/(2m_0\mu)$ (where α reaches 90°), which yields the quantity independent of p, $K = I\sqrt{B_m}$ (ROEDERER, 1970; LEJOSNE; KOLLMANN, 2020). The equatorial α (α_{eq}) should also be mentioned, which is the pitch angle with which a particle crosses the magnetic equator during a bounce. Particles with small enough α_{eq} can be lost to the high-latitude atmosphere within a bounce period. That happens when this angle is below the loss cone angle, that is,

the minimum equatorial pitch angle required for the particle return from the mirror point and not escape into the atmosphere (JORDANOVA et al., 2020, p. 60). In turn, μ determines the kinetic energy of the particle associated with the local α.

Figure 2.6 - Drift shell formed by the trajectory of a mirroring particle in a dipole.

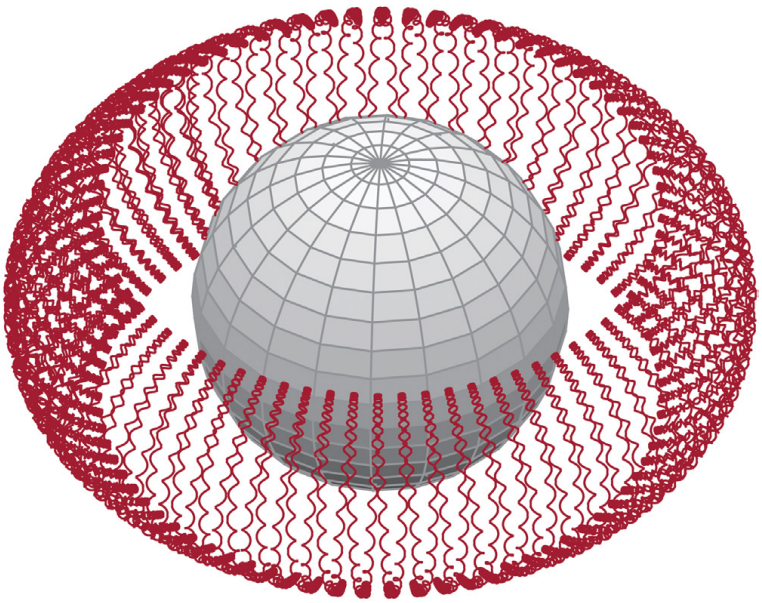

SOURCE: Jordanova et al. (2020, p. 61).

The α_{eq} is also the pitch angle that can be related to K. In Table 2.2 are presented estimations of $K(\alpha_{eq})$ values computed for the point $r = 6.6R_E$, MLT= 0 UT, with the dynamic magnetosphere model from Pfitzer et al. (1988), relative to a quiet condition on 2017/01/26. In this table, $\alpha_{eq} = 5°$ gives an estimate of the loss cone angle at geosynchronous since below this value K could not be defined. Notice that K is in general symmetric with α_{eq}, so that the K values for $90° < \alpha_{eq} \leq 180°$ would range similar to those shown for $\alpha_{eq} \leq 90°$. Note also that for $K \lesssim 0.06$ the particles realize the bounce practically upon the magnetic equator, similarly to 90° equatorial pitch angles of $K = 0$.

Table 2.2 - Second invariant K respective to several equatorial pitch angles at geosynchronous.

α_{eq} $[deg]$	$K(\alpha_{eq})$ $[R_E G^{1/2}]$
5	4.05
10	1.64
20	0.55
30	0.25
40	0.12
50	0.06
60	0.03
70	0.01
80	0.002
90	0.000

Another global characteristic of the geomagnetic field is the noon-midnight asymmetry arising from the compression of the magnetopause on the dayside and the stretching on the nightside. For radiation belts, this asymmetry basically causes the distortion of the drift shells from the circular form presented in Figure 2.6, along with an effect called drift shell splitting (ROEDERER, 1970). Because of this effect, drift orbits of low and high equatorial pitch angles are well separated, being more circular and located at smaller L^* for low α_{eq} (high K) than for high α_{eq} ($K \to 0$), which in turn lies typically at higher L^*. This is the explanation of why L^* depends on $K(\alpha)$.

Another aspect to be discussed is the basic distinction between the L parameters that will be mentioned in the analysis and discussions of the results. The dipole L represents a reasonable approximation of the drift shell location in regions where the magnetic field is dipolar, expressed as $L = r_e/R_E$, in units of R_E (where r_e is the geocentric radial distance to the drift shell at the equator and L represents this equatorial distance normalized). When considering more sophisticated geomagnetic field models, the McIlwain L (McILWAIN, 1961) has been widely used to represent the drift shell, but still does not account for the conservation of Φ and the asymmetry of the field (ROEDERER; LEJOSNE, 2018). Therefore, when used for this purpose, it also represents an approximation of L^*. Thus, the Roederer's L^* calculated here with TS04 provides a more realistic estimate for the drift shell.

2.2.2 Relativistic electron diffusion and dynamics

It is necessary to define the differential-directional flux j coming from a given direction in space and collected by a detector. This parameter $j = j(E, \alpha, \vec{r})$ represents the measured number of particles dN of kinetic energy between E and $E + dE$, per unit energy dE, per unit time dt, and unit solid angle $d\Omega$, that cross a surface of unit area dA perpendicular to the incidence direction, as follows:

$$j = \frac{dN}{dA \cos\theta_n d\Omega dE dt}, \tag{2.26}$$

where θ_n is the angle between the normal of dA and the direction along which $d\Omega$ is oriented. The Liouville's Theorem for trapped particles states that the phase space density (hereafter PhSD) given by j/p^2 is a constant across the dynamical path of particles conserving μ, K, and L^*, in the absence of external sources or losses (ROEDERER, 1970; TURNER et al., 2012a).

PhSD is conserved as long as each invariant is also conserved. However, given that plasma waves are ubiquitous in the near-Earth space, violation involving the three invariants or a combination of them is likely to occur (SHULZ; LANZEROTTI, 1974). The immediate consequence is the particle diffusion across the invariant space determined by (μ, K, L^*), which breaks down the conservation of PhSD. To explain this, consider τ_c, τ_b, τ_d as the gyro, bounce and drift periods respectively, and small fluctuating fields of timescale δt in stochastic resonance with the periodic motions of particles, which are specified by a given PhSD. As $\tau_c \ll \tau_b \ll \tau_d$, if $\delta t \lesssim \tau_d$, only Φ and L^* are violated, causing diffusion in L^*, or hereafter *radial diffusion*. For $\delta t \lesssim \tau_c$, μ and K are also violated, and the particles are furthermore subjected to energy and pitch angle diffusion, respectively.

Thorne (2010) outlined the main plasma waves that play a major role in wave-particle interactions leading to relativistic electron diffusion across the outer belt. It can be highlighted the role of ULF waves in radial diffusion, as well as of VLF chorus, EMICs and plasmaspheric hiss for pitch angle diffusion/scattering, and their consequences for PhSD in terms of either gain or loss.

The drift-resonance condition satisfied by azimuthally symmetric ULF mixed modes is given by (e.g., Elkington (2006)):

$$\omega = m\omega_d, \tag{2.27}$$

where ω is the wave frequency, m is the associated azimuthal mode number and ω_d is the bounce-averaged drift frequency of the electrons.

Such a stochastic resonance promotes radial diffusion in relativistic electrons, which means random walks in L^* either outward or inward. If outward, radial diffusion causes adiabatic deceleration of electrons on the path out of the inner magnetosphere, since μ and K are not violated. It also contributes to electron losses near the magnetopause down to $L^* = 4-5$ during periods of both enhanced compression of this boundary and ULF wave activity (SHPRITS et al., 2006; TURNER et al., 2012b; OZEKE et al., 2014b; XIANG et al., 2018).

Inward radial diffusion is responsible to accelerate electrons from a source population adiabatically, that is, by moving them to magnetospheric regions of stronger magnetic fields, while conserving μ and K. This happens because radial diffusion is a stochastic process, which always tends to smooth out peaks left in the PhSD, causing the displacement of electrons from regions of higher to lower PhSD (REEVES et al., 2013). Thus, radial diffusion can also act as an acceleration mechanism, evidenced by monotonic gradients in PhSD (i.e., $\partial PhSD/\partial L^*$ at fixed μ and K) of positive slope at $L^* \lesssim 5$, as recently obtained with NASA Van Allen Probes observations (e.g., Boyd et al. (2018)). However, growing peaks in the PhSD measured within this region cannot be explained only by inward diffusion and it has been recognized that gyro-resonant interaction with chorus waves locally produce this extra gain in PhSD (GREEN; KIVELSON, 2004; REEVES et al., 2013; LI et al., 2014b).

Studies carried out in the last decades have shown that electron flux enhancements are well correlated with enhanced Pc5 wave power, which shed light on the role played by drift-resonant interactions for electron energization in the outer belt (Elkington (2006) and references therein). Elkington et al. (1999) and Elkington et al. (2003) quantified and demonstrated the potential of acceleration from the drift-resonance by Pc5s in the toroidal mode, which was also extended to the asymmetric resonance case. Moreover, it was found that Pc5 in the poloidal mode can contribute both to outward radial diffusion and acceleration of outer belt electrons. However, this is less significant than effects of compressional and toroidal modes because the wave power carried by high-m poloidal modes is much low (ELKINGTON, 2006). Enhanced Pc5 wave activity was also invoked to explain sudden losses observed with GOES and NOAA-POES spacecraft during geomagnetic storms (TURNER et al., 2012b).

On the other hand, the gyroresonance condition satisfied by VLF chorus, EMICs

and VLF hiss (considering the relativistic limit) is described as (SUMMERS et al., 1998):

$$\omega - kv_{\parallel} = \frac{n\Omega}{\gamma}, \tag{2.28}$$

in which ω is the wave frequency, k is the wave number in the direction of propagation, and $v_{\parallel}$ is the parallel and resonant velocity, along with n as the cyclotron harmonic and Ω as the electron gyrofrequency.

The three high-frequency wave types are capable of transporting relativistic electrons into the loss cone through pitch angle scattering (e.g, Baker et al. (2018)), which primarily involves violation of K, in addition to μ and Φ, as a result of the gyroresonance. VLF chorus can furthermore lead to significant energy diffusion of the relativistic electrons in regions of low plasma density as it occurs outside the plasmapause (SUMMERS et al., 1998). This represents an effective mechanism of acceleration acting on low-energy seed electrons injected from the plasma sheet during substorms or enhanced convection (JAYNES et al., 2015). Currently, it is believed that the acceleration by VLF chorus emissions produce the multi-MeV electrons reported in the outer belt, as well as the growing peaks in the radial profiles of PhSD, not explained by radial diffusion (BOYD et al., 2018). Table 2.3 summarizes the diffusion processes generated by each wave aforementioned through resonant interactions, highlighting their role in electron flux dropouts.

Table 2.3 - Plasma waves recognized to be mainly effective for driving flux dropouts of outer belt electrons.

Wave	**Frequency**	**Violate**	**Efficient electron loss by**	**Efficient electron loss to**
Hiss/Chorus Emissions	$0.1 - 10$ kHz*	μ, K, Φ	pitch angle diffusion (scattering)	atmosphere
EMICs	$0.1 - 5$ Hz	μ, K, Φ	pitch angle diffusion (scattering)	atmosphere
ULF, Pc5	$\sim 2 - 7$ mHz	Φ	*outward* radial diffusion	magnetopause

(*) It considers the Extremely-low frequency (ELF) range ($0.1 - 1$ kHz), apart from the VLF range ($1 - 10$ kHz).

In this situation of stochastic wave-particle interactions, the quasi-linear theory is sufficient to model slower processes on the order of hours to days affecting the time

and spatial evolution of PhSD (e.g., Agapitov et al. (2015)). The Fokker-Planck equation applied to the drift motion describes the drift-averaged PhSD (f) in time and space, which is written out as (SHULZ; LANZEROTTI, 1974; FOK, 2020):

$$\frac{\partial f}{\partial t} = \sum_{ij=1}^{2} \frac{\partial}{\partial J_i} D_{ij} \frac{\partial f}{\partial J_j} + \frac{\partial}{\partial J_3} D_{33} \frac{\partial f}{\partial J_3} - \frac{f}{\tau} + S, \tag{2.29}$$

where J_1,J_2 and J_3 represent the three adiabatic invariants μ, K and L^*, respectively, $f = f(t, J_1, J_2, J_3)$ is the PhSD, D_{ij} are the cross-diffusion coefficients between $J_1 = \mu$ and $J_2 = K$, D_{33} is the drift-averaged radial diffusion coefficient model (hereafter named D_{LL}), τ represents electron lifetimes used to define the loss term on the right-hand side of the equation and S is the source term.

Solving the full Fokker-Planck equation requires implementation of a 3D model, such as DREAM3D (TU et al., 2013; TU et al., 2014). 3D modeling can be robust enough to reproduce dropouts and enhancements in PhSD comparable to observations, as long as the wave power of all types of wave-particle resonances investigated are properly quantified. This is because the wave power of the ULF wave modes and high-frequency wave modes serve as input for the radial diffusion and cross-diffusion coefficient models, respectively. Consequently, the global representation of such wave modes is required, in which the observations in the inner magnetosphere as provided by the Van Allen Probes are crucial, together with the proposition of empirical models of the observed wave power distribution. This scenario becomes easier to handle when the diffusion is considered, for example, across L^* only. This is the case of the 1D radial diffusion modeling considered in this work.

2.2.2.1 Causes of flux dropouts

Flux dropouts in the radiation belts were first related to the diamagnetic effect of the ring current during storm time, i.e, with the global decrease of the geomagnetic field induced by the storm-time symmetric ring current (Turner et al. (2012a) and references therein). The *Dst* effect (Dessler and Karplus (1961), McIlwain (1966), Li et al. (1997)) generates flux dropouts fully adiabatic that often take place at the geosynchronous orbit during the main phase of storms (KIM; CHAN, 1997). In this process, electrons are not actually lost to the atmosphere or the magnetosheath. In a given drift shell, once the local magnetic field intensity decreases in response to the storm main phase, the absolute value of the magnetic flux enclosed by the drift shell decreases, causing the drift shell to expand radially outward to conserve the

previous value of Φ (its third invariant). In the meantime, electrons decelerate to conserve μ, as explained previously for the outward diffusion. This is the cause of adiabatic losses in the main phase, which are removed from observations of PhSD so that nonadiabatic processes can be distinguished (e.g., Chen et al. (2006)). During the recovery phase, this drift shell moves back to prestorm radial locations where the electrons are accelerated to prestorm energies (ROEDERER, 1970, p. 79).

Concerning nonadiabatic processes, there are two major classes of flux dropouts that can operate together in the storm main phase: magnetopause shadowing-driven and EMIC wave-driven (XIANG et al., 2017). Magnetopause shadowing (e.g., Turner et al. (2012b), Hudson et al. (2014), Alves et al. (2016), Kang et al. (2018), Tu et al. (2019)) is the process that causes expressive outer belt electron dropouts across the magnetopause, close to the equator, whenever this boundary is highly compressed on the dayside. As a result, drift shells affected by this mechanism are no longer closed and L^* cannot be defined. Low-K populations characteristic of high-L^* are most commonly affected, but significant shadowing dynamics can also lead to dropouts of high-K relativistic electrons located at low-L^* (e.g., the intense geomagnetic storm on 22-23 June 2015 investigated by Xiang et al. (2017) and Tu et al. (2019)). Such a mechanism becomes highly effective for sudden losses through the act of outward radial diffusion (SHPRITS et al., 2006; TURNER et al., 2012b). Outward diffusion thus operates as a secondary mechanism that moves electrons from $L^* \sim 4-5$ of higher PhSD to be lost across the last closed drift shell (maximum L^*; say $L^* \sim 5-6$) of lower PhSD due to the shadowing.

In terms of fast outer belt depletions on timescale of a few hours or less, pitch angle scattering by EMIC waves is the other dynamic mechanism of major concern (Tu et al. (2019) and references therein). It mainly affects high-K and high-μ populations, therefore multi-MeV electrons at low-L^*, specifically in the heart of the outer belt within $L^* \sim 4-4.5$ (TURNER et al., 2014; SHPRITS et al., 2017; XIANG et al., 2018). Pitch angle scattering causes ultimate electron losses to the atmosphere through precipitation from the loss cone (SHULZ; LANZEROTTI, 1974, p. 60).

Slower atmospheric losses are generally driven by pitch angle scattering from the electron-gyroresonance with whistler mode chorus and plasmaspheric hiss (THORNE, 2010). The timescale involved is days for chorus and tens of days for hiss waves during active times and MeV energies, which also depends on L (SHPRITS et al., 2007; ORLOVA et al., 2014). Chorus wave modes are likely to pitch angle scatter outer belt electrons outside the plasmapause, predominantly on the dawn side, while hiss

modes are most effective inside the plasmasphere and within plasmaspheric plumes.

2.2.3 Quantifying ULF wave-driven radial diffusion

The timescale of dropouts caused by the outward radial diffusion in conjunction with magnetopause shadowing is in the order of hours (OLIFER et al., 2018). However, similar to the slower atmospheric losses, outward diffusion produces gradual decreases in the outer belt PhSD (LI et al., 2014b; MANN et al., 2016; SHPRITS et al., 2017). These gradual changes in PhSD driven by radial diffusion are related to the magnitude of the radial diffusion rates of the electrons, that is, D_{LL}. The meaning of D_{LL} can be represented with the formula:

$$D_{LL} = \frac{\langle (\Delta L)^2 \rangle}{2t}. \tag{2.30}$$

Thus, D_{LL} represents the mean squared displacement of the radiation belt particles over a timescale t much greater than their drift period (e.g., Tu et al. (2012)). Since the L parameter is a normalized quantity, D_{LL} is commonly given in units of $[days^{-1}]$. On the other hand, assuming equatorially-mirroring relativistic electrons, the contribution of the ULF wave symmetrical resonance modes to D_{LL} is quantified as (FEI et al., 2006):

$$D_{LL}^{E} = \frac{L^6}{8B_E^2 R_E^2} \sum_{m=1} P_m^E(m\omega_d), \tag{2.31}$$

$$D_{LL}^{B} = \frac{\mu^2 L^4}{8e^2\gamma^2 B_E^2 R_E^4} \sum_{m=1} m^2 P_m^B(m\omega_d), \tag{2.32}$$

$$D_{LL} = D_{LL}^{E} + D_{LL}^{B}, \tag{2.33}$$

where D_{LL}^{E} and D_{LL}^{B} are the resulting electric and magnetic radial diffusion coefficients, respectively, whose sum gives the total D_{LL} as shown in Equation 2.33. They are proportional to the sum of the power spectral densities (PSD: P_m^E and P_m^B terms) of the ULF waves in the azimuthal electric field and the compressional magnetic field components, taken at the drift-resonant frequencies that satisfy the condition in Equation 2.27. L represents the model for the drift shell adopted (e.g., dipole L), B_E is the equatorial strength of the Earth's magnetic field at the surface, e is the electron charge, and γ is the Lorentz relativistic factor. In this formalism, a random correlation is assumed between electric and magnetic disturbances, although

this cannot be confirmed in practice (LEJOSNE; KOLLMANN, 2020).

For this calculation, it is essential to know the angular drift frequency at a given L on the equator, which for 90° pitch angle electrons and a given μ (first invariant) is expressed as:

$$\omega_d = \frac{-3\mu}{e\gamma(LR_E)^2}. \tag{2.34}$$

A pure dipole magnetic field is assumed in this expression (OZEKE et al., 2014a).

2.2.3.1 Empirical and statistical models of D_{LL}

In this section, the empirical and statistical models of radial diffusion coefficients used in this study are presented. They are all parameterized by the *Kp* geomagnetic index, which is considered a good proxy of ULF wave activity to quantify radial diffusion (DIMITRAKOUDIS et al., 2015).

The first model investigated was proposed by Brautigam and Albert (2000). The formalism behind calculating radial diffusion coefficients using this model differ from FEI et al.'s (2006), in the sense that D_{LL} is separated into *electromagnetic* and *electrostatic* counterparts, such as introduced by Falthammar (1965). Specifically, in relation to the derivation of the electromagnetic coefficients, or as of now D_{LL}^{M}, the authors used in-situ measurements of compressional magnetic field PSD of the geosynchronous orbit ($L = 6.6$), while magnetic field measurements from ground magnetometers mapped to the equatorial plane accounted for the inductive oscillations of the electric field at $L \sim 4$ (OZEKE et al., 2014a). In particular, this model considers that all power contained in the compressional magnetic field fluctuations concerns perturbations only in the main field, assuming a single symmetric resonance mode given by $m = 0$.

As it is known that D_{LL}^{M} alone overestimates particle fluxes at $L \lesssim 4$, as simulated by radial diffusion models (OZEKE et al., 2014a), D_{LL}^{static} was omitted in this work from the analysis and discussions. Thus, the electromagnetic radial diffusion estimates defined by Brautigam and Albert (2000) are calculated using the following equation:

$$D_{LL}^{M,BA}(Kp, L) = 10^{(0.506 \times Kp - 9.325)} \cdot L^{10}, \tag{2.35}$$

which is valid for $Kp = 1$ to 6 and covers L shells from 3 to 6.6. Outside this range, the rates are extrapolations of the fit equation. For $Kp < 1$ or $Kp > 6$, the results

of $Kp = 1$ and $Kp = 6$ are used, respectively.

Another empirical model discussed is that proposed by Liu et al. (2016). In this case, the model of electric radial diffusion coefficients was derived from seven-year ($2008 - 2014$) measurements by THEMIS of quasi-azimuthal electric field PSD. It covers a wider range of L shells (3.5 to 7.5), with the Kp values considered going from 0 to 5^+. D_{LL} was obtained in this model assuming $m = 1$, so that PSD values were taken at local resonance frequencies. In addition to traditionally organizing the PSD values found in terms of L, Kp, and MLT, these authors also obtained a parameterization in relation to μ, resulting in the fitting equation below for D_{LL}^{E}:

$$D_{LL}^{E,LIU}(Kp, L, \mu) = 1.115 \cdot 10^{-6} \cdot 10^{(0.281 \times Kp)} \cdot L^{8.184} \cdot \mu^{-0.608}. \tag{2.36}$$

The other model considered in this work is that of Ali et al. (2016). This model is based on three years ($2012 - 2015$) of electric and magnetic field PSD measurements in field aligned coordinates by the Van Allen Probes A and B. Radial diffusion coefficients were obtained for Kp indices not higher than 5. However, unlike the other empirical models presented, the D_{LL} from this model was actually evaluated along the probes' L^* location (within $3 - 5.5R_E$), rather than the often assumed simplified L shell. To this, the authors used the TS04 external magnetic field model in this calculation. Assuming the single-mode number $m = 1$, the acquired model of magnetic and electric D_{LL} components reads as follows:

$$D_{LL}^{B,ALI}(Kp, L^*) = \exp\left(-16.253 + 0.224 \cdot Kp \cdot L^* + L^*\right), \tag{2.37}$$

$$D_{LL}^{E,ALI}(Kp, L^*) = \exp\left(-16.951 + 0.181 \cdot Kp \cdot L^* + 1.982 \cdot L^*\right). \tag{2.38}$$

3 DATA AND METHODOLOGY

The objective of this work is to study flux dropouts related to the magnetospheric coupling with CIRs. These solar wind structures were frequent throughout the descending phase of solar cycle 24, a condition found at the final years of operation of the NASA's Van Allen Probes between 2016 and 2018, and whose data have not yet been fully explored by the space physics community. On the other hand, ULF wave-driven radial diffusion during such loss scenarios is the main dynamic mechanism to be investigated in the outer radiation belt through this methodology. This investigation was carried out from the point of view of data analysis and MHD simulation, to account for the radial diffusion quantification, and through data analysis and radial diffusion simulation, to account for the electron distribution function evaluation.

Based on these objectives, preliminary observations of the evolution of relativistic electron fluxes measured by Van Allen Probe A were made for the time interval of several CIRs cataloged for this thesis. In doing so, two similar CIR events that introduced distinct dropout dynamics into the outer belt were initially selected (called cases 1 and 2). For these events, the event-specific radial diffusion coefficients were calculated from MHD magnetic and electric fields. To validate these results, diffusion coefficients were also obtained from in-situ fields, measured by Van Allen Probe B (EMFISIS and EFW suites - Kletzing et al. (2013), Wygant et al. (2013)) and THEMIS spacecraft (FGM and EFI instruments - Auster et al. (2009), Bonnell et al. ()). It should be noted that the Van Allen Probe A has been without high-level electric field data since 2017. The data set used allowed the analysis of in-situ ULF waves and derived diffusion coefficients inside $3 < L < 9$, as modeled with MHD.

During the analysis, additional case studies of data-driven D_{LL} were necessary (to be explained in Chapter 5), so that two more events were added. The third case chosen (case 3) was driven by an Interplanetary Coronal Mass Ejection (ICME), while the forth event (case 4) was taken from the catalog of CIRs. Significant flux dropouts were observed in case 4, whereas no attempt is made to interpret flux results from case 3 since ICME-driven dropouts are outside the scope of this work (although the analysis of this event is relevant for discussions on data-driven D_{LL}). Thus, no background information is given concerning this ICME. Cases 1, 2, and 4 then compose the set of events investigated using the radial diffusion model.

This chapter will initially give more details about the data assets available for selecting CIR events, as well as those used for particle observations and input conditions in radial diffusion simulations, as provided with the Van Allen Probes and GOES

spacecraft. This is followed by a review of two relevant methods for data analysis, regarding the transformation of the measured fluxes into phase space density (the electron distribution function) and the calculation of ULF wave modes intensities from observed fields. Finally, a review is made of the main theoretical aspects of the proposed radial diffusion modeling and of the last closed drift shell parameter obtained through successive drift shell tracing.

3.1 Data assets

3.1.1 CIRs and related solar wind data

A CIR is formed in the interplanetary medium as a result of the interaction of high-speed streams (HSSs) originating from coronal holes in the Sun and the slow solar wind that emanates from above of streamer belts that encircle the solar magnetic equator (WOO; MARTIN, 1997; RICHARDSON, 2018). These solar wind streams expand radially across the heliosphere with different characteristic velocities ($\sim$ 700 km/s for the fast wind and $\sim 250 - 400$ km/s for the slow wind), temperature and density (HSSs are hotter and less dense), following the $\sim$ 27 days rotation of the Sun as seen from Earth. The two plasma flows (HSS and slow solar wind) end up meeting at very large distances near the ecliptic plane. However, because of the frozen-in condition inherent to both plasmas, the trailing fast wind cannot simply cross the slow wind and consequently, a compression region is formed ahead of the HSS (see top of Figure 3.1 for illustration). In the case of multiple recurrences of the HSS associated with a long-lasting coronal hole in the solar disk, the resulting interplanetary compression regions are referred to as CIRs. Otherwise, the single compression regions are classified as stream interaction regions.

In Figure 3.1, solar wind streams are denoted as S for the slow wind, S' for the compressed and accelerated slow wind, F' for the compressed and decelerated fast wind, F for the unperturbed fast wind, with S' and F' delimiting the interaction regions and R a rarefaction region. The bottom panels show a series of signatures in several solar wind parameters, expected for the passage of CIRs at 1 AU (astronomical unit), following Belcher and Davis (1971). This involves the analysis of time series of (but not restricted to) the bulk temperature (T), velocity (V), density (N), interplanetary magnetic field intensity (B), and transverse flow velocity (V_ϕ). CIRs cause significant enhancements in these parameters, except a decrease in plasma density and a reversal in the direction of propagation of the transverse flow velocity during the passage of the compressed and decelerated fast wind (indicated by F').

Figure 3.1 - Schematic of the formation of two CIRs and expected variations in the parameters of the solar wind at 1 AU.

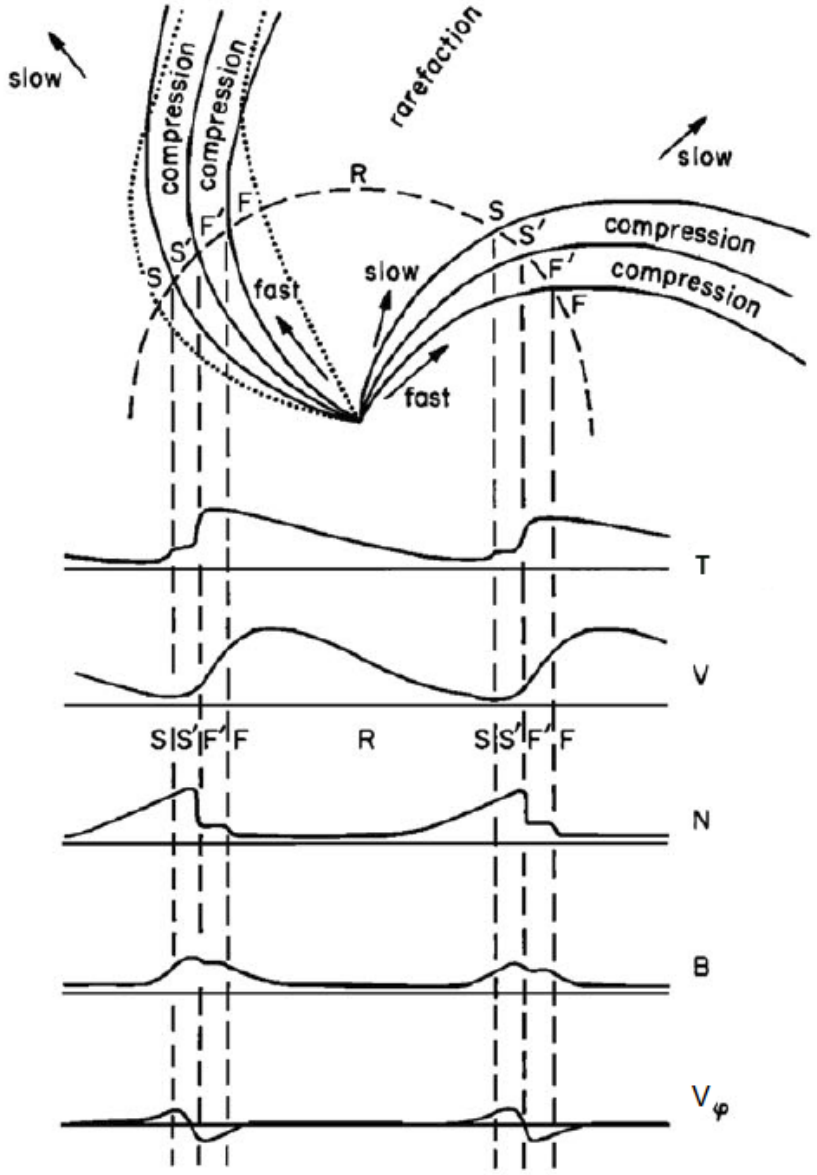

S (slow wind), F (fast wind), and R (rarefaction). S' and F' are denoting the passage and properties of the disturbed solar wind streams within the CIR. Solar wind parameters shown are the bulk temperature (T), velocity (V), density (N), interplanetary magnetic field intensity (B), and transverse flow velocity (V_ϕ). See text for details.

SOURCE: Adapted from Richardson (2018), after Belcher and Davis (1971).

Thus, to select CIR-events corresponding to the solar cycle 24, these properties were inspected in the solar wind data provided by the OMNIWeb database

(https://omniweb.gsfc.nasa.gov/form/omni_min.html), for the $2016-2018$ biennium. One-minute averages of combined spacecraft measurements taken at the L1 Lagrangian point (about 235 R_E from the Earth's surface) were used. This data set has already been time-shifted from the L1 point to the nose of the Earth's bow shock, for proper observations of the solar wind transients during the time of interaction with the magnetosphere. For example, two satellites available for data collection through OMNIWeb from 2016 to 2018 were ACE (1997 - present) and WIND (1995 - present).

As a by-product of these analyses, the recurrences of 11 CIRs were tabulated, which, in total, correspond to the arrival at Earth's bow shock of 46 stream interaction regions during the considered biennium. This is shown in Table B.1 in Appendix B. The coronal hole history catalog provided by Solen.info (http://www.solen.info/solar/coronal_holes.html) was used to identify the recurrence numbers and Earth-directed periods of coronal holes existing in this interval, as shown in the second and third columns of this table. Another catalog available on the DONKI-NASA website (https://kauai.ccmc.gsfc.nasa.gov/DONKI/search/) was used to obtain information on the arrival date of the HSS generated by these coronal holes, as indicated in the forth column. Such a catalog can be used in subsequent follow-up studies on verification, for example, whether the inner magnetosphere responded similarly or not to interactions with those series of CIRs.

3.1.2 Particle flux measurements

3.1.2.1 Van Allen Probes A and B

NASA's Van Allen Probes mission, formerly known as Radiation Belt Storm Probes (RBSP), went into operation on August 30, 2012. Its goal was to perform daily/dual-point measurements of particle fluxes from the inner and outer zones of the radiation belts over several L shells and with better temporal and energy resolutions than those obtained in previous missions (e.g., CRRES, LANL and GOES) (BAKER et al., 2013). Over their operation lifetime ($2012-2019$), the twin Van Allen Probes A and B executed almost identical elliptical orbits with a small inclination of $10^\circ \pm 0.25^\circ$, an apogee altitude of the order of 30,000 km and ~ 600 km for the perigee (STRATTON et al., 2013).

Among the different instruments carried on board, the mission had an Energetic Particle, Composition, and Thermal Plasma Suite (ECT). It consists of three types of detectors dedicated to measurements of flux, energy spectra, and angular distri-

butions of $1 - 50$ keV ions and electrons (HOPE; Funsten et al. (2013)), 30 keV $-$ 5 MeV electrons and 20 keV $-$ 1 MeV ions (MagEIS; Blake et al. (2013)), and $\sim$ 1 to >10 MeV electrons and $20 - 75$ MeV protons (REPT; Baker et al. (2013)). As this work is concerned with the flux changes of relativistic electrons (< 2 MeV), data set either provided by MagEIS and REPT were utilized for the analyses. In addition, transformation of the particle fluxes into phase space density for fixed first and second adiabatic invariants (μ and K) requires continuous measurements of the energy spectra (10s of keV to a few MeV) and pitch angle distribution ($\sim 0°$ to $90°$) for the entire Van Allen Probes orbit, which is effectively achieved using the data set from both instruments.

Although the multiple sensors were designed to minimize background contamination in electron flux measurements due to penetrating radiation and bremsstrahlung photons (BAKER et al., 2013), efforts had to be made to correct the fluxes obtained with MagEIS (CLAUDEPIERRE et al., 2015) and REPT (BOYD et al., 2019). These authors showed that this was critical when local counting rates were low, so that the backgrounds could be dominated by the influence of galactic cosmic rays throughout the outer zone and by 100s of MeV protons in the inner zone, generating effects on multi-MeV and $\sim$ MeV energies, respectively. Bremsstrahlung photons generated by energetic electrons through interaction with the spacecraft material have been shown to be responsible for background contamination in 100s of keV electron fluxes measured by MagEIS in the heart of the outer belt (CLAUDEPIERRE et al., 2015). However, as the large-scale dynamics given by the corrected fluxes were preserved in the uncorrected data, this uncorrected data set was the choice for our event analysis.

In fact, Van Allen Probes ECT detectors (essentially solid-state telescopes) measure the counting rate of particles, at a given energy, passing through the area of the sensors with an incidence direction within a solid angle constrained to the instrument configuration (WALT, 2005). The differential (energy resolved) and directional (pitch angle resolved) fluxes are then determined from this quantity and represent the measured number of particles per second, solid angle, unit area, and energy (units of $[1/s.sr.cm^2.keV]$). They are typically a function of a parameter of location (here the L shell) and UTC time, besides energy, and pitch angle. For the Van Allen Probes, this type of data is publicly released by the ECT science team as Level 3 (`https://www.rbsp-ect.lanl.gov/science/DataDirectories.php`)

3.1.2.2 GOES spacecraft

While Van Allen Probes measurements cover a wide range of L shells (typically $2 < L < 6$) within the trapped radiation zones, those from the US Geostationary Operational Environmental Satellite (GOES) are almost fixed at $L = 6.6$, the so-called geosynchronous orbit. Thus, the GOES trajectory along multiple longitude positions is favorable for the validation of MHD simulations of the magnetosphere, both in terms of magnetic fields and particle fluxes (e.g., Fei et al. (2006), Tu et al. (2012)), and for the construction of variable outer boundary conditions in radial diffusion simulations (e.g., Castillo et al. (2019)). The GOES magnetic field and particle flux data sets were used in this research in both cases.

We analyzed 1-minute averages of magnetic field observations from both GOES-13 (104.5° W) and GOES-15 (74.8° W) satellites, launched in 2006 and 2010, respectively. Electron fluxes were taken only from GOES-15. These are differential-directional measurements, provided with nine solid-state-detector telescopes of the Magnetospheric Electron Detector (MAGED). Each of the telescopes reports electron fluxes resolved in a given pitch angle from $\sim 0°$ to more than 90°, as well as in five energy bands ($30 - 50$ keV, $50 - 100$ keV, $100 - 200$ keV, $200 - 350$ keV and $350 - 600$ keV), with central energies being: 40, 75, 150, 275, and 475 keV. Since GOES-13 and -15 were designed to fly upright or inverted, telescope 1 (T1) is the only invariant in relation to its field-of-view (FOV) direction (0° south). The other telescopes undergo east-west and north-south swaps whenever the satellite changes direction (JAYNES et al., 2013). This means that T1 always measures fluxes at the same pitch angle of $\sim 80°$, whereas T2 to T9 switch pitch angles depending on the change in FOV during upright or inverted directions.

GOES average data sets, including MAGED 5-minute fluxes and corresponding local pitch angles at 1-minute cadence, are available, as separated files, at `https://satdat.ngdc.noaa.gov/sem/goes/data/avg/`. These electron flux data have been corrected for high-energy proton contamination (HANSER,).

3.2 Methods for data analysis

3.2.1 Transformation of observed electron flux to phase space density

As stated previously, particle differential-directional fluxes are usually determined in relation to the local pitch angle (α), energy (E), and radial position ($\vec{r}$), where the changes may not represent actual diffusion processes in progress. This is because

these reference coordinates are not preserved, due to slowly time-varying spatial asymmetries of the geomagnetic field (ROEDERER; LEJOSNE, 2018). It is more appropriate to analyze such particle distributions in a true invariant coordinate system based on the conservation of the three adiabatic invariants of motion (μ, K, and L^*). In this way, fully adiabatic changes are removed and nonadiabatic processes can be distinguished (SHULZ; LANZEROTTI, 1974). In this case, Liouville's theorem assigns the phase space density (here denoted as PhSD) as the distribution function (f) to be conserved, as long as the invariants remain constant.

The transformation of the measured differential-directional flux $j(E, \alpha, \vec{r}, t)$ along a satellite path into $f(\mu, K, L^*, t)$, at fixed μ and K values, can be described as follows. First, a pair of fixed μ' and K' values is chosen, then a global magnetic field is required to calculate the corresponding K of a sample of local pitch angles ($5° - 90°$) at each instant of time (t_i) and given satellite location ($\vec{r}$). Interpolation is done to acquire the pitch angle (α_i) assigned to K'. In case K' is outside the instantaneous range of K values due to a change in the magnetic field configuration, α_i is no longer defined, as well as the instantaneous PhSD and L^*. However, if α_i is defined, the process of getting PhSD continues, and a new interpolation is performed on α (measured pitch-angle distribution) in order to obtain $j(E, K', \vec{r}, t_i)$. This leads to a set of interpolated fluxes at α_i, relative to each energy channel (E) provided by the satellite. Also, a kinetic energy (E_i) corresponding to μ' can be derived by equating the two relations that define the particle's relativistic momentum squared (based on the conservation of μ and on the energy-momentum equation (GREEN; KIVELSON, 2004)):

$$p^2 = \frac{2m_0 B\mu'}{\sin^2(\alpha_i)}; \quad p^2 = \frac{(E_i^2 + 2m_0c^2E_i)}{c^2}, \tag{3.1}$$

where m_0 is the electron rest mass, B is the local magnetic field strength (either measured or modeled), and c is the speed of light.

A final interpolation is done over E (measured energy spectra) to obtain the corresponding flux at E_i, which leads to $j(\mu', K', \vec{r}, t_i)$. To complete the set of invariant coordinates for representing PhSD, L^* at K' must also be obtained for each instant t_i. This can also be done by interpolating over a previous sample of L^* values calculated for a distribution of local pitch angles, as explained previously for the invariant K. The instantaneous PhSD fully described in the adiabatic reference space is finally obtained through (HARTLEY; DENTON, 2014):

$$\frac{j(\mu', K', L^*(K'), t_i)}{p^2} = \frac{j(\mu', K', L^*(K'), t_i) \times c^2}{E_i(E_i + 2m_0c^2)}. \tag{3.2}$$

Figure 3.2 summarizes those steps described to calculate PhSD at fixed μ and K values in an instant of time. As a rule, PhSD is often given in the GEM (Geospace Environment Modeling) unit of $[c/MeV.cm]^3$. For this, the following equation is the one really applied in this work to convert the differential-directional electron fluxes (j) into PhSD (f) (similar to Chen et al. (2005)):

$$f(\mu', K', L^*(K'), t_i) = \frac{j(\mu', K', L^*(K'), t_i)}{E_i(E_i + 2m_0c^2)} 3.325 \times 10^{-8}, \tag{3.3}$$

with E_i and m_0c^2 in MeV, and j in units of $[1/s.sr.cm^2.keV]$.

Figure 3.2 - Flowchart listing procedures to compute phase space densities from electron flux measurements.

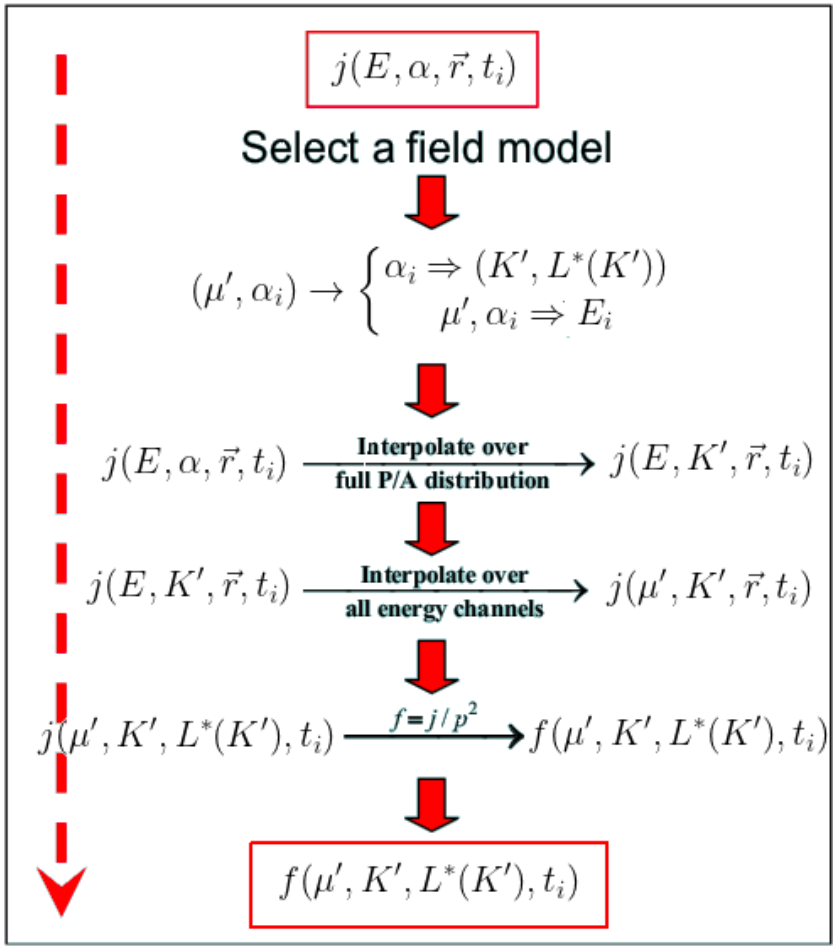

In an instant of time t_i, for a satellite located at position $\vec{r}$, choose a pair of first and second invariants (μ', K') for the PhSD to be fixed. From a sample of K values calculated for a distribution of local pitch angles with the selected magnetic field model, find the local pitch angle α corresponding to K', hereafter α_i. With the pair (μ', α_i), determine the energy E_i corresponding to μ' by using Equations 3.1, in which the local magnetic field strength B either measured or modeled will be required. Also, determine $L^*(K')$, i.e., $L^*(\alpha_i)$. The next steps will be to interpolate the electron flux $j(E, \alpha, \vec{r}, t_i)$ over the measured pitch angle distribution and then over the measured energy spectra to obtain $j(E_i, \alpha_i, \vec{r}, t_i)$, which is equivalent to $j(\mu', K', L^*(K'), t_i)$. Finally, Equation 3.3 is used to derive the PhSD in the GEM unit as $f(\mu', K', L^*(K'), t_i)$.

SOURCE: Modified from Tu (2011, p. 15).

Some general aspects of the code developed for this thesis to deal with the described approach are: (a) linear interpolation was applied in all required interpolation instances, in which an exponential fit was assumed for the interpolation of j over

energy (E); (b) in contrast with previous works, for the estimation of E_i (instant energy correspondent to μ'), B modeled with TS04 was used instead of the measured field strength provided by the spacecraft magnetometers. It was found that this improved comparisons with previously published data for the 22-23 June 2015 storm by Tu et al. (2019). Specifically, the temporal variations in PhSD and spatial coverage between these data were very similar.

Other settings related to the conversion of Van Allen Probes flux measurements are: (i) the data set used for K and L^* invariants are from the magnetic ephemerides files, publicly available at (`https://www.rbsp-ect.lanl.gov/data_pub/`). The calculation of these invariants involved the use of TS04 as the external magnetic field model. (ii) Since the data from these magnetic ephemerides files are given with a 5-minute resolution, the flux data provided by the REPT and MagEIS instruments had to be initially averaged out to match this 5-minute resolution. Their original resolution is $\sim$ 11s (the spacecraft spin period). (iii) Regarding the energy spectrum defined for interpolation of electron flux at fixed μ, we followed the recommendations of Boyd et al. (2019) for the construction of a continuous spectrum, using differential-directional flux data from both REPT and MagEIS instruments. In short, only MagEIS data were used for energies up to 2 MeV, a combined spectrum was needed for energies between 2 and 3 MeV, and only REPT measurements were used for fluxes at energies above 3 MeV. Also, REPT data at energies above 10 MeV was discarded to minimize the effects from background contamination due to cosmic rays or inner zone protons.

The settings considered for conversion of GOES flux measurements are: (i) as there are no available data products for magnetic ephemerides of the GOES spacecraft, we launched, in MATLAB®, the library IRBEM-LIB (BOSCHER et al., 2012) using time-dependent TS04 model for shell-tracing and computation of K and L^* of the events, at local pitch angles from 30° to 90°, with a 10° step. The subroutine "onera_desp_-lib_make_lstar_shell_splitting" was used. In addition to L^*, it also gives as outputs B_m, B_{min}, and I, that is, the B strength at the mirror point, at the equator, and the quantity related to K. Since these are pitch-angle dependent values, the local (modeled) B strength was then derived from the conservation of μ, using B_m as the reference field (see Equation below), for which any of the local pitch angles (α') implemented works:

$$B = B_m(\alpha') \sin^2(\alpha'). \tag{3.4}$$

The derived $K(\alpha', t)$ and $L^*(\alpha', t)$ invariants and $B(t)$ were the necessary input data

to obtain PhSD in fixed μ and K values from the GOES fluxes. The energy spectra provided by the GOES spacecraft for fluxes at up to 0.475 MeV central energy allows the analysis of PhSD up to $\mu \sim 400$ MeV/G, at $L^* \sim 6$ (r = 6.6 R_E) as calculated with TS04. Hence, to obtain PhSD at higher values of μ, required to evaluate the dynamics of outer belt relativistic electrons up to the geosynchronous orbit, the exponential fit assumed for the flux energy spectrum was taken for the *extrapolation* of fluxes above 0.475 MeV at μ-related energies (E_i). To validate the PhSD data set calculated using this approach (based on flux extrapolation), a cross-calibration analysis was performed, which will be discussed in Chapter 6.

3.2.1.1 Error estimates

The phase space density matching technique (REEVES et al., 2013; MORLEY et al., 2013) was tested at the interval of our case study 2 ($20 - 22$ November 2017), in order to estimate the errors generated in PhSD by the developed code. According to Liouville's theorem, two spacecraft orbiting the same drift shell (L^* space) must observe the same PhSD for fixed μ and K, unless they have reached any loss or source region in the radiation belts.

Figure 3.3 exemplifies this test. The top panel shows the conjunction times (between Van Allen Probes A and B) selected for analysis, represented by the black circles. A dropout is seen in this chart starting from ~ 0 UT on November 21, followed by enhancements later on November 22. For each of the conjunctions (where $|L^*_A - L^*_B| \leq 0.1\ R_E$), a difference (matching) factor of the error related to the PhSD values calculated with both probes was obtained by dividing the larger phase space density by the smaller phase space density, regardless of satellite. Factors around 1 (but not much greater than 2) represent that most of the uncertainty comes from the global magnetic field model applied to obtain the adiabatic invariants instead of instrumental cross-calibration uncertainties (REEVES et al., 2013).

The bottom panel displays the dispersion of these PhSD factors in relation to the associated mean relative errors in B (the magnitude of the local magnetic field). This mean relative error in B was derived at each conjunction time, calculating the average of the relative ratios between the measured and modeled values of B, obtained for the two probes as $(B_{mes} - B_{mod})/B_{mes}$. For the PhSD data analyzed at $\mu = 3433$ MeV/G and $K = 0.11\ G^{1/2}R_E$, the mean PhSD factor obtained was 1.19. Morley et al. (2013) found an average PhSD factor of 1.06 for the $11 - 12$ October 2012 interval (for equal μ and K values), with the caveat that in this matching analysis only the REPT flux data were used by these authors. On the other hand,

Reeves et al. (2013) found for a similar event that a relative error of 15% in B would generate a PhSD factor below 2, and a factor of ~ 1.4 for an error in B of 4%. The PhSD factors shown in Figure 3.3 roughly agree with those estimates. Therefore, the developed code can be considered validated. It shows for a dynamic interval in the outer radiation belt that the difference factors generated from the dual PhSD measured by the Van Allen Probes were mainly generated by errors in B, associated with the use of the TS04 model during the PhSD transformations.

Figure 3.3 - Phase space density observations from Van Allen Probes A and B during case study 2 (top), along with matching factors between these probes' PhSD, plotted against the mean relative errors found in local B (bottom).

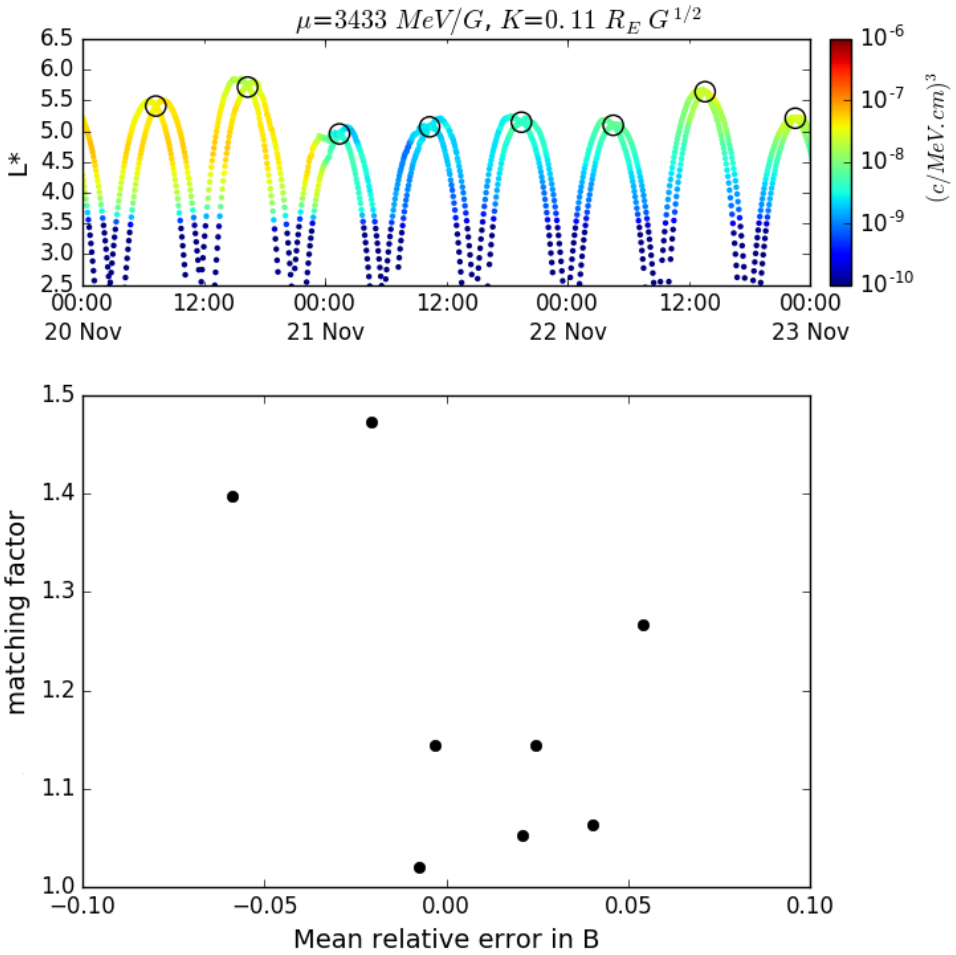

Calculations using the TS04 magnetosphere model.

SOURCE: Produced by the author.

3.2.2 ULF waves in field aligned coordinates

In Chapter 4, it will be shown that quantifying radial diffusion requires determining ULF wave power. This can be done from fluctuating electric and magnetic fields, described in the geomagnetic field aligned reference frame because trapped particle motion in the magnetosphere occurs naturally in this system (FALTHAMMAR, 1965; FEI et al., 2006). Nowadays, plasma waves measurements are ubiquitous in magnetospheric scientific missions and are usually determined in geocentric reference frames, such as the geocentric solar ecliptic (GSE).

GSE is the system in which the x-axis points from the earth towards the sun, with the y-axis pointing towards dusk along the ecliptic plane. The z-axis is parallel to the ecliptic pole (KIVELSON; RUSSELL, 1995). If the orientation of the magnetic pole is concerned, the solar magnetic (SM) system is the one in which the z-axis is parallel to the northern magnetic dipole, and the y-axis is perpendicular to the Earth-Sun line in the dusk direction, as in GSM. A tilt angle around the y-axis makes GSM to differ from the SM coordinates, leading the SM x-axis not to point directly at the Sun.

Figure 3.4 - Application of the FAC system to a satellite position $\vec{r}$ in a geomagnetic field line obtained with the T96 magnetosphere model (TSYGANENKO, 1995), at quiet conditions.

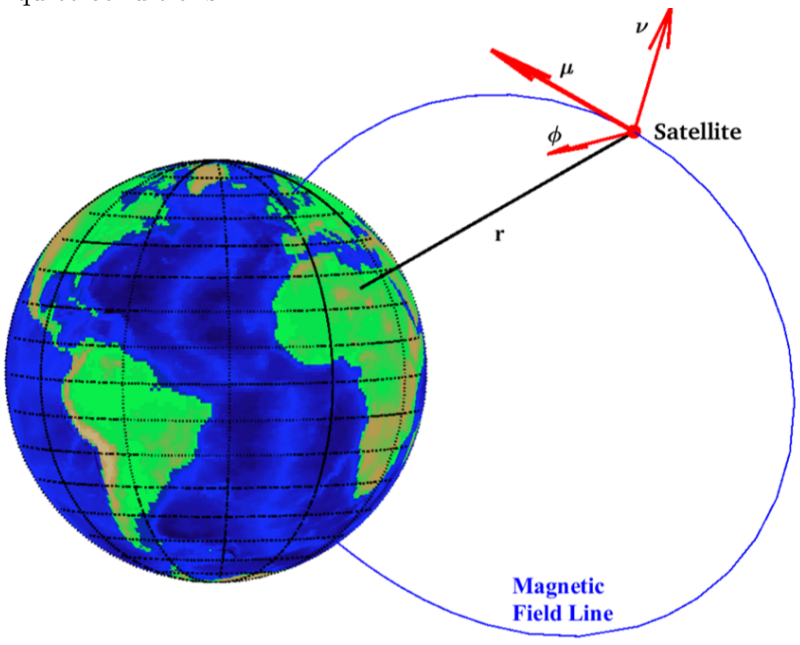

SOURCE: Regi et al. (2016).

Recently, Regi et al. (2016) listed a few techniques for rotating in-situ magnetic field vectors from the GSE to the mean field aligned coordinate (FAC) system, including the widely known moving average procedure. In considering a time series of the local magnetic field $\vec{B}(t)$ measured by a satellite located at $\vec{r}(t)$, such a method can be used to find the associated slowly-varying background magnetic field $\vec{B_0}(t)$. In this work, moving average was the method implemented to obtain $\vec{B_0}(t)$. With the knowledge of $\vec{B_0}(t)$ (representing the local mean orientation of the geomagnetic field) and $\vec{r}(t)$, the instantaneous-local unit vectors of the FAC system can be calculated as (REGI et al., 2016; ALVES et al., 2017):

$$\begin{cases} \hat{\mu}(t) = \vec{B_0}(t) / \left\| \vec{B_0}(t) \right\|; \ (compressional) \\ \hat{\phi}(t) = \vec{r}(t) \times \vec{B_0}(t) / \left\| \vec{r}(t) \times \vec{B_0}(t) \right\|; \ (toroidal) \\ \hat{\nu}(t) = \hat{\mu}(t) \times \hat{\phi}(t); \ (poloidal) \end{cases} \tag{3.5}$$

As indicated in Equations 3.5 and illustrated in Figure 3.4, the unit vectors $\hat{\mu}(t)$, $\hat{\phi}(t)$ and $\hat{\nu}(t)$ resolve parallel, azimuthal and radial directions to $\vec{B_0}(t)$, which allow the observation of ULF waves in compressional, toroidal and poloidal modes, respectively.

The rotation matrix defined from geocentric (GSE) to FAC coordinates, at instant t, then becomes:

$$R(t) = \begin{bmatrix} \hat{\mu_x}(t) & \hat{\mu_y}(t) & \hat{\mu_z}(t) \\ \hat{\phi_x}(t) & \hat{\phi_y}(t) & \hat{\phi_z}(t) \\ \hat{\nu_x}(t) & \hat{\nu_y}(t) & \hat{\nu_z}(t) \end{bmatrix} \tag{3.6}$$

in which the magnetic field vector $\vec{B}(t)$ is rotated through:

$$\vec{B}_{FAC}(t) = R(t)\vec{B}_{GSE}(t), \tag{3.7}$$

Finally, ULF fluctuations at frequencies much higher than set to find $\vec{B_0}(t)$ are determined from $\vec{B_{FAC}}(t)$, by making $\vec{b_{FAC}}(t) = \vec{B_{FAC}}(t) - \vec{B_0}(t)$. Hence, $\vec{b_{FAC}}(t)$ provides the instantaneous vector of magnetic fluctuations described in the FAC coordinates, from which ULF wave modes can be inspected.

The rotation matrix $R(t)$ can also be used to transform electric field vectors, in order

to acquire the associated electric field components of the toroidal and poloidal wave modes, that is, the radial electric field (E_ν) and the azimuthal electric field (E_ϕ). In reality, compressional waves can also induce E_ϕ. It is worth mentioning that the toroidal and poloidal modes arise from the theory of field line resonances proposed by Dungey (1967), in which ULF waves are treated as standing Alfvén waves along the Earth's magnetic field lines frozen in the conducting ionosphere (WATERS, 2000; SHPRITS et al., 2008). The compressional mode is related to MHD waves of the fast mode (McPHERRON, 2005), which can also be coupled in field line resonances, i. e., toroidal and poloidal modes, in the magnetosphere (WATERS, 2000).

Among the set of field-aligned magnetic field components $\{B_\mu, B_\phi, B_\nu\}$ and electric field components $\{E_\nu, E_\phi\}$, those that can cause radial diffusion in relativistic electrons are the compressional magnetic field (B_μ; from now on $B_\parallel$), and the azimuthal electric field (E_ϕ), as shown by Falthammar (1965).

In addition to the FAC rotation approach presented, E_ϕ and $B_\parallel$ wave components can also be determined by having the original electric and magnetic field vectors, near the equator, given in SM cylindrical coordinates (ρ - radial, ϕ - azimuthal, z - vertical) (e.g., Ali et al. (2016)). $B_\parallel$ in the FAC system corresponds directly to B_z in SM, while E_ϕ fluctuations in FAC correspond to E_ϕ fluctuations in SM, since their respective unit vectors $\hat{\phi}_{FAC}$ and $\hat{\phi}_{SM}$ both point eastward (same sense of the electron drift motion and, hence, appropriate to calculate D_{LL}^E).

This is a useful approach, since that of FAC requires the electric field measurements to have the same resolution of the measured magnetic fields because this is the resolution of the rotation matrix, $R(t)$. In the latter approach, $\vec{B}$ and $\vec{E}$ can have different cadences, which is convenient when handling data sets from different instruments, such as those from EFW and EMFISIS in the Van Allen Probes.

When converting the SM-**E** field vector to cylindrical coordinates, in order to obtain the E_ϕ time series, it is defined that:

$$\begin{cases} \hat{\phi}(t) = \hat{z} \times \hat{\rho}(t) \\ E_\phi(t) = \vec{E}(t) \cdot \hat{\phi}(t) \end{cases} \tag{3.8}$$

with $\hat{z} = [0, 0, 1]$ and $\hat{\rho}(t)$ determined from the time-dependent satellite position vector, in spherical coordinates.

These relations, along with B_z in SM, were applied to derive E_ϕ and $B_\parallel$ from Van

Allen Probes and THEMIS SM-electric and magnetic field data, as well as to obtain magnetic field data from GOES. These coordinate transformations were also applied to the global fields of the MHD simulations of cases 1 and 2.

In the case of the transformation of GOES magnetic field measurements, it should be mentioned that these measurements are provided in the ENP reference system, namely E-earthward (in the orbital plane), N-normal (points east in orbital plane) and P-parallel (points north in the orbital plane, parallel to the Earth's spin axis for a zero degree inclination orbit). A specific code was developed to transform the GOES magnetic fields in ENP to GEI (geocentric inertial coordinates) and later to SM to allow the calculation of $B_{\parallel}$.

Based on the geocentric to field-aligned transformations described in this chapter, the results of in-situ and modeled ULF waves in the compressional and poloidal modes will be presented in Chapters 4 e 5. They are relevant for the quantification and analysis of event-specific radial diffusion coefficients.

3.3 1D radial diffusion simulation

In radiation belts studies, the following radial diffusion equation is widely applied to model the evolution of the drift-averaged PhSD of a particle population with known μ and K adiabatic invariants (SHULZ; LANZEROTTI, 1974):

$$\frac{\partial f}{\partial t} = L^{*2}\frac{\partial}{\partial L^*}\left(\frac{D_{LL}}{L^{*2}}\frac{\partial f}{\partial L^*}\right) - \frac{f}{\tau}, \tag{3.9}$$

where $f(L^*, t)$ represents the phase space density distribution at fixed μ and K, with L^* also determined at the given K, D_{LL} (L^*, t) is the chosen radial diffusion coefficient model (the approximation L shell = L^* can be assumed in some D_{LL} models to be discussed hereafter), and f/τ accounts for the loss terms added to the diffusion model for investigation of dropouts.

In Equation 3.9, τ represents the electron lifetimes related to either gradual atmospheric losses induced by wave-particle interactions with plasmaspheric hiss and whistler-mode chorus waves (SHPRITS et al., 2017) (known to occur respectively inside and outside the plasmapause (TU et al., 2009)), or due to losses at magnetopause induced by the compression of this boundary on the dayside (e.g., Yu et al. (2013), Tu et al. (2019)). Meanwhile, the effect of outward radial diffusion near the magnetopause is intrinsically accounted for by the input D_{LL} model. Fast-localized

atmospheric losses induced by interactions with EMIC waves (as in Shprits et al. (2016)) are generally not included in this modeling approach, since there is no available empirical model of τ for this case. Also, no source term was considered in this equation.

On the other hand, Equation 3.9 is a partial differential equation (PDE) that can numerically be treated as a diffusive initial value problem over the simulation domain, for which the determination of inner and outer boundary conditions is required. The Crank-Nicolson implicit finite difference scheme (CRANK; NICOLSON, 1947) is used to solve a modified version of this PDE, in which the factor $1/L^{*2}$ is combined with the formula of $D_{LL}(L^*, t)$ on the right-hand side (WELLING et al., 2012). This is done by first considering a D_{LL} function of the type

$$D_{LL} = D_0(t) \cdot L^{*M'}, \tag{3.10}$$

and then a change of variables of space in Equation 3.9, defined as:

$$L^* \rightarrow x : x \propto (1/L^*)^{N'}. \tag{3.11}$$

This transformation leads to a simplified PDE as follows:

$$\frac{\partial f}{\partial t} = A(x)\frac{\partial}{\partial x}\left(D\frac{\partial f}{\partial x}\right) - \frac{f}{\tau}, \tag{3.12}$$

in which

$$D \propto \frac{D_{LL}}{L^{*(N'+3)}} = D_0(t) \cdot L^{*(M'-N'-3)}. \tag{3.13}$$

If $M' = N' + 3$, $D \propto D_0(t)$ is obtained, thus eliminating the aforementioned L^* dependence within the spatial derivative. The Crank-Nicolson solution method is then applied to the Equation 3.12. This method is an improvement of the forward time centered space scheme (FTCS) and allows the solution to be second-order accurate in time and space (PRESS et al., 2007). Following this approach, the PDE is solved at the midpoint between t and $t + \Delta t$ (n and $n + 1$ time steps), so that, for constant D, the Equation 3.12 is discretized as:

$$\frac{f_j^{n+1} - f_j^n}{\Delta t} = A_j \cdot D \left[\frac{f_{j+1}^{n+\frac{1}{2}} - 2{f_j}^{n+\frac{1}{2}} + f_{j-1}^{n+\frac{1}{2}}}{(\Delta x)^2} \right] - \left(\frac{f}{\tau} \right)_j^{n+\frac{1}{2}}, \tag{3.14}$$

where the index j represents discretization in space.

The terms at time step $n+\frac{1}{2}$ are roughly equivalent to the average of the same terms between time steps n and $n+1$. Once the terms at time step $n+\frac{1}{2}$ are substituted by the corresponding averages in Equation 3.14, those terms that accompany the unknown variable f_j^{n+1} can be separated from the terms combined with f_j^n (which are known). It is convenient to define the quantity F during this step:

$$F = \frac{A_j D \Delta t}{2(\Delta x)^2}, \tag{3.15}$$

Finally, from the separation of unknown and known distribution function terms, it is generated a tridiagonal linear system like

$$\mathbf{A} f^{n+1} = \mathbf{R}, \tag{3.16}$$

with the matrix $\mathbf{A}$ dependent on F, Δt and τ^{-1}, and the matrix $\mathbf{R}$ dependent on the same factors plus the vector f^n.

Similar to explained by Welling et al. (2012), the solution vector f^{n+1}, defined at all mesh points in space, was obtained via LU matrix decomposition. A routine was written in IDL, as well as the core routine to advance the solution forward in time (TU, 2011).

Although the Crank-Nicolson method is stable for any size Δt (PRESS et al., 2007), Welling et al. (2012) have pointed out that for fixed Δt and a given D_{LL} model, there exists a grid convergence zone for the error between the numeric solution of f and the analytic result of f that will depend strictly upon the intensity of D_{LL}. In other words, it basically means that once Δt is fixed for the radial diffusion simulation, an optimal size Δx should be tested for each input D_{LL} model in order to obtain the numeric solution of f accurately, i.e., with the error generated being inside the grid convergence zone of the analytic solution. In all radial diffusion simulations carried out here, Δt was fixed at 15 minutes, while Δx was refined accordingly, for each D_{LL} model in consideration.

3.3.1 Simulation inputs

- The initial conditions in all runs were imposed using the first available PhSD profile in each selected event, acquired with measurements from the Van Allen Probes and GOES-15. The inner boundary condition defined at $L^* = 2.5$ (for empirical D_{LL}) or at $L^* = 3$ (for MHD-driven D_{LL}) was also obtained from this profile;

- The outer boundary was defined at $L^* = 6$ along with a time-dependent condition from the calibrated PhSD data obtained with GOES-15;

- The empirical models of D_{LL} from Brautigam and Albert (2000), Liu et al. (2016), and Ali et al. (2016) were used in all events. For case studies 1 and 2, D_{LL} from the MHD simulations have been also tested;

- The model of O'Brien and Moldwin (2003) was the constraint for the plasmapause location (L_{PP}) in all runs;

- Empirical electron lifetimes driven by hiss waves from the model of Orlova et al. (2014) were set inside L_{PP} in all runs, and compared with runs also including lifetimes driven by chorus waves outside L_{PP}, as modeled by Shprits et al. (2007);

- The last closed drift shell (LCDS) calculated with time-dependent TS04 was the constraint for shadowing losses in all runs.

The calculation of event-specific LCDS is explained below. Subsequently, the models used for electron lifetimes driven by chorus and hiss waves are detailed.

3.3.1.1 Calculation of Last closed drift shell

Throughout the simulation interval of the investigated case studies, a loss term indicated in Equation 3.9 was defined for the region outside the magnetopause boundary, so that the effects of magnetopause shadowing losses enhanced during storm time can be analyzed. In the meantime, the associated outward radial diffusion mechanism driven by ULF waves can be properly quantified and differentiated from the complex balance involving the relativistic electron flux dynamics triggered in these cases (REEVES et al., 2003).

The last closed drift shell (LCDS) obtained for $K \sim 0$ $R_E G^{1/2}$ was taken as the outermost trapping boundary for the radial diffusion simulations, above which elec-

tron lifetimes in the loss term were set to be on the other of the local and energy-dependent drift periods, i. e., $\tau \sim \tau_d$. For the computation of τ_d, 90° equatorial pitch angles have been also assumed (SHULZ; LANZEROTTI, 1974). Note that $\omega_d = 2\pi/\tau_d$ in which ω_d is given by Equation 2.34.

The LCDS parameter represents the maximum L^*, or closed drift shell, that particles with a determined K can experience on a drift motion, while conserving the three adiabatic invariants. The physical quantification of the LCDS then follows the Roederer prescription (e.g., Roederer and Lejosne (2018)) to calculate L^* at midnight using Equation 2.25, in which a successive radial search on L^* is used to return the maximum L^* value per time step. The dayside boundary is avoided because it can be affected by drift orbit bifurcations (ALBERT et al., 2018). This effect arises from the formation of a double-minina shape in the magnetic field intensity on the dayside, which causes particles to become trapped off the equator and undergo diffusion processes (e.g., Ukhorskiy et al. (2011)).

LCDS calculations of the events were performed using the LGM library (HENDERSON et al., 2018) in conjunction with time-dependent TS04 model of the magnetosphere. The algorithm for shell tracing and radial search in L^* is written in C, and is computationally expensive. Regarding the inputs, default values were used except for the external magnetic field model (already mentioned), the K value and the number of field lines used in the construction of drift shells, set as $K = 0.08$ and 96, respectively. The cadence of the output data is 30 minutes. This data set was interpolated to reduce the cadence to 15 minutes, in order to match the time step of the radial diffusion simulations.

The results showing the evolution of the event-specific LCDS calculated for the three cases are discussed in Chapter 6, along with the final results of radial diffusion modeling.

3.3.1.2 Empirical models of electron lifetimes constrained by L_{PP}

- **Electron lifetimes outside** L_{PP}: The loss term included in this region is due to pitch angle scattering by chorus waves. The model for τ_{CH} (dayside) is taken from Shprits et al. (2007). It considers a parameterization with respect to the maximum AE geomagnetic index during the previous 3 hours of each time step of the radial diffusion simulation, and also a dependence on L shell and the local kinetic energy E. In a dipolar geomagnetic field with $B_E \sim 0.3G$, local E (in MeV) can be derived as a function of μ and

L through:

$$E = \sqrt{0.511^2 + 0.307\mu L^{-3}} - 0.511. \tag{3.17}$$

Thus, between $t_1 = -3h$ and $t_2 = 0h$, are defined $Q_{CH} = max_{-3,0}AE$, and τ_{CH} in units of [days] as follows:

$$\tau_{CH} = 4.8 \times 10^{2.3 - 2.3 \times 10^{-3} Q_{CH}} \times L^{-1} \times E^2. \tag{3.18}$$

- **Electron lifetimes inside** L_{PP}: The dominant loss mechanism in the plasmasphere is the pitch angle scattering by hiss waves. The loss term is defined by considering the model for τ_{HI}, derived from Orlova et al. (2014). The model for the dayside is given as a function of the geomagnetic Kp index, L shell and local energy E as defined above. Thus, τ_{HI} in units of [days] is calculated with the following expressions:

$$log_{10}(\tau_{HI}) = g(E', L) + y(Kp);\ E' = log_{10}(E), \tag{3.19}$$

and

$$y(Kp) = 0.015465Kp^2 - 0.26074Kp + 1.0077. \tag{3.20}$$

The full expression for $g(E', L)$ is omitted at this point, but it refers to a polynomial function of degree 7.

4 RADIAL DIFFUSION COEFFICIENTS THROUGH MHD SIMULATION VALIDATED BY OBSERVATIONS

This chapter presents the results of MHD simulations carried out for two CIR-driven magnetospheric storms, emphasizing the study of event-specific radial diffusion coefficients in both events. For proper validations, these ULF wave-driven coefficients are here computed from the MHD fields in each simulation and from in-situ observations. The set of assumptions made in each of these calculations will be extensively discussed in the following sections.

The chosen events promoted different dropout dynamics in the external radiation belt, as measured by the Van Allen Probes (formerly RBSP): the entire external belt was affected in case 1, while in case 2 mainly its outermost region was affected. The objective here is to investigate how the derived diffusion coefficients can explain such electron losses through drift-motion encounters with the magnetopause. Therefore, additional analyses were made to address effects on the results of the radial diffusion coefficients, such as the evaluation of the magnetopause location and the measured ULF wave activity. The role of the phase of the storms on the intensification of these rates will also be highlighted.

The remainder of the chapter deals with comparisons involving in-situ coefficients, Kp-based empirical models, and MHD results, in order to quantify the correspondence between these models and the observations. Based on the results of these analyses, the validity of the MHD results is discussed, through single-point comparisons with satellite data sets and investigating the global representation of the simulated ULF wave power of the events.

4.1 Events overview

The impact of the two moderate magnetic storms in promoting enhanced radial diffusion of relativistic electrons from the Van Allen belts is studied in this section, for which MHD simulations together with wave and particle observations using the Van Allen Probes dataset were carried out. From now on, Van Allen Probe A will be recognized as RBSP-A, and Van Allen Probe B as RBSP-B. Figure 4.1(a) shows the behavior of the electron fluxes along the RBSP-A and RBSP-B orbits a few hours before, during and after the passage of a corotating interaction region through the Earth's magnetosphere on March 27, 2017. The various solar wind parameters shown in this figure (b-e), including the proton bulk velocity, density, dynamic pressure, and IMF-B_z component, indicate that no other visible solar wind structure apparently

occurred during this time.

Figure 4.1 - Case study 1: Observations from Van Allen Probes (RBSP-A and RBSP-B), ACE and geomagnetic indices.

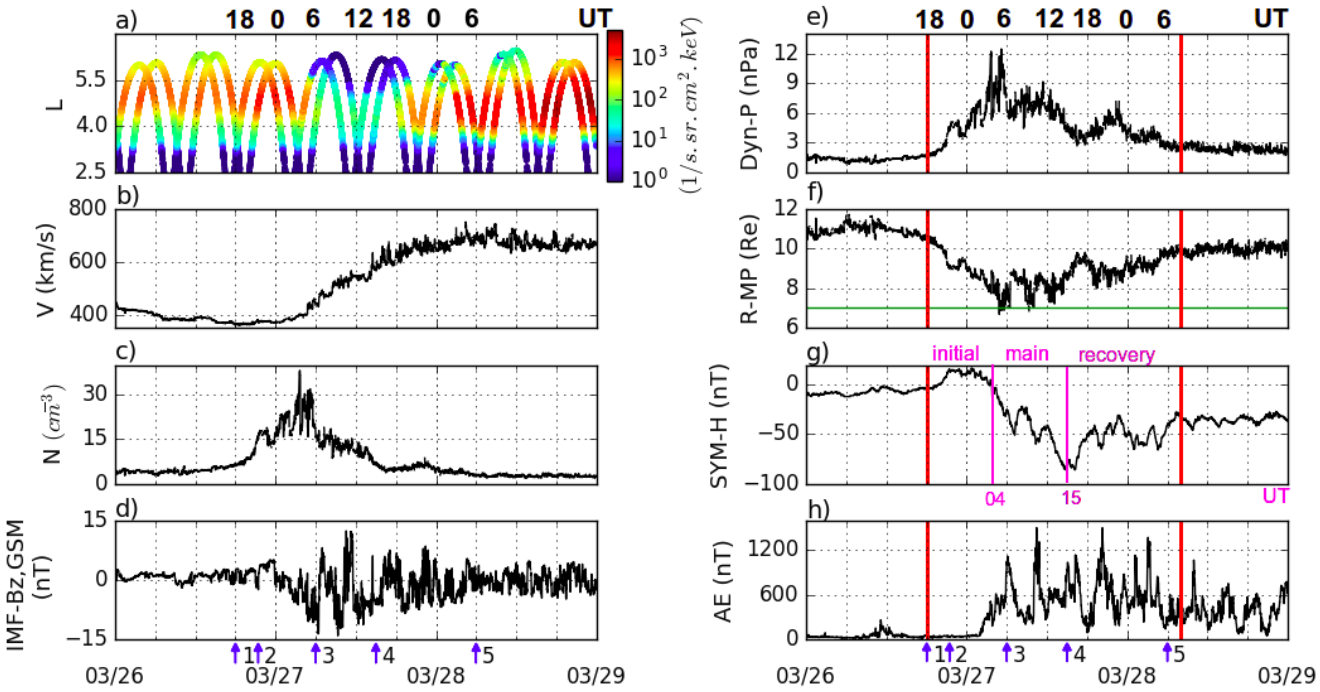

(a) Temporal and radial distribution of electron fluxes measured by the REPT instrument onboard the Van Allen Probes, at 1.8 MeV and 90° local pitch angle, and showing the occurrence of an intense dropout on March 27, 2017, from ∼ 4 UT to 20 UT. RBSP-B is leading RBSP-A. (b-e) Solar wind velocity, density, IMF-B_z component and dynamic pressure, characterizing the passage of a CIR. (f-h) Changes in the magnetopause location (R_{MP}) and in the geomagnetic indices SYM-H and AE, driven by the CIR on March 27. In panel (g), the phases of the magnetic storm are labeled, with indication of the start time of the main and recovery phases. The vertical red lines delimit the time period chosen to be simulated by the MHD model. The horizontal green line on the R_{MP} graph shows the radial distance of $7R_E$. The blue arrows accompanied by numbers 1-5 in panel (h) depict instants of the simulation to be discussed later in the text.

SOURCE: Produced by the author.

The passage of this CIR triggered many disturbances in the magnetosphere, such as the inward motion of the magnetopause up to ∼ $7R_E$ (calculated using the Shue et al. (1998) model) and the development of a moderate storm, along with a sustained substorm activity (Figure 4.1, f-h). The first two processes are known to favor the

occurrence of the fast dropout in the relativistic electron content (e.g., Kim et al. (2010)), as seen by the probes from $\sim$ 4 UT to 20 UT on 03/27 (panel (a)). However, between these two, only the mechanism related to the high compression of the magnetopause (widely known as magnetopause shadowing) can cause true losses to the outer belt, such as explained in section 2.2.2.1. Figure 4.1(a) also reveals that this rapid dropout on 03/27 reached the entire outer belt, which was previously denser in the region between $L \simeq 4$ and $L = 6$ during this event (see before 4 UT-03/27). Here the L parameter represents the McIlwain L (McILWAIN, 1961), calculated with the OP77Q (quiet) magnetosphere model (OLSON; PFTIZER, 1977).

Figure 4.2 - Case study 2: Observations from Van Allen Probes (RBSP-A and RBSP-B), ACE and geomagnetic indices.

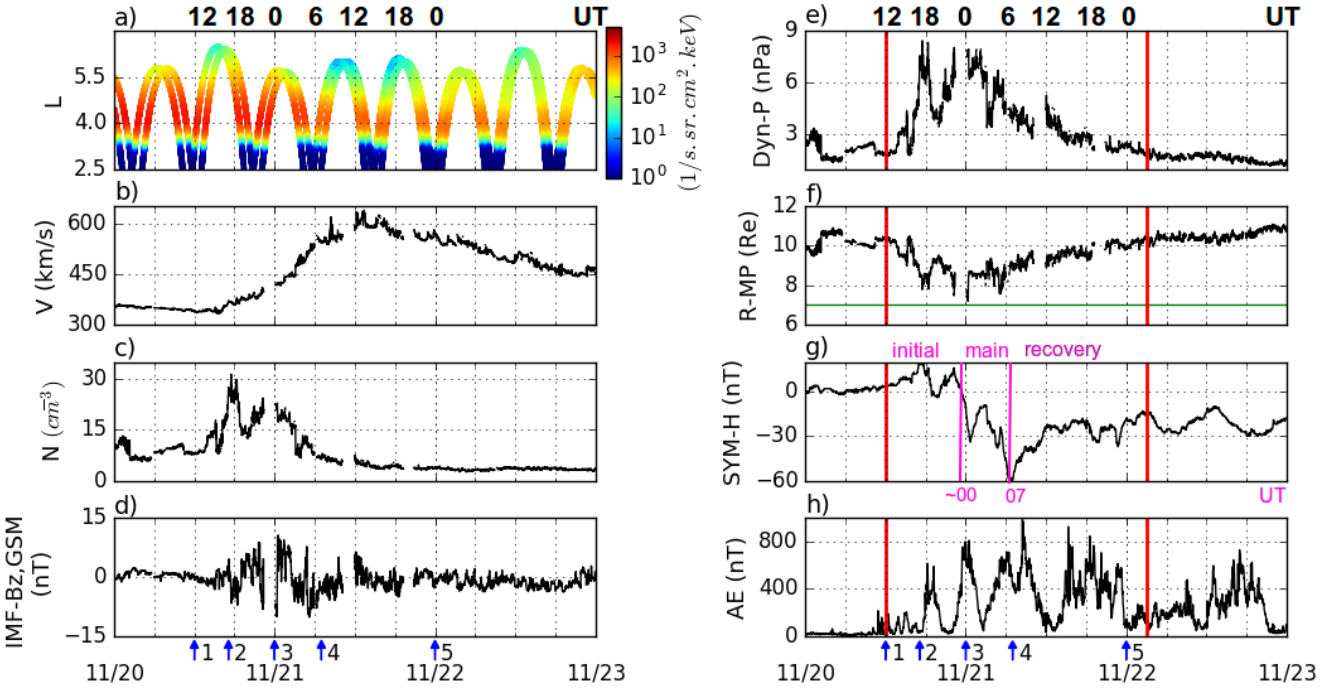

;

Same as Figure 4.1, now with the solar wind parameters (b-e) and geomagnetic indices (g-h) denoting the passage of a CIR on November 20-21, 2017, that resulted in the dropout of outer belt electrons for more external L shells in the same regime of energy and local pitch angle shown in panel (a). At the beginning, RBSP-A is the leading probe, but then both probes' L are merged.

SOURCE: Produced by the author.

The second dropout of interest is shown in Figure 4.2(a) and happened as a result

of another CIR-magnetosphere coupling on November $20 - 21$, 2017. It is also a non-complex CIR event, but with the solar wind parameters in panels (b-e) varying at slightly less enhanced values when compared to the previous event. However, the electron fluxes show a different dropout pattern, particularly encompassing external L shells ($L \gtrsim 5$) between 6 UT and 18 UT on 11/21, and that does not recover until the end of 11/22. As such, this has become an interesting event to address an outstanding question: *how do so similar CIRs impose such different conditions on the outer radiation belt in terms of relativistic electron losses?* Throughout this manuscript, a set of analyses is undertaken to address this question, mainly from the perspective of radial diffusion.

In addition, panels (f) of Figures 4.1 and 4.2 show that the empirically modeled magnetopause nose was similarly compressed to $\sim 7R_E$ in both events. However, caution is necessary as gaps in the solar wind data make it impossible to ensure that this was actually the minimum value in case 2. On the other hand, less intense storm and substorm activities occurred for this event (panels g-h in Figure 4.2). The red vertical lines in the panels on the right side of both figures indicate the period chosen for the MHD simulations, and the blue arrows at the bottom of panels (d) and (h) mark important instants of each simulation. These instants will be explored later in the text, when discussing the validations of the MHD-D_{LL}. The corresponding UT time information on these chosen instants, for each event, is summarized in Table 4.1.

Table 4.1 - UT time of selected instants of the MHD simulations identifying important storm-time dynamics in the magnetosphere.

		Case 1	**Case 2**
1	simulation start	18:00 UT, 03/26	12:00 UT, 11/20
2	storm sudden commencement	21:24 UT, 03/26	17:06 UT, 11/20
3	compressed dayside magnetopause *	06:00 UT, 03/27	00:00 UT, 11/21
4	minimum SYM-H	15:00 UT, 03/27	07:00 UT, 11/21
5	$\sim$ end of simulation	06:00 UT, 03/28	00:00 UT, 11/22

(*) Calculated with the model of Shue et al. (1998).

The phases of the magnetic storms identified in the panels (g) of the two figures were defined following the instructions in Parker (1962). In accordance with this paper and more recent literature, the initial phase is considered to be the period during which the *Dst* index (or the SYM-H index) is above its normal value, typically close to zero during magnetically quiet periods. This initial phase is due to the interaction

of the interplanetary shock wave, associated with the transient solar wind (CIR- or ICME-driven), with the magnetosphere (AKASOFU, 2018). It is followed by the main phase, which starts when SYM-H changes rapidly to negative values until reaching a minimum value, in response to the intensification of storm-time ring current and other major current systems flowing on the magnetic equator, as discussed about the TS04 model (TSYGANENKO; SITNOV, 2005). Finally, the recovery phase takes place when SYM-H gradually returns to undisturbed levels, mainly controlled by the decay of the ring current. These definitions for the initial and main phases facilitate the analysis of SYM-H in case 2, during which this index peaks twice to positive disturbed values, before entering the main phase of the storm.

Figure 4.3 further shows comparisons, for the two case studies, of the electron fluxes at fixed L shells in the outer belt observed by both RBSP-A and RBSP-B (panel (a)), and of the solar wind parameters and the modeled magnetopause standoff locations (panels b-g). Results of case 1 from the 27 March 2017 event are shown in blue, whereas those of case 2 from the 21 November 2017 event are shown in red. Note that for case 2, intervals of data gaps in the solar wind parameters and the magnetopause subsolar locations identified in Figure 4.2 are now filled with 1-hour shifted observations acquired by DSCOVR at the L1 point, in black. All time series have been plotted in a superposed epoch format in which the time of the main peak in the solar wind density was taken as the time zero (see panel (d)). The time zero also marks the start period of increase in the solar wind velocity (panel (c)), of the highly fluctuating IMF-B_z component (panel (e)), and of the maximum dynamic pressure within the CIRs (panel (f)). As speculated in the previous figures, these solar wind parameters are visually less enhanced during case 2 in relation to case 1. For instance, the velocity in case 2 is $\sim$ 100 km/s smaller throughout the interval after the time zero.

During both events, the modeled magnetopause in Figure 4.3(g) becomes most compressed to $7R_E$ preferably when the IMF-B_z turns southward, after the time zero. Meanwhile, Van Allen Probes observations shown in panels (a) and (b) detail that the dropout of case 1 outside $L = 5$ is fast (less than half a day) and causes a reduction of the relativistic electron fluxes by 4 orders of magnitude at $L = 5.5$, and by 2 orders at $L = 5.0$. On the other hand, the dropout of case 2 causes a minor and more gradual reduction of the relativistic electron fluxes of up to 1 order of magnitude. Also interestingly, the levels of the outer belt electron fluxes reported in both cases and L shells are very similar prior to the time zero.

Figure 4.3 - Superposed epoch comparisons of outer belt electron fluxes and solar wind parameters related to the CIRs of case study 1 (in blue) and case study 2 (in red).

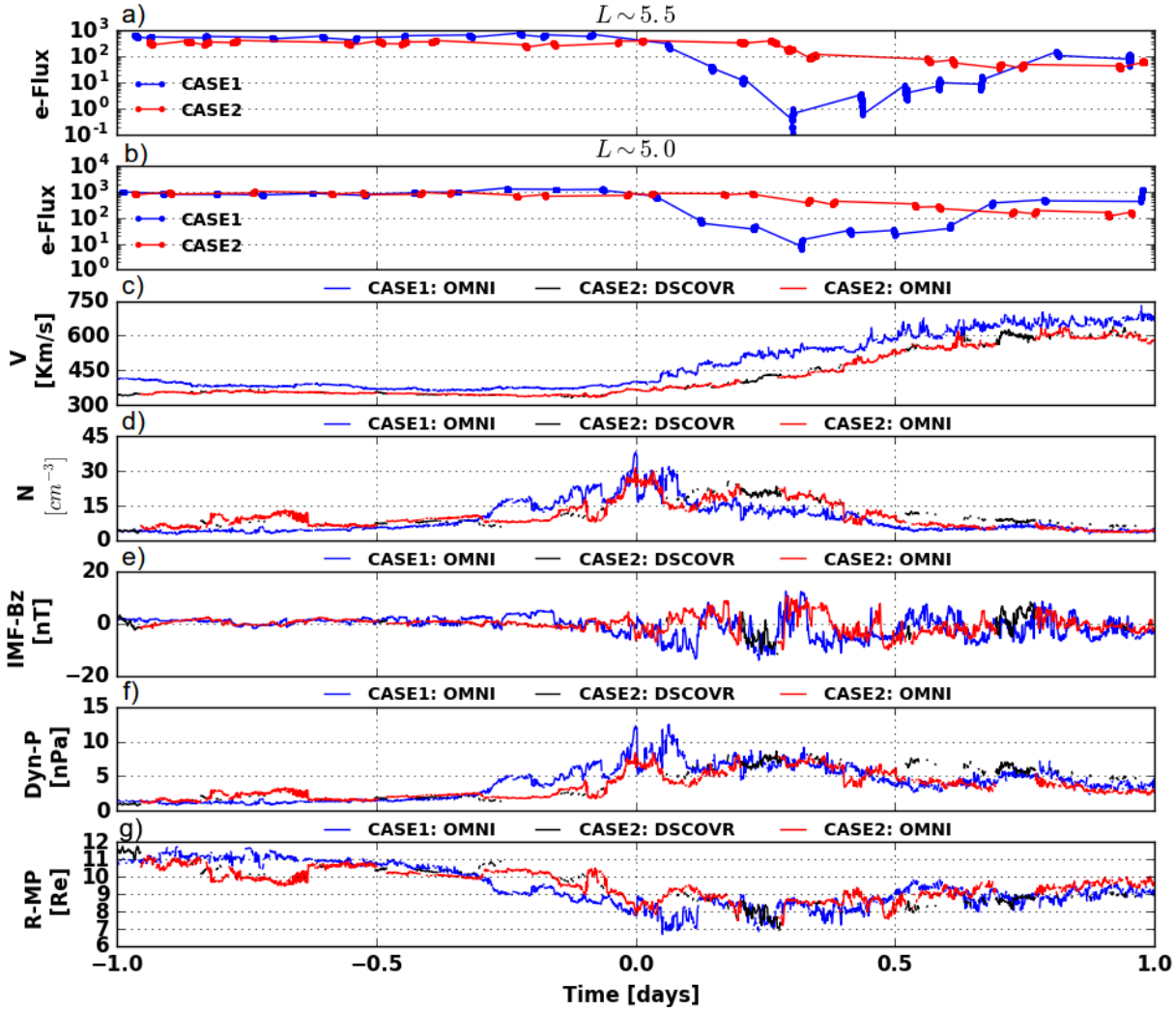

(a-b) Cutoffs of 1.8 MeV electron fluxes (units of $1/s.sr.cm^2.keV$) outside $L = 5$ from observations by RBSP-A and RBSP-B of Figure 4.1(a)-case 1 and Figure 4.2(a)-case 2; (c-f) solar wind (proton) velocity, density, IMF-B_z, and dynamic pressure collected at OMNIWeb. Data gaps from this database corresponding to case 2 are filled in black by 1-hour shifted observations from the DSCOVR satellite; (g) magnetopause subsolar locations as modeled by Shue et al. (1998).

SOURCE: Produced by the author.

4.1.1 Observations of ULF wave activity

In this chapter comparisons of radial diffusion coefficients obtained through MHD simulation for case studies with estimates from in-situ observations are provided. Figures 4.4 and 4.5 show observations of power spectral density of ULF waves acquired with measurements of E_ϕ (azimuthal electric field) and $B_\parallel$ (compressional magnetic field) from RBSP-B and three THEMIS satellites (TH-A, TH-D, and TH-E). They are restricted to L shells from 3 to 9, in order to correspond to the same region chosen for the MHD results. Likewise, the intervals defined for wave observations refer to the entire period of the MHD simulations. The same data set will subsequently be used to calculate the D_{LL} corresponding to the measured fields.

The **B**-field components are measured directly by the onboard magnetometers, but for **E**-field, only the components perpendicular to the spin axis of each satellite are measured. However, assuming $\mathbf{E} \cdot \mathbf{B} = 0$, the parallel component (E_x) can be determined (e.g., Ali et al. (2016)). These field components were initially derived in GSE coordinates (or in the modified version of GSE, in relation to **E**) and needed to be transformed to field aligned coordinates, as given in the SM cylindrical system. Subsequently, the background fields were removed from each component, which was done by applying a high-pass band filter using a 20-minute sliding window to smooth out the measured components. The resulting fluctuations at frequencies greater than 0.83 mHz characterize the ULF wave activity seen in Figures 4.4 and 4.5.

A fast Fourier transform (FFT) was then applied to these fluctuations using an hour-wide Hanning window, along with a data overlapping rate of 30 minutes. The temporal resolution of the measurements is that of the spin cadence of the probes, which is about 4s for THEMIS and 11s for RBSP-B. These high resolutions resulted in a broad band of frequencies resolved by the FFT. Therefore, power spectral densities were defined for frequencies up to 125 mHz for THEMIS spectra, and up to ∼45 mHz for RBSP-B spectra.

However, Figures 4.4 and 4.5 present information about the power spectra of the waves concentrated in the Pc5 and Pc4 ULF bands (∼ 2-7 mHz and 7-22 mHz, respectively), which correspond to frequencies susceptible to drift-resonate with outer belt electrons (in fact, Pc4 frequencies are important for drift-resonance with relativistic electrons in the case of high-m wave-particle interactions and lower L shells). In addition, no information about the L shell and MLT location of the probes is provided at this point, in order to focus discussions on the main characteristics of the waves in terms of frequency and on the relationship of their enhancement with the

different phases of the storm. The initial phase of both storms occurs from the beginning of the time set for observations to the interval of the main phase, as outlined in pink at the bottom of panels (b2) of these figures. The recovery phase appears next to the main phase interval in these graphs.

In case 1, the simultaneous spacecraft observations available indicate that the ULF wave power spreads over both Pc4 and Pc5 bands, being much higher in the Pc5 band (this is best seen in the RBSP-B magnetic measurements after 12 UT-03/27 in panel (a1) of Figure 4.4). On the other hand, stronger power spectral densities generated by azimuthal-electric fluctuations are more evenly distributed with frequency. It has been found that magnetic and electric ULF wave activity has been greatly enhanced since the start of the storm main phase (4 UT-03/27), although THEMIS observations have already shown important Pc5 power in both field components since the storm initial phase.

ULF wave measured during the storm in case 2 are generally less enhanced and more concentrated in the Pc5 band than in case 1. In particular, it is observed that the wave activity in E_ϕ appears to be more discrete in frequency. This can be seen more clearly in the Pc5 event of 11/21, after 6 UT, as measured by RBSP-B. A similar assumption can be extended to THEMIS Pc5 observations before 6 UT and before 18 UT of the same day. Regarding the role of the magnetic storm phases on ULF wave activity, RBSP-B shows a slight increase in $B_\parallel$-power within the period encompassing the transition from the main phase to the recovery phase (see spectra box from 6 to 12 UT of Figure 4.5, panel (a1)). As seen by TH-D, increased power spectral densities already occur during the storm's initial phase (see after 18 UT on 11/20, panel (b1)), similar to what is observed for case 1. For E_ϕ-power, on the other hand, despite data gaps for THEMIS, the wave packets in this component measured independently by the four probes are amplified in the final hours of the main phase and during the recovery phase.

These general results for the behavior of ULF wave activity during the phases of the storms in the two cases studied will form the basis for further discussions on the event-specific D_{LL} from in-situ observations. Also, bad data found in these spectrograms were removed from the results of D_{LL} to be presented.

Figure 4.4 - Case 1: Multi-satellite observations of (a1, b1) compressional magnetic field and (a2, b2) azimuthal electric field PSD of ULF waves in the frequency bands of Pc5 ($\sim 2-7$ mHz) and Pc4 ($7-22$ mHz), from March 26 (18 UT) to March 29 (6 UT).

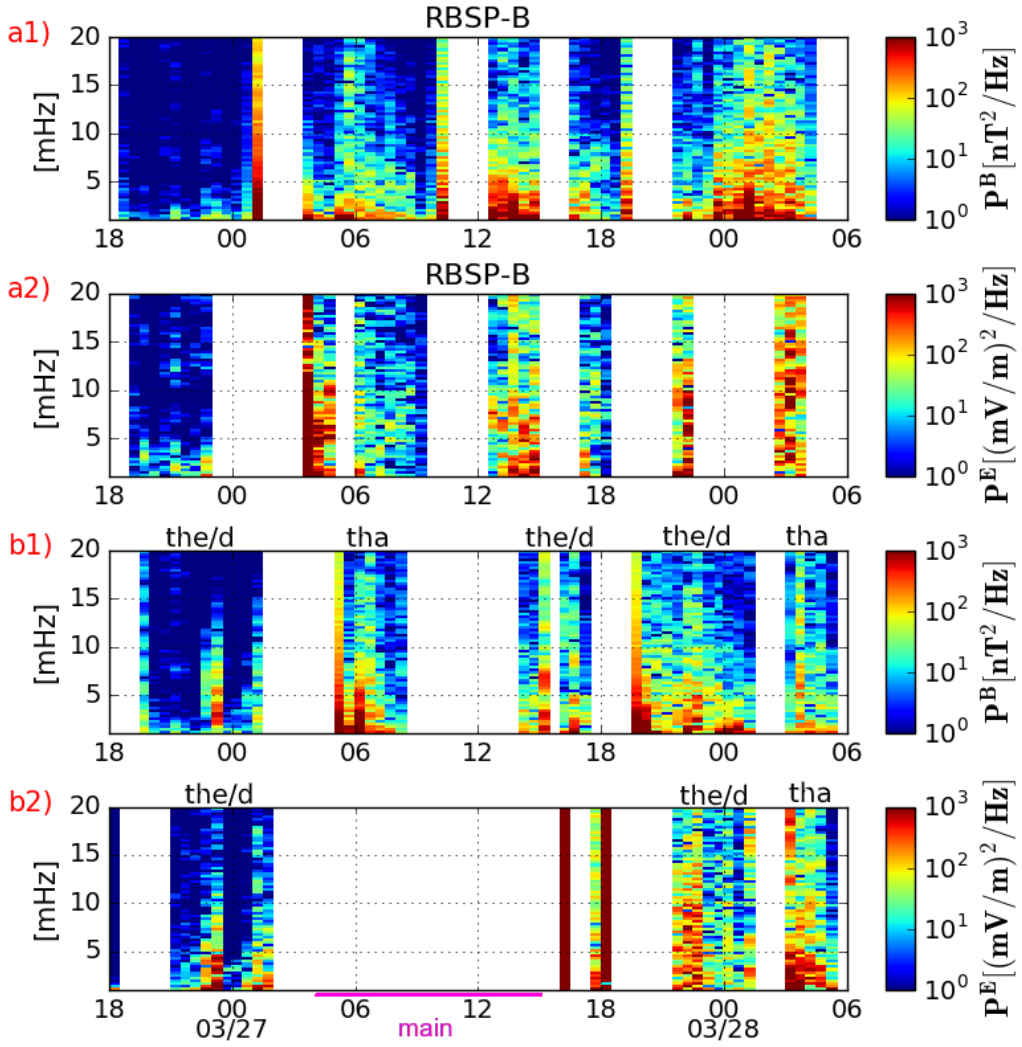

Panels (a1) and (a2) show RBSP-B measurements only, corresponding to passages within $3 < L < 6.5$, while panels (b1) and (b2) contain data from THEMIS-A, D and E during simultaneous passages through L shells from 3 to 9. Data gaps refer to actual missing data or passages of the four probes through L shells outside the considered intervals. Some bad data is still present around 18 UT on panel (b2). The duration of the main phase of the storm is also indicated on panel (b2).

SOURCE: Produced by the author.

Figure 4.5 - Case 2: Multi-satellite observations of (a1, b1) compressional magnetic field and (a2, b2) azimuthal electric field PSD of ULF waves in the frequency bands of Pc5 ($\sim 2-7$ mHz) and Pc4 ($7-22$ mHz), from November 20 (12 UT) to November 22 (0 UT).

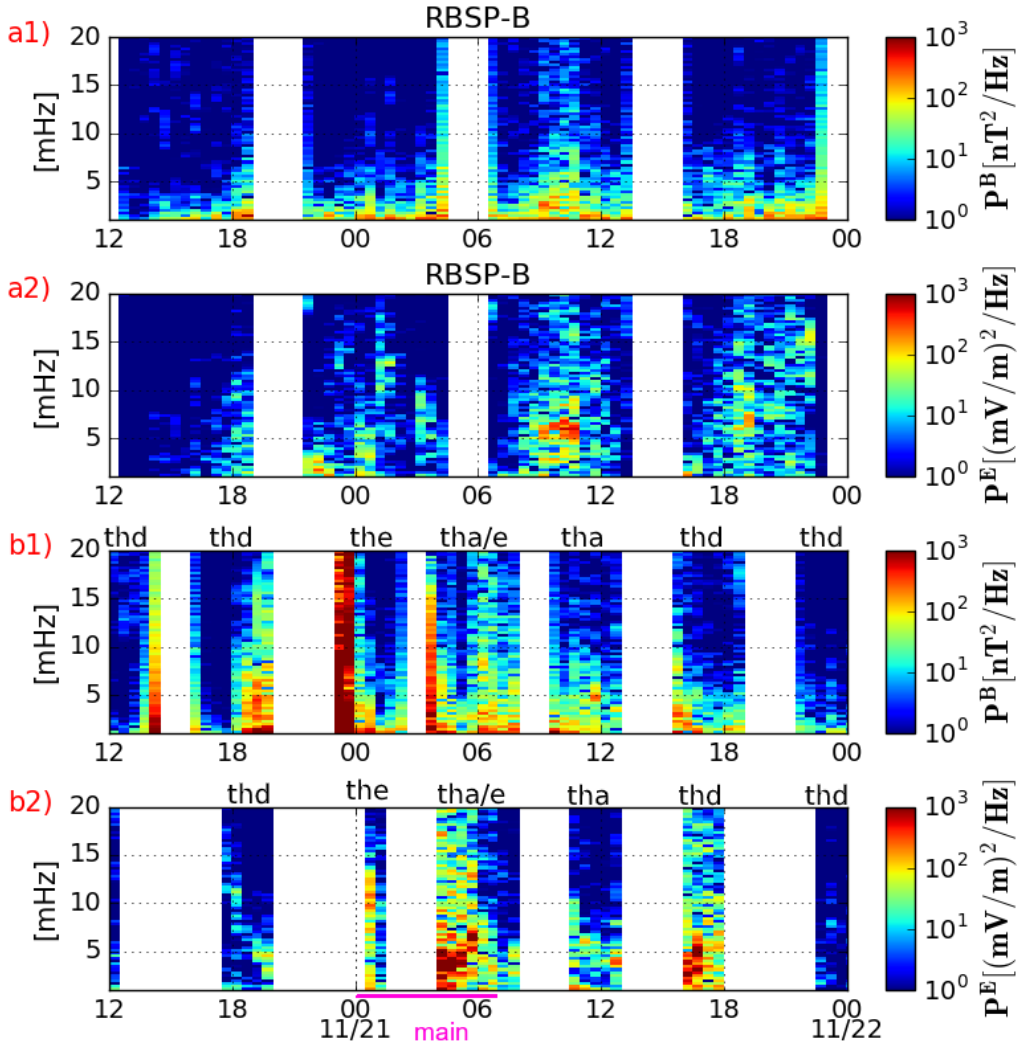

The same as in Figure 4.4.

SOURCE: Produced by the author.

4.2 Runs on SWMF/BATS-R-US

The Space Weather Modeling Framework/Block-Adaptive Tree Solar-Wind Roe-Type Upwind Scheme (SWMF/BATS-R-US) global MHD model (TÓTH et al., 2005; TÓTH et al., 2011), coupled with the Comprehensive Inner-Magnetosphere Ionosphere (CIMI) model (FOK et al., 2014) constitute the numerical approach used here to study the global interaction of the two CIRs with the Earth's magnetosphere. Runs

based on these models were carried out through requests to the Community Coordinated Modeling Center webpage (CCMC; https://ccmc.gsfc.nasa.gov/). A recent study involving the use of BATS-R-US for global modeling of ULF wave modes activity under different solar wind conditions, and also focusing on the description of the outer belt electron dynamics, can be found, for instance, in Alves et al. (2017).

The Global magnetosphere (GM) domain in BATS-R-US solves resistive MHD equations across distances comprising mostly the Earth's outer magnetosphere and the bow shock (typically from $\sim$ 30 R_E on the dayside/upstream to 100s of R_E downtail). In the near-Earth space, GM is coupled with CIMI (the Inner Magnetosphere (IM) domain) and the Ionosphere Electrodynamics (IE) domain for inner boundary conditions, and current system closure in the ionosphere. CIMI, in turn, solves the convection-diffusion equation in Fok (2020, p. 234) to model the distribution function of ring current and radiation belts, using the realistic magnetic fields and self-consistent electric fields obtained from the coupling with GM and IE, respectively.

In this work, the solar wind data provided by ACE and DSCOVR satellites were used to derive the outer boundaries of the simulation domain in case 1 (the 27 March dropout) and in case 2 (the 20-21 November dropout), respectively. The inner boundary was set at 2.5 R_E. The time interval chosen for each MHD simulation covers the initial and main phases of the storms, as well as the first hours of their recovery phases.

A fine grid resolution of 0.25 R_E was set to fill the domain -32 $\leq$ x $\leq$ 24, -24 $\leq$ y $\leq$ 24, and -20 $\leq$ z $\leq$ 20 R_E, in both runs, where the coordinates and output fields are given in the GSM system. Also, the simulated global magnetic fields were configured to present a dipole tilt (characteristic of each event) that has been updated over time. In doing so, it was expected to acquire more realistic MHD fields for the D_{LL} derivations. Figure 4.6 shows, by the red and green magnetic field lines, the tilted dipole obtained with the MHD simulation at an instant prior to the time span considered here for the global MHD analysis of case 2 (e.g., Figure 4.2). The tilt angle of the dipole represented in the GSM X-Z plane shown is of $-29.66°$. The orientation of the magnetic field vectors in the modeled magnetosphere has been also indicated.

Figure 4.6 - Magnetic field topology and intensity over the modeled magnetosphere at an earlier instant of the MHD simulation in case 2.

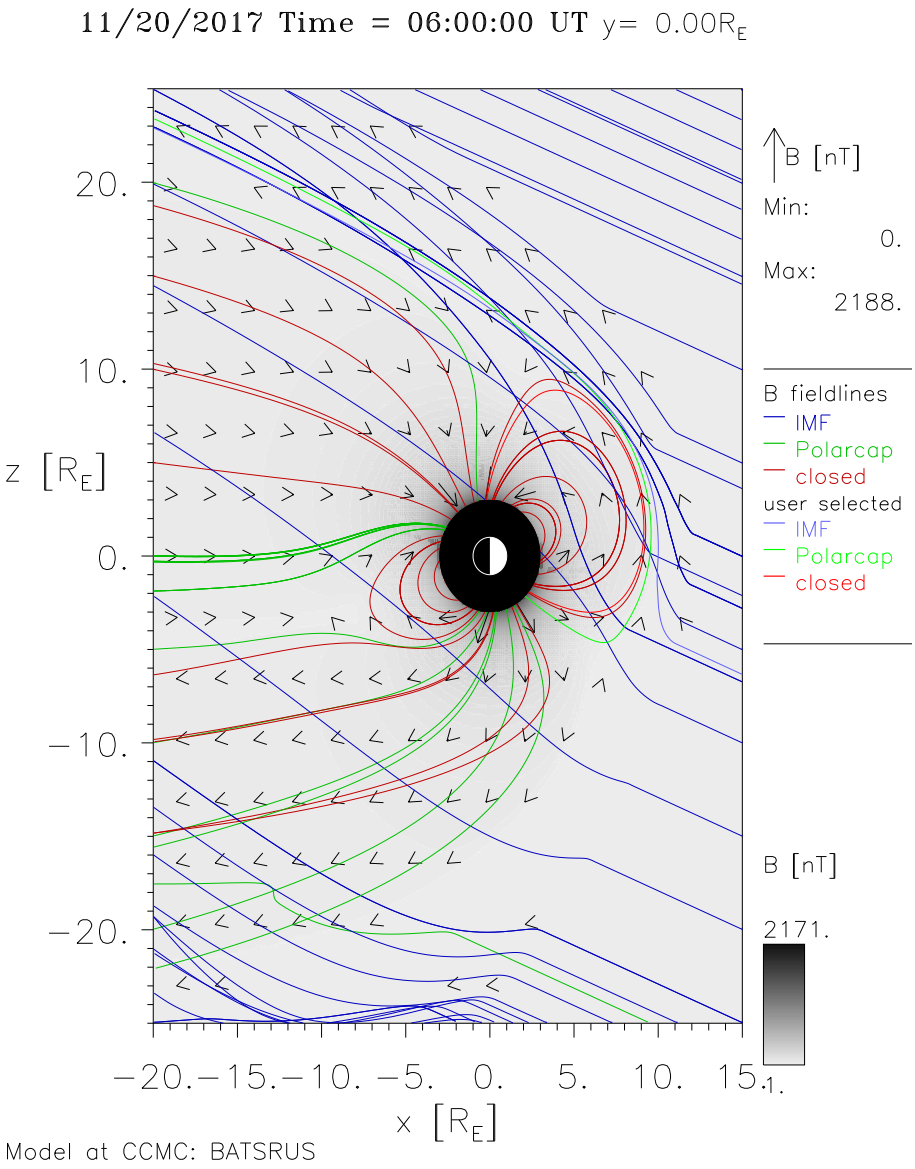

SOURCE: NASA/CCMC (2021).

The output data obtained from the runs originally have a cadence of 30s. However, a 1-minute cadence was chosen for both MHD simulations, due to several data gaps generated by the original cadence. Nevertheless, this reduced output frequency still enables us to analyze an important band spectrum of ULF waves in the Pc5 frequency regime, which is in fact responsible for the radial diffusion of electrons in the outer belt. The total duration of the MHD simulations was 38 hours for case 1

and 39 hours for case 2.

4.2.1 Location of the magnetopause nose calculated with BATS-R-US

Evaluating the magnetopause standoff distance can be crucial to determine the extent of radiation belt losses across this boundary during geomagnetic storms (e.g., Turner et al. (2012b)). Furthermore, this is a reference of maximum location for the analysis of radial diffusion coefficients. Beyond this limit, such rates can be ignored in relation to radiation belts because particle drift shells are no longer closed.

Figure 4.7 - Comparisons of the dynamic magnetopause standoff distance as modeled by the MHD simulations in cases 1 and 2, versus predictions from the Shue et al. (1998) model.

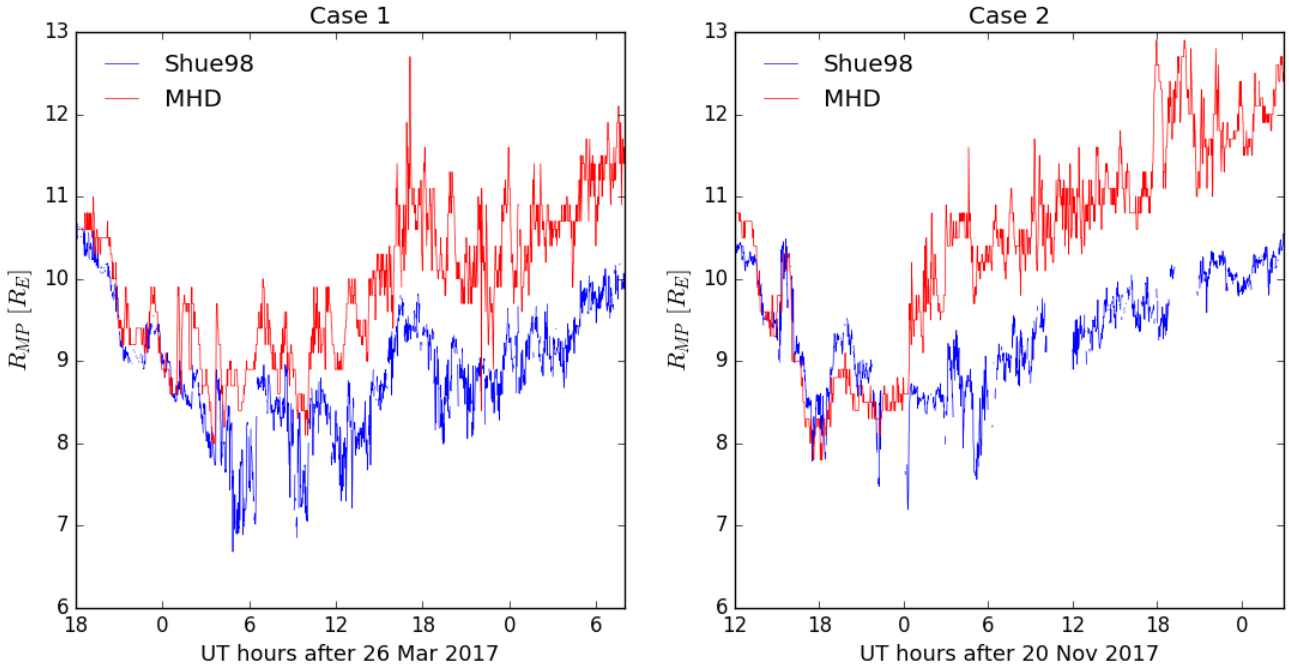

SOURCE: Produced by the author.

Figure 4.7 then compares the results for the magnetopause standoff location obtained via MHD simulation (red curves) in the two case studies, with previous presented in this Chapter empirical results such as defined by Shue et al. (1998) (blue curves). To calculate that by using the MHD approach, at each instant of the simulations the location along the SM x-axis of the maximum peak in the total current density

was obtained, which it was then considered to be the magnetopause nose distance to the Earth's center (similar to Medeiros et al. (2019) and Jauer et al. (2019)). This peaked current density is assumed to correspond to the dayside Chapman-Ferraro current that originates the magnetopause boundary through the pressure balance between the dynamic pressure of the solar wind and the magnetic pressure of the magnetosphere (CRUMLEY et al., 2007).

The comparisons show a good agreement of MHD results until the magnetopause is compressed to 8 R_E or nearby, in both cases. Thus, never reaching the minimum positions predicted by the empirical model in those events, of roughly 7 R_E. After this period of enhanced compression (after $\sim$ 6 UT-03/27 in case 1 and 0 UT-11/21 in case 2, despite data gaps) up to the end of the simulations, the magnetopause from MHD gradually recovers to nominal locations (10 R_E or so), but constantly at around 1 R_E farther than predictions from the Shue et al. (1998) model in case 1, or even higher than this threshold in case 2.

Shue et al. (1998) calculated that the standard deviation for the uncertainties related to their model is of $1.23R_E$. Such an error in representing observations is around the order of the discrepancies obtained between this model and the MHD results in case 1, and most of the time comparable to those discrepancies observed in case 2. This is a possible explanation for the lower radial distances of the magnetopause nose predicted by the Shue et al. (1998) model in the two cases, through storm time. On the other hand, it is worthy mentioning that while the magnetopause location from MHD has been taken along the SM x-axis (perpendicular to the Earth's dipole and for which coordinate transformations from the GSM system to SM were required), results from the Shue et al. (1998) model were directly derived for the subsolar point along the GSM x-axis. Yet, the results presented here for the magnetopause standoff distance computed with the MHD simulations will be the reference location for analysis of diffusion coefficients, that were also obtained via the global simulations.

Speaking of limitations related to both discussed models of the magnetopause location, the Shue et al. (1998) model can be based on crossings over a large area as well as assume the functional form in Equation 2.5 to describe the magnetopause shape (SAMSONOV et al., 2020). On the other hand, location estimates from the coupled MHD model are very susceptible to modeled current systems in the magnetosphere such as the cross-tail and ring currents (e.g., Hudson et al. (2014)), which control the value of R_{MP} through their contributions to the magnetic field intensity on the magnetospheric side of the magnetopause.

4.2.2 Calculation of D_{LL} coefficients from the global MHD fields

To obtain the symmetric D_{LL} coefficients using MHD-derived electric and magnetic fields, we followed the method discussed in detail by Tu et al. (2012). The same assumptions were made here, especially those related to the use of only positive wave mode numbers for the calculations. This means that, in this work, it is neglected that part of the calculated power spectral densities might come from negative mode numbers, so that the actual diffusion coefficients would be reduced. By definition, these negative mode waves do not resonate with electrons due to their clockwise propagation in the azimuth plane, opposite to the electrons' drift direction.

The reasoning for omitting the asymmetric counterparts from these D_{LL} calculations is based on results previously obtained by Fei et al. (2006). They showed that, for a case study with a larger magnetopause compression (up to $\sim 5R_E$), the symmetric coefficients alone adjusted well the phase space densities obtained from radial diffusion model with those from the MHD particle simulation.

In the calculation approach performed here, the events' azimuthal electric field and compressional magnetic field along circular orbits on the SM equator are first derived. Those circular orbits represent the electrons' drift orbits at which D_{LL} will be calculated, assuming the geomagnetic field as a dipole. Both field aligned components are the relevant ones to contain ULF wave fluctuations that account for the radial diffusion of radiation belt electrons, as defined in Equations 2.31 to 2.33.

Throughout the simulation intervals, the MHD fields were interpolated to a polar grid of 48 uniform azimuthal locations (ϕ) along the circular "drift" orbits (as in Elkington et al. (2013)). The circular orbits were placed at radial distances (r) from 3 to $9R_E$, $0.1R_E$ wide (although $0.25R_E$ is the lowest grid resolution constrained in the MHD simulations, this finer radial separation was also obtained via interpolation). It is worthy mentioning that together with this interpolation step, coordinate transformations were required since as stated before, BATS-R-US inputs/outputs must be in GSM. Thus, input locations of the circular orbits defined as ($x = r\cos\phi, y = r\sin\phi, z = 0$) in the SM-equatorial plane needed first to be determined in GSM coordinates (x', y', z'), on which the field components were also interpolated in GSM. Subsequently, these GSM fields at coordinates (x', y', z') were converted into SM fields corresponding to previous coordinates ($x = r\cos\phi, y = r\sin\phi, z = 0$) on the SM equator. To finish the process, the SM (cartesian) fields were transformed to cylindrical coordinates, so that the field aligned components of interest defined as E_ϕ (r, ϕ, t) and B_z (r, ϕ, t)

could be derived; recall that B_z in SM is the same as $B_{\|}$ from the FAC system. The global E_ϕ component was determined from the convection electric field ($\mathbf{E} = -\mathbf{u} \times \mathbf{B}$), where $\mathbf{u}$ and $\mathbf{B}$ are the simulated plasma velocity and geomagnetic field vector, respectively. For those steps and the 2D-interpolations, the *CCMC Kameleon* software with libraries written in Python was used and is publicly available at https://ccmc.gsfc.nasa.gov/Kameleon/.

Subsequently, an FFT was computed along the azimuthal angle (ϕ - equivalent to zero at noon) to resolve the instant mode structure of the ULF fluctuations at each r value, which written out reads:

$$E_\phi(r,\phi,t) = \sum_{m=1} E^a_{\phi,m}(r,t)\cos m\phi + \sum_{m=1} E^b_{\phi,m}(r,t)\sin m\phi \tag{4.1}$$

$$B_z(r,\phi,t) = \sum_{m=1} B^a_{z,m}(r,t)\cos m\phi + \sum_{m=1} B^b_{z,m}(r,t)\sin m\phi \tag{4.2}$$

Consider a and b indices indicating the real and imaginary counterparts of the FFT signals. On top of these m-resolved fluctuations, another FFT was performed in the time domain, for fixed r, so that the final wave components became fully determined in terms of mode numbers (m) and the frequency spectrum. In this second FFT, the complex signals were previously multiplied by a Hanning window with a time length of 2 hours, which implies a lower band frequency of about 0.14 mHz. These 2-hour windows were let slide forward in time with an overlapping rate of 15 minutes. Given the 1-minute cadence of the input data, power spectral densities taken at the resonance frequencies and harmonics ($f_d = m\omega_d/2\pi$) were obtained whenever these frequencies were within $0.14 - 8.33$ mHz.

As a dipole magnetic field has been considered in these D_{LL} calculations, radial distances (r) from the MHD simulations used for the field interpolations upon the SM equator are taken as equivalent to L shell (L). Finally, the total PSDs found in E_ϕ and B_z fluctuations by considering the resolved m numbers (while satisfying the resonance condition) were implemented into Equations 2.31 and 2.32, and then maps of D_{LL}=D^E_{LL}+D^B_{LL} were derived.

Addressing ω_d and D_{LL} contributions in terms of SI units, adjustments were made in these formulas to end up with ω_d in units of [rad/s] and so f_d in [Hz], and a factor of 24*60*60 was needed to obtain D_{LL} rates in units of $[days^{-1}]$ once the other terms in Equations 2.31 and 2.32 were already in SI.

On the other hand, the division of the polar grid into 48 uniform slices resulted in mode numbers up to $m = 24$. However, the D_{LL} results to be shown next were derived for m numbers from 1 up to 9 because this work is centered in ULF resonance interaction with high-energy electrons. From the resonance condition for symmetric modes seen in Equation 2.27, one realizes that for a given frequency ω, the higher is the m considered, the lower is the electron energy at which resonance is matched since if ω_d decreases, energy shall also decrease. This chosen wave number coverage is also restricted to the Nyquist frequency of the data, and to the corresponding first invariant μ analyzed, accordingly.

4.2.2.1 Similar approach to derive D_{LL} from in-situ fields

Commonly, D_{LL} results obtained from MHD simulation are validated by empirical models of D_{LL} provided by the recent literature. However, there is a consensus in the space physics community that when dealing with case studies, one should consider calculating the event-specific radial diffusion coefficients directly from spacecraft observations, for proper comparisons and discussions (e.g., Ozeke et al. (2014a)). Based on that, it is provided in this section the set of assumptions necessary to obtain D_{LL} specifically from single-point observations.

The first assumption lies in resolving m from single-point measurements. In order to resolve electric and magnetic fluctuations up to a given m number, $2m$ azimuthal point measurements are required (TU et al., 2012). To overcome this limitation, $m = 1$ was first assumed. Second, under the circumstance of single-point measurement, PSDs were then obtained at a single azimuthal position of the electron's drift orbit, which leads to the proposition of a constant spectra along this drift orbit for deriving D_{LL}. This differs a bit from the concept of drift-averaged spectra considered by previous authors (e.g., Liu et al. (2016)) when deriving empirical D_{LL} from larger data sets. In such a case, there are more samples of PSD available with MLT, for a given L. At this point, it should be stated that although multiple spacecraft have been used for this analysis, no attempt to track their time-conjunctions in L and consequently to derive the drift-averaged spectra with respect to MLT was made.

Then, we follow the equations outlined by Ozeke et al. (2014a), by assuming the same set of conditions to calculate D_{LL} from observations, so that D_{LL}^E and D_{LL}^B can be defined as follows:

$$D_{LL}^E = \frac{L^6}{8B_E^2 R_E^2} P_m^E(L, f_d) \tag{4.3}$$

$$D_{LL}^{B} = \frac{L^8 4\pi^2}{9 \times 8 B_E^2} P_m^B(L, f_d) f_d^2 \tag{4.4}$$

Equations 4.3 and 4.4 were inferred analytically from the previous presented equations of Fei et al. (2006), where single mode fluctuations in E_ϕ and $B_\parallel$ (in SM coordinates) will be assumed. Here, the PSD terms P_m^E and P_m^B in these equations stand for the ULF wave power taken at resonance frequencies ($f_d = \omega_d/2\pi$) only, for a given first invariant μ.

As done with regard to the MHD simulations, event-specific radial diffusion coefficients were determined through Equations 4.3 and 4.4 for the two case studies. And as discussed previously in this chapter, in each event, electric and magnetic field data acquired by RBSP-B and three THEMIS spacecraft (TH-A, TH-D and TH-E) were utilized, which enable to calculate the total D_{LL} and to undertake the direct comparison with results from MHD.

4.2.2.2 Electron drift-resonant frequencies and energies

In this work, radial diffusion coefficients from MHD simulation are calculated for $m = 1 - 9$, and validated with radial diffusion coefficients from single-point observations assuming $m = 1$. In both cases, a dipolar geomagnetic field is used to derive the drift-resonant frequencies ($f_d = m\omega_d/2\pi$) across L shells, at given μ, with w_d defined by Equation 2.34. Figure 4.8(a) presents the L distribution of resonance frequencies for $m = 1$, worth of 90° pitch angles. They were computed for three μ values considered in this study: $\mu = \{700, 1318, 2083\}$ MeV/G. It is observed that $m = 1$ covers $f_d \lesssim 3$ mHz throughout L shells at this range of μ values. Thus, the magnetic and electric wave power implemented to calculate in-situ D_{LL} (e.g., from Figures 4.4 and 4.5) are restricted to low frequencies of the Pc5 band, specially for $L > 6$.

Figure 4.8(b) illustrates the L distribution of the kinetic energies (E; from Equation 3.17) corresponding to each μ value above, also assuming a dipolar geomagnetic field and 90° pitch angle electrons. Note that $\mu = 700$ MeV/G covers specifically relativistic electrons ($0.511 < E < 2$ MeV) throughout the outer belt region at $L \sim 3 - 7$. At the heart of the outer belt ($L = 4.5$), $E = 1.1$ MeV for $\mu = 700$ MeV/G, $E = 1.7$ MeV for $\mu = 1318$ MeV/G, and $E = 2.2$ MeV for $\mu = 2083$ MeV/G.

Figure 4.8 - (a) Local drift-resonant frequencies of equatorially mirroring electrons for $m = 1$, and (b) corresponding kinetic energies related to $\mu = 700, 1318, 2083$ MeV/G.

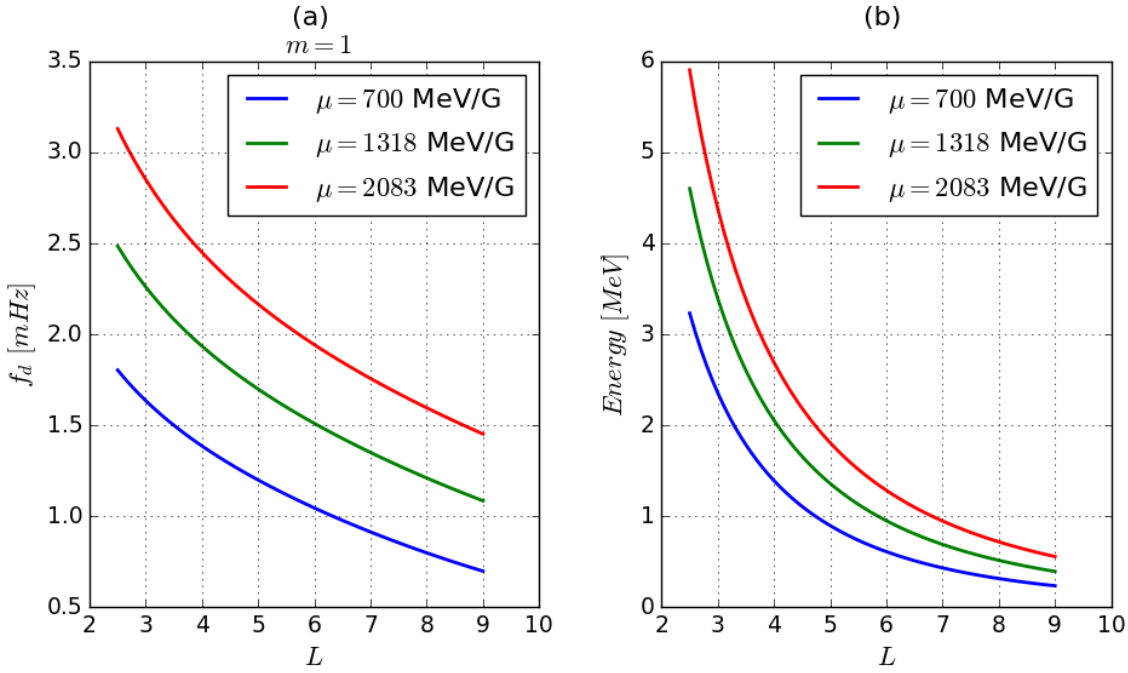

Calculations assuming $B_E \sim 0.3G$, and $B(L) = B_E L^{-3}$ for the magnitude of the local dipolar geomagnetic field.

SOURCE: Produced by the author.

4.3 Results and comparisons

Figures 4.9 and 4.10 present maps of D_{LL}^{MHD} corresponding to the two events, respectively, and calculated for the contribution of the MHD fields in separate (top panels), such as defined by Fei et al. (2006), together with the total D_{LL}^{MHD} obtained from these contributions, and their ratio (bottom panels). The first invariant $\mu = 1318$ MeV/G was chosen for the results shown in this Chapter. Also, the equatorial strength of the Earth's magnetic field at the surface (B_E) was fixed at 29,868 nT in all calculations of D_{LL} using Equations 2.31-2.33 and 4.3-4.4. This value corresponds to the intensity of B_E in 2015, which was computed with the three first Gauss coefficients from the IGRF-13 model (after Thébault et al. (2015)). The magnetopause standoff distance obtained from the MHD simulations is also shown in these maps as black curves.

Figure 4.9 - Case 1: D_{LL} from MHD simulation - D_{LL}^{MHD}.

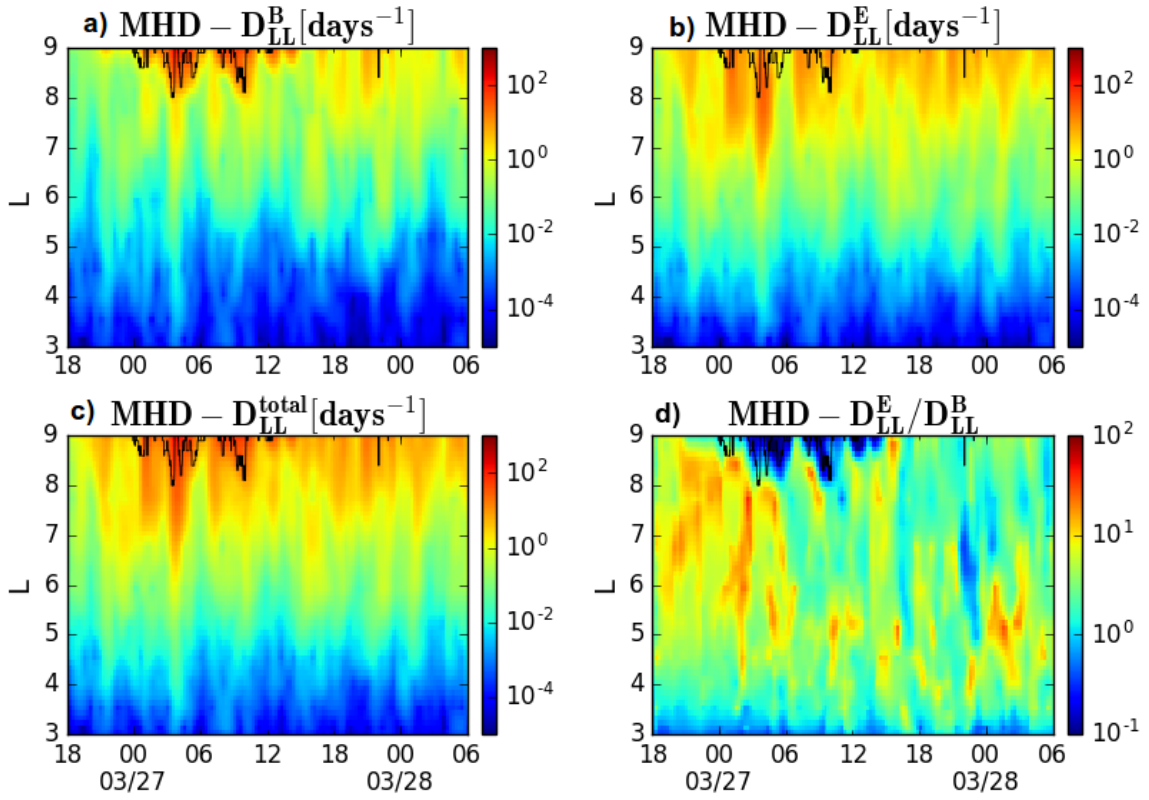

(a-b) Magnetic and electric radial diffusion coefficients obtained from the MHD fields in case 1 and calculated for $\mu = 1318$ MeV/G. (c-d) Total radial diffusion coefficients from these contributions on the left, followed by a map of the ratios between D_{LL}^{E} and D_{LL}^{B}. The black curve in these graphs correspond to the magnetopause location derived from the MHD simulation.

SOURCE: Produced by the author.

The primary goal of this analysis is to check whether in the most prominent dropout event (case 1) radial diffusion was in the same way more prominent in relation to the dropout of case 2. From the view of MHD simulation results, this was the case when particularly comparing maps of the total D_{LL}^{MHD} in Figures 4.9 and 4.10 (panels (c)). D_{LL}^{B} in case 1 is notably stronger than the rates of case 2 inside the magnetopause (see panels (a)), although by a factor of less than one order of magnitude. Note that the diffusion coefficients above this boundary can be discarded from the analysis because this is already an ultimate loss region for radiation belt particles. On the other hand, D_{LL}^{E} from case 1 (Figure 4.9 (b)) is notably more enhanced in $1-2$ orders than the rates of case 2 (Figure 4.10 (b)), especially above $L = 6$. In this regard,

it is interesting to notice in both cases that the deepest penetration of enhanced D_{LL}^{E} ($\sim$ 4 UT-03/27 in Figure 4.9(b), and $\sim$ 18 UT-11/20 in Figure 4.10(b)) is seen concurrent with the main compression of the modeled magnetopause. This effect in D_{LL}^{E} has been suggested by Murphy et al. (2015), and it is more likely to take place in the storm main phase. Similar results were reproduced by Fei et al. (2006) with MHD modeling. As a matter of fact, increased total D_{LL}^{MHD} rates also reached lower L during such periods in the results shown.

Figure 4.10 - Case 2: D_{LL} from MHD simulation - D_{LL}^{MHD}.

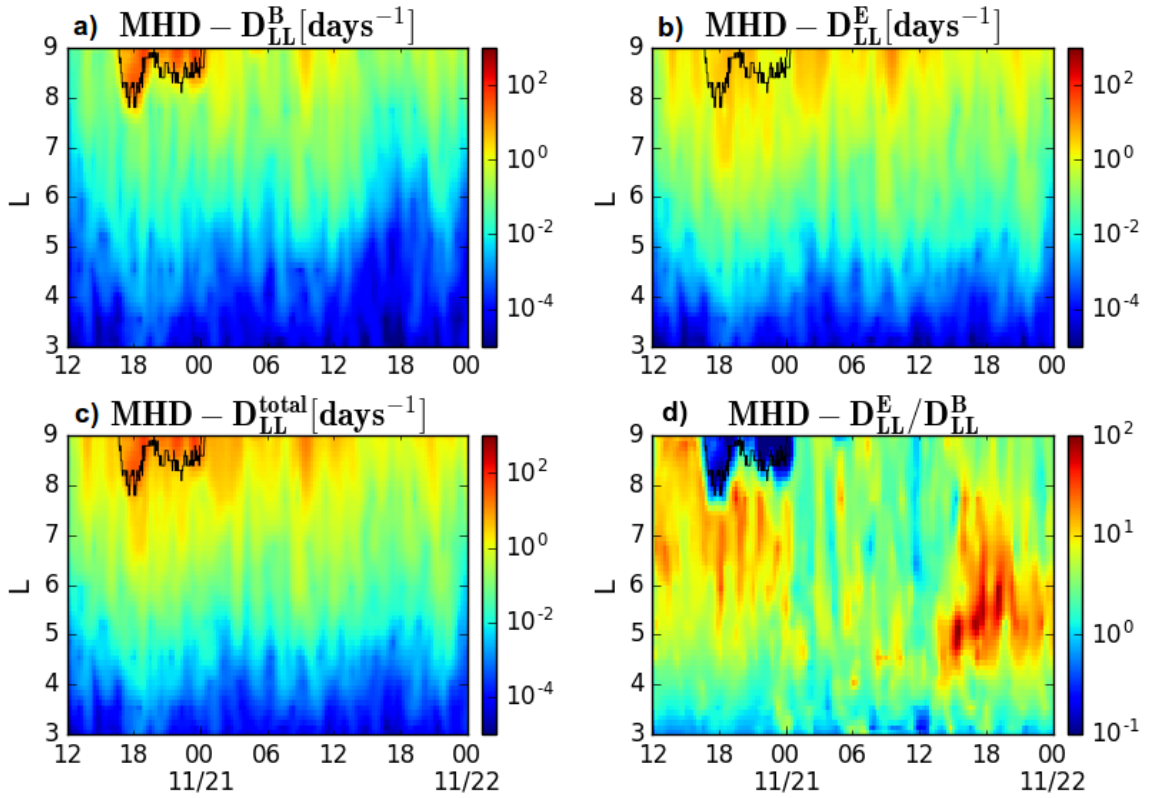

Same as in Figure 4.9.

SOURCE: Produced by the author.

Overall, results of D_{LL}^{E}/D_{LL}^{B} ratios on panels (d) of Figures 4.9 and 4.10 show that during both events the D_{LL}^{E} contribution starts larger with increasing L, and takes place together from beginning of the MHD simulations up to around their interval of magnetopause erosion. By contrast with case 1, a lack of important contribution

from D_{LL}^{B} in case 2 led to the strong predominance of D_{LL}^{E} in the final hours of the MHD simulation. More importantly, it is noted that the model is able to capture the pattern of D_{LL}^{E} generally greater than D_{LL}^{B} inside the magnetopause, which is intrinsic to the formalism of Fei et al. (2006). Similar responses can be inferred from results of D_{LL}^{MHD} computed for $\mu = 700$ and $\mu = 2083$ MeV/G (see Figures A.1 to A.4 in Appendix A.)

Next, the responses of D_{LL} from observations are analyzed. They are constrained to measurements provided by RBSP-B and THEMIS spacecraft, in the satellite array presented in Figure 4.11 (case 1) and Figure 4.12 (case 2). Therefore, Figures 4.13 and 4.14 show from (a) to (c) the resultant magnetic, electric, and total radial diffusion coefficients equally calculated for $\mu = 1318$ MeV/G. Ratios of D_{LL}^{E}/D_{LL}^{B} can be viewed in panels (d). Those D_{LL} rates are presented along the probes' instant L shell. It is important to mention that for RBSP-B, the McIlwain L is used again, while for THEMIS (TH-E, TH-A, and TH-D) it is used the dipole L calculated with IGRF, and available at NASA's CDAweb database. The 30-minute resolution of these D_{LL} bins relates to the windowing set for the FFT. For D_{LL}^{MHD}, the time-resolution was 15 minutes. Both resolutions are adequate for the analyses since these timescales are higher than the period a relativistic electron is expected to execute a complete drift motion about a fixed L. According to estimates provided in Figure 4.8, 1 MeV electrons at $L = 6$ conserving $\mu = 1318$ MeV/G have drift frequency of 1.5 mHz, which corresponds to a drift period of $\sim$ 11 minutes.

Figure 4.11 - Multiple spacecraft location in GSE on March 26, 2017 - case 1.

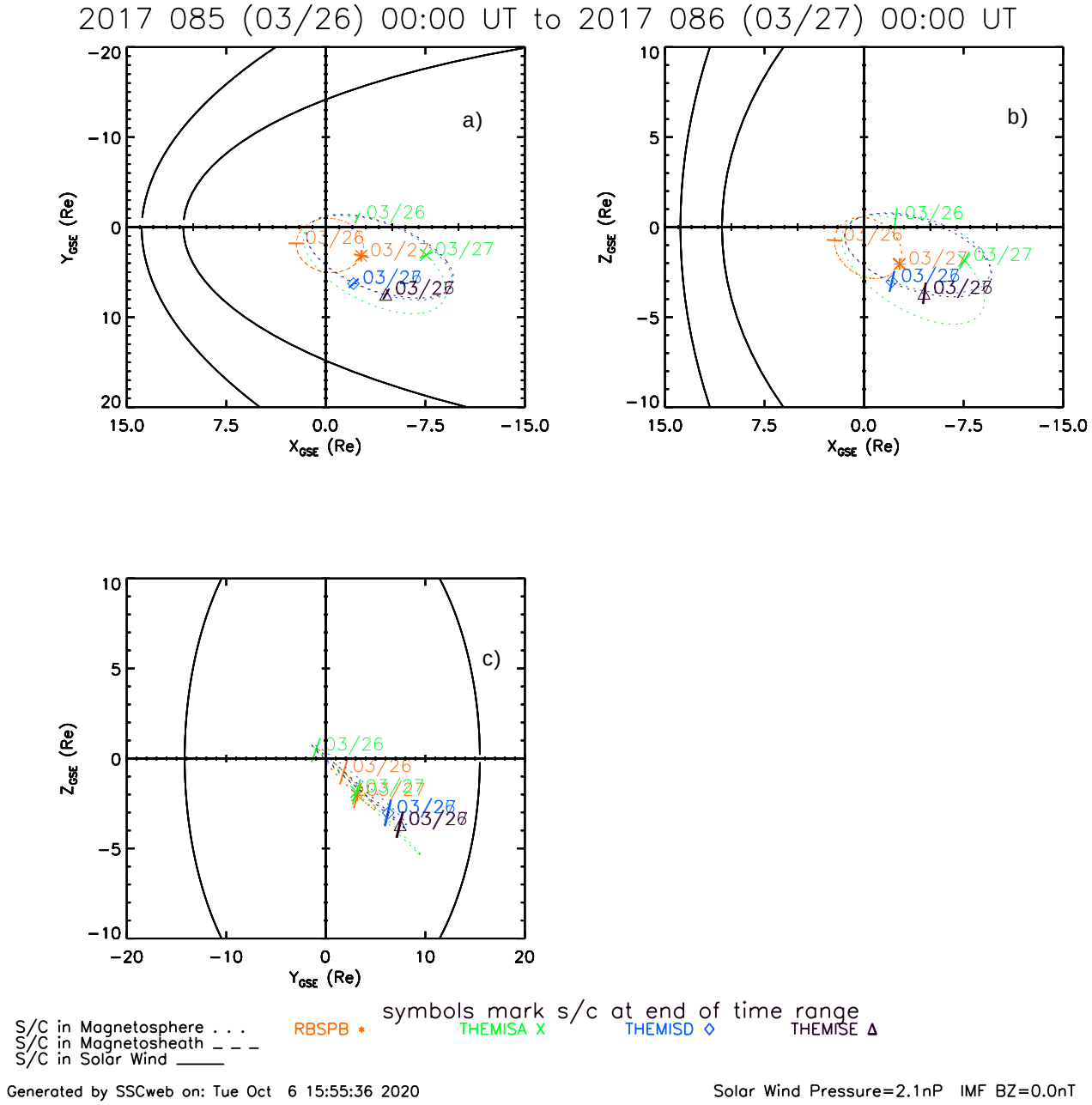

(a) Orbits along the equatorial plane showing that RBSP-B was probing the dusk side, while THEMIS-A, D and E were mostly at the pre-midnight sector. (b-c) Orbits along X-Z and Y-Z planes, respectively. The locations of the magnetopause and the bow shock calculated using solar wind pressure of 2.1 nPa and IMF-Bz of 0 nT, are projected to each plane of the panels, indicated by the black solid curves.

SOURCE: NASA/SPDF (2020).

Figure 4.12 - Multiple spacecraft location in GSE on November 20, 2017 - case 2.

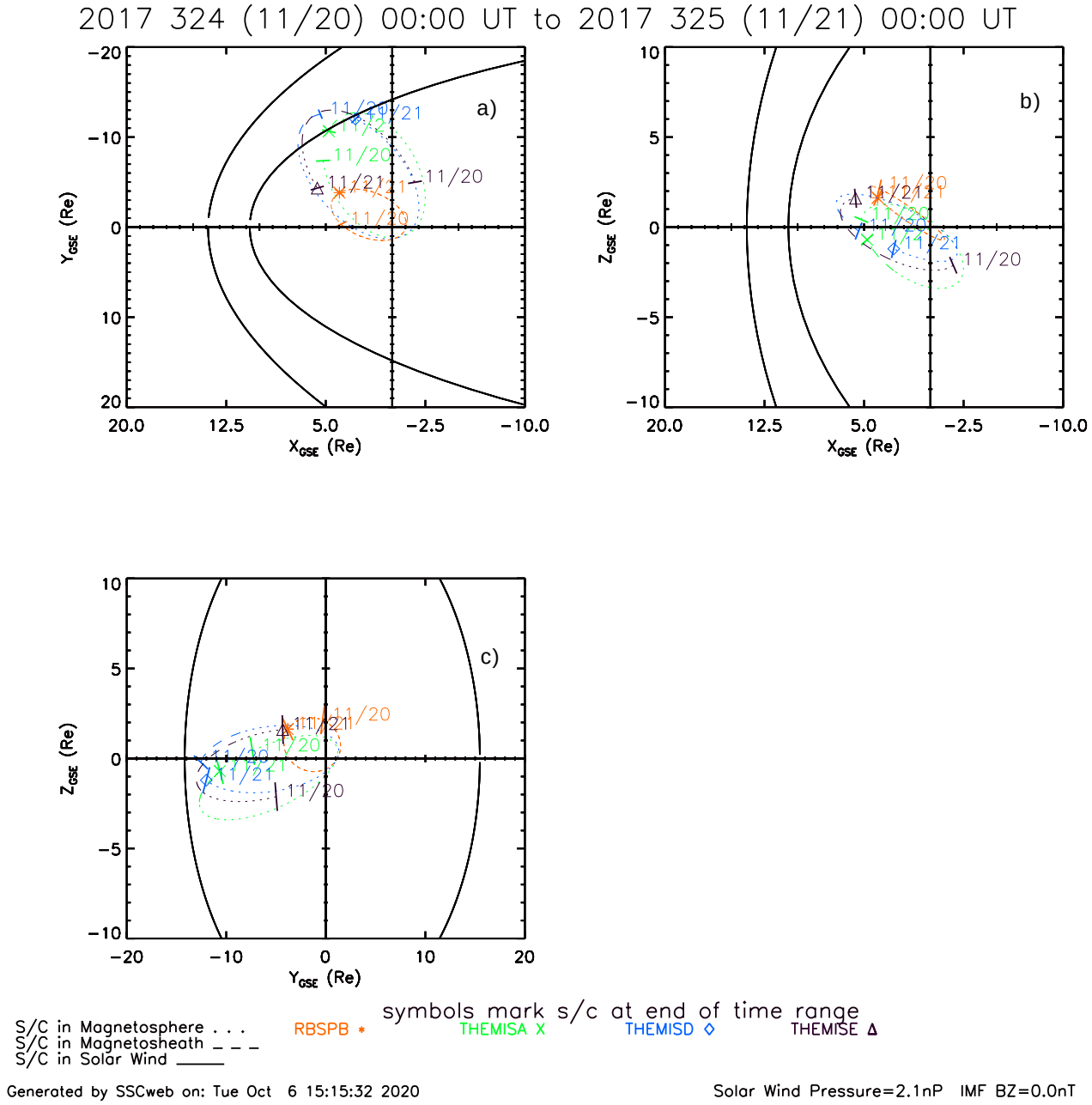

(a) Orbits along the equatorial plane showing that RBSP-B was close to noon, while THEMIS-D, E and A were mostly at the pre-noon sector. (b-c) Orbits along X-Z and Y-Z planes, respectively. The locations of the magnetopause and the bow shock calculated using solar wind pressure of 2.1 nPa and IMF-Bz of 0 nT, are projected to each plane of the panels, indicated by the black solid curves.

SOURCE: NASA/SPDF (2020).

Now, from the view of observations, it is seen that total radial diffusion coefficients were visibly stronger in case 1 than in case 2 throughout storm time, specifically at $L \lesssim 6$ (see panels (c) of Figures 4.13 and 4.14 for comparison). These results corroborate with previous Figures 4.4 and 4.5 showing that less ULF wave power has been also measured in the second case.

Figure 4.13 - Case 1: D_{LL} from observations for $\mu = 1318$ MeV/G.

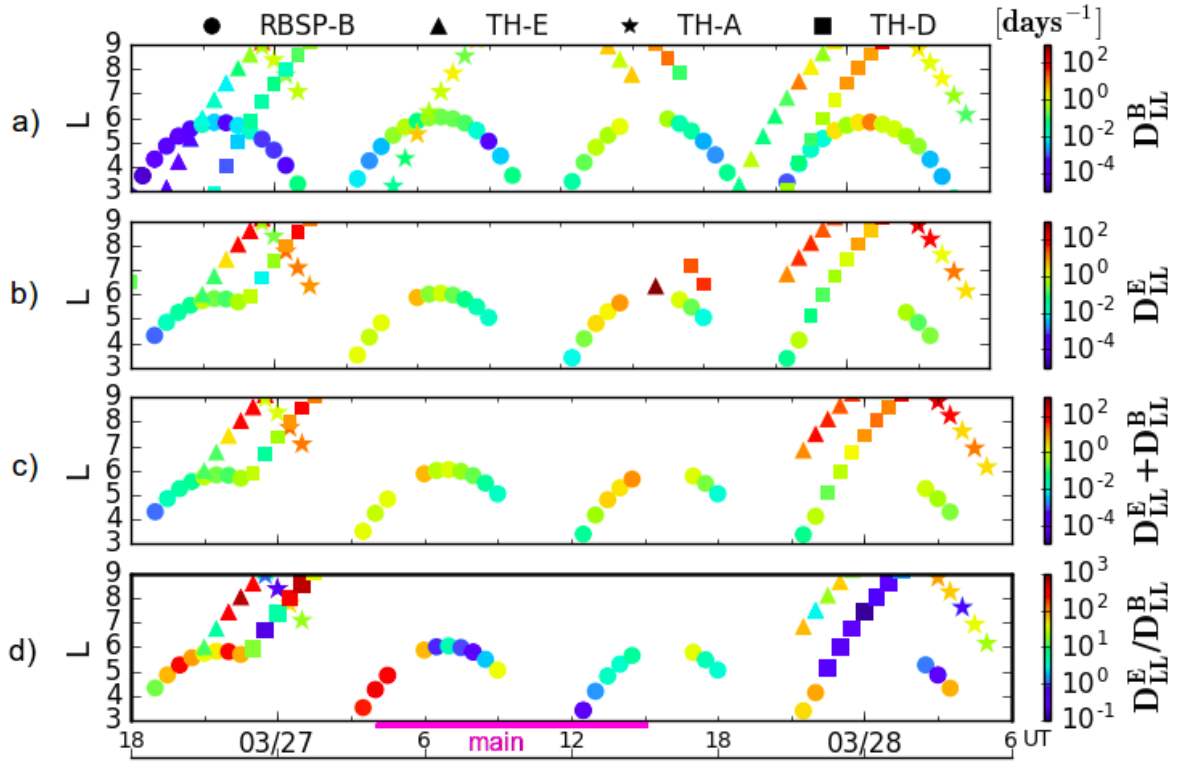

Derived radial diffusion coefficients shown along the satellites' trajectory, given by L. The time duration of the main phase of the storm is also indicated by the pink straight bar on the bottom most panel.

SOURCE: Produced by the author.

Figure 4.14 - Case 2: D_{LL} from observations for $\mu = 1318$ MeV/G.

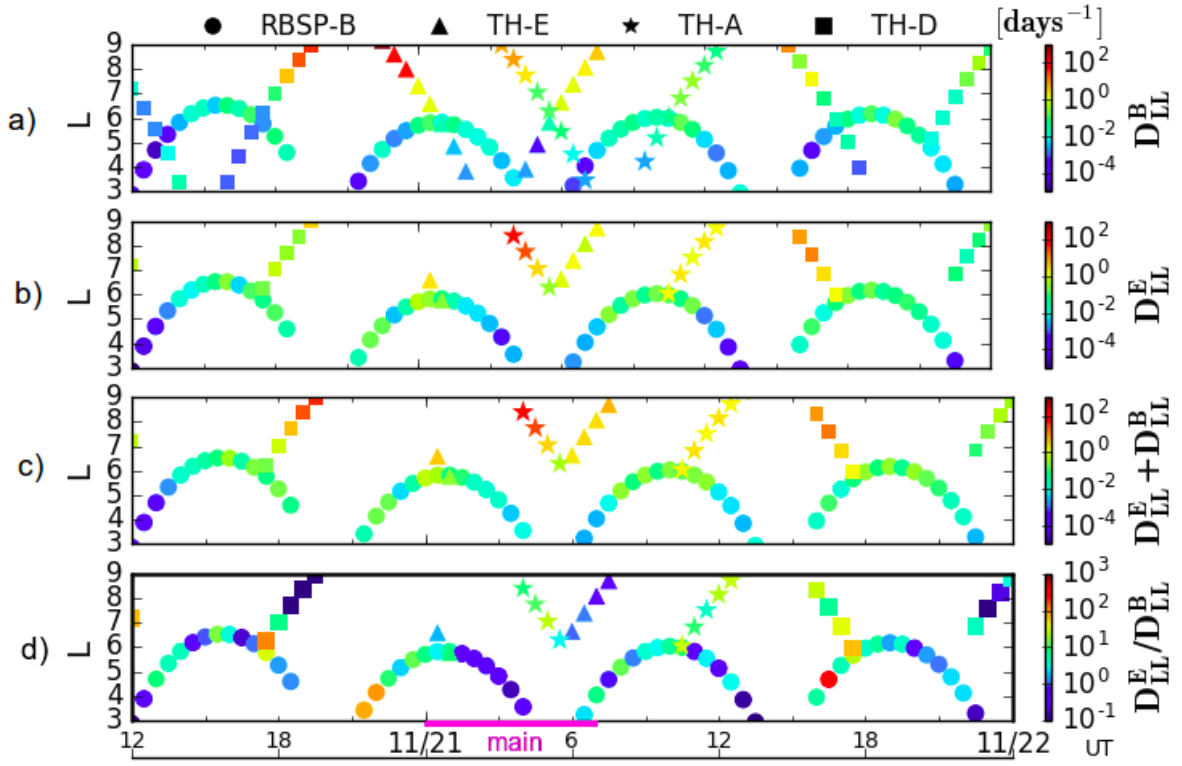

Same as Figure 4.13.

SOURCE: Produced by the author.

Considering the following dropout intervals elucidated for the two events (6 – 18 UT on 03/27-case 1 and on 11/21-case 2) and RBSP-B diffusion coefficients only, it is noted in case 1 that the total D_{LL} is already increased prior to the dropout observations (outbound pass between 3 and 6 UT in Figure 4.13(c)), due to the main phase of the storm (as obtained for the ULF waves). This is accompanied by a second instance of increase in the total coefficients down to $L \sim 4$ (from 12 to $\sim$ 15 UT still on panel (c)). This result from RBSP-B indicates that enhanced radial diffusion at low-L may have contributed to the deep dropout of case 1 reported in Figure 4.1(a).

Regarding results related to the dropout of case 2 (Figure 4.14), in spite of the low rates seen in the amplitude range shown, it is found that the total rates in panel (c) are relatively increased approaching RBSP-B's apogee. And that can also be extended to explain this dropout particularly spanning higher L shells as seen by

the Van Allen Probes (Figure 4.2(a)), because enhancements in D_{LL} are observed approaching RBSP-B's apogee (meaning higher L), and so does the dropout.

Despite the data gaps mainly affecting results from THEMIS in case 1, total storm-time D_{LL} estimates taken at high-L sites probed by the three THEMIS are, in both cases, stronger than RBSP-B low-L coefficients (see Figures 4.13 and 4.14, panels (c)), because of the proximity with the compressed magnetopause (shown in Figure 4.7) and the high-intensity ULF wave activity driven by the storms in this region. This latter effect was shown to have started with the initial phase of the storms (mentioned on discussions of Figures 4.4 and 4.5). Also, larger PSD values of the latter two figures concentrate at very low frequencies of the Pc5 band, which resonate with radiation belt electrons at higher L, according to Figure 4.8.

The analysis of D_{LL}^{E}/D_{LL}^{B} ratios in these plots (Figures 4.13 and 4.14, panels (d)) shows the general behavior of D_{LL}^{E} greater than D_{LL}^{B} across L shells, in both cases. This is enhanced mainly in response to the initial phase of the storms, most likely to be associated with the onset of large-scale convection in the magnetosphere and the effect of magnetopause compression that both acts to increase D_{LL}^{E} at most, as seen on results from MHD. However, ratios from observations in case 1 are much larger than in case 2 during these intervals. After that, within the domain of the main phase of the two storms, D_{LL}^{B} become comparable to D_{LL}^{E} or even higher than this contribution. This result has been explained by Olifer et al. (2019) to be related with intervals of strong southward IMF component, as visibly obtained for case 1 (see after 0 UT-03/27 in Figure 4.1(d)).

Direct comparisons between results of D_{LL} from observations, named D_{LL}^{OBS} from now on, and MHD simulation were obtained for the two events, which are shown respectively in Figures 4.15 and 4.16. In order to do this one-to-one comparison, linear interpolation was applied to obtain simulated diffusion coefficients from MHD at the L shells where D_{LL}^{OBS} coefficients were derived. At this point, another approximation related to the calculation of radial diffusion coefficients from single-point measurements is introduced: RBSP-B and THEMIS probes can be up to $\sim 5R_E$ far from the plane containing the magnetic equator while performing their elliptical orbits, which means that those rates are not strictly obtained along drift orbits upon the magnetic equator, as done with regard to the MHD approach. As a consequence, the range of equatorial pitch angles affected by D_{LL}^{OBS} differ a bit from 90°, being smaller at the point of major inclination of the probes.

Figure 4.15 - Case 1: Radial diffusion coefficients interpolated from D_{LL}^{MHD} maps versus in-situ D_{LL}^{OBS} ($\mu = 1318$ MeV/G).

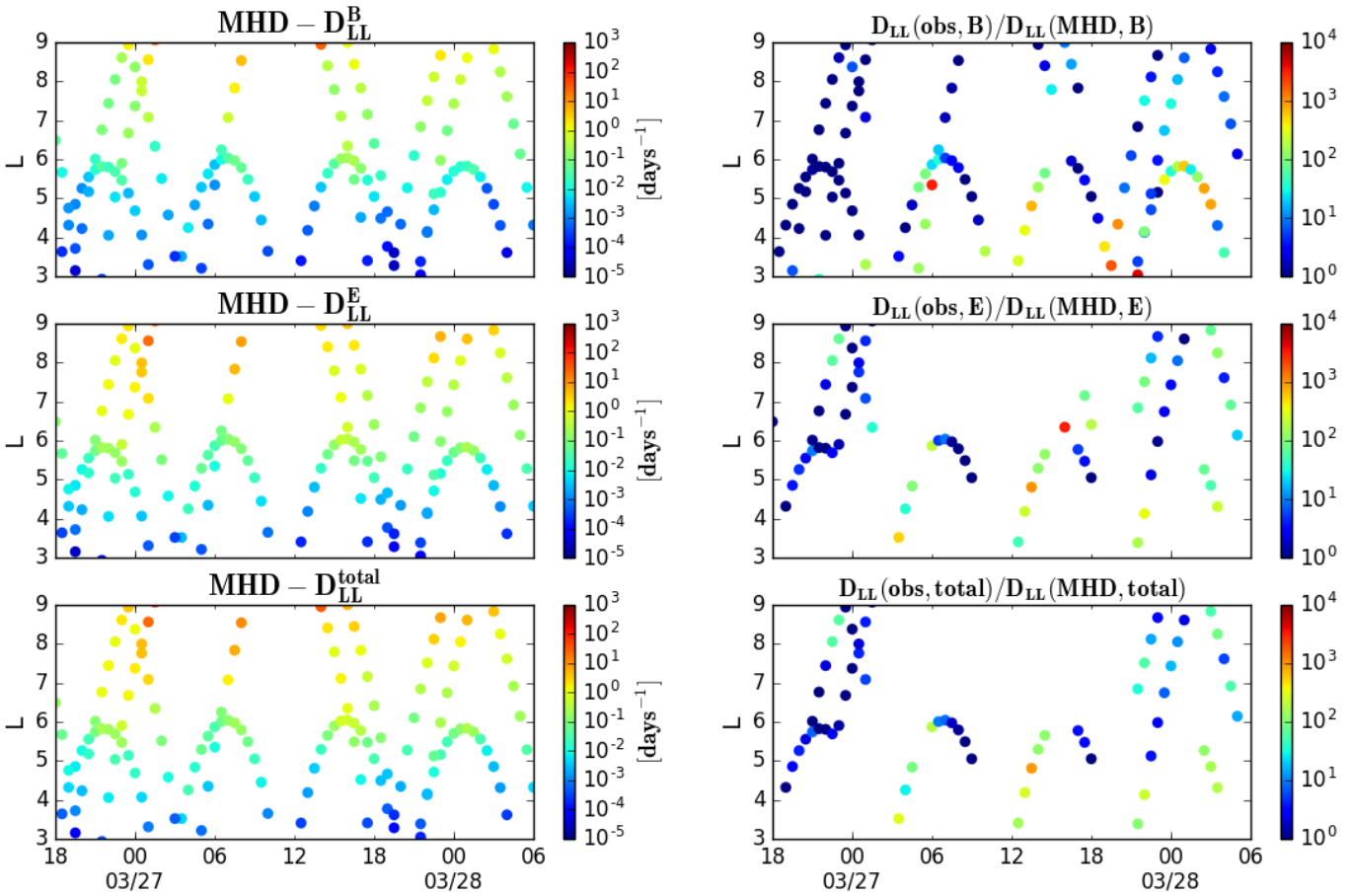

Left-hand panels show results of simulated rates derived approximately at the drift orbits where D_{LL} from observations is obtained. Right-hand panels depict the direct ratios between them, among the three components of D_{LL} (magnetic, electric and total). In these panels on the right, more reddish color indicates underestimation by D_{LL}^{MHD} components in relation to D_{LL}^{OBS} results, whereas more bluish color indicates overestimation by D_{LL}^{MHD} components.

SOURCE: Produced by the author.

Figure 4.16 - Case 2: Radial diffusion coefficients interpolated from D_{LL}^{MHD} maps versus in-situ D_{LL}^{OBS} ($\mu = 1318$ MeV/G).

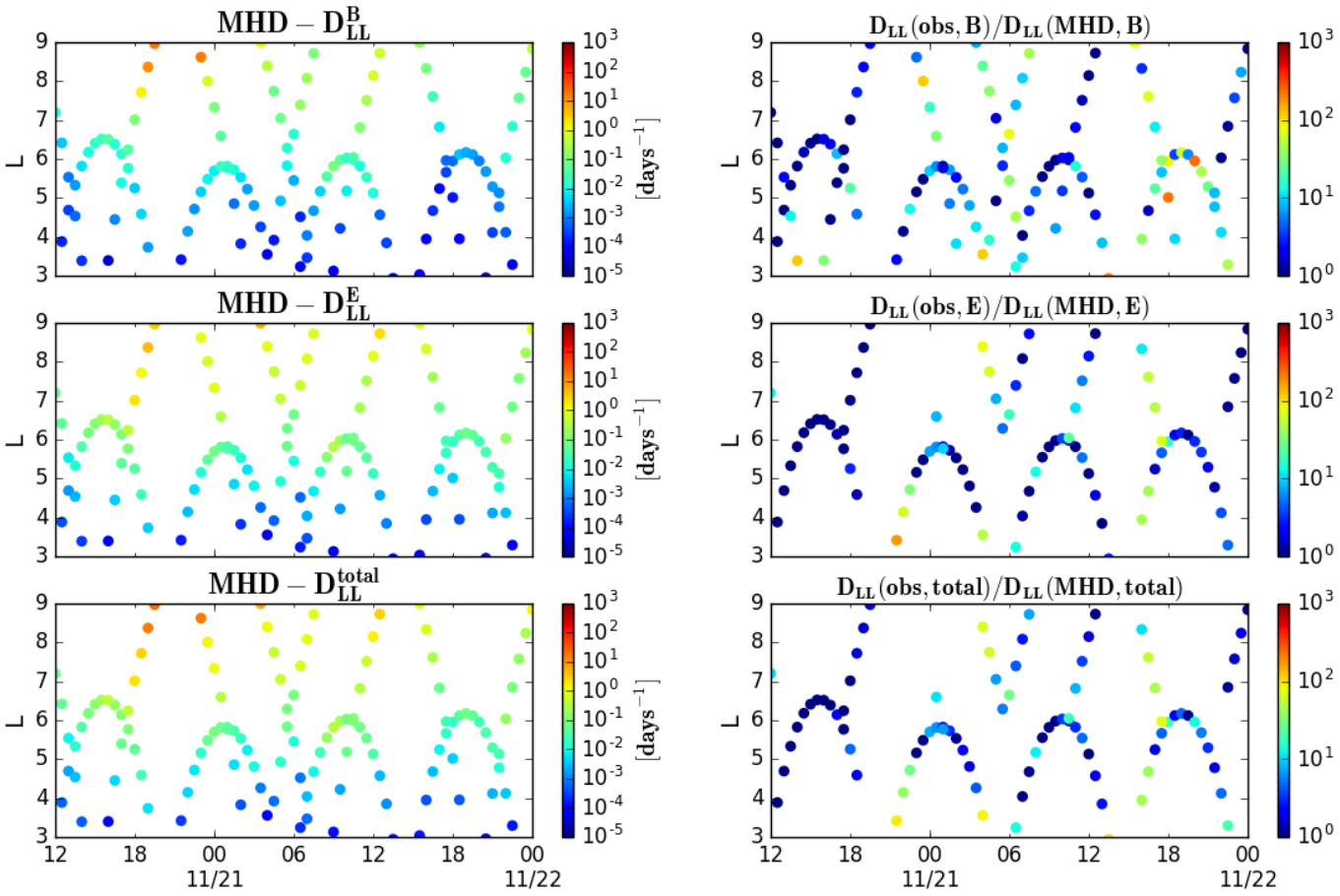

Same as Figure 4.15.

SOURCE: Produced by the author.

Despite that, the main conclusions about results in case 1 are (Figure 4.15, panels on the right): (i) total D_{LL}^{MHD} is most of the time underestimated, by ratios within $10 - 10^3$ defined as $D_{LL}^{OBS}/D_{LL}^{MHD}$; (ii) the underestimations are higher for D_{LL}^{B} from MHD throughout storm time. Also, in relation to observations, this component offers less gaps both around the region of coverage of the THEMIS satellites and RBSP-B; (iii) the main instances of underestimation affecting D_{LL}^{E} from MHD that can be observed from this data set occur at lower L shells, and it is on the order of $\sim 10^2 - 10^3$ of magnitude. This is especially seen along the two outbound passes of

RBSP-B on which enhancements in D_{LL}^{OBS} were reported before. This result implies that the MHD model did not capture the enhanced ULF wave activity triggered at lower L shells.

Results of case 2 (Figure 4.16, panels on the right) reveal a better performance by the MHD model to reproduce D_{LL}^{OBS} coefficients during storm time, with the ratios of underestimation in total D_{LL}^{MHD} not higher than $\sim 10^2$. Because of better data coverage provided by THEMIS in this event, it is seen that higher ratios of underestimation, of around 10^2, affect both low and high L shells.

Figures A.5 and A.6 from Appendix A exhibit further analysis of ratios of total D_{LL} computed also for $\mu = 700$ MeV/G and $\mu = 2083$ MeV/G, defined between diffusion rates from observations and simulations through BATS-R-US. This was done in order to find out whether the performance of the MHD model to reproduce D_{LL}^{OBS} is sensitive to μ. However, no clear distinction concerning underestimations by the model can be made among these μ-dependent ratios.

Now, comparisons of the event-specific coefficients given by D_{LL}^{MHD} and D_{LL}^{OBS} results are undertaken, in each case study, along with empirical/statistical models of D_{LL}. The models considered are from Brautigam and Albert (2000), Liu et al. (2016), and Ali et al. (2016). Moving to the comparisons, radial profiles with results from each type of D_{LL} estimate are provided. This analysis is performed for several three-hour intervals of the MHD simulation time-domains, in each case study, during which the Kp index is maintained fixed. Figure 4.17 shows results for case 1 and Figure 4.18 for case 2. It was given preference to intervals with larger coverage of data regarding results of D_{LL}^{OBS} from Figures 4.13 and 4.14. In the following plots, $\left\langle D_{LL}^{MHD} \right\rangle$ represents the radial profile of the mean of MHD-derived total coefficients along each interval Δt shown, that is, $\left\langle D_{LL}^{MHD}(L, \Delta t) \right\rangle$.

Here and thereafter, D_{LL}^{OBS} results will be the basis for comparisons with the other radial diffusion coefficient models since it is believed to be a good estimate of in-situ rates during a specific event (e.g., Olifer et al. (2019)). Overall, it is seen in both cases that the implemented coefficients are comparable or overestimate D_{LL}^{OBS} at lower levels of Kp (panels (a) in Figures 4.17 and 4.18), except for the model of Ali et al. (2016), which provides the lowest estimates below $L = 6$. However, during the course of the storms, represented by the growing Kp values seen in panels (b-e) for case 1 or (b-f) for case 2, the mean rates from MHD start to delimit a lower level for these coefficients, which most of the time can be taken as underestimates in case 1 (e.g., panels c-e in Figure 4.17). As pointed out earlier, simulated rates from MHD

in case 2 are notably more accurate with observations.

Figure 4.17 - Case 1: Empirical models and event-specific diffusion coefficients through MHD simulation validated by observations, over storm time.

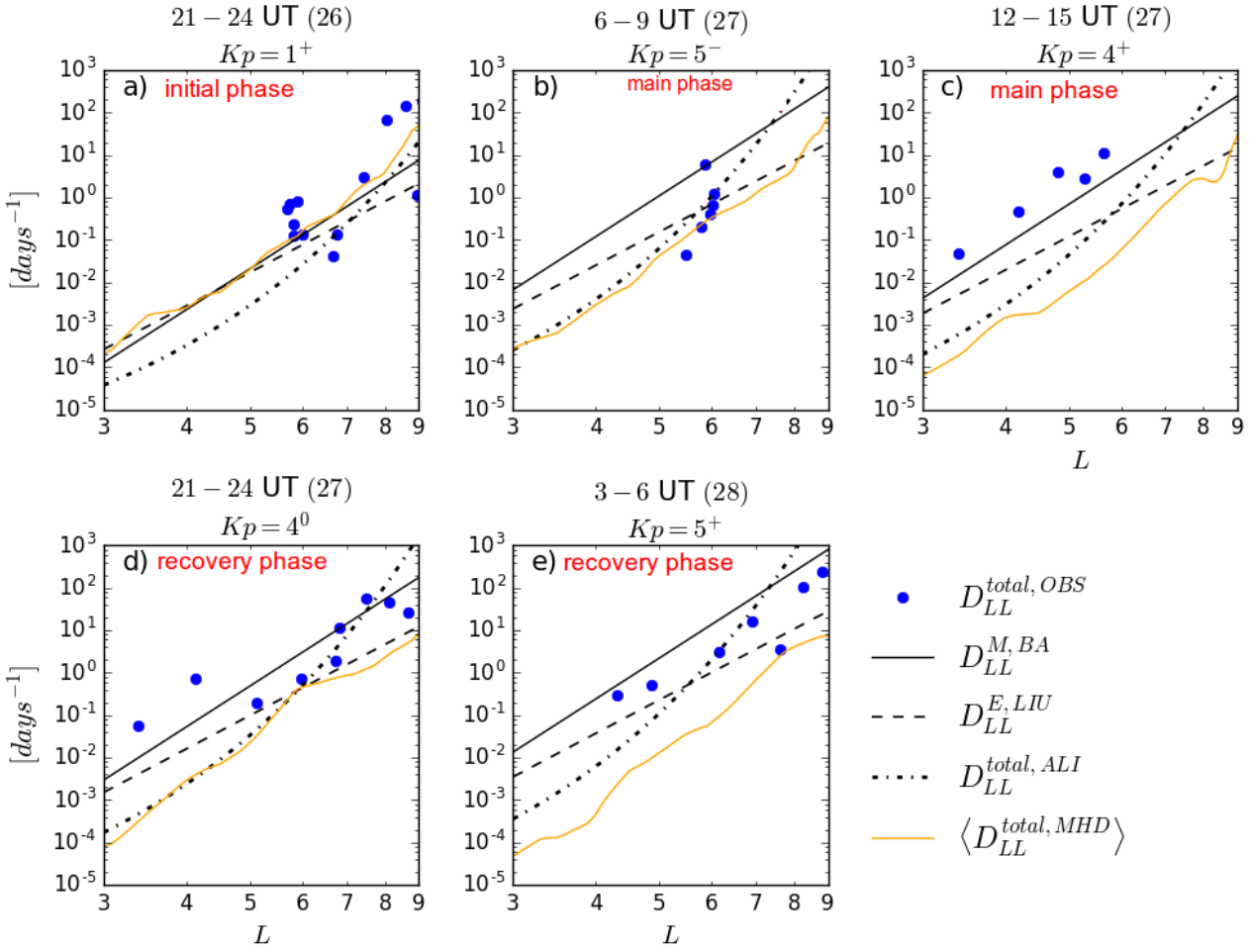

(a-e) Selected intervals, and corresponding Kp index and phase of the storm, for comparisons of radial profiles of various D_{LL} rates implemented. UT time of the intervals is indicated together with information of the day considered. L represents the L shell. $\Delta L = 0.1 R_E$ for the L grid of the D_{LL} models, and $\mu = 1318$ MeV/G.

SOURCE: Produced by the author.

Figure 4.18 - Case 2: Empirical models and event-specific diffusion coefficients through MHD simulation validated by observations, over storm time.

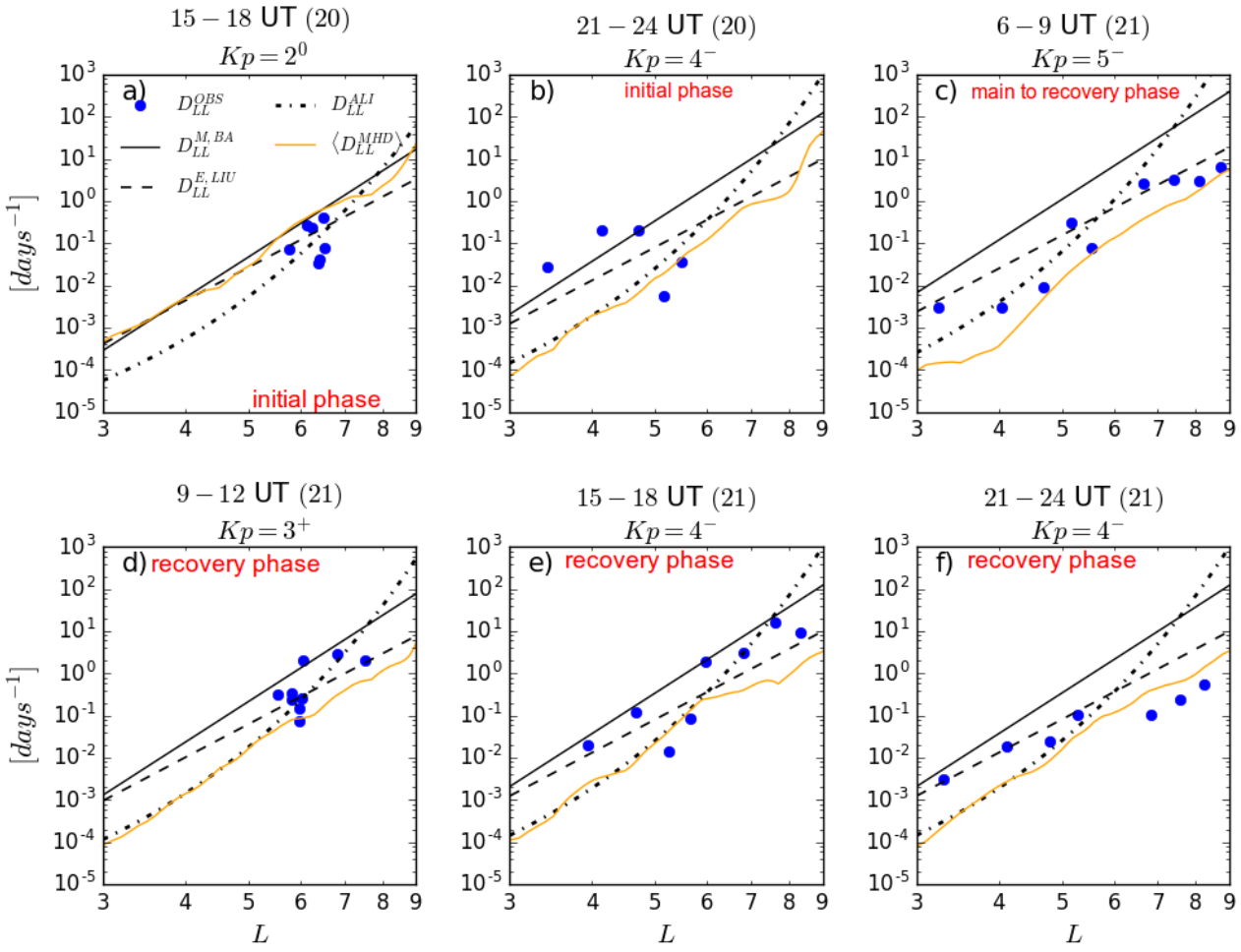

Same as Figure 4.17.

SOURCE: Produced by the author.

The results of the radial profiles of D_{LL}^{OBS} from the two cases clearly indicate that in-situ diffusion coefficients may vary significantly through the phases of the storms, in such a way that this response can also be distinct with L shell (see an example on results of Figure 4.17(d), for the recovery phase in case 1). Specifically, this profile shows that the coefficients peak both at $L \sim 4$ and $L \sim 8$, with this result not being expected from none of the tested models. This indeed illustrates that oftentimes, in-situ coefficients taken in a range of L shells can differ from the classical exponential fits over L, assumed in most of the empirical models (e.g., Brautigam and Albert

(2000), Liu et al. (2016)). These models, for example, could not be also precise to determine the high coefficients taking place during the main phase in case 1, when Kp was 4^+, which is a moderate value (Figure 4.17(c)). A similar result is found for the initial phase of case 2 (Figure 4.18(b)). These results unveil that empirical coefficients may be quite underestimated down to low-L through storm time, if the instantaneous Kp index is not representative of the global ULF wave activity in the magnetosphere.

As a final analysis of the performance of empirical models and the MHD-simulated radial diffusion coefficients during these case studies, it was calculated the coefficient of determination (R^2) for each of them, with respect to in-situ results, given by D_{LL}^{OBS}. R^2 is a measure of how predictable the variance of a dependent variable (say y) is in relation to variations from a known independent variable, perhaps a model ($\hat{y}$). Written out, this is given by an expression like:

$$R^2 = 1 - \frac{\sum(y_i - \hat{y}_i)^2}{\sum(y_i - \bar{y})^2} = 1 - \frac{SS_{res}}{SS_{tot}} \tag{4.5}$$

where SS_{res} represents the residual sum of squares relative to the investigated model, SS_{total} is the total sum of squares found in the sample data, and $\bar{y}$ is the mean value of this sample. A fit model is said optimal if results in $R^2 = 1$, otherwise if $R^2 = 0$ the model does not fit the dispersion of the data at all.

Based on these statistics, each D_{LL} model and the sample data of D_{LL}^{OBS} were applied, in logarithmic scale, into Equation 4.5. The time span of this analysis in each event-study is 36 hours, from the beginning of the MHD simulations. The empirical D_{LL} coefficients were acquired along the satellite's locations, indicated by the L shells. As Kp remains fixed during each three-hour interval, the instantaneous empirical coefficients taken are only functions of the probes' L. In this analysis, mean D_{LL}^{MHD} coefficients correspond to interpolations of $\left\langle D_{LL}^{MHD}(L, \Delta t) \right\rangle$ also taken along the probes' L, during each interval Δt.

Figure 4.19 shows results for case 1. First, one realizes that the obtained R^2 coefficients are very low, indicating a weak correspondence between models and observations in this event. Again, it is shown in panel (d) that MHD results are highly affected by underestimations. Some other general features are the significant overestimations by the model of Brautigam and Albert (2000) (panel (a)), which introduce too much error in relation to D_{LL}^{OBS}. On the other hand, the model of Liu et

al. (2016) is seen in panel (b) to mostly underestimate radial diffusion coefficients during this event. On the other hand, the model of Ali et al. (2016) (panel (c)) does a more balanced performance because there is no clear tendency of underestimation or overestimation until rates of 10^2.

Figure 4.19 - Case 1: Scatterplots of total radial diffusion coefficients from observations against modeled estimates, and the corresponding coefficients of determination R^2.

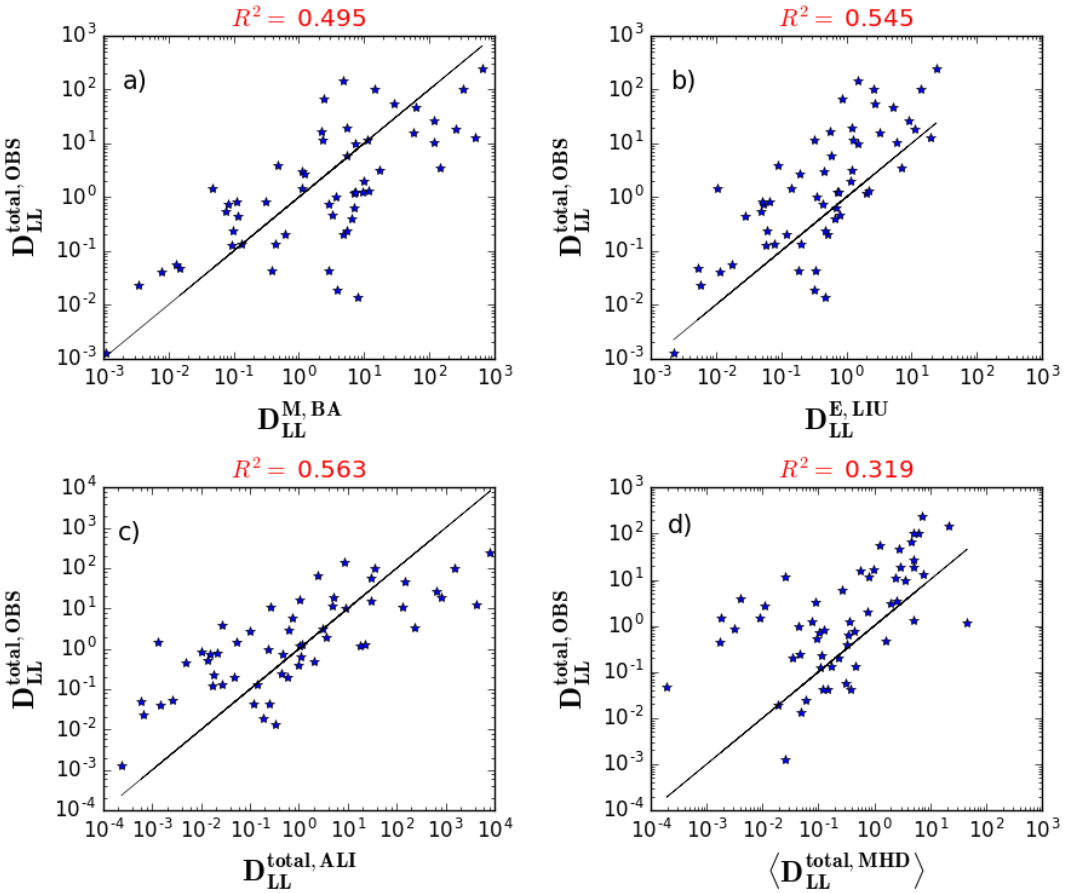

The black line shows $y = \hat{y}$ (data = model). Scatter points above this line stand for underestimations by the models, while points below the line represents overestimates by each model. $\mu = 1318$ MeV/G.

SOURCE: Produced by the author.

Figure 4.20 - Case 2: Scatterplots of total radial diffusion coefficients from observations against modeled estimates, and the corresponding coefficients of determination R^2.

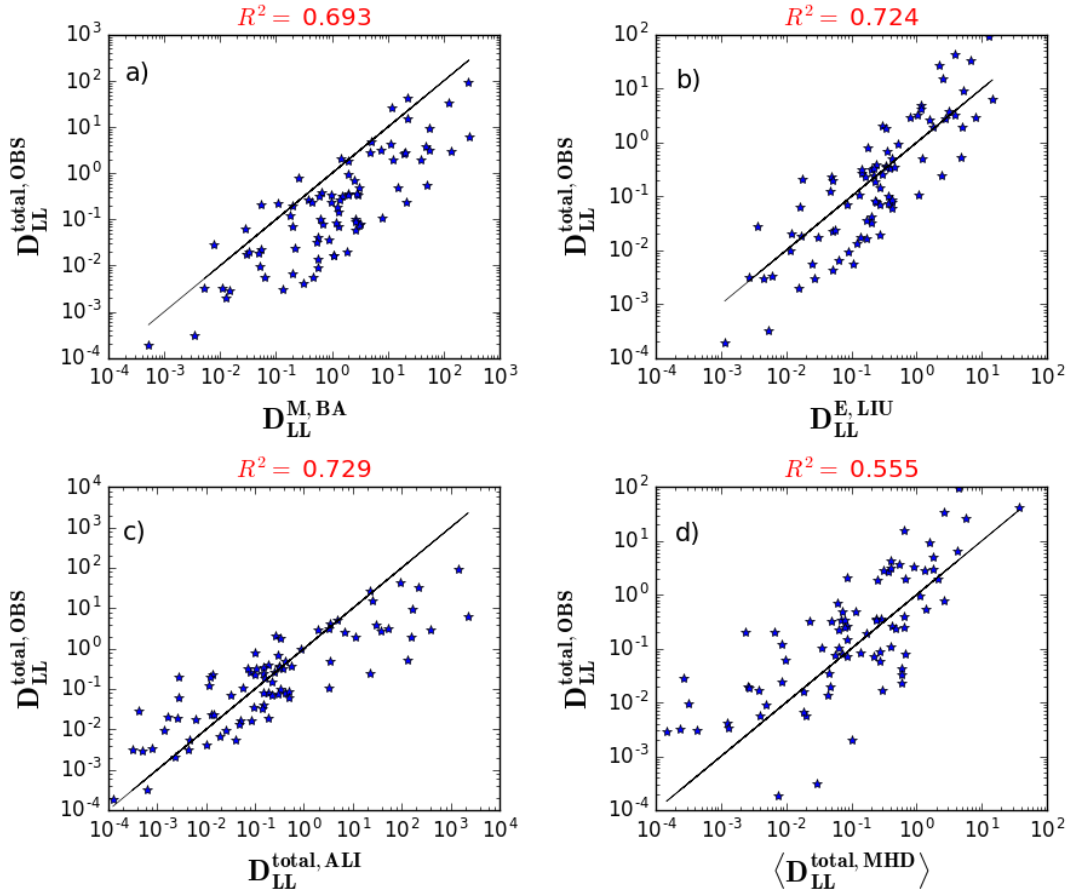

Same as Figure 4.19.

SOURCE: Produced by the author.

Results of case 2 in Figure 4.20 show greater R^2 coefficients among the models. Visually, the dispersion of the data in all panels seems to lie more concentrated around the identity function lines (shown in black). This leads to less residual squared errors relative to D_{LL}^{OBS}, and consequently to higher R^2 values. However, it is seen in panel (a) that the model of Brautigam and Albert (2000) still well overestimates in-situ radial diffusion coefficients in this particular case. Such as obtained in case 1, the models of Liu et al. (2016) and Ali et al. (2016) (panels b-c) present, quantitatively, the best fits for observations. However, for this case there is a more reliable

relationship between each model and data, indicated by the enhanced R^2 results. A little improvement is observed on results from MHD, given the increase in R^2 either. MHD's performance in case 2 (Figure 4.20 (d)) becomes comparable to the performances of Liu et al. (2016) and Ali et al. (2016) models in case 1 (Figure 4.19 (b-c)).

These analyses were expanded to the other values of μ (700 MeV/G and 2083 MeV/G), but no significant differences in R^2 were found. So far, these correlation analyses obtained for $\mu = 1318$ MeV/G have indicated that both empirical models based upon in-situ measurements only, i.e., from Ali et al. (2016) and Liu et al. (2016) were, in general, in best agreement with the event-specific coefficients of cases 1 and 2 obtained from observations. Another important finding relates to the possibility of empirical estimates given by these three well established models being underestimated over distinct phases of the storms, specially when D_{LL} peaks at $L < 6$. This period and region are known to highly affect radiation belt particles, for instance, through the occurrence of dropouts, which are enhanced by means of radial diffusion (TURNER et al., 2012a; TURNER et al., 2012b). If input radial diffusion coefficients are given underestimated to a diffusion model, losses to the magnetopause will be equally underestimated by the model. This is the reason why MHD simulations are required for acquiring proper estimates of event-specific D_{LL}, across L shells. In the two cases studied, the responses from MHD were shown to be also underestimated in comparison to storm-time diffusion coefficients obtained from in-situ ULF wave power. Thus, next section evaluates possible source regions of the reported underestimations.

4.4 Validations of simulated ULF wave power

In this section, the validity of MHD field components and respective power spectral densities applied to the D_{LL} calculations are addressed. The compressional magnetic field B_z and azimuthal electric field E_ϕ obtained in the SM coordinate system are compared to observational data set provided by satellites of GOES, THEMIS, and Van Allen Probes missions. Magnetic field data at the geosynchronous orbit ($r = 6.6R_E$) acquired with GOES-13 (G13) and GOES-15 (G15) are used for validations of B_z in the two case studies. On the other hand, joint validations of B_z and E_ϕ in a range of radial distances are provided with THEMIS-E (TH-E) measurements for case 1, while RBSP-B is the choice for case 2. Afterwards, it is analyzed the global distribution of the ULF wave power generated by BATS-R-US, during outstanding instants of the MHD simulations as listed in Table 4.1, for further discussions on

the underestimations of D_{LL}^{MHD}.

4.4.1 Single point comparisons

Figure 4.21 shows comparisons of MHD-B_z with respect to GOES-measured B_z for case 1. At that time, G13 was leading G15 in 4 hours. It is first noted from the pairs of time series analyzed (G13/MHD on the left and G15/MHD on the right) clear signatures of the expected day-night asymmetry in the geomagnetic field (stronger fields being observed close to noon, that is, MLT $\sim$ 12). Moreover, it is quite evident that the coupled MHD model could not resolve the multiple instances of magnetic dipolarization fronts (e.g., Runov et al. (2012)) taking place at MLT approaching 24 (nightside magnetosphere), which are characterized by "jumps" in the B_z component. These dipolarization fronts observed by the two satellites while they were both orbiting the nightside region might result from the intense substorm activity reported in the AE index of Figure 4.1(h).

The results in terms of power spectral densities confirm these observations. Overall, the MHD model does not reproduce the main ULF fluctuations from the nightside, likely driven by the substorm, regardless of frequency. In contrast, fluctuations from the dayside modeled magnetosphere in the Pc5 band well match G13 and G15 observations for frequencies up to $\sim$ 4 mHz. However, relevant power densities at frequencies above this range were missed by the model.

To further investigate the underestimations associated with the model on the nightside, Figure 4.22 shows results of B_z and E_ϕ validations with TH-E (set of panels (a) and (b) respectively) during a pass by the dusk sector. Actually, detrended/smoothed fluctuations are compared in each of these field components. For B_z (panels (a)), it is again clear that BATS-R-US underestimates Pc5 fluctuations in this region. For E_ϕ (panels (b)), the model was also unable to resolve the fast fluctuations seen by TH-E.

Regarding validations with G13 and G15 for B_z of case 2 (set of panels (a) and (b) from Figure 4.23), it is noted again, from the pairs of time series shown, a high accuracy of the model to reproduce observed data on the dayside magnetosphere. The comparisons in power spectral density elucidate this result (shown in middle panels). However, for the nightside, BATS-R-US noticeably underestimates the enhanced substorm activity caught by the satellite magnetometers around before 5 to 9 UT on 11/21. Such nightside underestimations reported so far are clear manifestations that the MHD model coupled with the CIMI model (that resolves the ring

current) lacked important physics governing the dynamics of the magnetotail, to deal with fast and more localized Pc5-phenomena driven by the substorm, at least in the time and spatial resolutions investigated.

Figure 4.21 - Case 1: Background MHD-B_z field along with ULF fluctuations validated with GOES data.

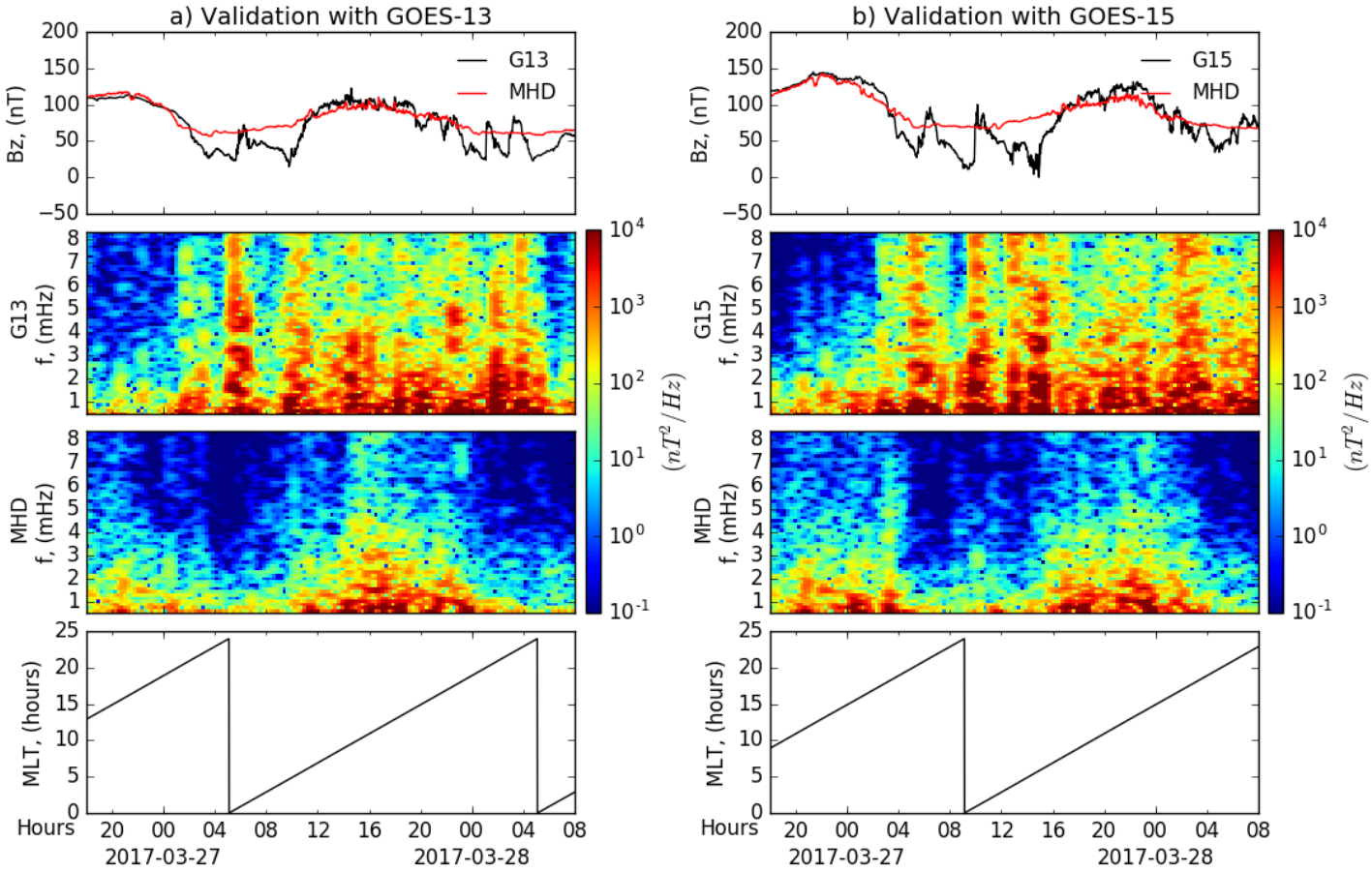

Time-series of MHD-B_z were obtained along the trajectories of G13 and G15 during case 1. Middle panels compare the corresponding power spectra obtained from these simulated fields with the measured spectra by (a) G13 or (b) G15. MLT locations of each satellite are indicated on the bottom panels.

SOURCE: Produced by the author.

Figure 4.22 - Case 1: Validation of nightside ULF fluctuations in MHD-B_z and MHD-E_ϕ with TH-E data.

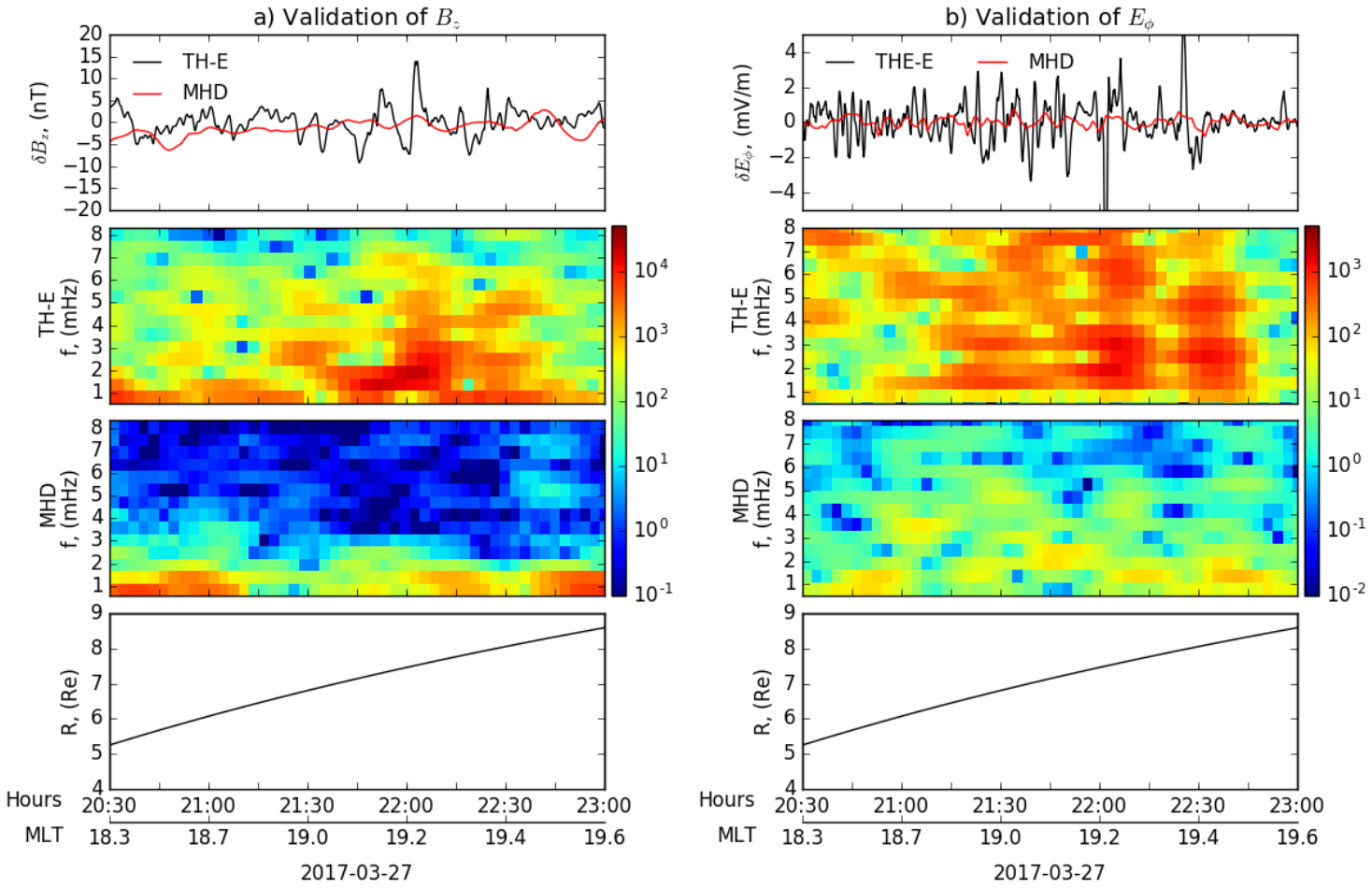

B_z and E_ϕ fluctuations observed along TH-E orbit versus ULF fluctuations modeled by BATS-R-US, for a short period of the probe's pass by the dusk side on March 27. Bottom panels show its radial location during the pass, with MLT locations being displayed upon the x-axis. The units of power for B_z and E_ϕ are $[nT^2/Hz]$ and $[(mV/m)^2/Hz]$, respectively.

SOURCE: Produced by the author.

Figure 4.23 - Case 2: Background MHD-B_z field along with ULF fluctuations validated with GOES data.

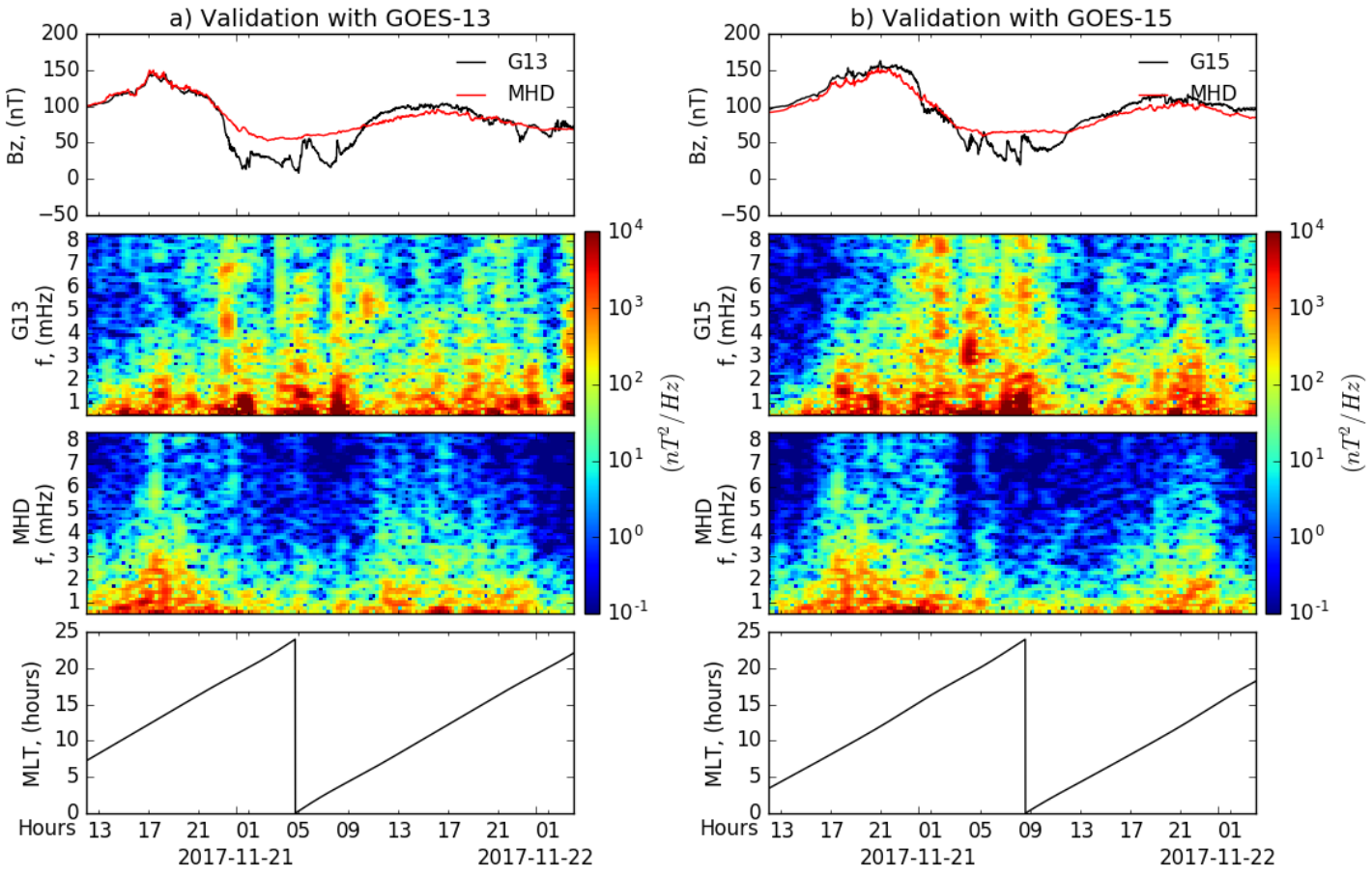

Such as in Figure 4.21, time-series of MHD-B_z were obtained along the trajectories of G13 and G15 during case 2. The MLT locations of each satellite are indicated.

SOURCE: Produced by the author.

In addition, differently from case 1, during case 2 there were no other available satellites for analysis of the fields components of interest on the nightside. Because of that, dayside fluctuations in B_z and E_ϕ obtained from the MHD model were further compared with data provided by RBSP-B (the same data used previously for discussions of the storm-driven ULF wave activity, in Figure 4.5, although a smaller window size was set for the FFT in this subsequent figure). Figure 4.24 (panels (a)) thus shows that fluctuations in B_z measured by the probe whenever approaching its apogee ($R \sim 4 - 6R_E$) are relatively well represented by the MHD

model, both in time and frequency. But for the fluctuations in E_ϕ (see panels (b)), it is clear that the model could not reproduce all the power spectrum related to the storm-time Pc5 fluctuations seen by the probe (example, after 6 UT on 11/21), also implying in underestimations by the model.

Figure 4.24 - Case 2: Validation of dayside ULF fluctuations in MHD-B_z and MHD-E_ϕ with RBSP-B data.

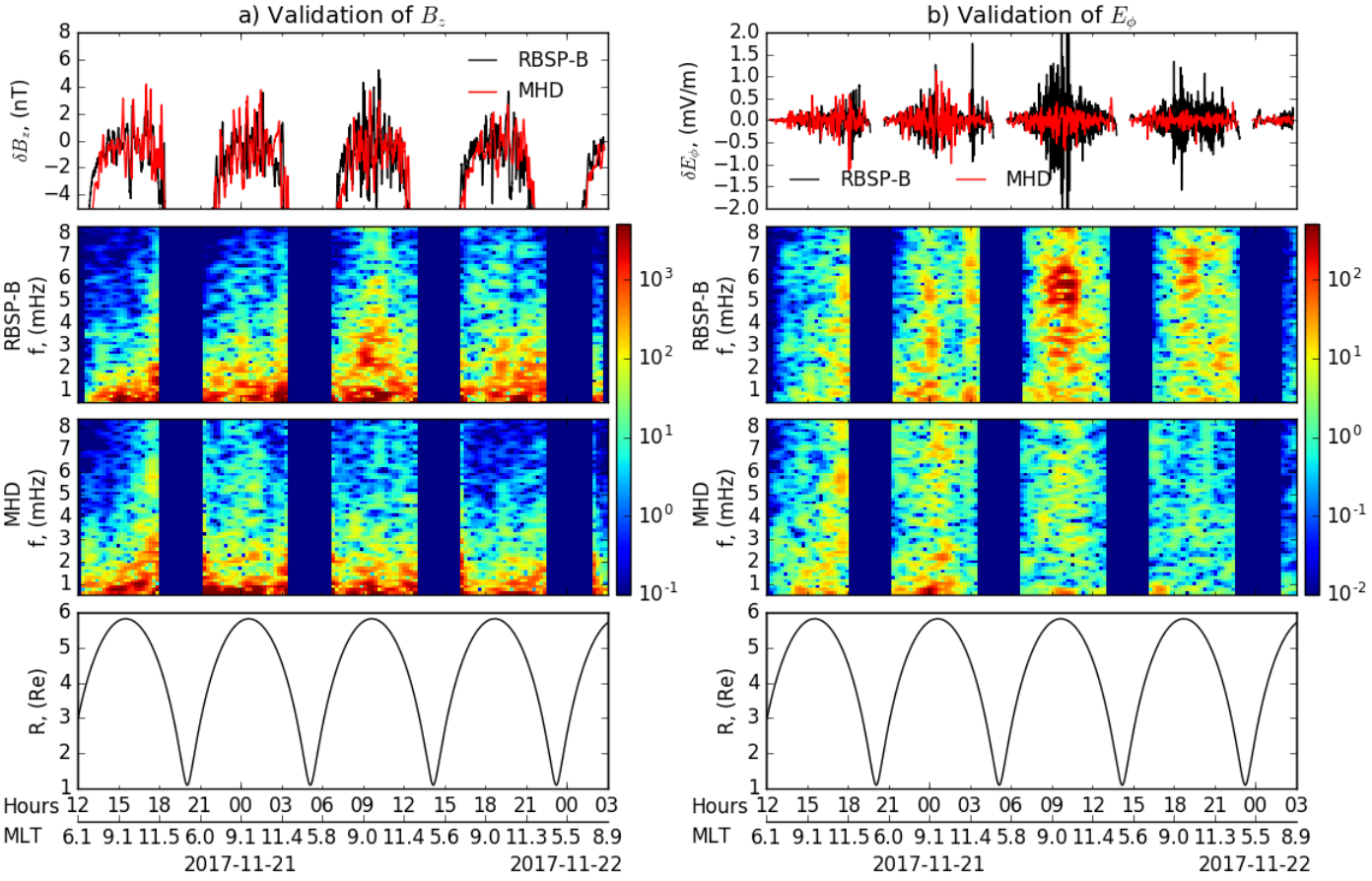

B_z and E_ϕ fluctuations observed along RBSP-B orbit versus ULF fluctuations modeled by BATS-R-US during interval of case 2. Bottom panels show the probe's radial positions, with MLT locations being displayed upon the x-axis. The units of power for B_z and E_ϕ are $[nT^2/Hz]$ and $[(mV/m)^2/Hz]$, respectively.

SOURCE: Produced by the author.

4.4.2 Equatorial view in L and MLT

Single-point comparisons of the simulated ULF wave power contained in the compressional magnetic field and azimuthal electric field with in-situ measurements have demonstrated that a main source region for the underestimations in D_{LL}^{MHD} is found onto the nightside sector. This has been shown for a range of radial distances covered by the MHD simulations performed, but constrained to the MLT locations of the probes considered in the case analyses.

Now, it is analyzed the L-MLT distribution of the ULF wave total power spectral density (TPSD) in the equatorial plane during five instants selected from the simulation intervals, marked by the blue arrows in Figures 4.1 (case 1) and 4.2 (case 2). Table 4.1 refers to the UT time of each of these instants chosen, namely: 1) beginning of MHD simulations, 2) storm's sudden commencement, 3) compressed dayside magnetopause, 4) minimum SYM-H, and 5) around end time of the MHD simulations. PSD values from MHD resolved at each L and MLT are summed over the range $1.11 - 8.33$ mHz, yielding the total power spectra in units of $[nT^2/Hz]$ for $B_{\parallel}$ or $[(mV/m)^2/Hz]$ for E_{ϕ}, shown in plots of the following figures. Local drift-resonant frequencies implemented to obtain D_{LL}^{MHD} and D_{LL}^{OBS} at the three chosen μ-invariants are within this frequency band.

The instant **3** is chosen based on the intervals of high compression of the subsolar magnetopause. As inspected with the MHD results from Figure 4.7, the standoff distance is equal to $8.9R_E$ for case 1 at 6 UT-03/27, and to $8.7R_E$ in case 2 at 0 UT-11/21. From now on, references to the magnetopause location at instant **3** in cases 1 and 2 regard to theses results from MHD on the same figure. Figure 4.25 shows results of TPSD-$B_{\parallel}$ for instants **1** to **5** in case 1 ($\Delta t = 0 - 36h$). It is seen that the ULF-wave magnetic power generated from the MHD simulation is highly concentrated in the dayside through storm time. Besides, no significant power occurs on the nightside, mainly concerning postmidnight and premidnight sectors, similarly to what has been found in the validations with the two GOES and TH-E (Figures 4.21 and 4.22).

Regarding the L dependence of such effects, dayside concentrations of $B_{\parallel}$ power are much larger for higher L due to the external driving by the solar wind, whereas lack of the same wave power around the nightside sectors goes deeper down to $L = 3$ when the compression of the magnetopause is ongoing (Figure 4.25, instant **3**, $\Delta t = 12h$). In this instant, the magnetopause compressed to $8.9R_E$ drives the strong TPSD-$B_{\parallel}$ of $\sim 10^5$ nT^2/Hz on the dayside shown in this plot. With the start of the storm's

recovery phase (instant **4**, $\Delta t = 21h$), the total power is enhanced on the dayside to above nonstorm levels in all L shells that were below the magnetopause location at instant **3**. For nightside observations, the TPSD-$B_{\parallel}$ is seen most refilled at instant **5** ($\Delta t = 36h$) up to $L \sim 6$. Noteworthy, the reduced nightside power in TPSD-$B_{\parallel}$, affecting lower L shells during more active times (e.g., instant **3**, $\Delta t = 12h$), is consistent with the region of main underestimations seen in D_{LL}^{B} from MHD after around 6 UT-03/27 of Figure 4.15 (top panel on the right).

Figure 4.25 - Case 1: Equatorial L-MLT distribution of compressional magnetic field total PSD during five relevant instants of the MHD simulation.

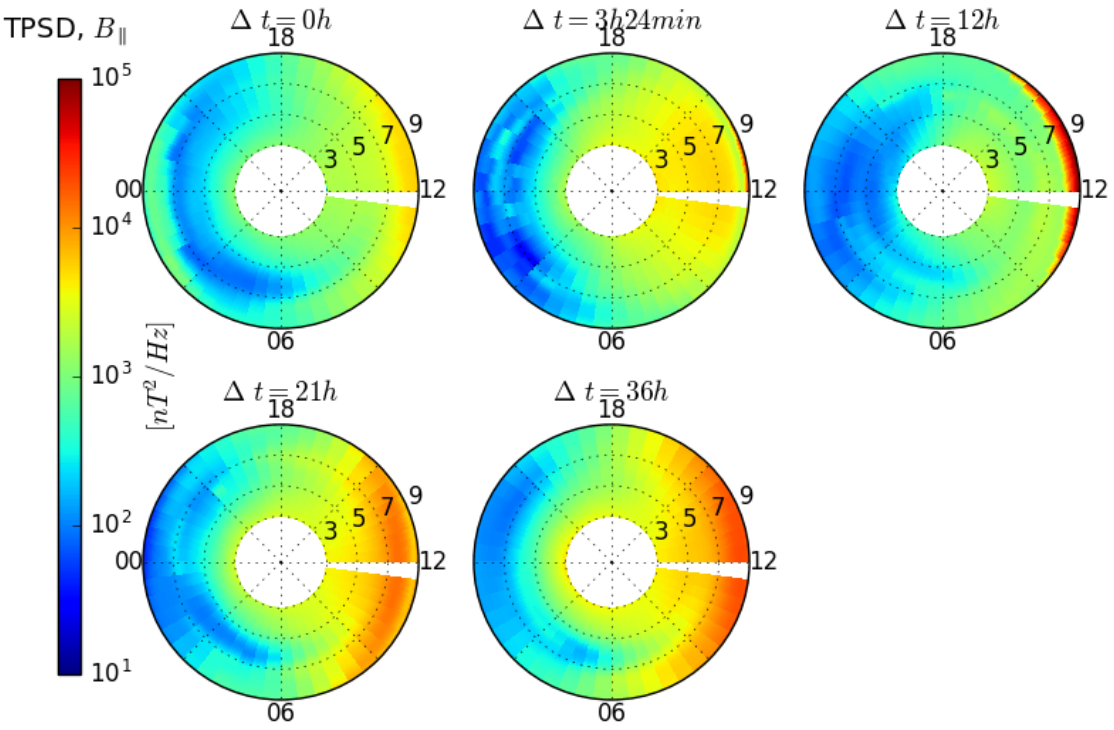

Δt from 0 to $36h$ regards to instants **1-5** selected from the MHD simulation, for consideration of storm-time dynamics in the magnetosphere simulated by BATS-R-US. MLT sectors are projected along the angular plane, for L shells from 3 to 9.

SOURCE: Produced by the author.

Figure 4.26 presents TPSD maps from the contribution of E_{ϕ}, for case 1. Similar responses are found regarding the role of the solar wind in driving enhanced ULF-

E_ϕ power on the dayside, with increasing L and magnetic activity. Also, this total power substantially drops when the magnetopause is being compressed (instant **3**, $\Delta t = 12h$), which depletes the distribution around midnight in almost all L shells. Similarly to TPSD-$B_\parallel$, this scenario of reduced TPSD-E_ϕ is overcome during the storm's recovery phase, but not enough to reproduce TH-E E_ϕ power around the dusk, regardless of frequency (shown in Figure 4.22, panels (b)).

Figure 4.26 - Case 1: Equatorial L-MLT distribution of azimuthal electric field total PSD during five relevant instants of the MHD simulation.

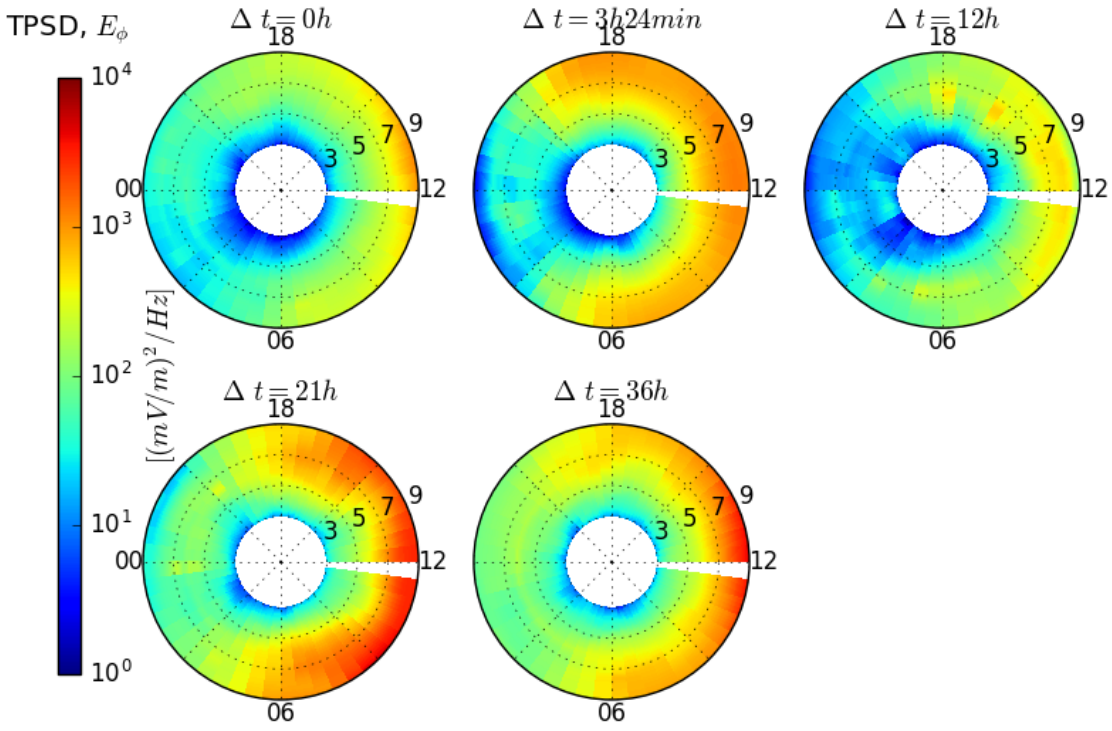

Δt from 0 to $36h$ regards to instants **1-5** selected from the MHD simulation.
SOURCE: Produced by the author.

Results from Figures 4.27 and 4.28 show that less magnetic and electric TPSD was simulated inside the magnetopause ($L < 8.5$ for instants **2** ($\Delta t = 5h06min$) and **3** ($\Delta t = 12h$)), throughout storm time in case 2 than in case 1. However, ULF wave total power from contributions of $B_\parallel$ and E_ϕ is seen to be substantially larger around the midnight sector during the instant **3** in case 2 than observed in case 1 (compare

for $B_{\parallel}$ pair of Figures 4.25 and 4.27 at $\Delta t = 12h$, and for E_{ϕ} the pair of Figures 4.26 and 4.28 at $\Delta t = 12h$). Later on, during the recovery phase of the storm given by instants **4-5** ($\Delta t = 19 - 36h$), TPSD-$B_{\parallel}$ values drastically drops on the nightside for $L > 3$. This is consistent with the period and L-region in which D_{LL}^{B} from MHD got larger ratios of underestimation, shown in Figure 4.16 (top panel on the right) between 7 UT-11/21 and 0 UT-11/22. In the same Figure 4.16 (middle panel), D_{LL}^{E} from MHD is seen to be more comparable to observations, which has to do with the global distribution of TPSD-E_{ϕ} responding better to the active times imposed by the CIR in case 2.

Figure 4.27 - Case 2: Equatorial L-MLT distribution of compressional magnetic field total PSD during five relevant instants of the MHD simulation.

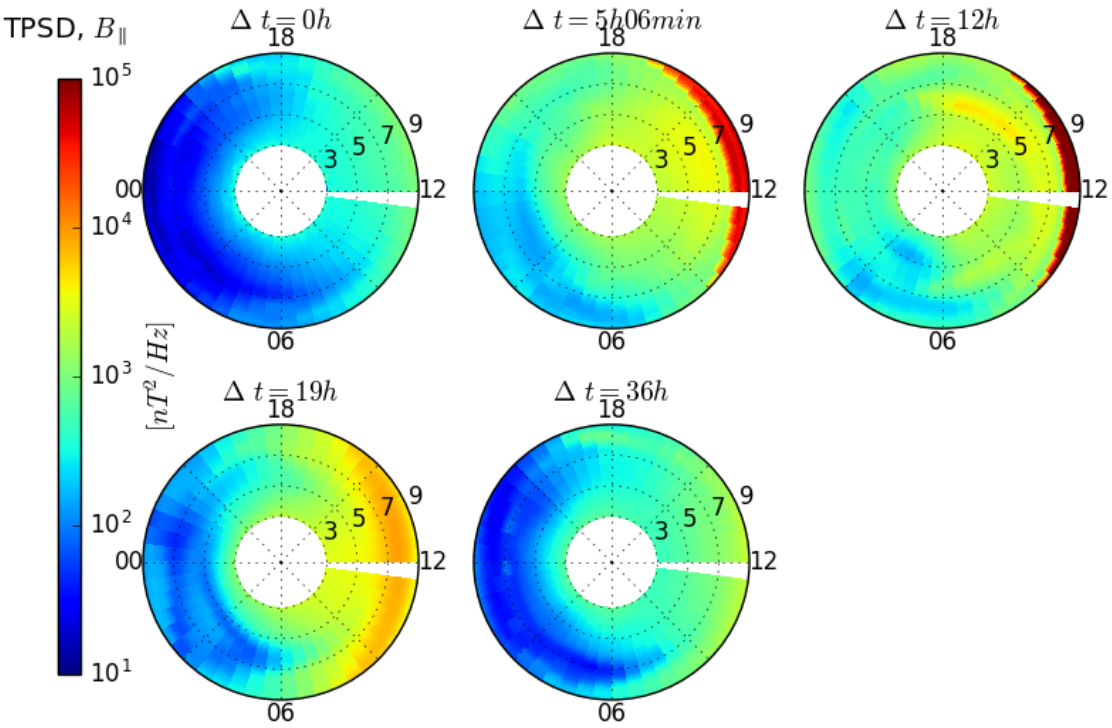

Δt from 0 to $36h$ regards to instants **1-5** selected from the MHD simulation.

SOURCE: Produced by the author.

Figure 4.28 - Case 2: Equatorial L-MLT distribution of azimuthal electric field total PSD during five relevant instants of the MHD simulation.

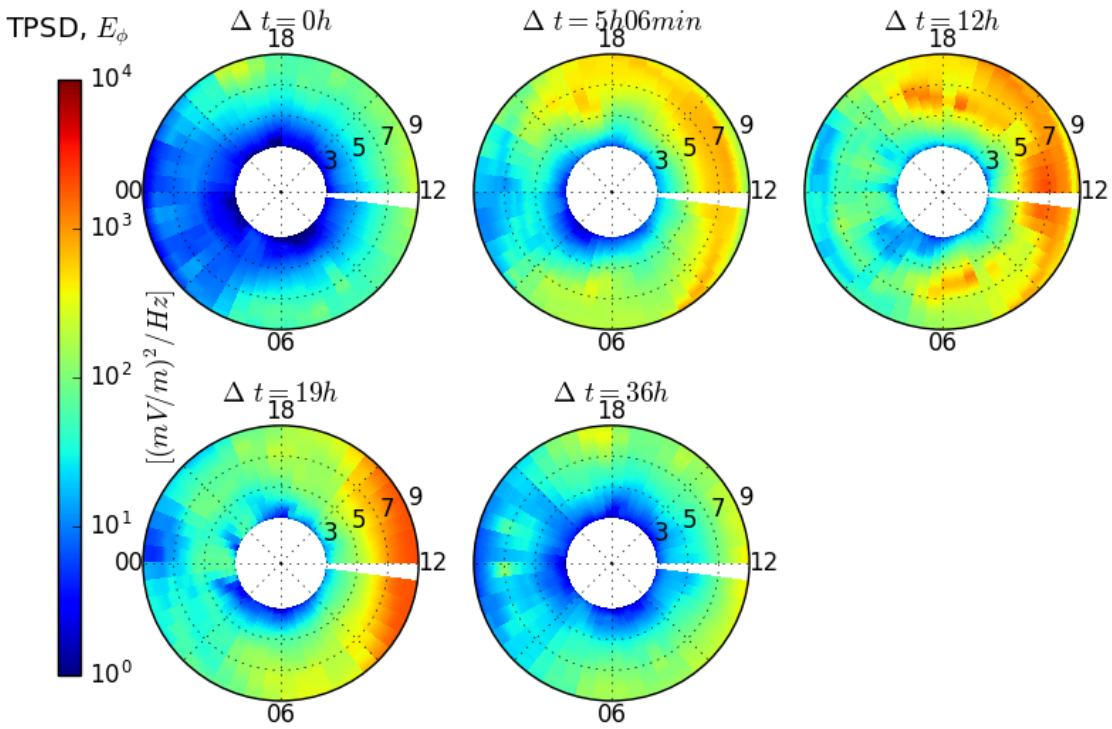

Δt from 0 to $36h$ regards to instants **1-5** selected from the MHD simulation.

SOURCE: Produced by the author.

5 ON THE CORRESPONDENCE OF EMPIRICAL D_{LL} MODELS AND OBSERVATIONS IN CASE STUDIES

The coefficients of determination (R^2) between the diffusion coefficients from observations and the tested empirical models shown in Figures 4.19 and 4.20 have, in each case, indicated that during an event with less ULF wave activity excited in the magnetosphere, the correspondence between them would significantly enhance. For instance, this was also observed in the correlations with MHD diffusion coefficients since R^2 values improved for the second event, where much less wave power was found to have been generated through the storm than in case 1 (instants **1**-**5** of Figures from 4.25 to 4.28, but instant **3** ($\Delta t = 12h$)).

Two more case studies will be investigated in this chapter to quantitatively enhance the discussions on the correspondence of empirical diffusion coefficients and observations throughout storm time, and to verify the hypothesis being tested, that is, whether those empirical models provide better fits for in-situ data during less active times, in terms of ULF wave activity. Those aspects can be key for the analysis of the particle distributions to be obtained in this work with radial diffusion simulations, mainly using the models of Brautigam and Albert (2000), Liu et al. (2016) and Ali et al. (2016) as inputs for D_{LL}.

To contextualize, Murphy et al. (2016) showed with a statistical study that, on average, moderate conditions of Kp would lead to underestimation of data-driven D_{LL}, and more disturbed conditions in Kp to the opposite effect (overestimation), at $L \sim 6.6$. However, these trends were found based on comparisons of the total ULF-E_ϕ wave power as a function of Kp as modeled by Ozeke et al. (2014a), with ground observations of cumulative power derived from the D-magnetic component. They have assumed that such power is representative of the real ULF disturbance in E_ϕ at space, if mapped to the equatorial plane. Although no correlation analysis using this database was provided, it was shown a large variability of factors up to 10^4 higher or lower in the total wave power, generated by use of the model averages for 105 storm events. This is a qualitative indication of a weak correspondence with the storm-time wave power, and consequently of D_{LL}, when a bunch of event-specific data is taken into account.

In our case studies, two conditions were established for the selection of the two other events: i) the third event should have a maximum Kp larger than the previous case studies ($Kp_{max} = 6^+$ for case 1 and $Kp_{max} = 5^0$ for case 2), while the fourth event had to have the lowest maximum Kp of the set or a value comparable to that of

case 2, and ii) preference should be given to intervals when the satellites RBSP-B, TH-A, TH-D, and TH-E (used to derive the observed diffusion coefficients) were probing similar regions in the magnetosphere to the sectors mostly probed in case 1 (dusk for RBSP-B, and premidnight for THEMIS) and case 2 (prenoon for both RBSP-B and THEMIS). This restriction of having satellites at similar sites in the magnetosphere as in cases 1 and 2 is to ensure that possible differences in the results of D_{LL}, in cases 3 and 4, are not related to local dynamics inherent to distinct regions of observation set for these events. Given these conditions, case 3 is from now on the event with greater geomagnetic activity as specified by Kp ($Kp_{max} = 8^{-}$), and that the satellites probed the same sectors of case 1. Whereas case 4 has maximum Kp equal to that of case 2 ($Kp_{max} = 5^{0}$), as well as satellites probing a similar region to that of this event.

Figures 5.1 and 5.2 show the locations in GSE of the four satellites on the first day of analysis of case 3 ($01-03$ October 2013) and case 4 ($04-05$ December 2017), which can be compared to the locations of the same probes during case 1 (Figure 4.11) and case 2 (Figure 4.12). No significant changes in the orbit of the satellites along X-Z and Y-Z planes are noticed for case 4 (Figure 5.2) since this event occurred just a couple of days later than case 2 (Figure 4.12). But for case 3, which is around three years and a half before case 1, the probes' apogees were no longer sited to the south of the ecliptic plane. They were rather to the north of it towards positive X(GSE) for RBSP-B, and roughly upon this plane concerning the three THEMIS (see panels (b) of Figures 4.11 and 5.1 for comparisons).

Figure 5.1 - Multiple spacecraft location in GSE on October 1st, 2013 - case 3.

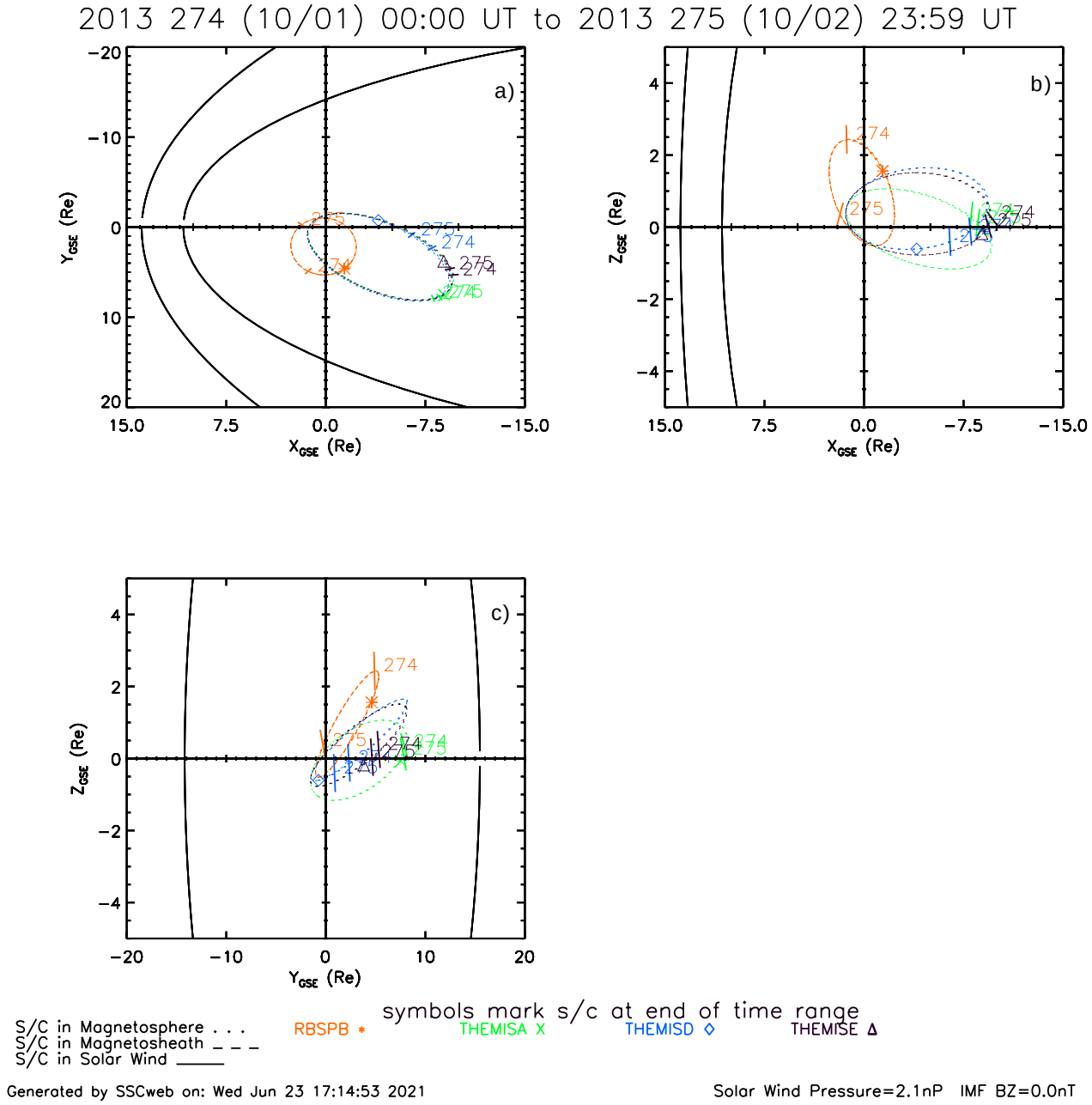

(a) Orbits along the equatorial plane showing that RBSP-B was probing the dusk side, while THEMIS-A, D and E were mostly at the pre-midnight sector as in case 1. (b-c) Orbits along X-Z and Y-Z planes, respectively. The locations of the magnetopause and the bow shock calculated using solar wind pressure of 2.1 nPa and IMF-Bz of 0 nT, are projected onto each plane of the panels, indicated by the black solid curves. See text for more details.

SOURCE: NASA/SPDF (2021).

Figure 5.2 - Multiple spacecraft location in GSE on December 4, 2017 - case 4.

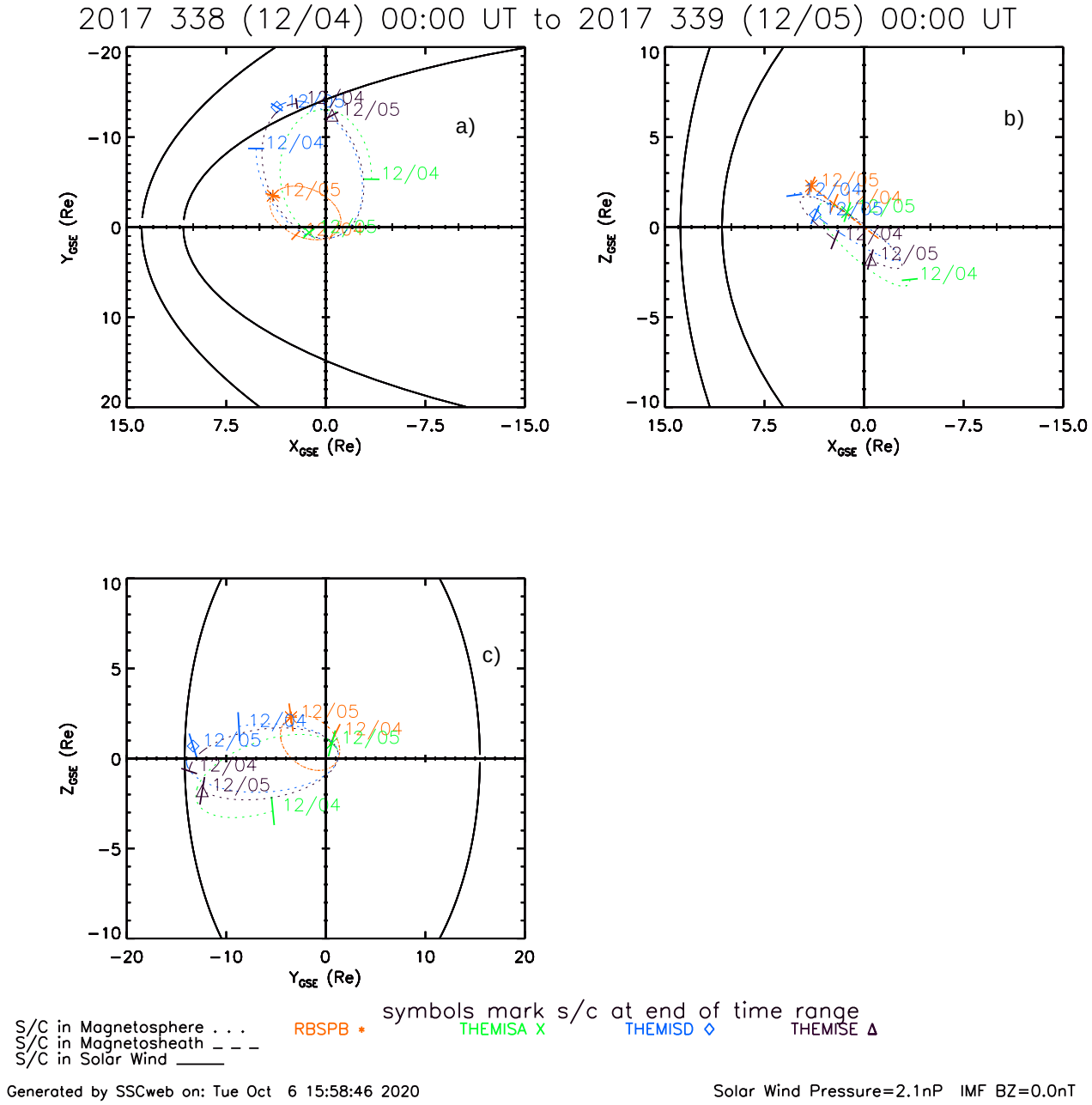

(a) Orbits along the equatorial plane showing that RBSP-B was close to noon as in case 2, while THEMIS-D, E, and A were slightly shifted towards dawn. (b-c) Orbits along X-Z and Y-Z planes, respectively. The locations of the magnetopause and the bow shock calculated using solar wind pressure of 2.1 nPa and IMF-Bz of 0 nT are projected onto each plane of the panels, indicated by the black solid curves.

SOURCE: NASA/SPDF (2020).

5.1 Events overview

The interval of case 3 ($01 - 03$ October 2013) was selected because the chosen satellites for the D_{LL} calculations were at similar sectors in the magnetosphere to those of case 1. However, the magnetic storm associated with this event was triggered as a result of the arrival at Earth of an ICME, at beginning of October 2. Despite data gaps, the solar wind parameters shown in Figure 5.3(b-e) can give a few details about this ICME, such as the instant that the interplanetary shock wave hits the magnetosphere (seen by the abrupt excursions of these parameters around 2 UT on 10/02), and the intense dynamic pressure (panel (e)) and southward IMF values (panel (d)) reached from this dayside interaction.

As a consequence, the magnetopause was highly compressed to 6 R_E or even below (panel (f)), according to the Shue et al. (1998) model. This extreme compression of the magnetopause certainly contributed to the dropout of outer belt electrons seen in panel (a) starting at $\sim$ 5 UT on 10/02, although the levels of particle flux measured by the Van Allen Probes were already very low prior to this dropout (for a comprehensive analysis of this flux dropout, see Xiang et al. (2016)). Right after such interval dominated by dropout dynamics in the inner magnetosphere (at 21 UT-10/02), the outer belt was significantly refilled. On panel (g) of the same figure, the SYM-H time-series unveils how fast (less than four hours) the initial and main phases developed within the course of this storm, of SYM-H minima equals -90 nT, against -86 nT of case 1. Meanwhile, the AE graph shows a double-peak signature with values increasing up to 2000 nT.

On the other hand, the geomagnetic conditions in case 4 ($04 - 05$ December 2017) resemble the magnetic activity of case 2, as introduced in this chapter about the maximum Kp condition established for these two events selection. In terms of SYM-H minima, Figure 5.4(g) shows that this index was above -50 nT during case 4, against -60 nT of case 2 (on previous Figure 4.2(g)). Thus, the magnetic storm generated in this last case study is classified as weak (GONZALEZ et al., 1994). It was triggered because of a CIR that hit the Earth's magnetosphere on December 4, as observed by the gradual changes in the solar wind parameters (panels b-e). Note that only 36 hours of data containing the storm intervals is shown in this summary plot, similarly to observations of case 3. The full passing of this CIR together with the HSS can be seen in Figure A.7 from Appendix A. The CIR compressed the magnetopause to around $7R_E$ (shown by the green line in Figure 5.4(f)), similarly to cases 1 and 2. In turn, the outer radiation belt experienced a dropout of electrons that recovered

a few hours later on 12/05 ($\sim$ 15 UT), down to $L \sim 4.7$ (Figure 5.4(a)). Finally, the substorm activity was sustained during the storm recovery phase (Figure 5.4(h)), as those driven by HSSs.

Figure 5.3 - Case study 3: Observations from Van Allen Probes (RBSP-A and RBSP-B), ACE and geomagnetic indices.

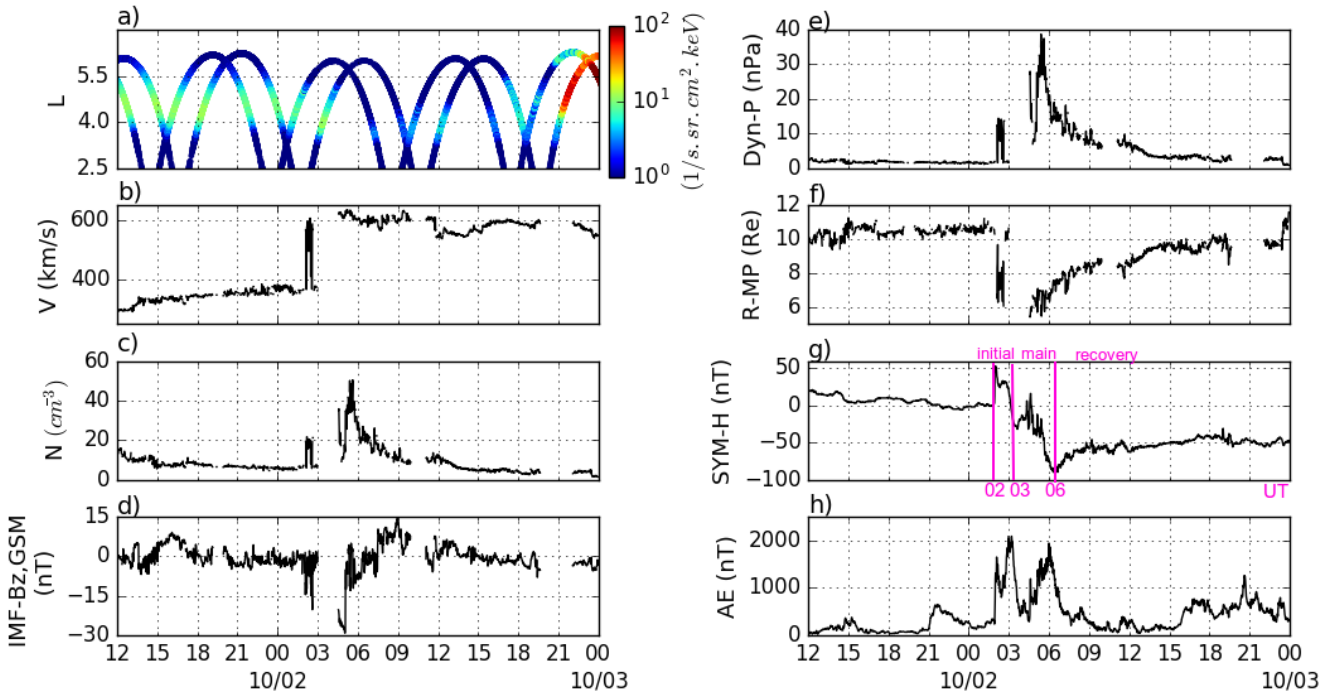

(a) Temporal and radial distribution of electron fluxes measured by the REPT instrument onboard the Van Allen Probes, at 1.8 MeV and 90° local pitch angle (RBSP-B is leading RBSP-A). (b-e) Solar wind velocity, density, IMF-B_z component and dynamic pressure, characterizing the passage of an ICME on October 2, 2013. (f-h) Changes in the magnetopause location (R_{MP}) and in the geomagnetic indices SYM-H and AE. In panel (g), the phases of the magnetic storm are labeled, together with the indication of their start time.

SOURCE: Produced by the author.

Figure 5.4 - Case study 4: Observations from Van Allen Probes (RBSP-A and RBSP-B), ACE and geomagnetic indices.

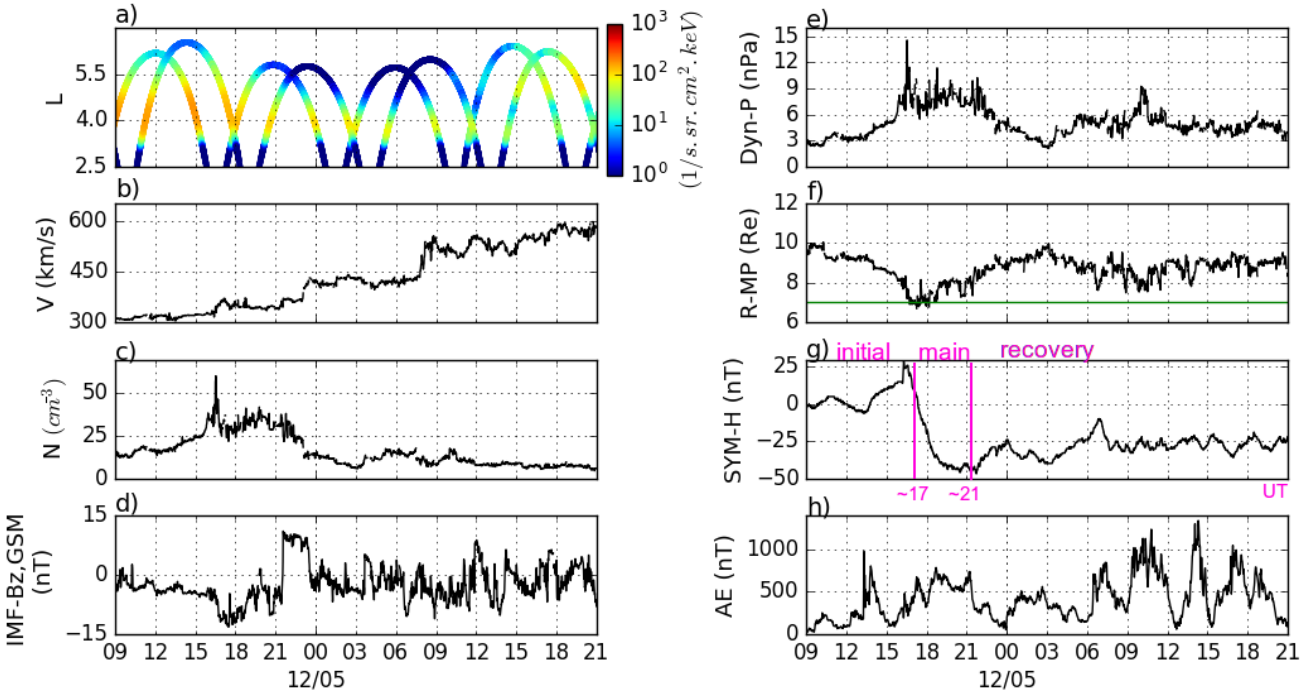

Same as Figure 5.3, but for the passage of a CIR on December 4, 2017. RBSP-A is leading RBSP-B on panel (a). .

SOURCE: Produced by the author.

Now, recall to the conditions in terms of the maximum Kp, imposed to end up with the two events selected. This is represented in Figure 5.5, where time-varying Kp indices corresponding to the four case studies are plotted together, within a fixed interval of 36 hours spanning completely the initial and storm main phases, and partially the recovery phase. As desired, the case 3 reaches the largest maximum Kp among the events (8^-), against 6^+ of case 1, while case 4 reaches a maximum Kp of 5^0, equals to the value of case 2. Kp peaks to its maximum in case 3 likely associated with the arrival of the interplanetary shock from the ICME, and then falls off once, until returning to enhanced values below the maximum index. On the other hand, the enhanced indices of case 1 are sustained throughout the storm interval considered such that the indices of the cases 2 and 4 barely reach or overtake values of case 1. The results of Kp in the cases 3 and 4 are used here to derive time-dependent empirical radial diffusion coefficients, as done previously for cases 1 and

2, to test the viability of the corresponding empirical models to reproduce increased coefficients from observations throughout storm time, depending on the level of global ULF wave activity indicated by Kp.

Figure 5.5 - Time evolution of Kp index through storm-time in each case study.

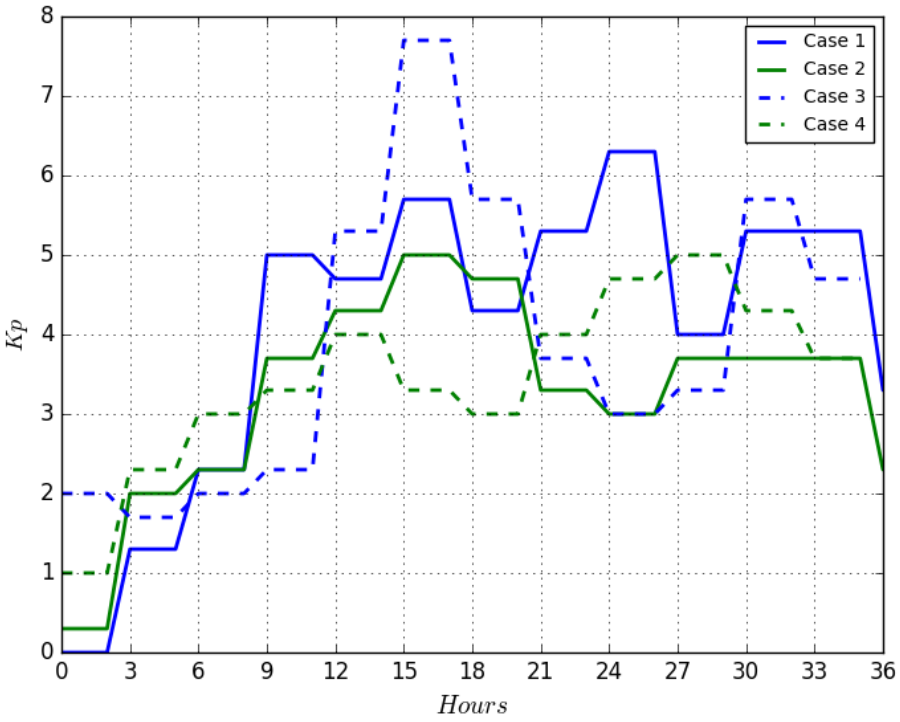

.

SOURCE: Produced by the author.

The actual level of wave activity can be inferred directly from ground observations. Hence, comparisons of measured ULF wave activity are further provided with the station of MCMU (Fort McMurray), from the magnetometer array of the CARISMA network (MANN et al., 2008). The corrected geomagnetic coordinates (CGM) of this station are: magnetic latitude = 64.17°; MLT = 0 at 8 UT; L = 5.35 (conversions from geographic to CGM coordinates are available at https://omniweb.gsfc.nasa.gov/vitmo/cgm.html). Figure 5.6 contains dynamic spectrograms of each case study, obtained for fluctuations in the X (northward) and Y (eastward) geomagnetic components. Left (right) panels show results for fluctu-

ations in X (Y). The results are for the same interval considered in the previous analysis of Kp. These spectrograms are shown with respect to the day of the year, with UT hours displayed as tenths of the day. The time 0 UT corresponds to MLT = 16, and 12 UT to MLT = 4. This data set has sampling frequency of 1 Hz.

Figure 5.6 - Dynamic spectrograms for ground observations of ULF waves in all case studies.

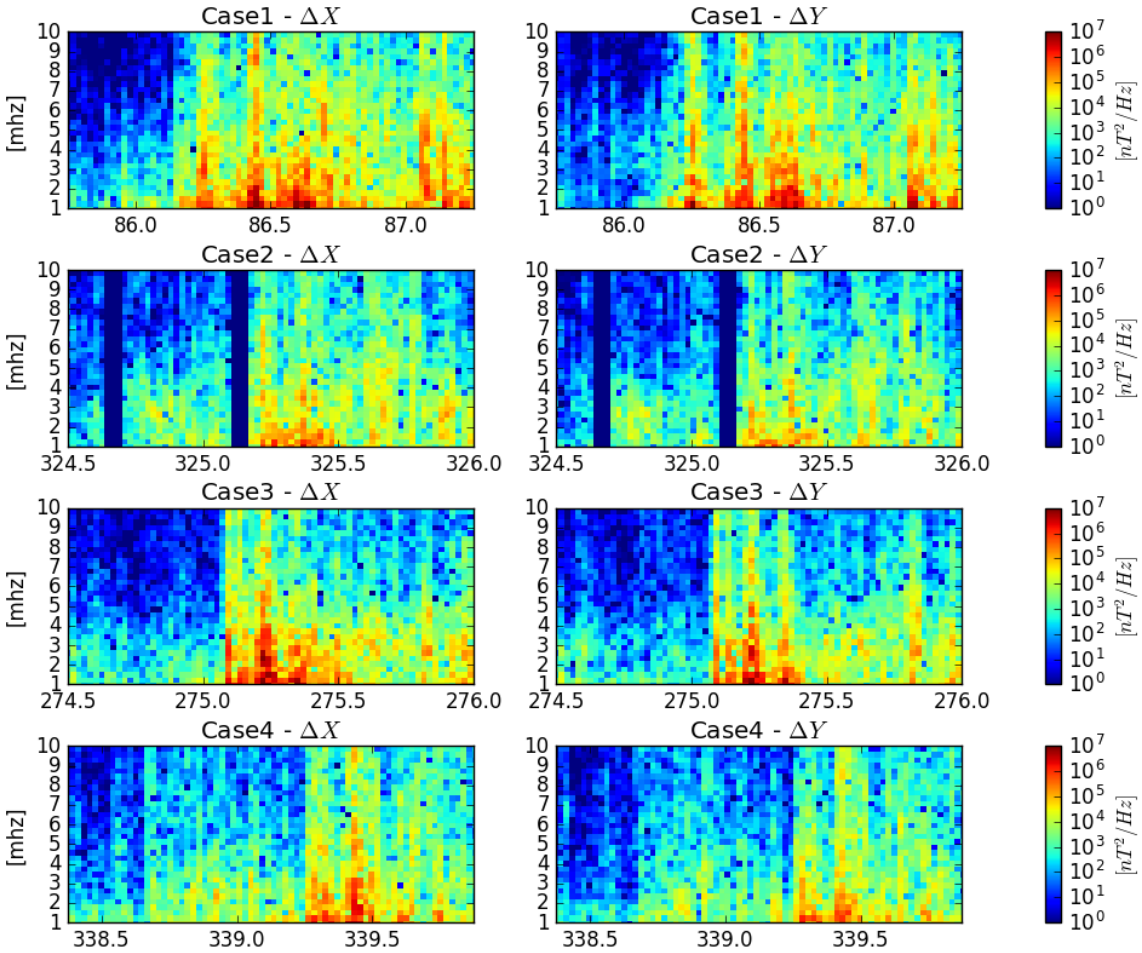

The x-axis shows the day of the year among the cases, with UT hours given as tenths of the day. At 0 UT, the station MCMU is located at MLT = 16 (dusk side), while at 12 UT (half of the day) the station is at MLT = 4 (postmidnight sector). .

SOURCE: Produced by the author.

First, it is seen that the station captures enhanced ULF wave activity, in both components, when mostly acquiring fluctuations from the dusk and midnight sectors,

associated with the ongoing storm dynamics of each event (see legend of Figure 5.6 for details). Also, wave power is dominant at lower frequencies of the Pc5 band (<4 mHz) for all events and components. However, among the events, this larger power of $10^5 - 10^7$ $[nT^2/Hz]$ can differ in intensity and duration such that case 1 has the largest activity in duration, and wave power comparable to that of case 3 (relative to both components). In addition, Figure 5.6 shows that the Pc5 wave activity at this power level in case 4 is seen to be comparable to the same activity in case 2, in both components. Thereby, this analysis of ground observations of the ULF wave power activity in the Pc5 band has confirmed the results from the evolution of Kp in the four events, shown in Figure 5.5, in which the cases 1 and 3 are the most active for the waves, and the cases 2 and 4 are the least active.

5.1.1 Observations of ULF waves at space

In-situ measurements of ULF waves provided by RBSP-B and three THEMIS spacecraft were used to determine the event-specific diffusion coefficients in cases 3 and 4, as obtained for cases 1 and 2. Figures 5.7 and 5.8 show dynamic spectrograms of fluctuations in E_ϕ and $B_\parallel$, for each event, calculated using FFT over previously filtered data, such as defined before. In case 3, the duration of the storm initial phase (started at 2 UT-10/02 UT) and the main phase (started at 3 UT-10/02) together was less than 4 hours as represented in Figure 5.7.

Before the storm in this event, no relevant and continuous wave activity is observed with the data available. The waves are then rapidly excited in response to the storm onset at 2 UT-10/02, seen mostly to affect the magnetic component during the main phase ($\sim 3 - 6$ UT on 10/02), as measured by RBSP-B, TH-E, and TH-D (panels (a1) and (b1)). This enhanced wave power spreads in frequency, although greater power spectral densities are seen over the Pc5 band ($\sim 2 - 7$ mHz). On the other hand, data gaps in E_ϕ from THEMIS compromise the full analysis of waves in this component in the main phase. During the recovery phase after ~ 6 UT-10/02, which lasts longer than shown, RBSP-B registers an enhanced activity in E_ϕ close to 12 UT on 10/03 (panel (a2)) that does not really affects the region probed by TH-A and TH-E, around the same time (panel (b2)). Meanwhile, the activity in $B_\parallel$ within this period is moderate, until a second instance of increase in the Pc5 power observed over the spectra box from 18 UT-10/02 to 0 UT-10/03 for RBSP-B (panel (a1)) and TH-D (panel (b1)).

Figure 5.7 - Case 3: Multi-satellite observations of (a1, b1) compressional magnetic field and (a2, b2) azimuthal electric field PSD of ULF waves in the frequency bands of Pc5 ($\sim 2-7$ mHz) and Pc4 ($7-22$ mHz), from October 1 (12 UT) to October 3 (0 UT).

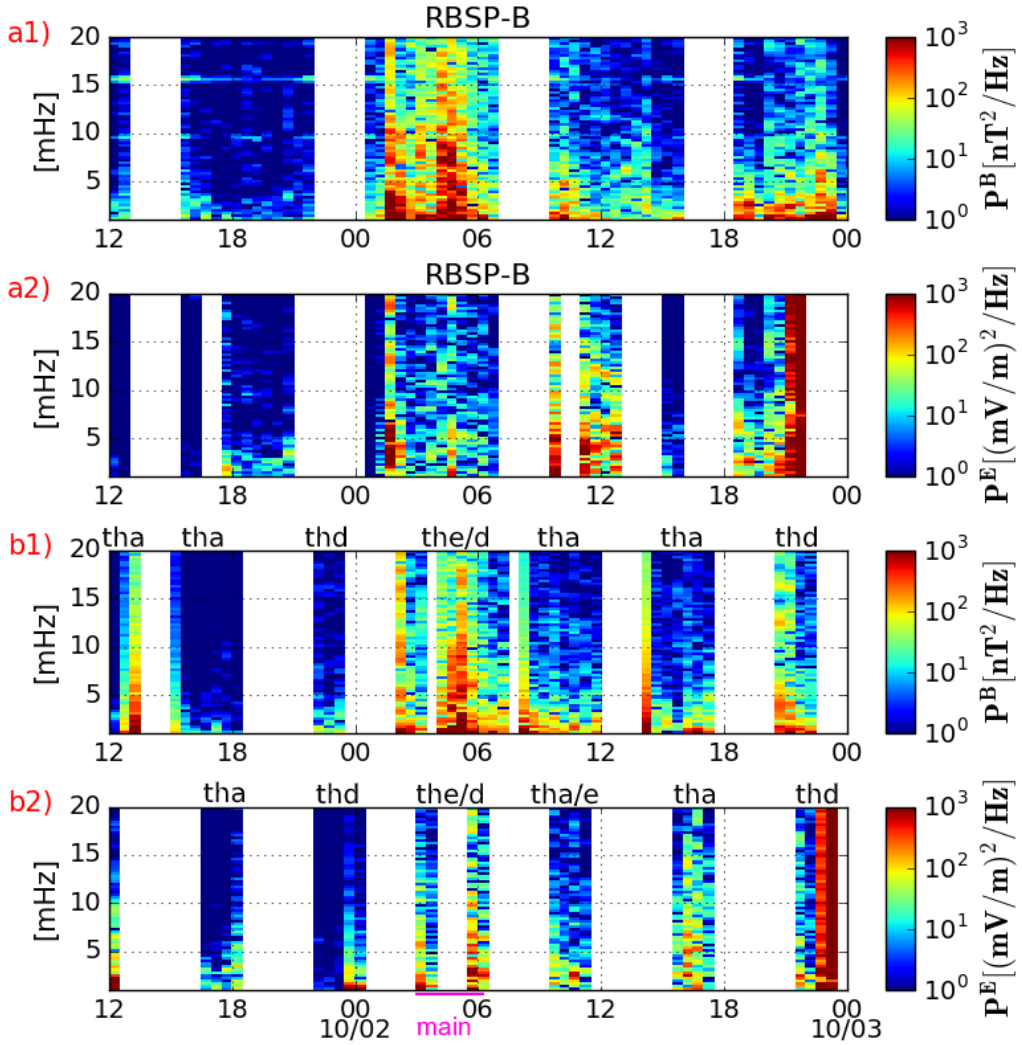

Panels (a1) and (a2) show RBSP-B measurements only, corresponding to passages within $3 > L > 6.5$, while panels (b1) and (b2) contain data from THEMIS-A, D and E during simultaneous passages through L shells from 3 to 9. Data gaps refer to actual missing data or passages of the four probes through L shells outside the considered intervals. Instances of bad data are found on panel (a2) after 21 UT-10/02 and on panel (b2) at ~ 0 UT-10/02. The duration of the main phase of the storm is also indicated on panel (b2).

SOURCE: Produced by the author.

Figure 5.8 - Case 4: Multi-satellite observations of (a1, b1) compressional magnetic field and (a2, b2) azimuthal electric field PSD of ULF waves in the frequency bands of Pc5 ($\sim 2-7$ mHz) and Pc4 ($7-22$ mHz), from December 4 (9 UT) to December 5 (21 UT).

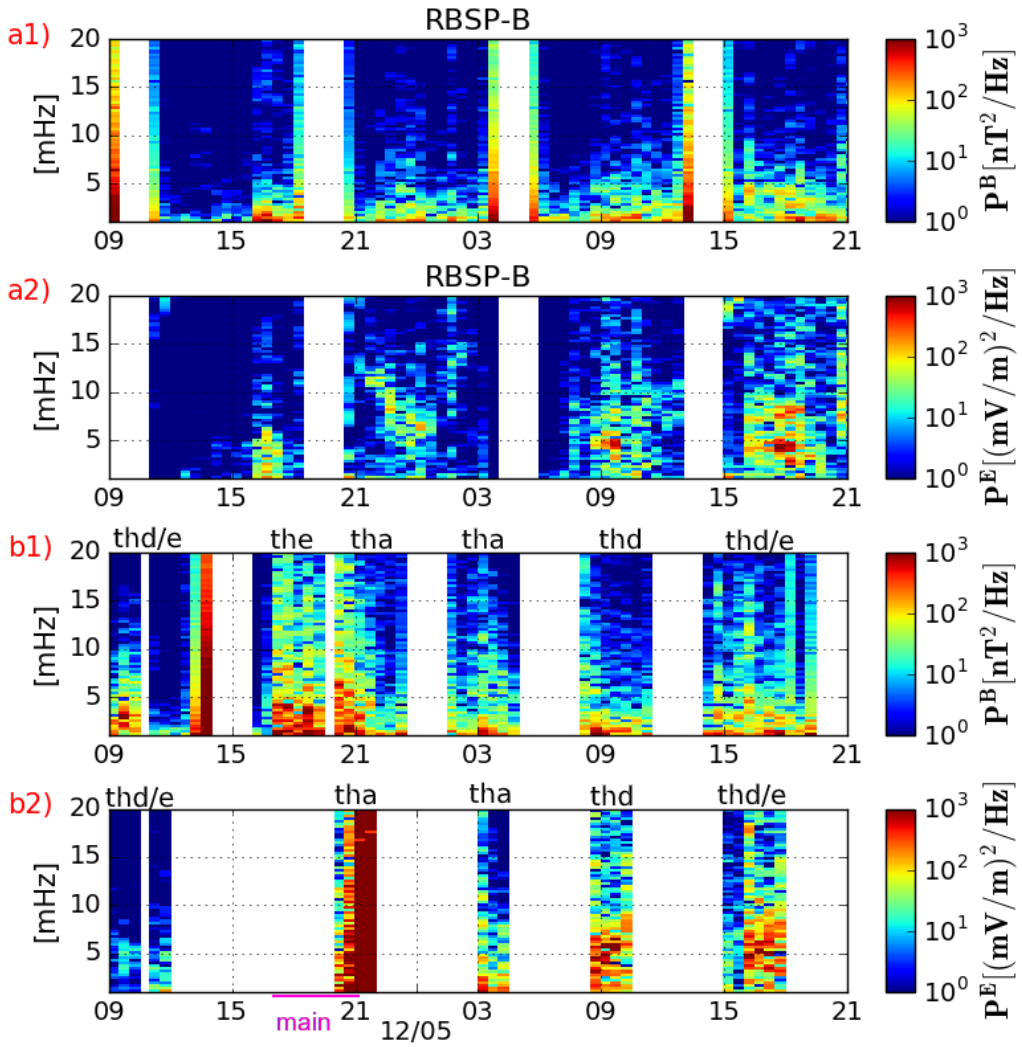

The same as in Figure 5.7. Instances of bad data are found on panel (b2) at $\sim$ 21 UT-12/04.

SOURCE: Produced by the author.

Spectrograms of case 4 (Figure 5.8) show results of ULF wave power from the storm initial phase ($9-17$ UT on 12/04) to the first 24 hours of the recovery phase (started at 21 UT-12/04). The initial phase in this event is seen to not greatly contribute to the enhanced wave activity during storm time, as measured by RBSP-B (panels a1-a2), whereas TH-D indeed measures significant wave power in $B_{\parallel}$ through this period

(panel (b1) around 9 UT-12/04). Because of long-term data gaps on THEMIS-E_ϕ data, there is little to be said about ULF wave activity in this component during the initial and main phases, as seen by TH-A, TH-D or TH-E. The main phase defined within $17-21$ UT on 12/04, in turn, highly increases the wave power in $B_\parallel$ from THEMIS (panel (b1)), to levels obtained in case 3 (see panels (a1) and (b1) of Figure 5.7 for comparisons).

However, the same level of activity is not observed with RBSP-B, either in $B_\parallel$ or E_ϕ, throughout this phase (panels a1-a2). Afterwards, with the start of the recovery phase, the $B_\parallel$-wave power decreases, according to THEMIS observations, while no significant change is noted concerning RBSP-B. In contrast, the E_ϕ-power greatly intensifies as measured by TH-D and TH-E (panel (b2)), and by RBSP-B (panel (a2)). Overall, the results in case 4 are quite similar to those of case 2 (shown in Figure 4.5), mainly in terms of the E_ϕ-power, where again is found that Pc5 waves measured by RBSP-B are discrete in frequency, whereas the wave activity obtained with THEMIS is now visually more broadband.

5.2 Results and comparisons

This section will present the results of in-situ diffusion coefficients (D_{LL}^{OBS}) relative to case studies 3 and 4, acquired with the wave power data set that has just been discussed. Due to the assumption of single mode resonance ($m = 1$) used to calculate D_{LL}^{OBS}, only wave power relative to local drift-resonant frequencies from the previous spectrograms shown were considered. Nevertheless, one expects to see in Figures 5.9 (for case 3) and 5.10 (for case 4) variations in the intensity of D_{LL}^{OBS} modulated by the phases of the storms and the location of the probes, similar to obtained with ULF waves in the Pc5-band spectrum. The first invariant of $\mu = 1318$ MeV/G has been also considered in these analyses.

Figure 5.9(c) shows that total diffusion rates in case 3 are enhanced within the storm initial and main phases ($2-6$ UT on 10/02) across L shells because of enhancements in D_{LL}^{E} ($15-21$ UT on 10/01, panel (b)), accompanied by increases in D_{LL}^{B} ($0-6$ UT on 10/02, panel (a)). In the recovery phase (after 6 UT-10/02), enhancements driven by ULF activity in E_ϕ (Figure 5.7(a2)) plays a role in the intensification of the these total estimates, especially at $L < 6$, as measured by RBSP-B (see Figure 5.9(b)). The graph of D_{LL}^{E}/D_{LL}^{B} ratios in panel (d) confirms these observations, in which significant larger ratios ($\sim 10^3$) at $L > 5$ occurs before the storm onset at 2 UT-10/02, rather than over the initial phase as discussed for case 1, and during its recovery phase (Figure 5.9(d), ~ 12 UT-10/02) because of the role of D_{LL}^{E}. The lowest

ratios ($\sim 10^{-1}$) are seen concentrated over the main phase interval, as reported with results from cases 1 and 2 due to the sudden increase in D_{LL}^{B}.

Figure 5.9 - Case 3: D_{LL} from observations for $\mu = 1318$ MeV/G.

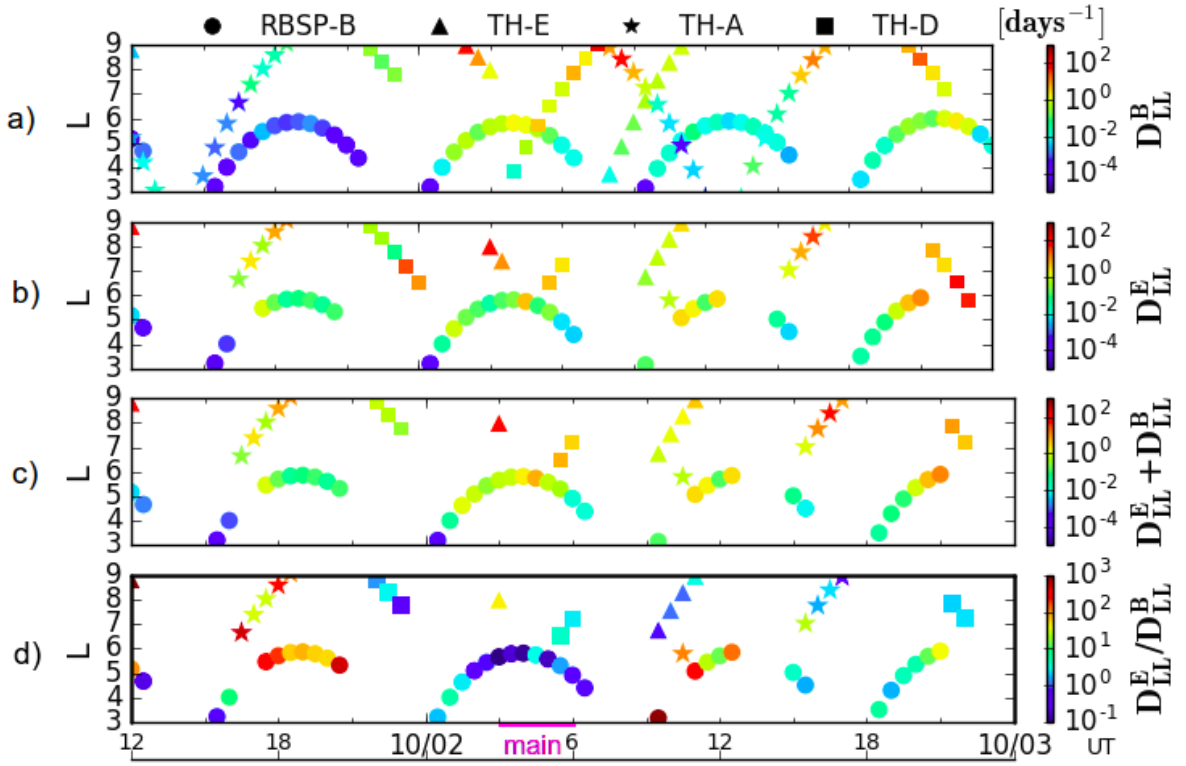

Derived radial diffusion coefficients shown along the satellites' trajectory, given by L. The time duration of the main phase of the storm is indicated by the pink straight bar on the bottom panel.

SOURCE: Produced by the author.

In the case 4 (Figure 5.10(c)), low-L total D_{LL}^{OBS} starting from the storm initial phase are generally less stronger than in case 3 throughout storm time, and have magnetic and electric coefficients (Figure 5.10(b-c)) comparable to those obtained in case 2 (Figure 4.14(b-c)). However, high-L total estimates in Figure 5.10(c) indeed increase through the phases of the storm such as expected from the enhancements in the ULF wave activity measured by THEMIS (Figure 5.8, panels b1-b2). Actually, a minor enhancement in diffusion coefficients taken along RBSP-B's locations, approaching the apogee, takes place during the recovery phase (see in Figure 5.10(c) passes

from $\sim$ 9 to 20 UT on 12/05)> This minor enhancement in D_{LL}^{OBS} (total) results from simultaneous enhancements affecting both magnetic and electric components. D_{LL}^{E}/D_{LL}^{B} ratios within this period in Figure 5.10(d) then slightly tends to the unity, also seen at higher L shells. Outside the mentioned interval, the ratios do not change much in response to the effects of the storm initial and main phases such that D_{LL}^{B} was most of the time comparable or roughly one order of magnitude lower than D_{LL}^{E}.

Figure 5.10 - Case 4: D_{LL} from observations for $\mu = 1318$ MeV/G.

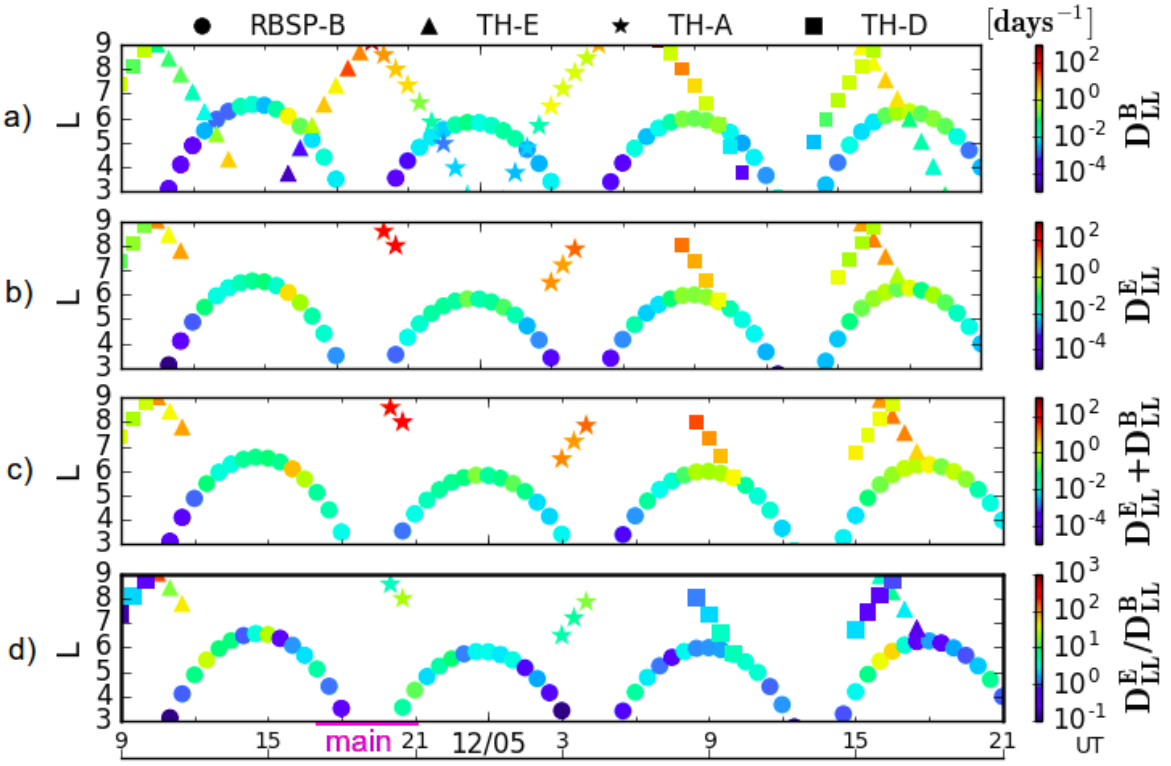

The same as Figure 5.9.

SOURCE: Produced by the author.

Those observed diffusion coefficients are subsequently presented as a function of L only, during several three-hour intervals corresponding to fixed Kp, selected for the comparisons with continuous radial profiles provided with the investigated empirical models of D_{LL}. This is similar to the analyses performed for cases 1 and 2 previously, with the caveat that there are no results from MHD simulations for the two additional cases studies. Figure 5.11(a) shows the responses for a nonstorm period

during case 3 and, as expected, observations consistently match empirical predictions at $L \sim$ 5-6, whereas partially at $L \sim 8.5$. Over storm time, in-situ coefficients are seen to be in poor agreement with the models in almost all intervals shown (panels b-f, except (e)). This is especially verified in the main phase as modeled by Brautigam and Albert (2000) (panel (c)), and during the recovery phase, concerning the three models (panel (d)).

Figure 5.11 - Case 3: Radial profiles of empirical estimates of D_{LL} before and during storm time, validated by observed diffusion coefficients (D_{LL}^{OBS}).

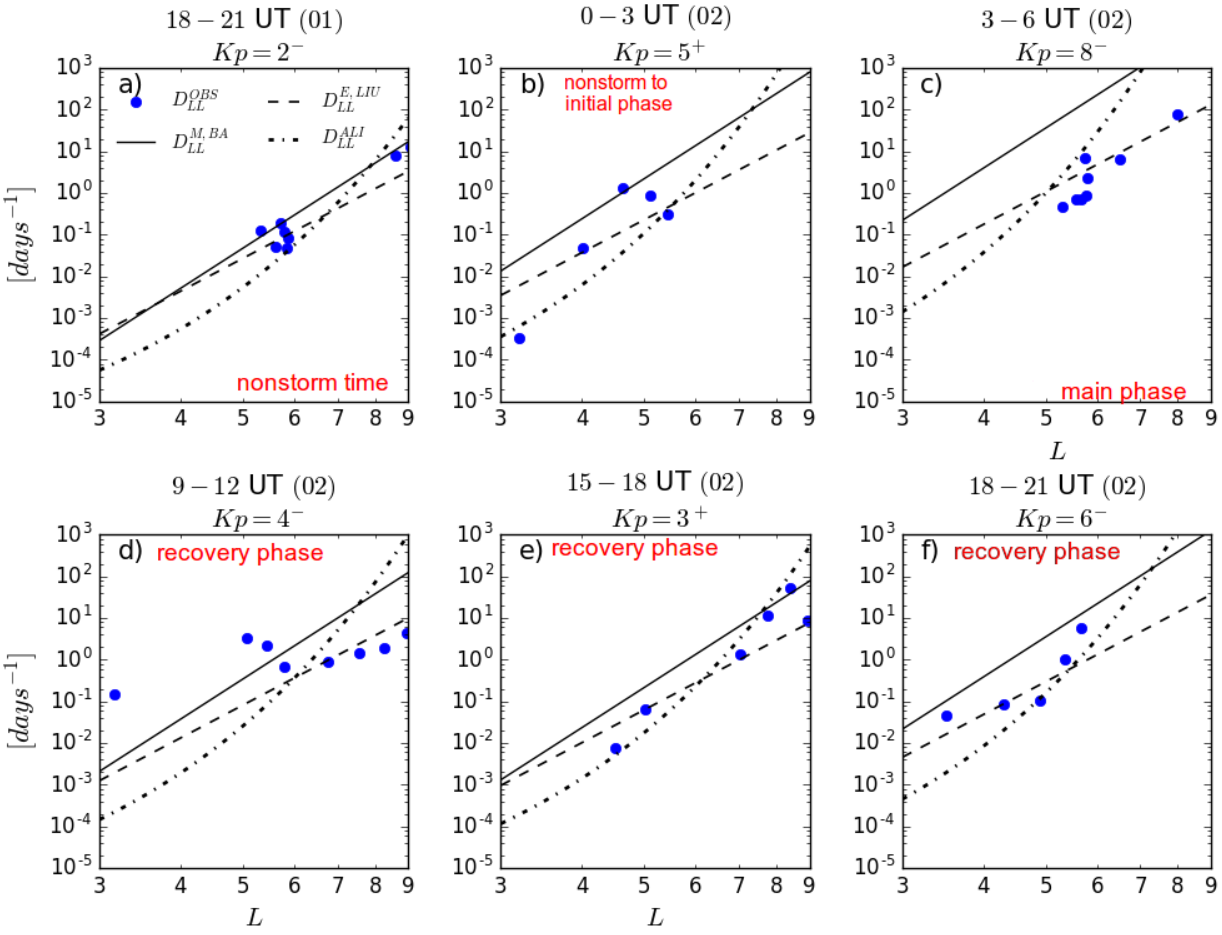

(a-f) Selected intervals, and corresponding Kp index and phase of the storm, for comparisons of radial profiles of various D_{LL} rates implemented. The UT time of the intervals is indicated together with information of the day considered. L represents the L shell. $\Delta L = 0.1 R_E$ for the D_{LL} models. $\mu = 1318$ MeV/G.

SOURCE: Produced by the author.

Still about case 3, the interval shown corresponding to the main phase in Figure 5.11(c) relates to the period of maximum Kp index of the event. During this particular period, it is found that this intense-Kp condition imposed to drive the diffusion coefficients caused the models to mostly overestimate storm-time observed coefficients (up to 3 orders of magnitude). In turn, observations from the early recovery phase (panel (d)) are rather underestimated at $L < 6$, as Kp drops to moderate conditions, while in-situ coefficients peak inside this region. Both results are consistent with the trends of variation in D_{LL} (empirical) averages established by Murphy et al. (2016), as discussed in the beginning of this chapter. Those features also explain the underestimations of low-L D_{LL}^{OBS} from both cases 1 and 2, at corresponding moderate levels of Kp (on discussions of Figures 4.17(c-d) and 4.18(b)).

On the other hand, results in case 4 (Figure 5.12) are shown starting from the initial phase of the storm. Throughout storm time, the available observations of diffusion coefficients visually respond better to fits from the statistical model of Ali et al. (2016). This is perfectly seen in comparisons of panel (c) of this figure. However, this model fails to accurately determine initial- and main-phase observations (panels a-b), which can be up to one order higher or lower around these intervals. Comparisons from Figure 5.12(f) also show that this model highly overestimates diffusion coefficients at larger L shells, such as verified in previous analyses of cases 1 and 2. The other two models mostly well overestimate initial phase rates, while determination of main phase D_{LL}^{OBS} coefficients is similarly complex. Overestimations by the model of Brautigam and Albert (2000) are of major concern even when Kp is not so large (e.g., panels c-f). In addition, there is no clear evidence of enhanced low-L coefficients for association with model underestimations under moderate conditions of Kp. In summary, these results for radial profiles of D_{LL} in case 4 are very similar to those obtained in case 2 (Figure 4.18).

Table 5.1 contains a compilation of the coefficients of determination (R^2) obtained for each of the four case studies. They were computed at the three aforementioned (700, 1318, and 2083 MeV/G) values of μ . Here, these R^2-values assess the level of relationship existing between observed (storm-time) radial diffusion coefficients and empirical estimates as modeled by Brautigam and Albert (2000), Liu et al. (2016), and Ali et al. (2016). All data samples acquired with observations within the time span of 36 hours so far considered for each event (e.g., Figures 5.9 and 5.10) were used, from the same range of L shells ($3 < L < 9$). The empirical estimates from the three models were derived for the locations of the observations and corresponding three-hour Kp value.

Figure 5.12 - Case 4: Radial profiles of empirical estimates of D_{LL} during storm time, validated by observed diffusion coefficients (D_{LL}^{OBS}).

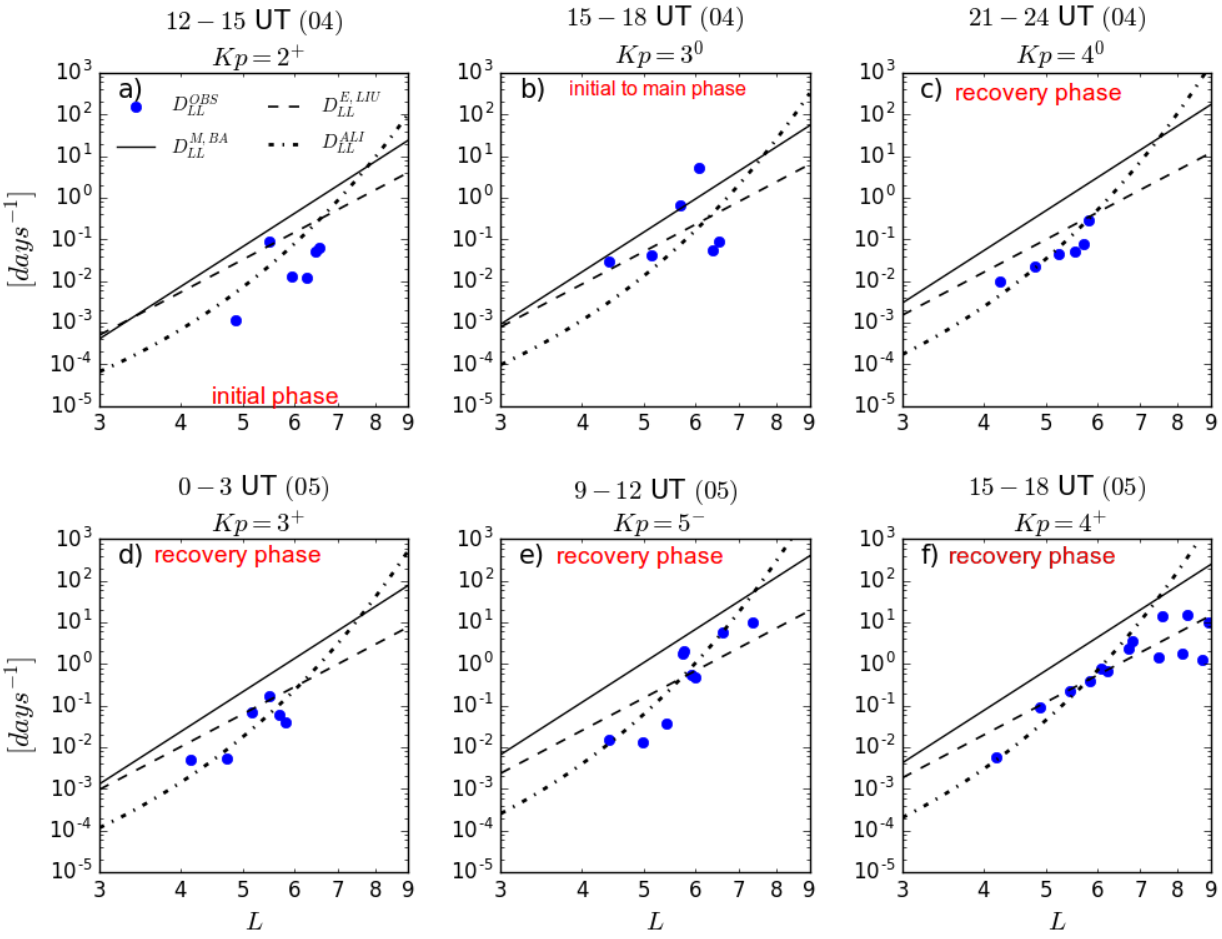

Same as Figure 5.11.

SOURCE: Produced by the author.

The results from Table 5.1 have been tested for a significance level of 1%, by applying the null hypothesis testing based on the computation of the *p-value* (available at https://www.socscistatistics.com/pvalues/pearsondistribution.aspx). This percentage attests to the risk of the correlation coefficients (R) being zero (rather than the values acquired), or in other words, to the probability of both observations and models having no correlation at all. As all of the correlation coefficients tested false for the null hypothesis, one can take those presented R^2 values as statistically significant.

Table 5.1 - Coefficients of determination (R^2) between D_{LL}^{OBS} and estimates from the empirical models, obtained at three values of μ (in red) for each case study.

	B & A (2000)			**LIU et al. (2016)**			**ALI et al. (2016)**		
μ [MeV/G]	700	1318	2083	700	1318	2083	700	1318	2083
Case 1 N = 56	0.45	0.49	0.42	0.49	0.54	0.49	0.49	0.56	0.53
Case 2 N = 83	0.71	0.70	0.74	0.72	0.72	0.75	0.69	0.73	0.76
Case 3 N = 59	0.60	0.60	0.51	0.62	0.66	0.55	0.60	0.65	0.54
Case 4 N = 78	0.67	0.73	0.70	0.70	0.76	0.73	0.69	0.76	0.75

N is the number of pairs from the data samples used.

It has been found that: (i) there is no notable dependence of R^2 on μ in any case, among the models; (ii) models in cases 2 and 4 indeed have a stronger correlation with observations than in cases 1 and 3, which were shown to have been more active in terms of ULF wave activity, as inspected from a ground station and at space; in addition, empirical results of case 1 are the least correlated with observed data; for instance, the model of Brautigam and Albert (2000) in case 2 is 32% more precise to estimate the variance of the observations at $\mu = 2083$ MeV/G than it is in case 1, for the same μ value; and (iii) as a whole, the three models do a similar job to represent storm-time diffusion coefficients.

Basically, the results from Table 5.1 together with those from the analysis of the radial profiles can be interpreted as follows: due to the large variability of storm-time radial diffusion coefficients in intensity, and across L shells, average estimates given by these empirical models are weakly to moderately capable of resolving such variability indicated by the observations. However, this becomes even more complicated to overcome when handling most disturbed events. It was shown from the radial profiles analysis that in the large Kp regime (typical occurrence around the storm main phase), observed radial diffusion rates are likely comparable to overestimated by in-situ derived empirical D_{LL}, such as modeled by Ali et al. (2016) and Liu et al. (2016), or highly overestimated when using Brautigam and Albert (2000)'s model, which is semi space-based. Further, in the case when Kp is moderate, observed rates tend to be underestimated. This would affect physical representation of enhanced diffusion coefficients that eventually take place inside $L < 6$, mainly during the early recovery phase when Kp decreases (e.g., results from cases 1 and 3). Again, it

should be emphasized that these results are in accordance with those proposed by Murphy et al. (2016), although this thesis has effectively verified them in detailed case studies of in-situ diffusion rates, along with correlation analysis with the set of three empirical models.

Hence, the proposed study of storm-time radial diffusion coefficients during these four events have shown that might be right that those *empirical models provide better fits for in-situ data of D_{LL} during less active times, in terms of ULF wave activity*, according to our results. However, the validity of these results found for this hypothesis should be also verified in a statistical study, which is beyond the scope of this thesis.

6 RESULTS FROM RADIAL DIFFUSION MODELING

In this chapter, results concerning the radial diffusion simulations of the chosen case studies will be presented. Electron flux dropouts related to case study 1 ($26-28$ March 2017), case study 2 ($20-22$ November 2017), and case study 4 ($04-06$ December 2017) are investigated through modeling, and compared to observations of the phase space density obtained with the Van Allen Probes. The loss mechanisms tested in the radial diffusion simulations that solved Equation 3.9 were magnetopause shadowing, outward radial diffusion driven by empirical D_{LL} models and the event-specific D_{LL}^{MHD}, pitch angle scattering by hiss, and pitch angle scattering by chorus. It should be mentioned that no source term due to local heating was included for the runs.

Observations of the wave activity related to whistler-mode chorus and plasmaspheric hiss were undertaken using high-resolution magnetic field data provided by EMFISIS instruments on the Van Allen Probes (not shown). In cases 2 and 4, the activity of ELF hiss waves ($0.1-1$ kHz) is enhanced to magnetic power spectral densities of $10^{-5}[nT^2/Hz]$ as soon as the CIRs hit the magnetosphere, that is, at $\sim$ 12 UT-11/20 and 9 UT-12/04, respectively. The activity of VLF chorus waves ($1-10$ kHz) enhances to magnetic power spectral densities of $10^{-8}-10^{-6}$ $[nT^2/Hz]$ a few hours delayed, concomitant with the occurrence of the electron dropouts in both cases. On the other hand, case 1 is the event that reports a much lower wave activity for either wave types, especially during the dropout.

6.1 Phase space density observations

Figure 6.1 depicts the time evolution, in relation to L^*, of phase space density data converted from electron fluxes j measured by RBSP-A. The events being considered are the case studies 1, 2, and 4 that relate to CIR-driven flux dropouts of 1.8 MeV electrons from the outer belt, identified in Figures 4.1, 4.2, and 5.3 (panels (a)), respectively. In Figure 6.1, the PhSD data shown for each event are fixed at the first invariant value $\mu = 1318$ MeV/G, and second invariant value $K = 0.08\ R_E G^{1/2}$. Thus, the μ value chosen is the same one considered in the D_{LL} analysis of relativistic electrons using MHD simulation and observations (e.g., Figures 4.9 and 4.13 for case 1). At $L = 4.5$, it corresponds to the 1.7 MeV population in a dipolar geomagnetic field. Since these calculations of D_{LL} are valid for $\sim 90°$ pitch angles, $K \to 0$ must be also considered for the PhSD analysis (see Table 2.2 for reference). As calculated with the TS04 magnetic field model, $K = 0.08\ R_E G^{1/2}$ corresponds to equatorial pitch angles between $\sim 50°$ (at probe's apogee) and $65°$ (at probe's perigee). Data gaps

seen in PhSD throughout these events has to do with gaps in L^*, generated by passes of the probe farther from the magnetic equator (not shown), and consequently at higher latitude than that of the mirror points of the covered equatorial pitch angles.

Figure 6.1 - RBSP-A observations of phase space density during the case studies 1, 2, and 4.

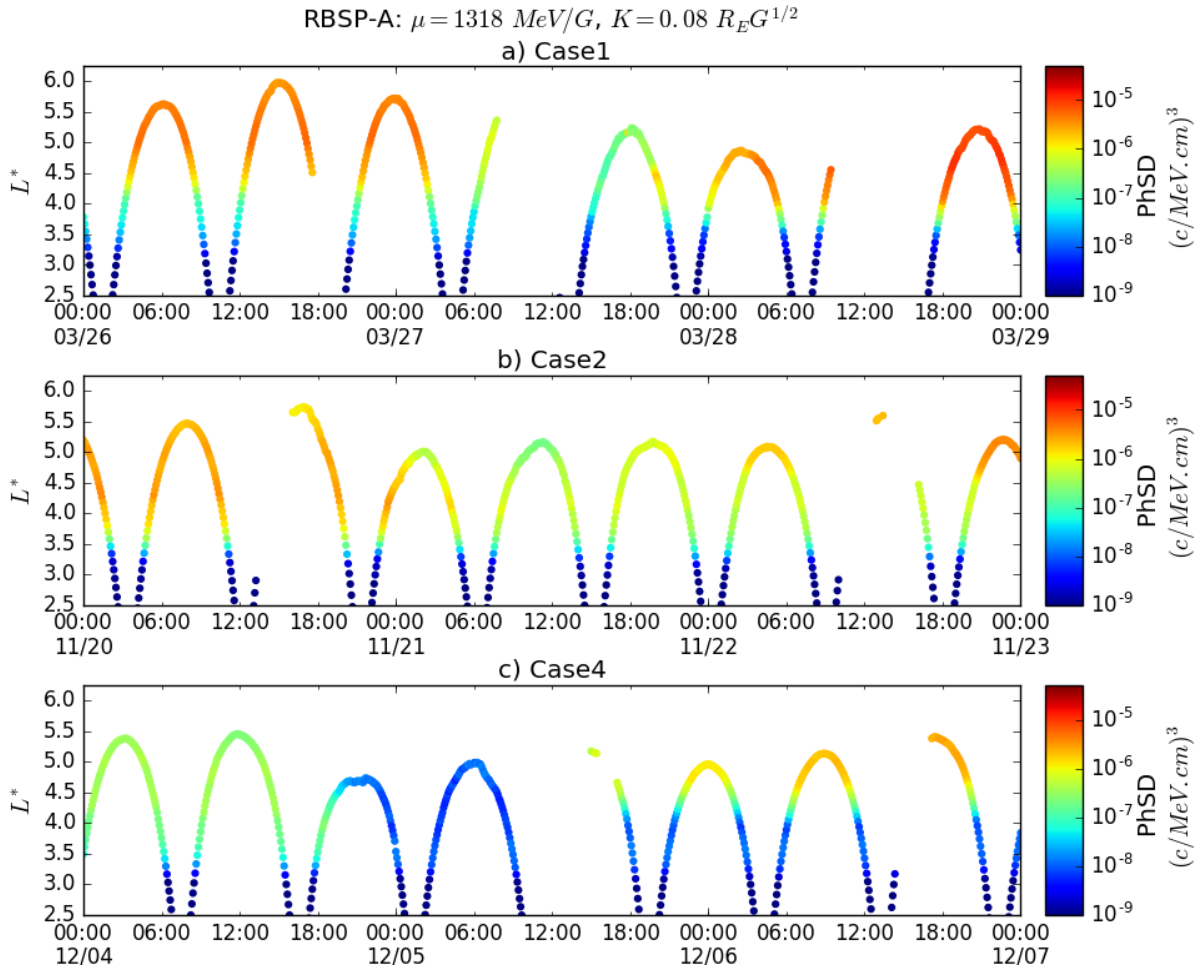

(a) Case study 1; (b) Case study 2; (c) Case study 4. PhSD is plotted along the probe's L^* data calculated with the TS04 model. .

SOURCE: Produced by the author.

Nonetheless, dropouts in PhSD can be viewed in the three events, i.e., on 03/27 for case 1 (Figure 6.1, panel (a), after 5 UT), on 11/21 for case 2 (panel (b), after 0 UT), and on 12/04 for case 4 (panel (c), after 18 UT). By contrast with electron fluxes,

those dropouts are indicative of true electron losses, as well as for the enhancements in PhSD that follow these dropouts, since adiabatic variations are removed. The dropout of case 1 (panel (a)) is the most significant, involving a decrease in PhSD by a factor of $\sim 1/100$, against a factor of $\sim 1/10$ in cases 2 and 4 (panels b-c). The results from case 4 in panel (c) actually demonstrate that prior to the dropout, the electron PhSD values were already very low in the outer belt, and then decreased to background levels due to the dropout. Outward radial diffusion driven by wave-particle interactions with ULF waves accompanying the effect of magnetopause shadowing, so far investigated, may be the cause of those dropouts.

6.1.1 Cross-calibration analysis

Calibrated PhSD data from GOES-15 relative to the PhSD from RBSP-A were used to build dynamic conditions at the outer boundary ($Lmax = 6$), and initial condition within $L^* = 2.5 - 6.0$ in all radial diffusion simulations. The GOES-15 PhSD data were transformed from electron fluxes j extrapolated in energy to obtain observations at $\mu > 400$ MeV/G. The magnitude of the local magnetic field B derived with time-dependent TS04 model was required to calculate the PhSD using Equation 3.3, since the PhSD data from the Van Allen Probes were also calculated using modeled B.

Figure 6.2 shows validations of modeled B along the path of GOES-15 at geosynchronous orbit, throughout the interval of each case study. The measurements of B from GOES-15 (G15 in these plots) have sampling of 1 minute, whereas modeled estimates were obtained with a cadence of 15 minutes (the same of the radial diffusion runs). In this figure (panels a-c), fast fluctuations in measured B with amplitude $\sim 30 - 60$ nT are associated with substorm activity on the nightside, during storm time (seen mostly on the second day of observation). On the other hand, fluctuations seen with much smaller amplitudes relate to ULF waves. However, it is necessary to concentrate these validations on slower variations of B at timescales greater than the drift period of trapped relativistic electrons, of a few minutes. Although no information of the satellite's location in MLT is given, it was discussed previously that at geosynchronous orbit, the noon-midnight asymmetry of the geomagnetic field modulates the observations acquired with GOES (e.g., Figures 4.21 and 4.23). Hence, it is seen in Figure 6.2(a-c) that the modeled B well captures this diurnal modulations of the geomagnetic field intensity during the events.

Figure 6.2 - Validations of the magnetic field strength modeled with TS04 along GOES-15 orbit during (a) case 1, (b) case 2, and (c) case 4.

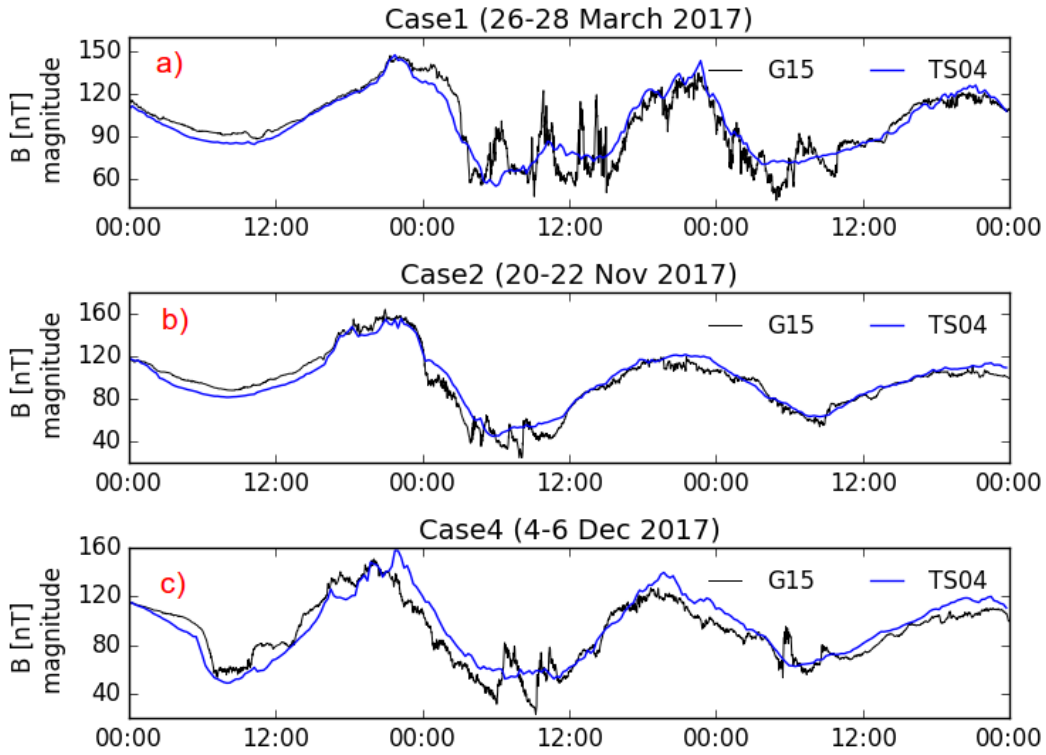

The geomagnetic field intensity at geosynchronous orbit peaks on the dayside (before 0 UT) and drops on the nightside (before 12 UT). "Jumps" in B measured by GOES-15 on the nightside are caused by substorm activity. .

SOURCE: Produced by the author.

Subsequently, it is shown in Figure 6.3 concurrent PhSD observations of RBSP-A, RBSP-B, and GOES-15 during case 1, before calibration of the GOES-15 PhSD data. Figures A.8 and A.9 in Appendix A show the results of cases 2 and 4, respectively. The dropout of case 1 (Figure 6.3) on 03/27 is then best identified with the addition of observations from RBSP-B, in comparison to Figure 6.1(a). GOES-15 uncalibrated PhSD distributions from Figure 6.3 also report the dropout on 03/27 at $\sim$ 12 UT (see PhSD data from $5 \lesssim L^* \lesssim 6$), but at significant lower levels than those obtained with RBSP-B. Overall, the PhSD data from GOES-15 at $\mu = 1318$ MeV/G exhibit lower levels throughout the period considered.

Figure 6.3 - Van Allen Probes (RBSP-A and RBSP-B) and GOES-15 observations of phase space density during case 1.

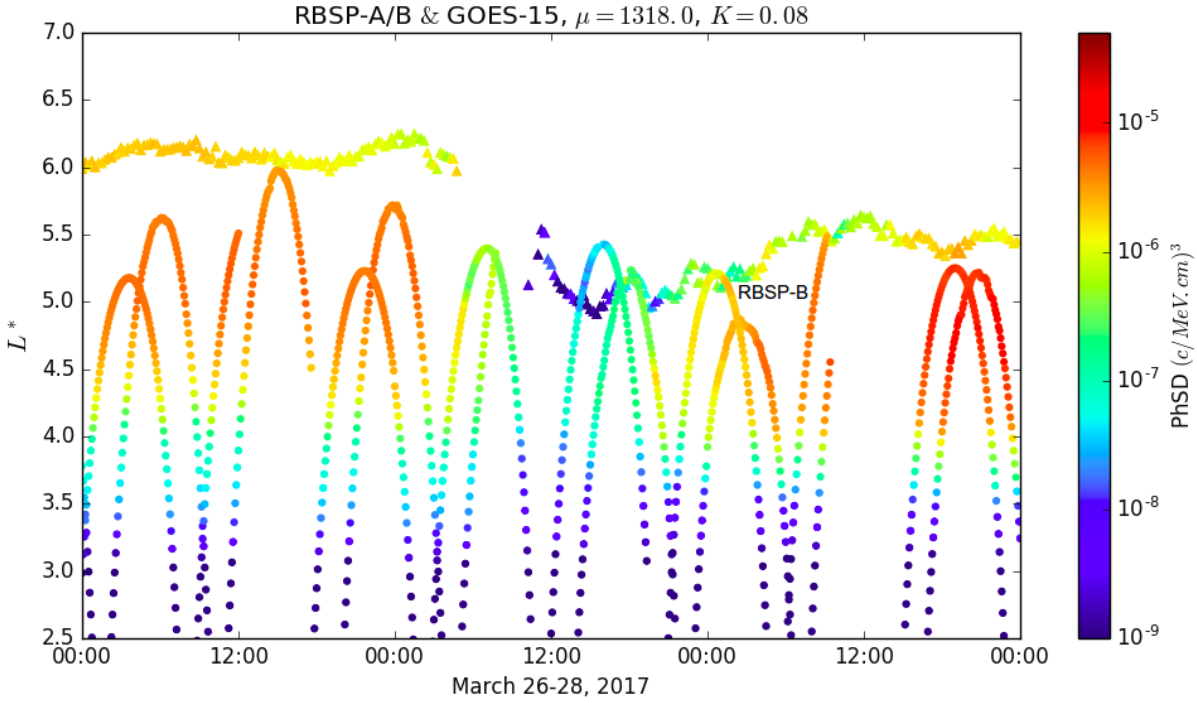

PhSD is plotted along the probes' L^* data calculated with the TS04 model. The PhSD data from GOES-15 shown are not calibrated. The apogee of RBSP-B during an inbound on 03/28 is indicated. Gaps in L^* at geosynchronous orbit ($5 \lesssim L^* \lesssim 6$) are rather related to the proximity of the last closed drift shell, to be discussed afterward.

SOURCE: Produced by the author.

Also in Figure 6.3, it is important to notice the changes in the L^* from GOES-15 calculated for $r \sim 6.6 R_E$ and time-varying MLT. Prior to storm-time (initiated at 18 UT-03/27), the probed population is found at $L^* \approx 6$. This is also observed in case 2 (Figure A.8) until the magnetic storm is initiated at 12 UT-11/20. During the storm main phases of these events, L^* values visually decrease to ~ 5 (e.g., Figure 6.3, within $4 - 15$ UT on 03/27). This is explained by the *Dst* effect enhanced with the development of the ring current. To prevent decreases in the magnetic flux Φ enclosed by the drift shells, these same drift shells move outward in order to conserve the previous value of Φ. As a result, GOES-15 located at geosynchronous orbit measures electron populations from smaller L^* values (e.g., Green and Kivelson (2001)). In case 1 (Figure 6.3), the L^* at GOES-15 orbit gradually recovers to greater values during the recovery phase after 15 UT on 03/27. In the meantime, the PhSD

relatively increases, but at lower levels than enhancements observed by the Van Allen Probes around the apogees at L^* near that of GOES-15 (e.g., RBSP-B's apogee at $\sim$ 0 UT on 03/28 indicated in the same figure).

In order to calibrate the PhSD data of GOES-15 with RBSP-A data, conjunctions in L^* between these probes were searched throughout March 2017. Storm-time periods were avoided. It was found conjunctions during 17 days, yielding an amount of 246 conjunction points for analysis, considering $\Delta L^* \leq 0.5 R_E$ for the probes' separation. Thus, in this analysis the conjunctions are not restricted to $\Delta L^* \leq 0.1 R_E$ as assumed in Chapter 3 (section 3.2.1.1) so that more conjunction points could be acquired. But before the cross-calibration, matching factors (MF) were also obtained from the dual PhSD measurements of each conjunction instance, calculated for $\mu = 1318$ MeV/G and $\mu = 700$ MeV/G. They attest to the error, between measurements, for determining the local PhSD, which is generally associated with uncertainties from the magnetic field model used or ultimately to calibration mismatch of the observed particle fluxes. Basically, matching factors were calculated as follows:

$$MF = \frac{Larger\ PhSD(L_1^*)}{Smaller\ PhSD(L_2^*)} \tag{6.1}$$

where L_1^* and L_2^* are respectively the L^* values of the probe with larger PhSD and that with smaller PhSD, in which $\Delta\ L^* = |L_1^* - L_2^*|$.

Figure 6.4 presents the respective results in panels (a) and (b), from PhSD values also computed for $K = 0.08\ R_E G^{1/2}$. It is noted that MF values are up to one order of magnitude larger for $\mu = 1318$ (panel (a)) than for $\mu = 700$ (panel (b)) throughout $\Delta L^* \leq 0.5 R_E$. MF values at $\mu = 1318$ ranges up to ~ 40, against MF < 5 at $\mu = 700$. Considering MF $= 2$ as the lower limit for calibration mismatch over $\Delta L^* \lesssim 0.1 R_E$ (e.g., Reeves et al. (2013)), MFs of low-μ in panel (b) are below this threshold, which implies that the electron fluxes extrapolated of GOES-15 to obtain the PhSD data at $\mu = 700$ MeV/G are generally accurate with electron fluxes measured by RBSP-A. However, for $\mu = 1318$ MeV/G in panel (a), MFs are already 2 or greater inside $\Delta L^* = 0.1 R_E$. This demonstrates that the electron fluxes from GOES-15 extrapolated to obtain PhSD at this large μ value are least accurate with those measurements by RBSP-A.

Figure 6.4 - Matching factors of dual PhSD measured by RBSP-A and GOES-15 (uncalibrated) for 246 L^*-conjunctions in March, 2017.

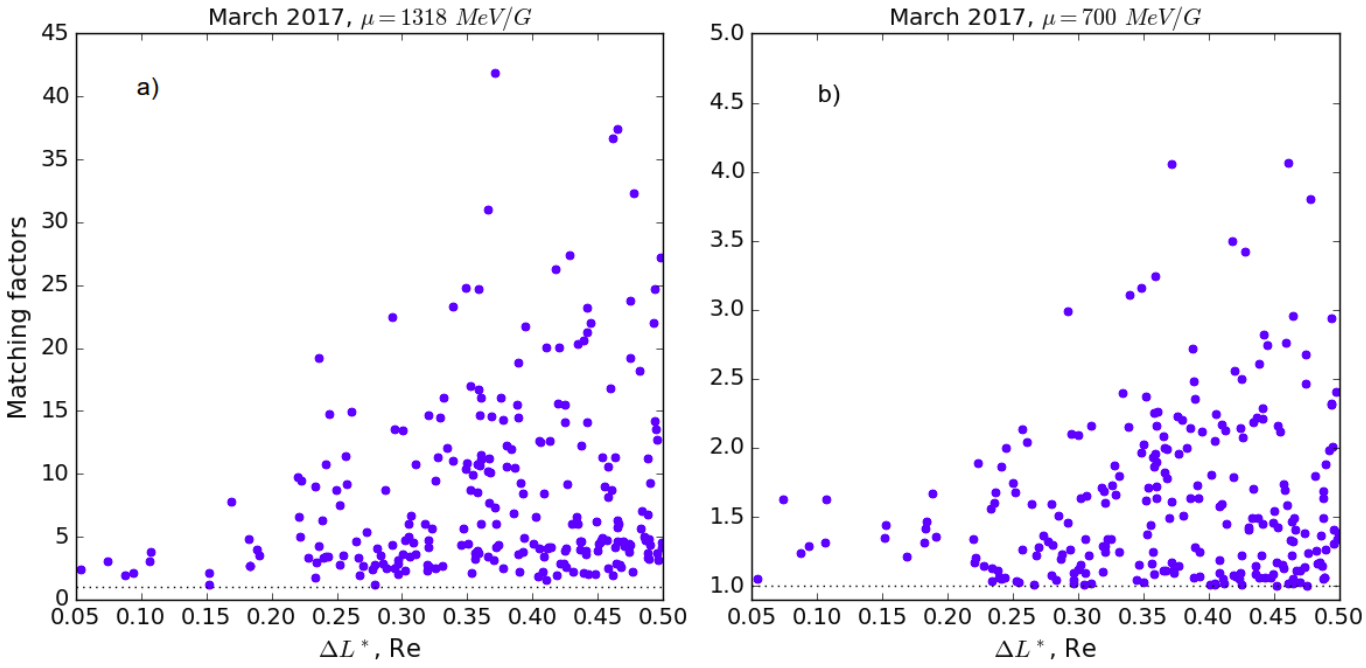

The L^* data set used was obtained with the TS04 model, for $K = 0.08\ R_E G^{1/2}$. The dotted line is a reference for MF = 1.

SOURCE: Produced by the author.

Reducing the conjunction width to $\Delta L^* \leq 0.3$, it was obtained calibration factors equal to 1.33 ($\mu = 700$) and 5.50 ($\mu = 1318$) from this data set. These calibration factors represent the mean factors in PhSD defined as:

$$Factor = \frac{PhSD_{RBSPA}(L_1^*)}{PhSD_{G15}(L_2^*)} \tag{6.2}$$

Here, L_1^* and L_2^* correspond to the L^* location of RBSPA and GOES-15, respectively, where $\Delta L^* = |L_1^* - L_2^*|$.

A total of 57 conjunctions was considered in these calculations. Figure 6.5 contains the results of the PhSD matching factors after calibrating the GOES-15 data with the derived calibration factors. In panel (a) are results for $\mu = 1318$ MeV/G. The correction of the PhSD values of GOES-15 drastically diminishes the MFs not to greater than 6 over $\Delta L^* \leq 0.3 R_E$, at this μ value. But in comparison with results

from $\mu = 700$ MeV/G (panel (b)), MF values at $\Delta L^* \lesssim 0.1 R_E$ are ranging close to 2 for $\mu = 1318$, instead of ~ 1.5 as seen for the lower μ value. This indicates that the PhSD data at $\mu = 1318$ were corrected with the calibration, but the data at $\mu = 700$ are still more accurate with the PhSD from RBSP-A. In this regard, Table 6.1 confirms this result, showing that the mean MF values reduced after the calibration of GOES-15 PhSD for both μ values, but with the larger mismatch still affecting data at $\mu = 1318$.

Figure 6.5 - Matching factors of dual PhSD measured by RBSP-A and GOES-15 (calibrated) for 57 L^*-conjunctions in March, 2017.

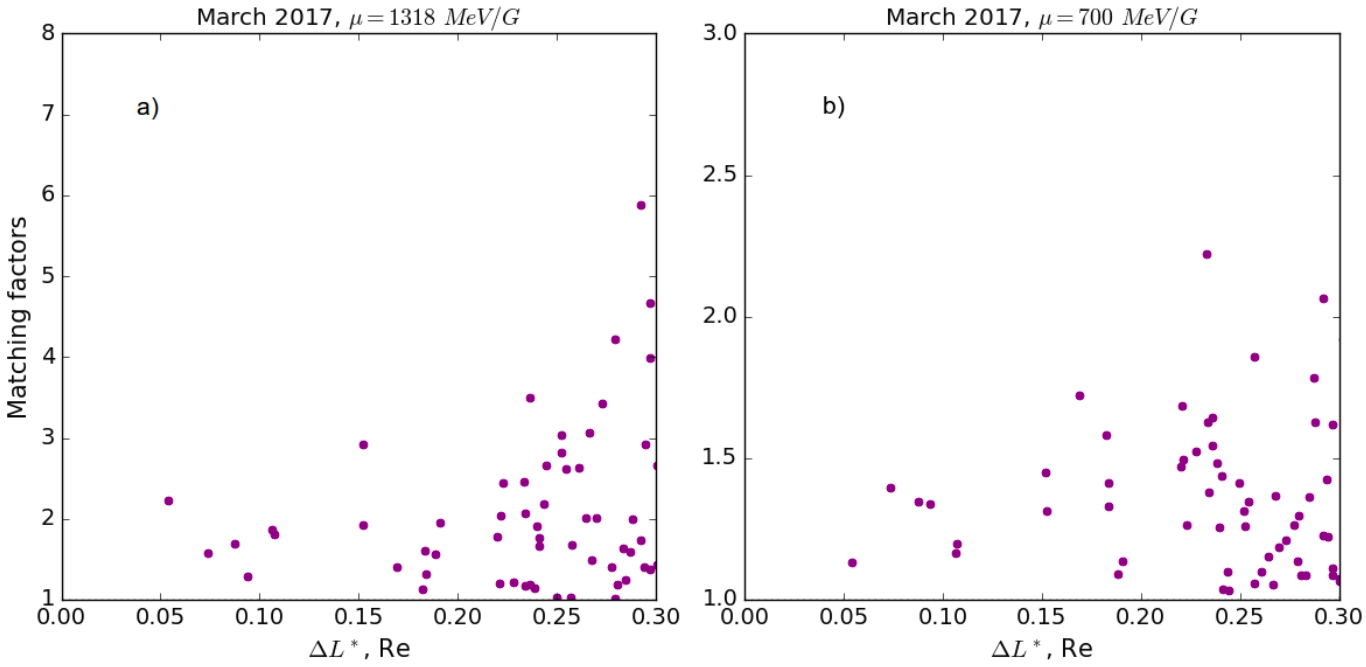

Same as in Figure 6.4.

SOURCE: Produced by the author.

Table 6.1 - Averages of MFs inside $\Delta L^* \leq 0.3 R_E$, before and after calibration of GOES-15 PhSD.

	$\mu = 1318$ MeV/G	$\mu = 700$ MeV/G
before	5.51 ± 4.47	1.78 ± 0.60
after	2.07 ± 0.97	1.36 ± 0.25

To test the accuracy of the calibrated PhSD data of GOES-15 with the RBSP-A data, radial profiles of combined PhSD values from the two probes at times of conjunction in L^* were observed. This is needed to define the initial conditions across $L^* = 2.5-6$ for the radial diffusion runs. It was chosen combined data from intervals at quiet conditions preceding the storm time of each case study. For case 1, we picked the phase space densities along an outbound pass of RBSP-A starting at $\sim$ 12 UT on 03/26 (see this pass in Figure 6.3 going from $L^* = 2.5$ up to the conjunction point with GOES-15 at $L^* = 6$). The profile of this combined PhSD data with respect to L^* is depicted in Figure 6.6, which corresponds to $\mu = 1318$ MeV/G. In blue is the curve of the PhSD profile acquired with RBSP-A throughout the outbound pass, and the red star stands for the calibrated PhSD estimated for GOES-15 at this conjunction point. Even if the probes' separation is small ($\Delta L^* < 0.1 R_E$), it is clear that the mismatch of the GOES-15 calibrated PhSD persisted. This was critical for the other events in which the RBSP-A passes chosen for the profiles had larger separation at the conjunction with GOES-15 ($\Delta L^* > 0.3 R_E$).

On the other hand, it is shown in Figure A.10 the respective result for $\mu = 700$ MeV/G during the same interval of case 1 and spacecraft conjunction. In agreement with results from the matching factor analysis, the radial profile using combined PhSD from RBSP-A and the calibrated estimate from GOES-15 is smooth as desired to obtain initial conditions for the radial diffusion simulations. Also, the same accuracy was verified in the chosen profiles of case studies 2 and 4 (not shown). Thereby, these observations justify the choice, hereafter, of performing radial diffusion runs only for $\mu = 700$ MeV/G.

Figure 6.6 - Case 1: Radial profiles of PhSD for $\mu = 1318$ MeV/G, from an outbound pass of RBSP-A on 03/26 together with the calibrated estimate from GOES-15 at the conjunction ($L^* \sim 6$ and $\Delta L^* = 0.09$).

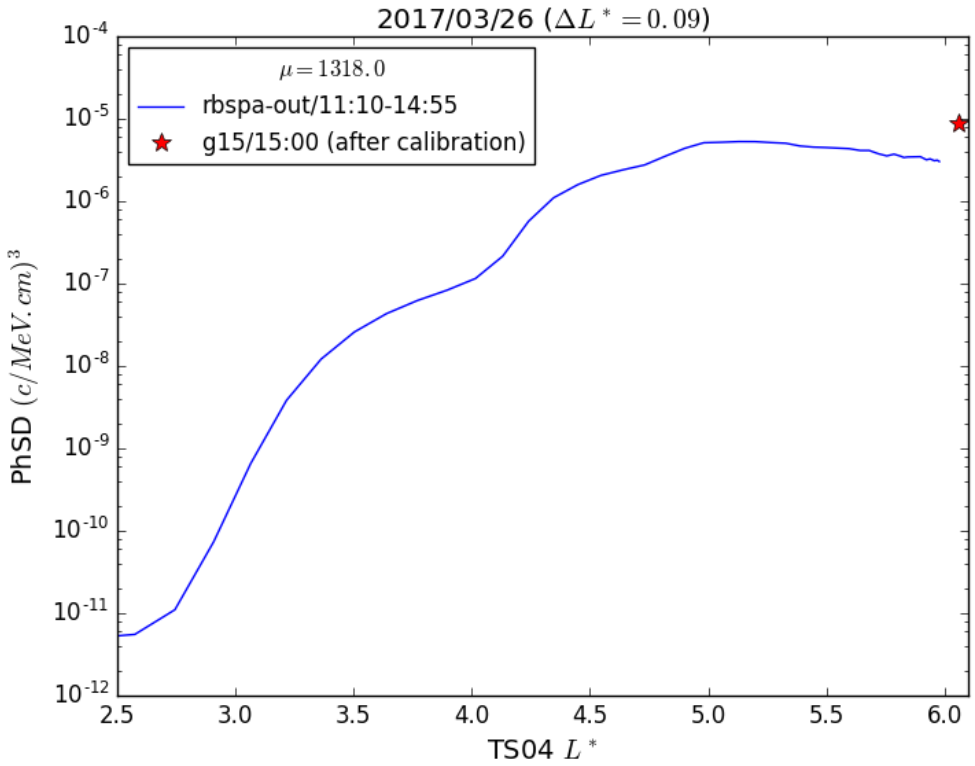

The L^*-conjunction occurred at $\sim$ 15 UT.

SOURCE: Produced by the author.

6.2 Results of the simulation inputs

6.2.1 Outer boundary condition

The domain set for the radial diffusion simulations is $L^* = 2.5 - 6$ for empirical D_{LL} and $L^* = 3 - 6$ for D_{LL}^{MHD}. Recall that although the inner boundary of the MHD simulations was defined at $L^* = 2.5$, the calculation of D_{LL}^{MHD} was restricted to $L^* = 3$, in considering a dipolar geomagnetic field where $L^* = L$. The grid and time resolutions in both cases are $0.1R_E$ and 15 minutes, respectively. The inner boundary condition at $Lmin = 2.5$ or $Lmin = 3$ was made static.

Figure 6.7 - Time-series of calibrated PhSD data from GOES-15 set for dynamic outer boundary conditions in the radial diffusion simulations of (a) case 1, (b) case 2, and (c) case 4, and computed for $\mu = 700$ MeV/G and $K = 0.08\ R_E G^{1/2}$.

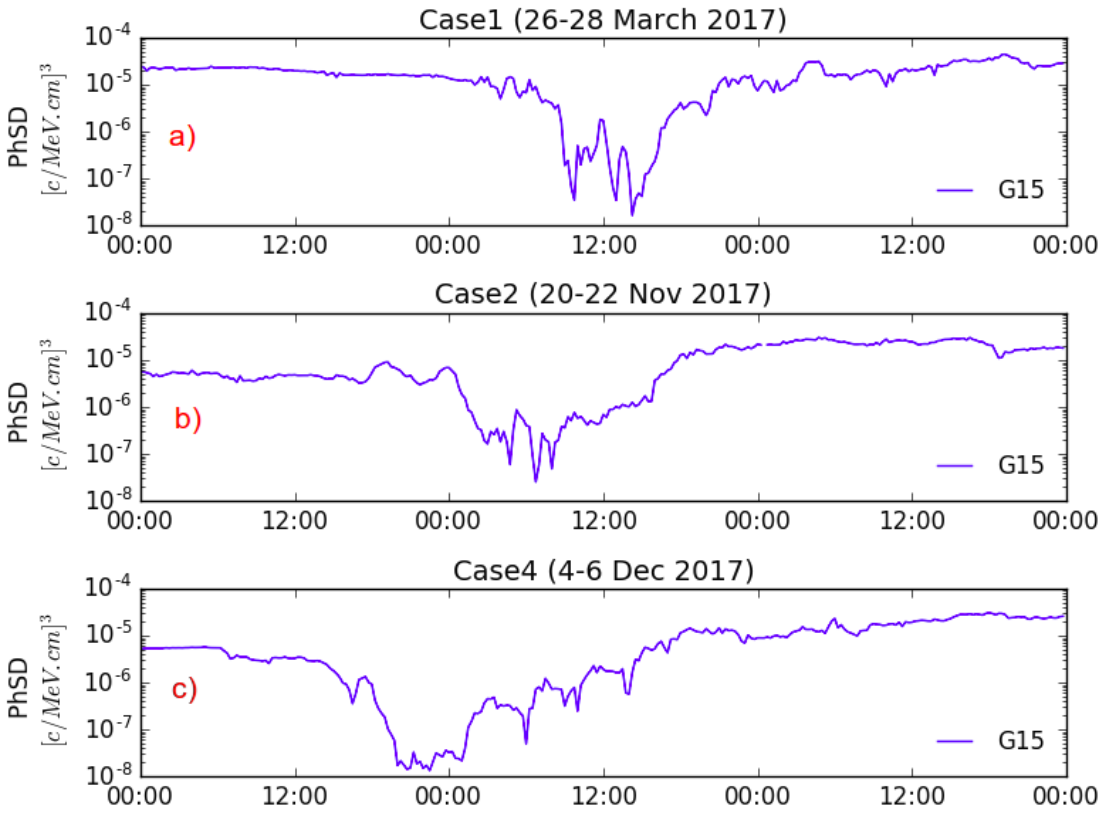

Dropouts of case 1 (panel (a), on 03/27) and case 2 (panel (b), on 11/21) are dominated by irregular variations in PhSD possibly driven by substorms, as shown in Figure 6.2. The dropout of case 4 (panel (c), on 12/05) is dominated by electron injections, starting at 0 UT until $\sim$ 15 UT. Assuming a dipolar geomagnetic field at $L = 6.6$, the injected electrons producing enhancements in PhSD would correspond to $\sim$ 0.5 MeV populations for $\mu = 700$ MeV/G.

SOURCE: Produced by the author.

Figure 6.7 shows the time-series of PhSD used for outer boundary condition of (a) case study 1, (b) case study 2, and (c) case study 4. This data relative to $\mu = 700$ MeV/G and $K = 0.08\ R_E G^{1/2}$ were derived from the uncalibrated PhSD distributions previously presented in Figures 6.3 (case 1), A.8 (case 2), and A.9 (case 4). As discussed for those figures, the PhSD distributions at GOES-15 orbit from Figure 6.7(a-c) capture remarkable dropouts by a factor of $\sim$ 1/1000 in the three events, associated with the ongoing magnetic storms. The observed enhancements

in PhSD are, overall, of up to one order of magnitude relative to prestorm values. Note that the phase space densities under dropout in cases 1 and 2 (panels (a-b)) are subjected to fast variations related to the effect of the substorm activity on the ambient magnetic field discussed in Figure 6.2. Concerning case 4, the substorm activity prompts successive energetic electron injections at ~ 0.5 MeV that gradually recovers the PhSD, as seen on early December 5 until $\sim$ 15 UT. These variations at the outer boundary are important for the radial diffusion simulation to drive the dropouts and enhancements in PhSD down to low-L^* regions, as measured by the Van Allen Probes in the events.

To build the dynamic outer boundary conditions in each run, it was assumed that this PhSD data from GOES-15 were constantly obtained at $Lmax = 6$. In reality, results from the L^* discussed for Figures 6.3, A.8, and A.9 have shown that the L^* values observed at geosynchronous orbit indeed change from $L^* \approx 6$ throughout storm time. It should be pointed out that such assumption has been made in previous works. For instance, Li et al. (2014b) used PhSD data acquired with the Van Allen Probes between $L^* = 5$ and $L^* = 6$ to make a realistic constraint for the outer boundary, which was also set at $L^* = 6$.

6.2.2 Modeled electron lifetimes and constraints

Figure 6.8 shows dynamic maps of the electron lifetimes (τ) resulting from the gyroresonance with whistler-mode hiss and chorus waves obtained, respectively, for case 1 (a-b), case 2 (c-d), and case 4 (e-f). Equations 3.17-3.20 were used in these calculations. The time-dependent plasmapause location (L_{PP}) given by O'Brien and Moldwin (2003) is overplotted in black, and was used as the constraint to define loss terms due to chorus outside L_{PP}, and due to hiss inside L_{PP} (TU et al., 2009). First, it is noted in all cases that the modeled plasmapause is rapidly relaxed outward as the storm initial phase develops, but hours later is eroded to $L^* \sim 3.5 - 4.0$ because of the storm-time convection (CARPENTER; ANDERSON, 1992).

The behavior of the electron lifetimes due to hiss (panels (a), (c), (d)) inside L_{PP} is that of values in the range from 10 to below 100 days $\sim$ before the storms. Then these values decrease to below 10 days as soon as the plasmapause is eroded. In case 1 (a), lifetimes even lower of $\lesssim 5$ days are seen to last longer than obtained in cases 2(c) and 4(d). Less slower atmospheric losses were driven by chorus outside L_{PP}, as indicated by the results of panels (b), (d), and (f). Cases 1(b) and 4(f) gets the lowest lifetimes of 1 day or less during storm time, preferentially at $L^* > 5$. Lifetimes below 10 days dominate the storm period in case 2(c). Although the models of the

lifetimes (Orlova et al. (2014) for hiss and Shprits et al. (2007) for chorus), and of L_{PP} are given with respect to L shell (L), $L = L^*$ was assumed for those inputs in all runs.

Figure 6.8 - Dynamic maps of electron lifetimes inserted in the radial diffusion simulations of (a-b) case 1, (c-d) case 2, and (e-f) case 4, computed for $\mu = 700$ MeV/G.

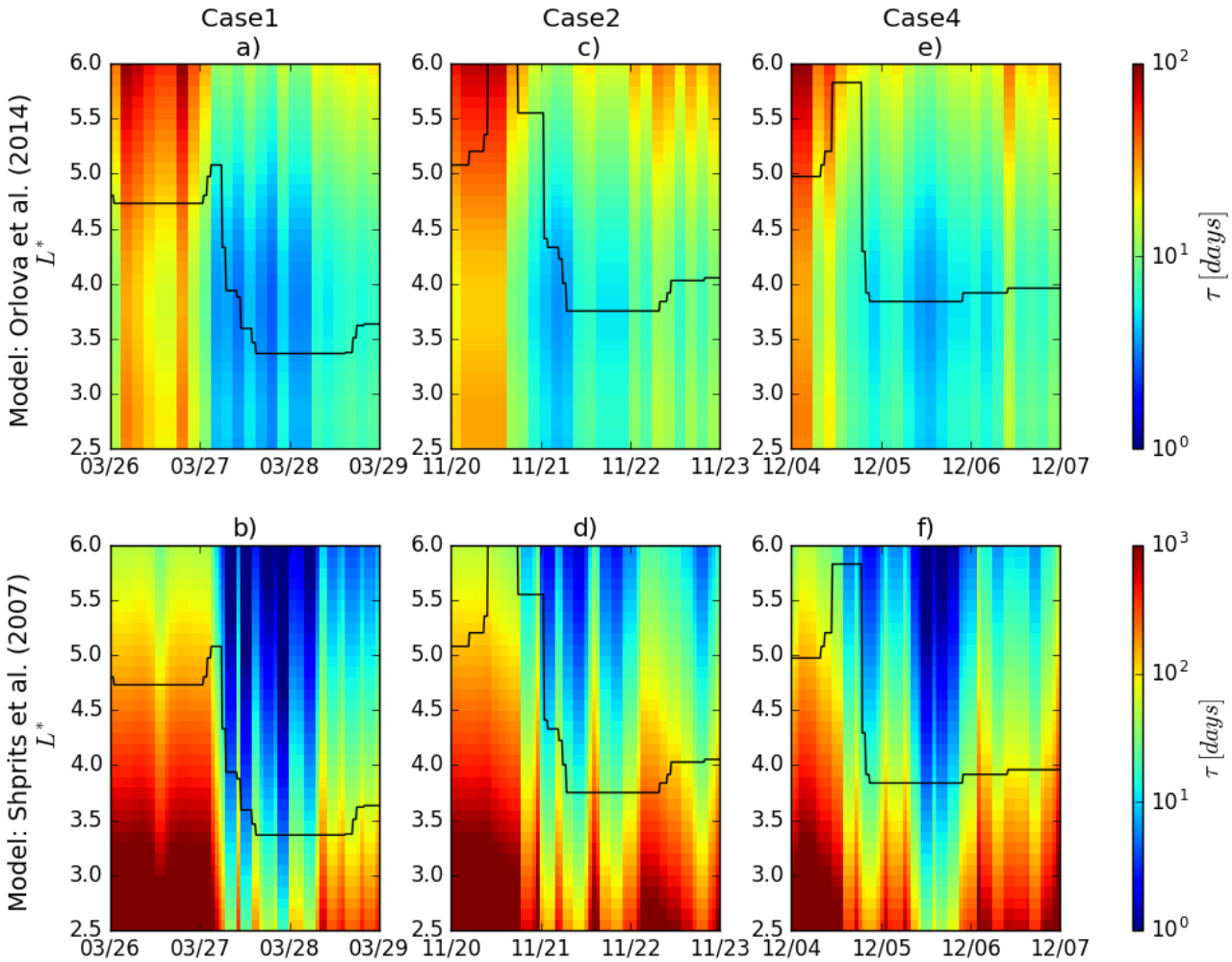

The black curve is the modeled plasmapause location, L_{PP}. (Top panels) Lifetimes due to hiss from Orlova et al. (2014) inserted inside L_{PP}; (Bottom panels) Lifetimes due to chorus from Shprits et al. (2007) inserted outside L_{PP}. The storm initial phases start at 18 UT on 03/26 (case 1), at 12 UT on 11/20 (case 2), and at 9 UT on 12/04 (case 4).

SOURCE: Produced by the author.

Next, the dynamics of the last closed drift shell (LCDS) are analyzed. This parameter was used in the radial diffusion simulations to determine magnetopause shadowing losses during those events. The results are shown in Figure 6.9. The LCDS represents the last L^* of trapped populations, above which drift shells are opened. Because L^* decreases during the storm main phase due to the expansion of the drift shells, the LCDS also decreases as obtained for the three cases shown (panels a-c). Early in this text in the section 4.2.1, it was discussed that the extent of the magnetopause compression in cases 1 and 2 were very similar, with a maximum of $\sim 7R_E$ as modeled by Shue et al. (1998) (e.g., Figures 4.1 and 4.2, panels (f)). The results from MHD (Figure 4.7) have also indicated similar values for the main compression between the two cases, of $\sim 8R_E$. In turn, these results from the LCDS in Figure 6.9 indicate that the extent of compression in the inner magnetosphere was about 0.5 R_E larger for case 1 than for case 2.

Figure 6.9 - Dynamics of the last closed drift shell set for magnetopause shadowing losses in the radial diffusion simulations of (a) case 1, (b) case 2, and (c) case 4, computed for $K = 0.08\ R_E G^{1/2}$.

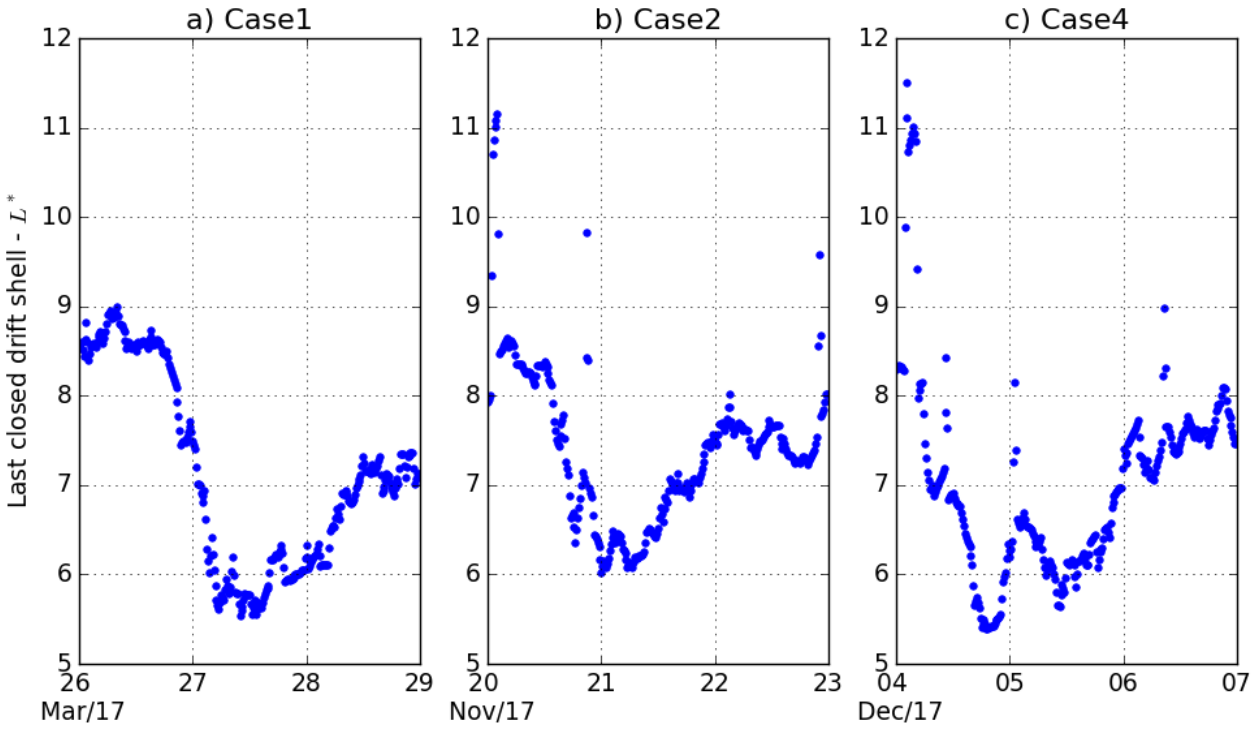

The storm initial phases start at 18 UT on 03/26 (case 1, (a)), at 12 UT on 11/20 (case 2, (b)), and at 9 UT on 12/04 (case 4, (c)).

SOURCE: Produced by the author.

More specifically, it is seen that whereas in case 1 (panel (a)) the LCDS goes lower than $L^* = 6$ and remains for several hours on 03/27, in case 2 (panel (b)) it does not. Since $Lmax = 6$ in the radial diffusion simulations, the LCDS had no effects for dropouts in the runs of case 2. Conversely, the runs of case 1 (panel (a)) and case 4 (panel (c)) had a loss term defined above the LCDS whenever below $Lmax = 6$, by using the local drift period to represent the electron lifetimes. In fact, case 4 is the most affected by the expansion of the drift shells during storm-time, in which the LCDS value drops to below 5.5 at the end of 12/04. Because of a three-hour-long northward turning of IMF-B_z (see Figure 5.4(d), from 21 UT-12/04 to 0 UT-12/05), the LCDS values in Figure 6.9(c) then increases to $L^* > 6.5$, as the drift shells are driven inward following the relaxed magnetopause (see the same interval in Figure 5.4(f)). But it did not take long for the LCDS to drop again to $L^* < 6$, on 12/05. Later over the recovery phase, which is after 21 UT-12/05, the LCDS is recovered to prestorm values around 8, also obtained in case 2 at the end of 11/22 (Figure 6.9 (b-c)). In case 1 (panel (a)), it is observed to recover to $L^* < 7.5$, until 0 UT-03/29.

6.2.3 Empirical D_{LL}

Outward radial diffusion is the loss process that operates subsequent to magnetopause shadowing (e.g., Xiang et al. (2017)). In this regard, it has been demonstrated with MHD simulation and observations in Chapter 4 that enhanced storm-time radial diffusion coefficients were closely related to the dropouts of cases 1 and 2. The D_{LL} results from observations in case 4 were very similar to those obtained in case 2 (by rates in the range $10^{-2} - 10^{0}$ [1/day]), which was generally 2 orders of magnitude lower inside $L = 6$ than in case 1.

Concerning empirical storm-time estimates, the responses of three models were so far analyzed in radial profiles, and through their correspondence with radial diffusion coefficients driven by on-orbit data, i.e., D_{LL}^{OBS}. It was found that the models from Liu et al. (2016), Ali et al. (2016), and Brautigam and Albert (2000) are in best agreement with the storm-time D_{LL}^{OBS} derived for cases 2 and 4, in which both events presented lower ULF wave activity than reported for cases 1 and 3. As for the radial diffusion simulations, such empirical D_{LL} models were implemented to the runs, and the error of results from each model relative to the measured PhSD will be compared, as well as errors from the use of D_{LL}^{MHD} maps already presented for cases 1 and 2 in Figures 4.9 and 4.10 .

Figure 6.10 - Maps of empirical D_{LL} set to reproduce storm-time radial diffusion coefficients in the radial diffusion simulations of (a-c) case 1, (d-f) case 2, and (g-i) case 4, using the models from Brautigam and Albert (2000) (top), Liu et al. (2016) (middle), and Ali et al. (2016) (bottom).

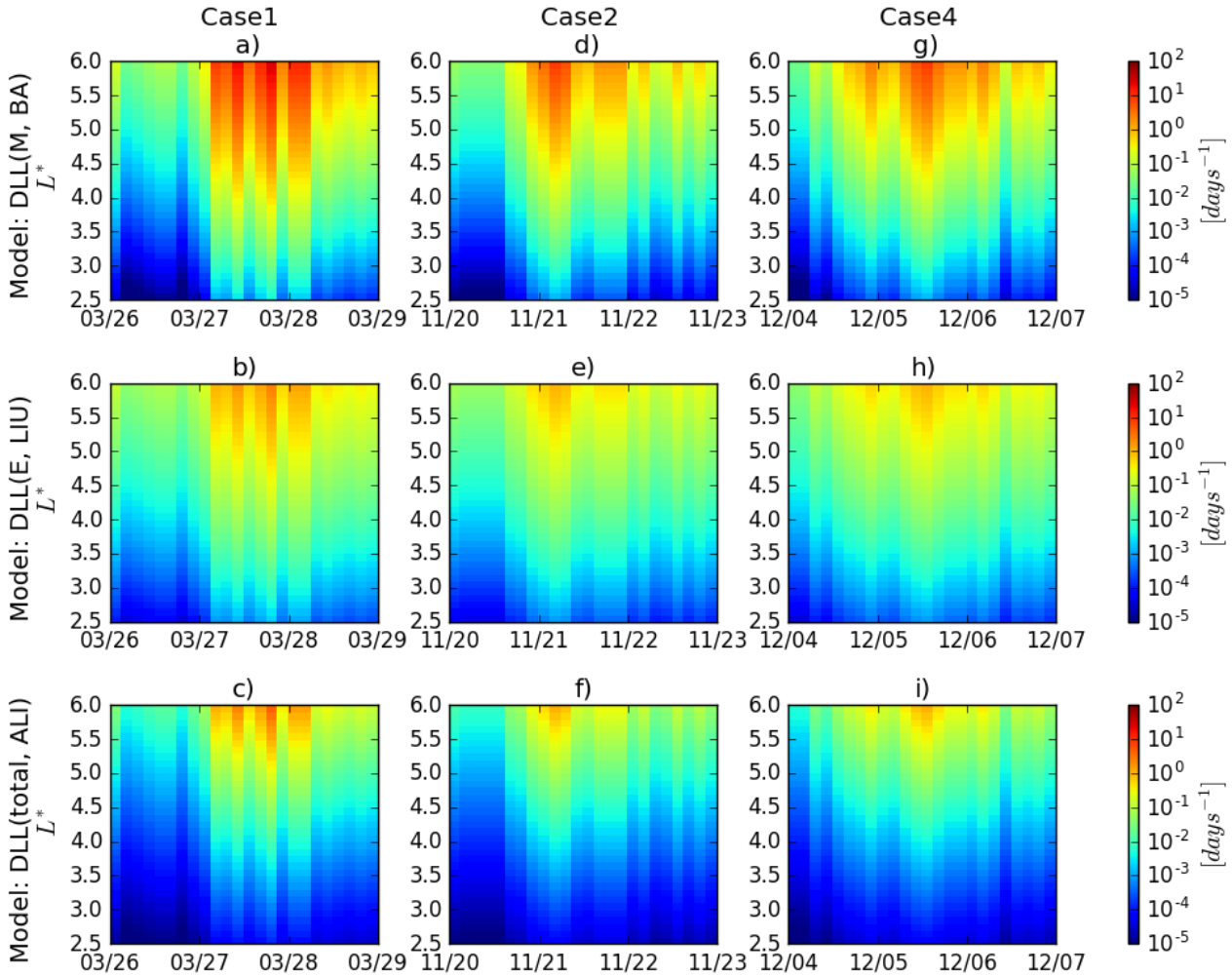

$D_{LL}^{E,LIU}$ from panels (b), (e), and (g) was computed for $\mu = 700$ MeV/G. The storm main phases occur at $4-15$ UT on 03/27 (case 1, a-c), at $0-7$ UT on 11/21 (case 2, d-f), and at $17-21$ UT on 12/04 (case 4, g-i).

SOURCE: Produced by the author.

Figure 6.10 shows all the empirical D_{LL} maps tested among the three events. The results from these three models also confirm that case 1 was the most active for radial diffusion during storm time, and cases 2 and 4 got similar distributions of enhanced D_{LL} coefficients. The models estimate enhanced $D_{LL} \gtrsim 10^0$ [1/day], which pene-

trates down to $4 \leq L^* < 5.5$ in these events. It will be evaluated hereafter how these properties in empirical D_{LL} may explain the extent of the dropouts investigated.

6.3 Results of the simulated PhSD

6.3.1 Case study 1

The results of the phase space densities simulated for the D_{LL}^{MHD} of case 1 ($\mu = 700$ MeV/G) are shown in Figure 6.11(b), for the interval between 18 UT-03/26 and 6 UT-03/28. In this run, only hiss loss inside L_{PP} and magnetopause shadowing losses outside the LCDS have been considered. The same figure shows the Van Allen Probes data (panel (a)) and the corresponding error of the simulated values in panel (c), defined by the ratio $PhSD_{MODEL}/PhSD_{RBSP}$. In this calculation, $PhSD_{MODEL}$ is interpolated to the L^* location of each Van Allen Probe. It can be seen in (b) that the model is capable of accurately reproducing the timing of dropouts and enhancements, showing that the PhSD variations at geosynchronous orbit have a great control on low-L^* PhSD distributions, through radial diffusion (e.g., Brautigam and Albert (2000)). However, the model is not fully capable of accounting for all the losses down to $L^* = 4$, which explains the increase of the ratios (relative error) to ~ 5 or more around this region on 03/27 (panel (c)). Subsequently, the ratios are reduced to $\sim 10^{-1}$, indicating an underestimation of the enhancements.

Still in Figure 6.11(c), it can be noted that the ratios at $L^* < 4$ are those that increased the most, reaching ~ 10 since the start of the dropouts on 03/27. Such an overestimation in PhSD within this region is a limitation of the model, related to the cumulative effect of D_{LL} over time. The analysis of ratios within this region is discarded, focusing on the results from $4 \leq L^* \leq 6$. Specifically for these plots, the effect of enhanced atmospheric loss by hiss in the storm main phase will not be represented, since L_{PP} of the three cases is eroded to below $L^* = 4$ in this period.

Figure 6.11 - Case 1: Comparison between observed and simulated PhSD distributions.

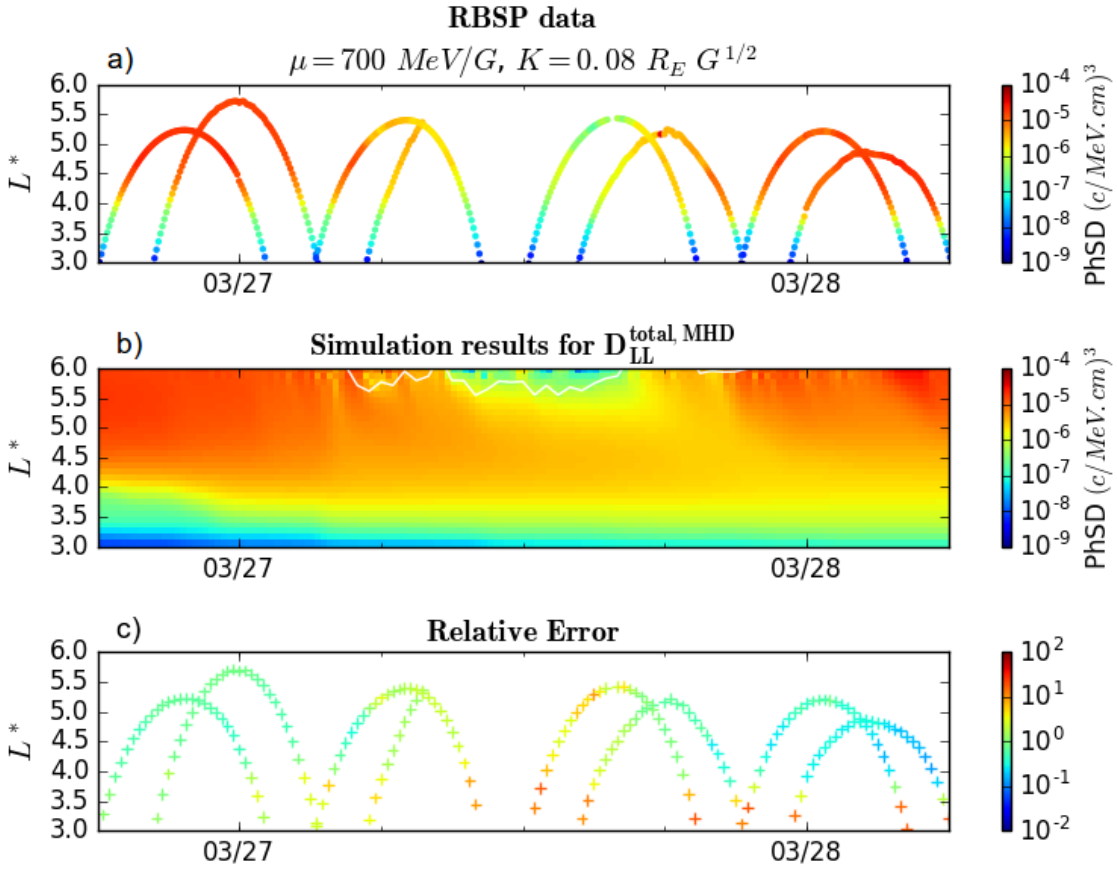

(a) Observed PhSD distributions of RBSP-A and RBSP-B as a function of time and L^*; (b) map of the simulated PhSD distributions using D_{LL}^{MHD} as input and hiss loss inside L_{PP}, but without chorus loss outside L_{PP} added (the LCDS data are overplotted in white); and (c) the corresponding relative error of these simulated values along the probes' L^*.

SOURCE: Produced by the author.

Figure 6.12 presents graphs of relative errors of all four simulation results obtained for case 1, including those from MHD and from runs using the three empirical D_{LL} models. The ratios calculated from the PhSD data of RBSP-A are shown in the top panels (a-b), and the ratios relative to the PhSD data of RBSP-B are shown in the bottom panels (c-d). The L^* location of the respective probe is also plotted in these panels. In addition, panels (a) and (c) contain the results of runs that do not consider chorus loss outside L_{PP}, while panels (b) and (d) show ratios that do consider chorus loss outside L_{PP}.

Figure 6.12 - Case 1: Analysis of relative errors in the simulated PhSD distributions (μ = 700 MeV/G and $K = 0.08\ R_E G^{1/2}$) of the four radial diffusion models, with and without chorus loss considered outside L_{PP}.

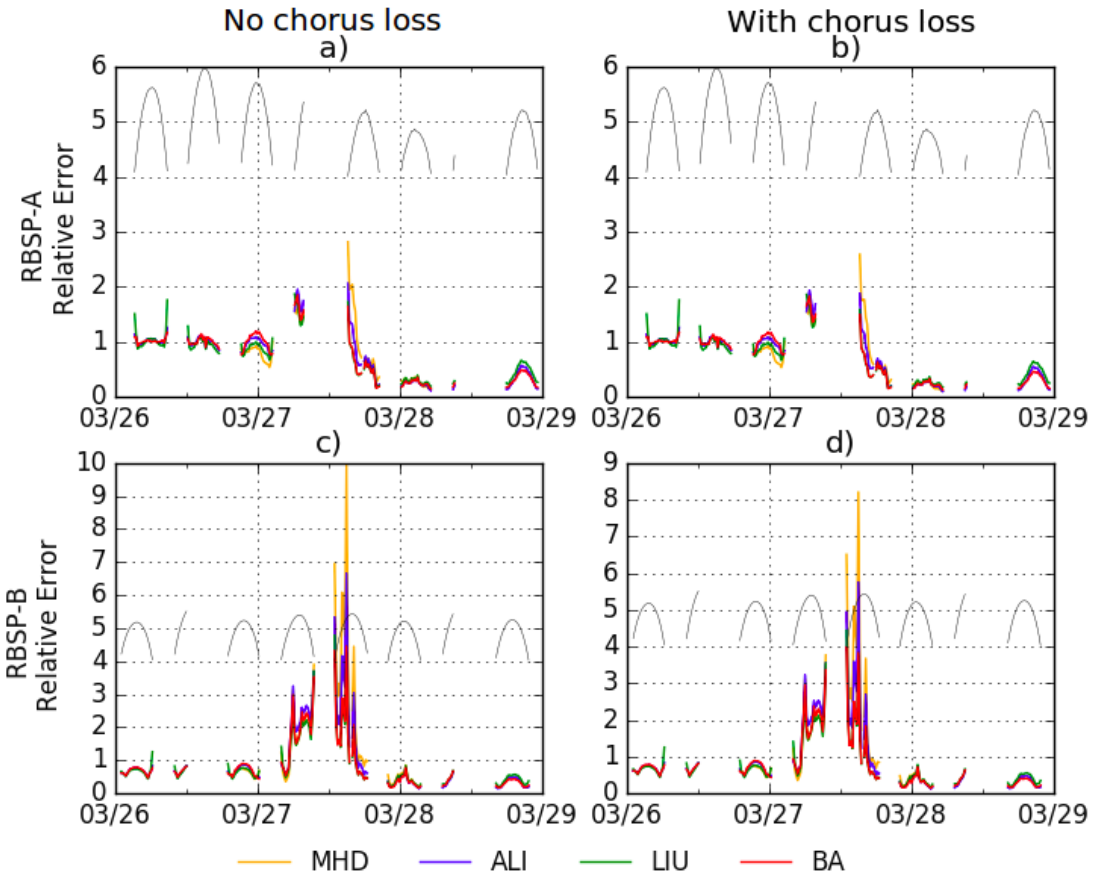

(a-b) Ratios relative to RBSP-A PhSD distributions and respective L^* of calculations (a) not considering chorus loss and (b) considering chorus loss outside L_{PP}; (c-d) Ratios relative to RBSP-B PhSD distributions and respective L^* of calculations (c) not considering chorus loss and (d) considering chorus loss outside L_{PP}. Empirical D_{LL} models: ALI (Ali et al. (2016)), LIU (Liu et al. (2016)), and BA (Brautigam and Albert (2000)).

SOURCE: Produced by the author.

Despite the gap in L^* affecting RBSP-A PhSD distributions on 03/27, it is noticed in the results that do not consider chorus loss simulated in Figure 6.12(c) that the run with D_{LL}^{MHD} can overestimate PhSD during the dropout by up to a factor of 10 in case 1, as verified with RBSP-B. Apart from this interval on 03/27 with the largest error in $L^* \sim 5$ of all D_{LL} inputs (panel (c), after 12 UT), the different results in panels (a) and (c) similarly show dropout-related overestimation in PhSD

by ratios that do not exceed 4. The panels (b) and (d) of this figure indicate that the inclusion of chorus loss reduced the error for dropouts modeled with D_{LL}^{MHD} on 03/27 to a maximum factor of ~ 8, as seen in (d). The results from the empirical D_{LL} models show little change in the relative errors of the same period. From the end of 03/27 until 03/29, the ratios in all panels become smaller than 1, indicating that the enhancements are underestimated by the models and do not appear to be affected by the inclusion of chorus loss, as shown in the panels (b) and (d).

6.3.2 Case study 2

The simulated phase space densities in Figure 6.13(b) were run with D_{LL}^{MHD} from case 2 ($\mu = 700$ MeV/G) in the interval of 12 UT-11/20 to 0 UT-11/22. The loss term included is due only to pitch angle scattering by hiss inside L_{PP}, of minima at $L^* = 3.5$. It was previously shown in Figure 6.9(c) that the LCDS does not reach $Lmax = 6$ during this event, so that magnetopause shadowing losses are not expected for the runs related to case 2. Comparing the panels (a-b) of this figure, it can be seen that the model is generally accurate to reproduce dropouts and enhancements in the L^* shells covered by the Van Allen Probes. In panel (c), the low-amplitude ratios below ~ 5 over this interval reveal that the model was more accurate to represent the storm-time PhSD measured by the Van Allen Probes than for case 1 (compare to Figure 6.11(c)).

It should be reminded that this is the event in which the dropout mainly involved external drift shells, but that reached down to $L^* \sim 4.5$ on 11/21, as observed in Figure 6.13(a). However, the model propagated losses only up to $L^* = 5.5$ (see panel (b)). This is the reason for the minor overestimation in PhSD around the region between ($4.5 \leq L^* \leq 5$) of RBSP-A and RBSP-B passes on 11/21 - panel (c). In addition, the overestimations in $L^* < 3.5$ are related to the limitation of the model reported in case 1.

Figure 6.13 - Case 2: Comparison between observed and simulated PhSD distributions.

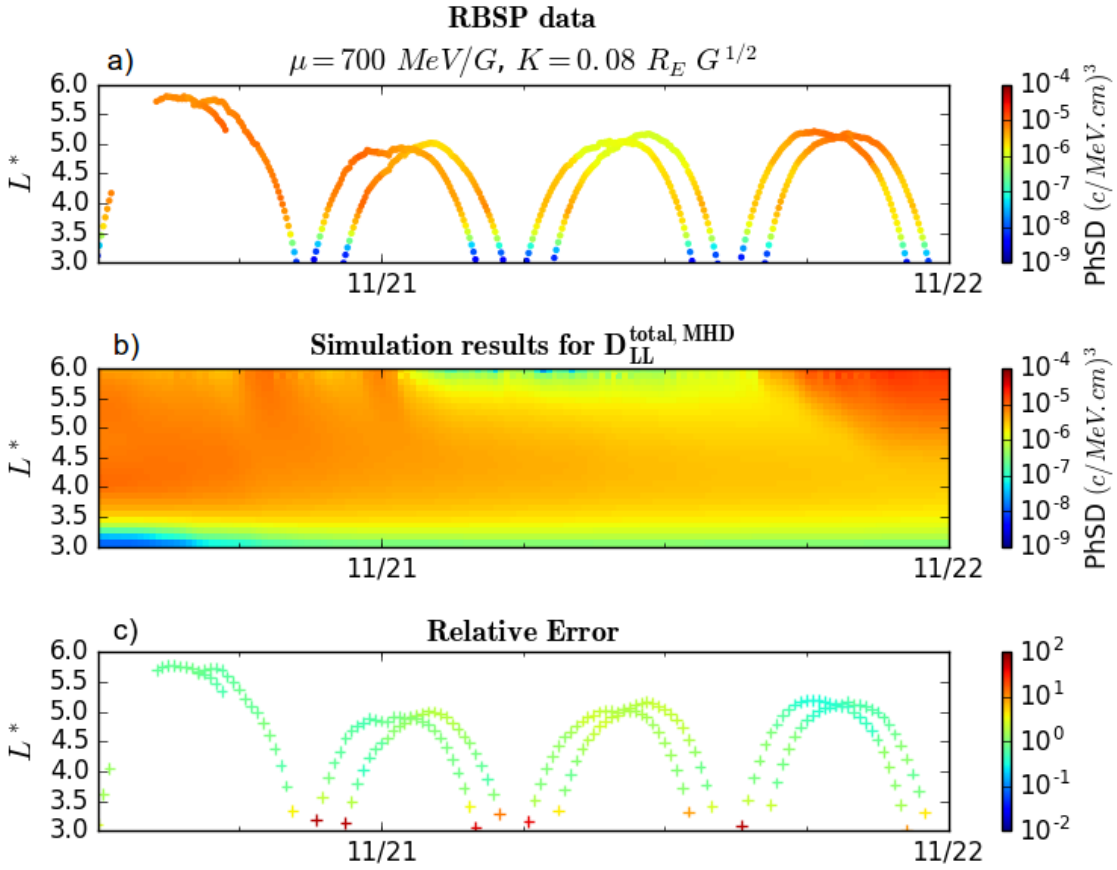

Same as in Figure 6.11.

SOURCE: Produced by the author.

The results of the relative errors represented in Figure 6.14(a-d) corroborate the previous analysis. They show that the errors in measured PhSD are very small for the four radial diffusion models, with ratios not exceeding 2.5. Slightly increased ratios in all models refer to the period of the dropout on 11/21 (see $\sim$ 12 UT in the panels). The results of panels (b) and (d) demonstrate that the loss term due to modeled electron lifetimes of a few days driven by chorus (shown in Figure 6.8(d)) did not produce any substantial effect for the PhSD distributions of this case.

Figure 6.14 - Case 2: Analysis of relative errors in the simulated PhSD distributions (μ = 700 MeV/G and $K = 0.08\ R_E G^{1/2}$) of the four radial diffusion models, with and without chorus loss considered outside L_{PP}.

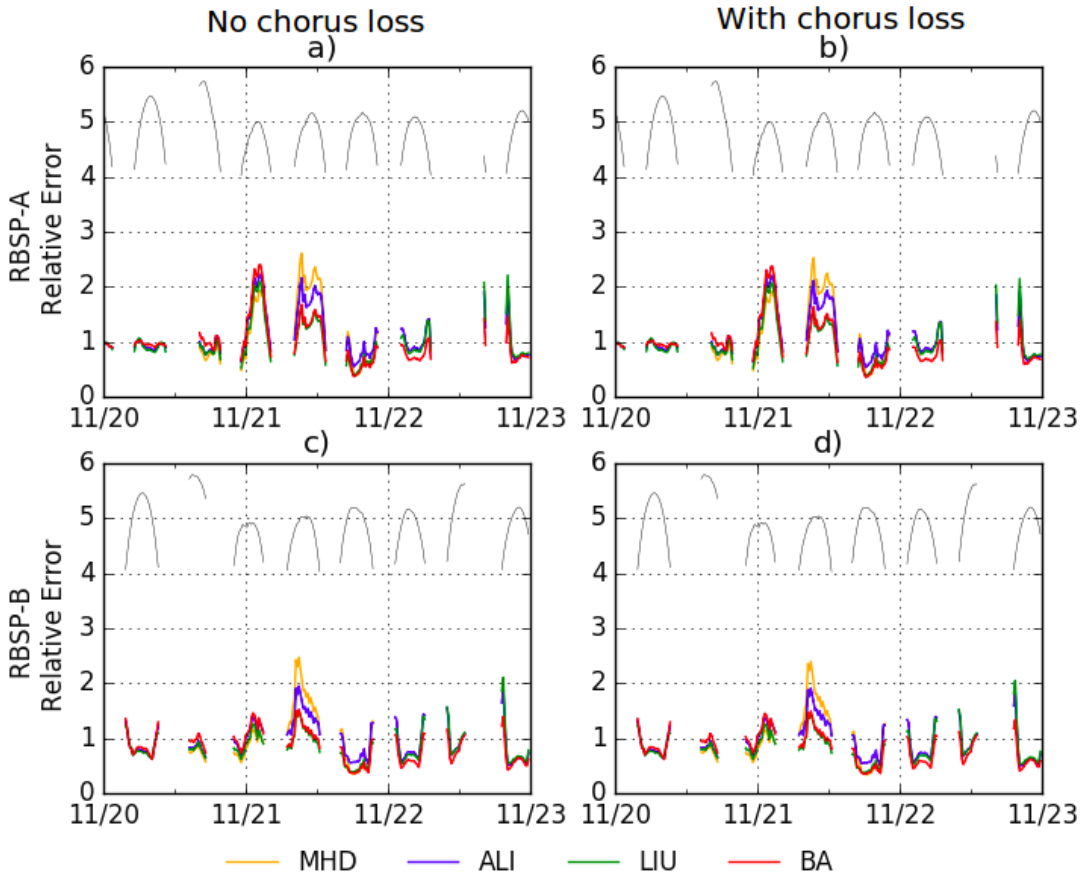

Same as in Figure 6.12.

SOURCE: Produced by the author.

6.3.3 Case study 4

Figure 6.15 shows the simulation results of case 4. The radial diffusion simulation was run using the statistical D_{LL} from Ali et al. (2016) as input, which allowed evaluating the full interval from 0 UT-12/04 to 0 UT-12/07. Such as the measured PhSD data shown in (a), the modeled PhSD distributions in (b) start at low levels throughout the outer belt on 12/04, mainly within $L^* = 5.5$. Around 17 UT-12/05, losses are reproduced above the modeled LCDS (panel (b)), but they are too mild compared to the major dropout observed in (a) that reaches $L^* \sim 4$. Because of

this, the relative errors within this period suddenly increase by factors above ~ 50 (see panel (c)). Later in panel (b), the enhancements to above prestorm values are reproduced up to $L^* \sim 4.5$, although the model propagates them down to $L^* = 4$ on 12/06. This causes the PhSD to be overestimated approaching $L^* = 4$, as observed in (c). Still in panel (c), it can be seen that the ratios from $L^* \sim 3.5$ are close to 1, but below this region the ratios peak again due to the limitation of the model to simulate PhSD in such lower L^* shells.

Figure 6.15 - Case 4: Comparison between observed and simulated PhSD distributions.

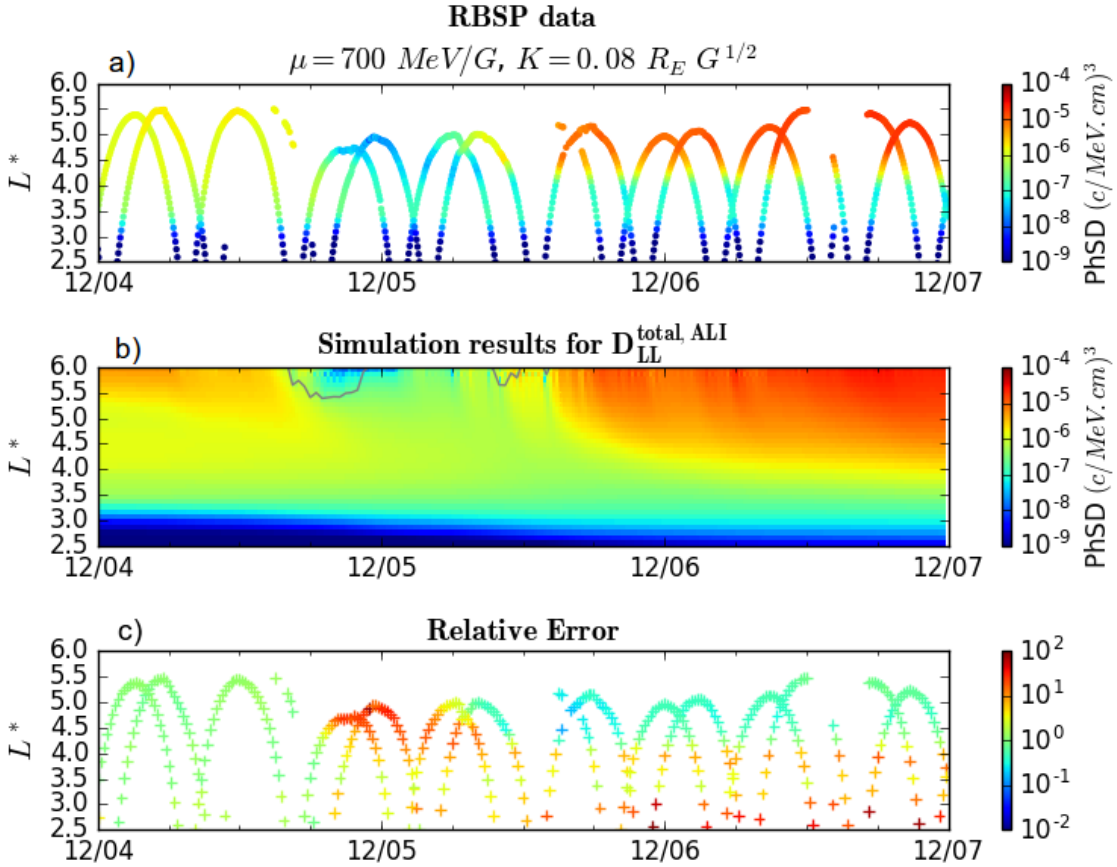

(a) Observed PhSD distributions of RBSP-A and RBSP-B as a function of time and L^*; (b) map of the simulated PhSD distributions using empirical D_{LL} from Ali et al. (2016) as input, as well as hiss loss inside L_{PP}, but without adding chorus loss outside L_{PP}. The LCDS data are overplotted in gray; and (c) corresponding relative error of these simulated values presented along the probes L^*.

SOURCE: Produced by the author.

Figure 6.16 - Case 4: Analysis of relative errors in the simulated PhSD distributions (μ = 700 MeV/G and $K = 0.08\ R_E G^{1/2}$) of the three radial diffusion models, with and without chorus loss considered outside L_{PP}.

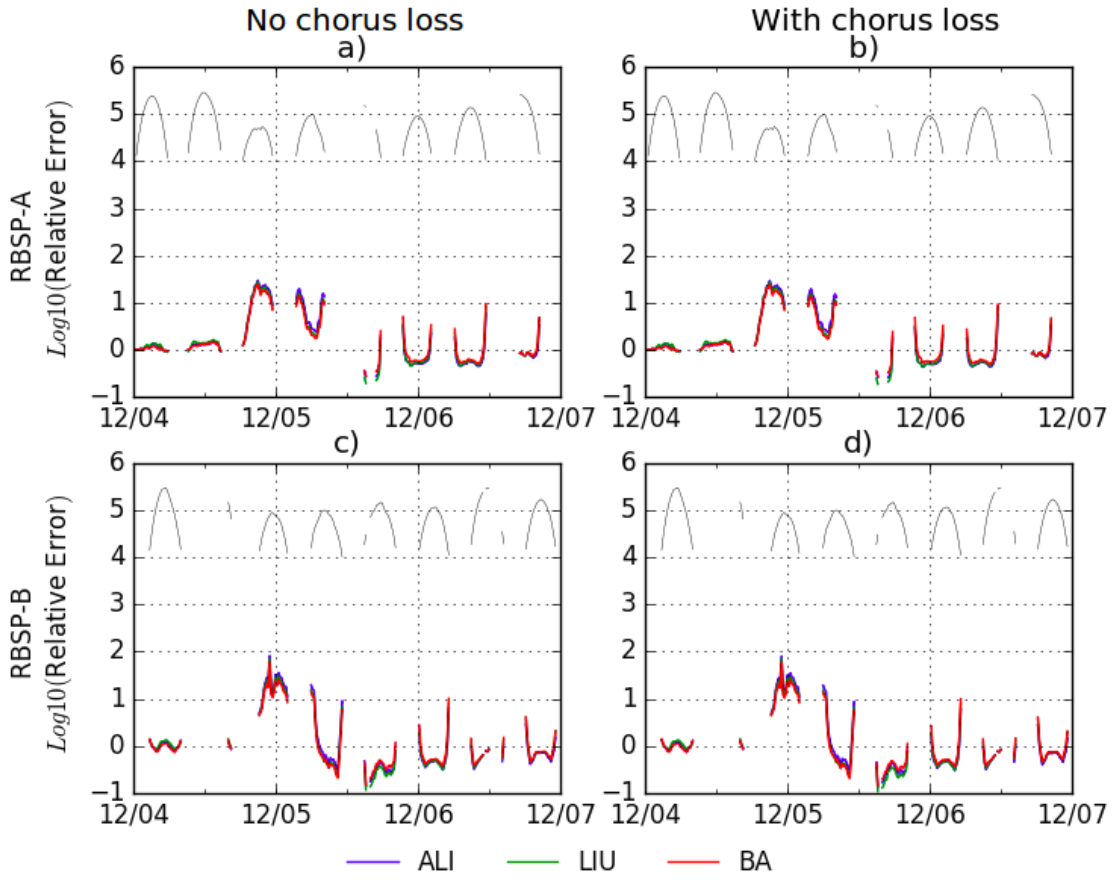

Same as in Figure 6.12.

SOURCE: Produced by the author.

Figure 6.16 shows the temporal distribution of the relative errors in the range of $4 \leq L^* \leq 6$ (in logarithmic scale), obtained from the results in PhSD, in addition to those simulated with the D_{LL} models of Brautigam and Albert (2000) and Liu et al. (2016). It can be noted that the models are equivalent to reproduce the storm-time PhSD data of RBSP-A and RBSP-B, as quantified by the ratios presented. Furthermore, it can be seen in these graphs that the ratios are higher during the dropout, after 12 UT-12/05 until $\sim$ 12 UT-12/06. As an example, RBSP-B ratios reach a maximum of almost 100 at $\sim$ 0 UT-12/05 (panels (c-d)). These elevated errors at first increase with L^* at $L^* \leq 5$, which can also be seen in RBSP-A ratios

(panels (a-b)). However, the errors then decrease with increasing L^* within the same region, which implies an overestimation of PhSD in lower L^* by factors of around 10. Thereafter, from 12/05 to 12/07, the ratios remain in these values in response to overestimation during the PhSD enhancements, as discussed for Figure 6.15. There is a short period after 12 UT-12/05 (Figure 6.16(a-d)) that shows ratios as low as 10^{-1}, indicating an underestimation of the PhSD at the beginning of its recovery. Finally, the chorus loss outside L_{PP} again has no meaningful effect on PhSD during a less active event in terms of the Kp index (e.g., Figure 5.5).

6.4 Discussions

The calibration technique applied to GOES-15 PhSD data using extrapolated electron fluxes in three case studies allowed to evaluate, by means of radial diffusion simulation, the dynamics of relativistic outer belt electrons ($E < 2$ MeV) with the first invariant up to $\mu = 700$ MeV/G. Specifically, case 1 is the event with the strongest and deepest flux dropout dynamics compared to the dropout in case 2, as it can be seen with REPT electron fluxes at 1.8 MeV and $\alpha = 90°$ (Figures 4.1(a) and 4.2(a)). Both dropouts are related to CIR passages with solar wind bulk speed, density and dynamic pressure varying at similar maximum values (Figure 4.3, panels (c), (d), and (f), respectively). The results of the magnetopause subsolar location, calculated with the empirical model of Shue et al. (1998) and MHD simulations, also showed similar values for the two events for the extension of the magnetopause compression to $\sim 7R_E$ or above (Figure 4.7). However, the analysis of the event-specific LCDS at $K = 0.08\ R_E G^{1/2}$ was determinant to distinguish the extent of magnetopause shadowing losses for near-equatorially mirroring electrons in both cases (Figure 6.9(a-b)). It was found that in case 1 the LCDS decreases up to $L^* \sim 5.5$ during the storm main phase, while the minimum LCDS value in case 2 does not reach $L^* = 6$ in the same phase. In case 4, the main phase dropout is concomitant with the time that the LCDS reaches $L^* < 5.5$ (Figure 6.9(c)).

These results are consistent with the scenario presented by Olifer et al. (2018) in which the LCDS is found much closer to the outer radiation belt than predicted by models of the magnetopause standoff distance, inducing rapid losses that reach $L = 4 - 5$ through outward radial diffusion mediated by ULF waves. These same authors showed evidence of rapid losses during four moderate to intense magnetic storms, on timescales of up to ~ 2 hours. It was found that such events had excursions of the LCDS to $L^* < 5$ that were highly correlated with flux dropouts observed at the GPS orbit ($L^* \gtrsim 4$). Xiang et al. (2018) investigated the depen-

dence of these loss processes on μ, K and L^* in a statistical study. They found that outward radial diffusion combined with magnetopause shadowing generates larger dropouts than EMIC wave scattering at $L^* > 4.5$, and also cover a wider range of μ and K populations compared to lower L^* shells, including our chosen value of $\mu = 700$ MeV/G. Moreover, many numerical studies have also attempted to model magnetopause shadowing losses and outward diffusion having the LCDS as a constraint and successfully shed light on the role of these mechanisms in radiation belt dropouts (FEI et al., 2006; YU et al., 2013; CASTILLO et al., 2019; TU et al., 2019).

Regarding the radial diffusion simulations carried out here for the three case studies, it was obtained that the simulations resolved dropouts and enhancements in the outer belt consistently with observations along the Van Allen Probes' trajectories, although case 4 is the event with least accurate results for the dropouts. In this case, the radial diffusion runs using the empirical D_{LL} models of Brautigam and Albert (2000), Liu et al. (2016) and Ali et al. (2016), and a variable outer boundary condition fixed at $Lmax = 6$, only reproduced the magnetopause shadowing losses defined above the LCDS, as seen in Figure 6.15(b). Consequently, the effect of outward radial diffusion that drives losses inside the geosynchronous orbit was not enough to model the dynamics of this dropout both outside and inside $L^* = 4$. This limitation was quantified by the significant relative errors of up to 100 in both Van Allen Probes' PhSD observations, occurring especially during the shadowing loss at the end of 12/04 (Figure 6.16). It was found that the time distribution of these errors is notably equivalent among the three D_{LL} models, which were shown to be all moderately accurate (i.e., $R^2 \sim 0.70$) to reproduce features of the storm-time D_{LL}^{OBS}.

Figure 6.17 is introduced to explain the origin of the major errors in the simulated PhSD distributions under dropout for case 4. It is convenient to separate the analysis of this figure in two intervals spanning the dropout dynamics: interval (1) from 18 UT-12/04 to 0 UT-12/05, and interval (2) from 0 to 6 UT-12/05. The color-coded data fixed at $L^* = 6$ represent the outer boundary conditions built on the calibrated PhSD data of GOES-15 at $\mu = 700$ MeV/G, used in all radial diffusion runs of case 4. The gray curve shows the actual L^* values of GOES-15. Below this curve are measurements from the Van Allen Probes A and B. Thus, the interval (1) marks the period of the main phase dropout, from 17 to 21 UT (12/04), as shown in the PhSD data of the three probes (RBSP-A, RBSP-B, and GOES-15 (see at $L^* = 6$)). During this interval, the real-time L^* value of GOES-15 drops to below 5. Hence, it seems unrealistic to make the approximation $L^* = 6$ for the GOES-15's L^* during this

period, which may be the explanation for the high overestimation of PhSD under the magnetopause shadowing losses shown in Figure 6.15(c). That is, by setting the instantaneous PhSD of GOES-15 measured as further as $L^* = 4.9$ at $L^* = 6$, a much faster D_{LL} model than those tested would be necessary to propagate the losses inwards so that they could reach $L^* \sim 4.9$ or less, which is where both Van Allen Probes stand.

Figure 6.17 - Concurrent observations during case 4 of PhSD ($\mu = 700$ MeV/G, $K = 0.08\ R_E G^{1/2}$) from the Van Allen Probes along their L^* locations, and from GOES-15 fixed at the outer boundary ($Lmax = 6$), together with the actual curve (gray) of L^* values at the geosynchronous orbit.

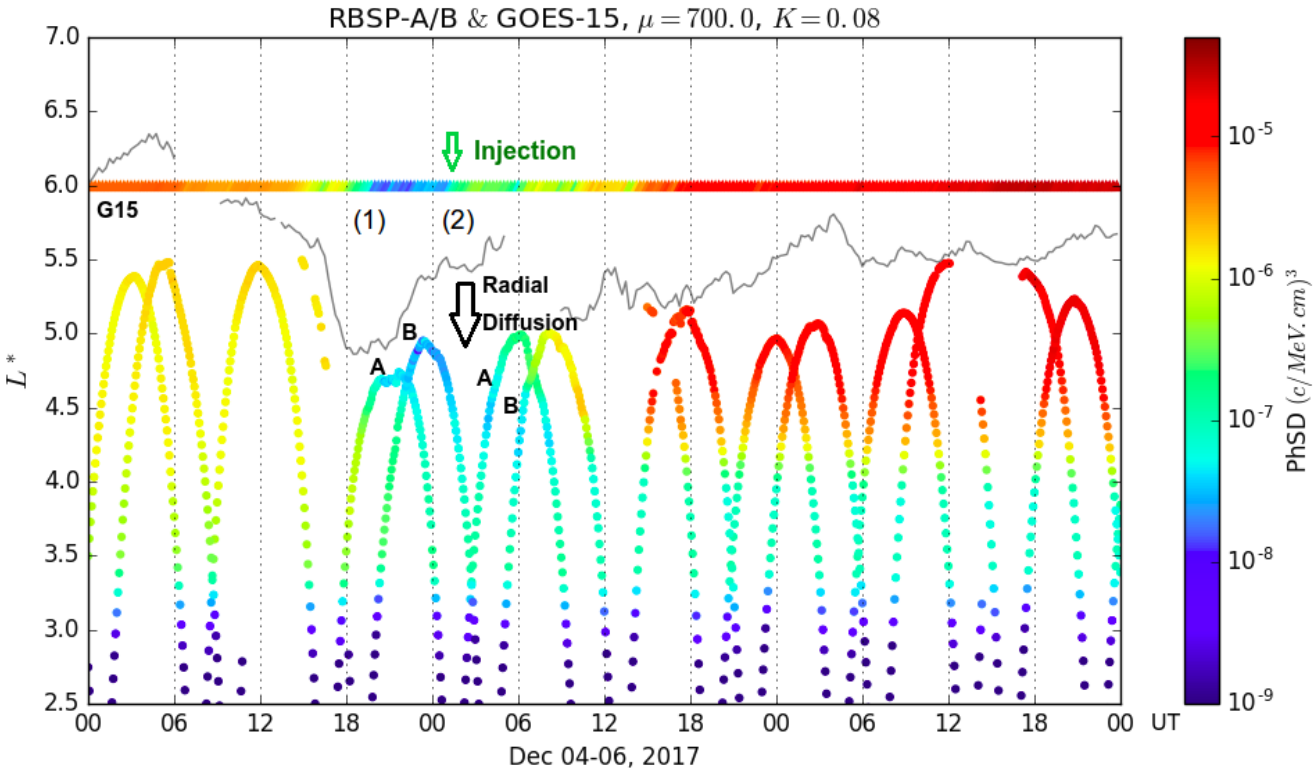

Interval (1): The L^* value at GOES-15 (in gray) drops to 4.9, so the approximation for the outer boundary fixed at $L^* = 6$ may not be valid to model the dropout. Interval (2): Energetic electron injections start at $\sim$ 1 UT on December 5, giving rise to an external source of PhSD at the outer boundary. The radial diffusion models simulate enhancements in PhSD down to $L^* = 4 - 4.5$ as a result of inward diffusion (see during $0 - 6$ UT on 12/05 in Figure 6.15(b)). Both described mechanisms operated to highly overestimate the simulated phase space densities during the dropout dynamics of case 4 seen by the Van Allen Probes A and B.

SOURCE: Produced by the author.

On the other hand, the interval (2) from 0 to 6 UT (12/05) in Figure 6.17 highlights the effect of substorm injections in the dropout simulation. The green arrow indicates the onset time ($\sim$ 1 UT) of energetic electron injections from a source in the plasma sheet (e.g., Turner et al. (2014)), identified with the PhSD observations of Figure 6.7(c). Note in Figure 6.17 that during interval (2), the L^* of GOES-15 is recovering towards $L^* \sim 5.5$. The obvious consequence of the injections for radial diffusion runs is the generation of an external source in the relativistic electron PhSD set at the outer boundary. As a result, the studied radial diffusion models acted as an acceleration mechanism in such a way that the PhSD enhancements were driven inward, as indicated by the black arrow. Meanwhile, the Van Allen Probes detectors still measured dropouts in this period, as seen through the inbound pass of RBSP-B. Subsequently, RBSP-A outbound starting at $\sim$ 3 UT remained observing dropouts until it reached $L^* \sim 4.8$, where the probe measured an enhancement in PhSD, likely driven inward via radial diffusion or locally activated by wave-particle interactions (e.g., with VLF chorus waves (BAKER et al., 2018; BOYD et al., 2018)). Thus, it will be assumed in this work that during interval (2) the inward radial diffusion, associated with a source in the outer boundary from the substorm injections at the geosynchronous orbit, caused an overestimation of the simulated PhSD distributions at the Van Allen Probes orbit. As a consequence, the effects of the dropout actually measured by these probes were minimized.

Also, as the Van Allen Probes did not observe enhanced PhSD at lower L^* concomitant with the injections' onset time in Figure 6.17, it is interpreted that such substorm injections were localized and only produced enhancements of PhSD at the site to which GOES-15 was traveling. Figure 6.18 shows the location of RBSP-A, RBSP-B and GOES-15 in the SM X-Y plane during the interval (2) on 12/05. At that time, GOES-15 was orbiting the dusk sector (in red), while RBSP-A (blue) and RBSP-B (black) were mostly in the prenoon sector. Thus, at $\sim$ 1 UT the injections started to occur roughly on the dusk side. In the mean time, RBSP-B was slowly starting the inbound pass towards noon, but still far from the locus of the injections. RBSP-A moved faster through its perigee, and finally observed the recovery in PhSD due to the injections (discussed previously) when it passed by its apogee of larger L^*.

Figure 6.18 - Location in the SM equatorial plane of the Van Allen Probes and GOES-15 during interval (2) on December 5, 2017 - case 4.

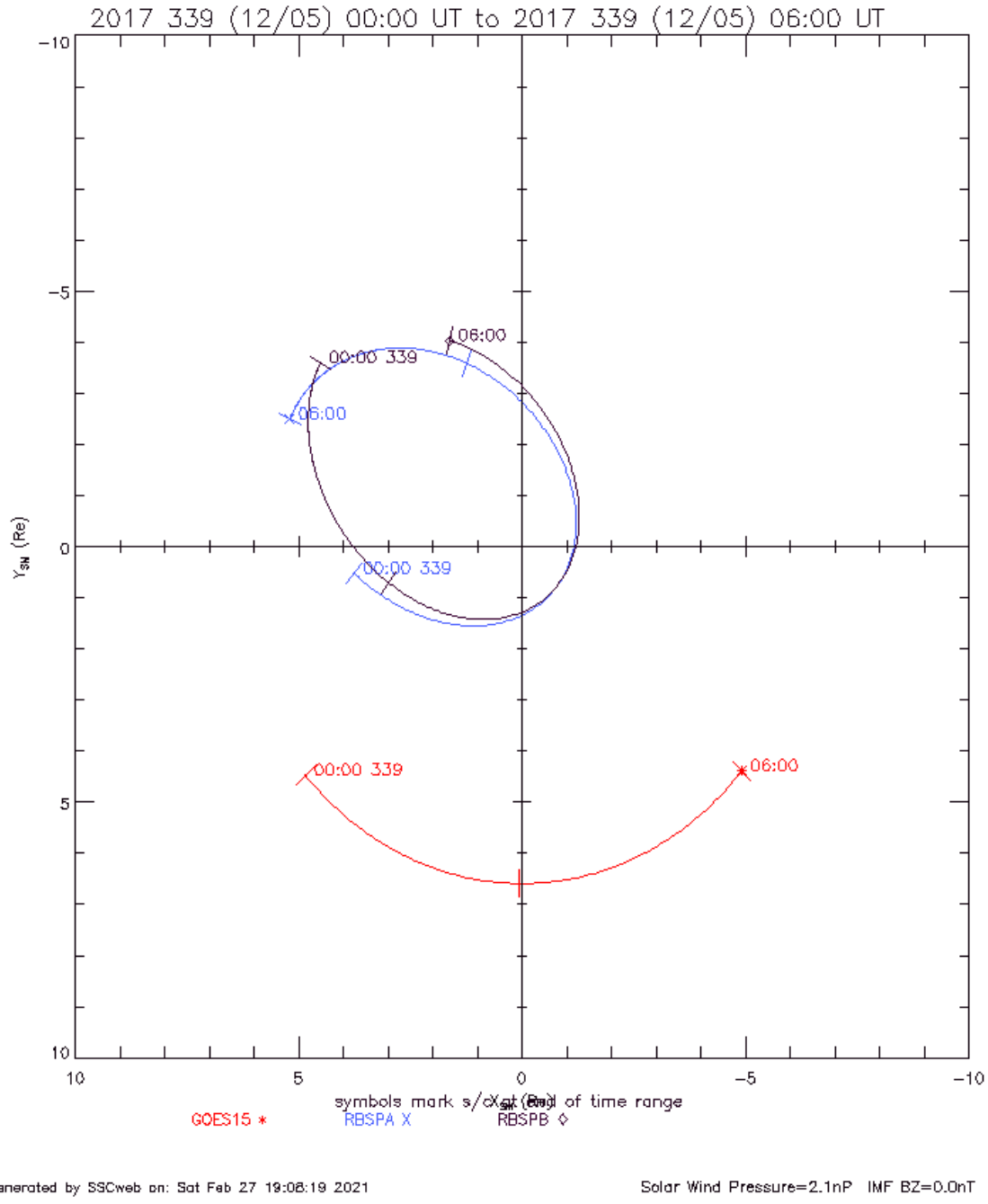

GOES-15 starts to see the injections at $\sim$ 1 UT on the dusk side. RBSP-A (blue) leads RBSP-B (black).

SOURCE: NASA/SPDF (2021).

Due to these issues that affect the simulation results of case 4, the proposal to model

this dropout and discuss the accuracy of the empirical D_{LL} models with storm-time D_{LL}^{OBS} could not be achieved. However, this case can be discussed considering the modeled enhancements, which reproduced the observations well down to $L^* = 4.5$ from the end of 12/05 ($\sim$ 21 UT) until 12/07, but only partially before 21 UT on 12/05 (see Figure 6.15). An additional source term due to local heating should be required to examine all sources of enhancements during this case (BRAUTIGAM; ALBERT, 2000; LI et al., 2014b).

Due to these limitations to study case 4, the focus from now on is to discuss the results obtained by modeling the distinct dropout patterns during the storm time of cases 1 and 2, based on physical quantification of D_{LL}. Considering ULF wave-driven radial diffusion, this thesis demonstrated that case 1 was more active than case 2 (e.g., pairs of Figures 4.9-4.10 and Figures 4.13-4.14). Thus, the radial diffusion simulations of case 1 (Figure 6.11(b)) and case 2 (Figure 6.13(b)) using event-specific D_{LL}^{MHD} and variable outer boundary condition at $Lmax = 6$ reproduced the main phase dropouts concurrent with the inward motion of the LCDS. As in case 2 the LCDS is above $Lmax = 6$ over the entire analyzed interval, the simulated dropouts were driven by losses at geosynchronous orbit propagated to low L^* through the storm-time D_{LL} (e.g., Brautigam and Albert (2000), Shprits et al. (2006)). The same effect produced additional losses by outward diffusion in case 1 through the large D_{LL} associated with this event.

On the other hand, RBSP-A and RBSP-B measured losses in PhSD as deep as $L^* = 4$ in case 1 (Figure 6.11(a)), while these losses reached $L^* \sim 5$ in case 2 (Figure 6.13(a)). Meanwhile, RBSP-B observed peaked storm-time D_{LL}^{OBS} at these depths (Figures 4.13(c) and 4.14(c)). However, both radial diffusion simulations overestimated the PhSD under dropout, around these respective regions, by factors up to 10 in case 1 (Figure 6.12) and up to 2.5 in case 2 (Figure 6.14). Considering that D_{LL}^{MHD} of case 1 underestimates D_{LL}^{OBS} from in-situ ULF waves by up to 3 orders of magnitude during the storm (Figure 4.15, right-bottom panel), within $L = 6$, it is likely that most of the error in PhSD simulated for this dropout is due to the amount of error contained in D_{LL}^{MHD}. In this case, smaller D_{LL} values modeled for the inner magnetosphere would produce less loss by outward diffusion at lower L^* shells, such as simulated with D_{LL}^{MHD}. Furthermore, the coefficients of determination (R^2) derived between D_{LL}^{MHD} and D_{LL}^{OBS} are equivalent to 0.319 for case 1 and 0.555 for case 2. Therefore, the error of the simulated PhSD distributions under dropout could be also interpreted in terms of the correspondence of D_{LL}^{MHD} with D_{LL}^{OBS}. It follows that the dropout of case 2 was better reproduced because its D_{LL}^{MHD} is

more accurate with D_{LL}^{OBS} than what happens between D_{LL}^{MHD} and D_{LL}^{OBS} of case 1. In support of this interpretation, it can be noted that the chorus loss modeled with Shprits et al. (2007) was too slow for these events, so that the correction in the simulation errors is fairly low (Figures 6.12 and 6.14). The simulation results obtained with the D_{LL} models of Brautigam and Albert (2000), Ali et al. (2016) and Liu et al. (2016), which proved to be equivalent in reproducing storm-time D_{LL}^{OBS}, confirm these findings for our cases 1 and 2.

In summary, the simulation results of the two cases indicate that magnetopause shadowing and outward radial diffusion are likely the main loss mechanisms for these dropouts, because EMIC-wave scattering (which is the other usual dominant loss mechanism for radiation belt electrons) is not expected to play a significant role in electron populations in the chosen μ and K regimes (e.g., Shprits et al. (2017), Xiang et al. (2018)). Consequently, although some level of inaccuracy of the simulated dropouts may arise from inaccurate electron lifetime parameterizations considered for the pitch angle scattering by whistler waves, it was demonstrated that the errors generated in PhSD under dropout are mainly related to errors in the modeled D_{LL}, either empirically or through global MHD. This result corroborates what was speculated by Murphy et al. (2016) and Olifer et al. (2019), who argued that accurately resolved storm-time D_{LL} should be required to properly model the outer radiation belt dynamics.

In this way, results of D_{LL}^{MHD} were shown to mainly underestimate D_{LL}^{OBS} through storm time, especially for case 1 (Figures 4.15 and 4.17). Validations of the MHD fields and the corresponding ULF wave power at the geosynchronous orbit and across several R_E demonstrated that underestimations in B_z, influencing underestimations of D_{LL}^{B} from MHD, have a source region on the nightside magnetosphere. It was speculated that the related substorm activity of the events could not be resolved in the time and spatial resolutions set for the MHD simulations. Conversely, underestimates of E_ϕ fluctuations generating underestimations in D_{LL}^{E} from MHD were either observed on the night side (case 1) and on the dayside (case 2). As discussed by Tu et al. (2012) to explain such underestimations in E_ϕ from MHD, the wave power in this field component may have been modeled at slightly different locations than the comparing probes' orbit, i.e., THEMIS or RBSP-B, since the same wave power is believed to be very localized.

In the case of empirical D_{LL} models based on Kp index, the more active geomagnetic conditions associated with greater in-situ ULF wave activity lead to a poor

representation of the storm-time D_{LL} coefficients, and vice versa, which explains why the dropout of case 2 with $Kp_{max} = 5^0$ is better simulated than the dropout of case 1 with $Kp_{max} = 6^+$. As suggested by Murphy et al. (2016), these more disturbed conditions induce a greater variability of storm-time diffusion rates with L shell, so that empirical models can underestimate or overestimate D_{LL} during the storm phases.

Another important limitation of the radial diffusion simulations to be considered in relation to the modeled dropouts is the time-dependent outer boundary condition made fixed at $Lmax = 6$, when in reality this condition should be also dynamic in L^*, according to the actual locations of GOES-15 (e.g., Li et al. (2014a)). This was critical to simulate the interval of the magnetopause shadowing loss in case 4, and likely during the same period in cases 1 and 2. It was observed in previous Figures 6.3, A.8, and A.9 that the GOES-15's L^* location highly changes from $L^* = 6$ throughout the storm phases in each case, especially in the main phase when it decreases $\sim 1R_E$, following the expansion of the drift shells. Perhaps, using the dynamic conditions derived from the calibrated PhSD of GOES-15 at its proper L^* values should reduce uncertainties in the modeled dropouts arising from the irregular mapping in L^* of these conditions, such as pointed out for interval (1) in case 4. In this situation, the outer boundary could be set at a larger $Lmax$ with a fixed condition that assumes the absence of outer belt electrons above the LCDS, for comparison with the current results obtained for $Lmax = 6$. The implementation of these new settings for the radial diffusion simulations will be a step forward in the analysis of these case studies.

7 CONCLUSIONS

This work investigated and quantified ULF wave-driven radial diffusion for flux dropouts of relativistic electrons (energies < 2 MeV) in the Earth's outer radiation belt during small to moderate magnetic storms of the descending phase of the solar cycle 24. Three cases were selected within the period $2016 - 2018$, for which flux dropouts in MeV energies were sampled from simultaneous observations of NASA's Van Allen Probes (RBSP-A and RBSP-B). Although two of these CIR events had very similar solar wind maximum parameters, one of them resulted in a stronger and deeper dropout (case 1) than the other event (case 2). It was also observed that the geomagnetic activity during the strongest dropout event specified by the Dst, AE and Kp indices, also exceeded those observed during the weakest dropout event. The main motivation of this thesis was then to resolve the dynamics in the inner magnetosphere that would have led so similar solar wind structures to drive distinct patterns of flux dropouts in the outer belt.

The MHD simulations carried out for these two cases allowed the calculation of analytical D_{LL} coefficients within the range $3 < L < 9$. In both cases, regardless of the μ analyzed, D_{LL}^{E} dominates the result of D_{LL}^{MHD} (total), especially when the modeled magnetopause is more compressed to $\sim 8R_E$. Most importantly, the intensities of D_{LL}^{MHD} are $1-2$ orders of magnitude higher in case 1 than in case 2 at $L > 6$ during storm time. Additionally, in-situ rates (D_{LL}^{OBS}) from ULF wave power observed by RBSP-B and THEMIS probes validated these results of D_{LL}^{MHD}, besides showing enhancements in the D_{LL} rates concomitant with both Van Allen Probes observations of the dropout at each event. As far as I know, this is a remarkable record because it has not yet been reported elsewhere. Previous works have commonly provided ULF wave observations to indirectly investigate the contribution of the outward radial diffusion mechanism in dropouts (e.g., Ukhorskiy et al. (2009) and Turner et al. (2012b)). On the other hand, in this work, in-situ radial diffusion coefficients were effectively quantified along the probes' trajectories, assuming $m = 1$ for the drift-resonance condition.

Using the TS04 magnetic field model of the magnetosphere, the magnetopause shadowing loss of trapped electrons with $K = 0.08\ R_E G^{1/2}$ was investigated for the two chosen events by computing the LCDS. The minimum LCDS observed was $0.5R_E$ deeper in case 1 than in case 2 during the storm main phase, which characterizes a greater effect of losses to the magnetopause in case 1. The radial diffusion simulations performed for both the cases were effective in reproducing this pattern during

the dropout intervals, enhanced by outward radial diffusion. Therefore, the observed losses to $L^* = 4$ were partially resolved by the simulation for case 1, while the losses to $L^* \sim 4.5$ were almost fully resolved in case 2. Based on the comparisons and correlation analysis between D_{LL}^{MHD} and D_{LL}^{OBS}, it was interpreted that uncertainties in D_{LL}^{MHD} are the main cause of uncertainties in the simulated dropouts, with case 1 being the most affected event. Other correlation analyses involving empirical D_{LL} models and D_{LL}^{OBS} results in two additional cases were also considered and demonstrated that this occurs because the empirical estimates based on the Kp index are less accurate during more active geomagnetic conditions, as observed in case 1.

Overall, the findings of this thesis on the role of storm-time radial diffusion for the dropout of relativistic electrons in the two studied cases are important because they apply to the scenario of small to moderate geomagnetic storms driven by CIRs, which is common to happen during the declining phase of solar cycles that lasts $\sim 2-3$ years. The simulation results indicate that the dropout dynamics of relativistic populations trapped near the magnetic equator are well represented by radial diffusion modeling and that scattering loss by whistler-mode chorus and hiss waves generally contributes less to main phase dropouts. Hence, it can be inferred that outer belt electrons under such conditions of trapping in the inner magnetosphere are mainly subjected to main phase dropouts driven by losses through the magnetopause during CIRs passages, as already recognized, for instance, by Morley et al. (2010) and Turner et al. (2012b). Besides, it is interesting to notice that small differences in the solar wind parameters within CIRs, at least in those that control the dynamic pressure ($D_p = (2/10^6) \cdot N \cdot V^2$), are capable of impacting the outer belt in a totally different manner in terms of dropouts. With due caution considering the limitation imposed by the small number of events analyzed here, the results of this study suggest that the proper quantification of D_{LL} and the behavior of the LCDS are fundamental and perhaps sufficient to describe the dropout dynamics in events related to CIRs, during the main phase of small to moderate geomagnetic storms. Obviously, similar analyses for a larger number of events will be necessary to prove this preliminary interpretation.

Based on the results of 1D simulation for the case studies associated with CIRs, the main conclusions of this thesis can be summarized as follows:

- Case 1 had deeper and stronger flux dropouts of relativistic electrons on 27 March 2017, dominated by magnetopause shadowing combined with outward radial diffusion, because of the greater inward motion of the LCDS

than in case 2 ($0.5R_E$ deeper) and associated intensification of D_{LL}^{MHD} throughout the storm time;

- Case 2 had comparatively minor flux dropouts of relativistic electrons on 21 November 2017, dominated by outward diffusion driven by losses at geosynchronous orbit;

- Case 4 had flux dropouts of relativistic electrons on $04-05$ December 2017, poorly determined with the radial diffusion runs due to (1) an unrealistic approximation of GOES-15's L^* at the outer boundary during the time of the main magnetopause shadowing losses and (2) effects of localized energetic electron injections in the dynamic condition of the outer boundary;

- Using modeled D_{LL} (either empirical or from MHD simulation) comparable to in-situ D_{LL}^{OBS} enhances the agreement of electron phase space densities in radial diffusion simulations with observed data. This is most easily achieved when handling events with less disturbed geomagnetic conditions;

- However, the performance of the D_{LL} empirical models by Brautigam and Albert (2000), Ali et al. (2016), and Liu et al. (2016) is found to be pretty much the same in reproducing the variability of in-situ D_{LL}^{OBS} of relativistic electrons in case studies, regardless of the geomagnetic conditions. As such, those models can be considered also equivalent to simulate phase space density distributions in the outer electron radiation belt.

The recommendations of this thesis for future work include:

- Explore the CIR events from the catalog (Table B.1) and, as a suggestion, to carry out a study focused on the role of loss mechanisms that lead to outer belt electron precipitation (not investigated here through observations), by taking advantage of the Van Allen Probes dataset and other recent missions.

- Make, for the radial diffusion simulation of events, a condition with GOES-15's calibrated PhSD also dynamic in L^* instead of inserting it fixed at $Lmax = 6$, and by having the outer boundary at a larger $Lmax$ value;

- Use the corrected electron fluxes available for MagEIS (in the Van Allen Probes) in order to obtain PhSD data less affected by background contam-

ination in the radiation zones. This will require the GOES-15's PhSD data to be recalibrated for use in new radial diffusion runs.

REFERENCES

AGAPITOV, O.; ARTEMYEV, A. V.; MOURENAS, D.; MOZER, F.; KRASNOSELSKIKH, V. Nonlinear local parallel acceleration of electrons through landau trapping by oblique whistler mode waves in the outer radiation belt. **Geophysical Research Letters**, v. 42, n. 23, p. 10–140, 2015. 32

AKASOFU, S. A review of the current understanding in the study of geomagnetic storms. **International Journal of Earth Sciences**, v. 4, n. 018, 2018. 63

ALBERT, J. Radial diffusion simulations of the 20 september 2007 radiation belt dropout. **Annales Geophysicae**, v. 32, n. 8, p. 925–934, 2014. 23

ALBERT, J. M.; SELESNICK, R.; MORLEY, S. K.; HENDERSON, M. G.; KELLERMAN, A. Calculation of last closed drift shells for the 2013 gem radiation belt challenge events. **Journal of Geophysical Research: Space Physics**, v. 123, n. 11, p. 9597–9611, 2018. 56

ALFVÉN, H. On the theory of magnetic storms and aurorae. **Tellus**, v. 10, n. 1, p. 104–116, 1958. 9

ALI, A. F.; MALASPINA, D. M.; ELKINGTON, S. R.; JAYNES, A. N.; CHAN, A. A.; WYGANT, J.; KLETZING, C. A. Electric and magnetic radial diffusion coefficients using the van allen probes data. **Journal of Geophysical Research: Space Physics**, v. 121, n. 10, p. 9586–9607, 2016. Available from: <https://agupubs.onlinelibrary.wiley.com/doi/abs/10.1002/2016JA023002>. xviii, 5, 36, 51, 55, 65, 88, 92, 93, 94, 105, 121, 123, 139, 140, 143, 146, 147, 150, 155, 159

ALVES, L. et al. Outer radiation belt dropout dynamics following the arrival of two interplanetary coronal mass ejections. **Geophysical Research Letters**, v. 43, n. 3, p. 978–987, 2016. 1, 33

ALVES, L. R.; SOUZA, V. M.; JAUER, P. R.; SILVA, L. A. da; MEDEIROS, C.; BRAGA, C. R.; ALVES, M. V.; KOGA, D.; MARCHEZI, J. P.; MENDONÇA, R. R. S. de; DALLAQUA, R. S.; BARBOSA, M. V. G.; ROCKENBACH, M.; LAGO, A. D.; MENDES, O.; VIEIRA, L. E. A.; BANIK, M.; SIBECK, D. G.; KANEKAL, S. G.; BAKER, D. N.; WYGANT, J. R.; KLETZING, C. A. The role of solar wind structures in the generation of ulf waves in the inner magnetosphere. **Solar Physics**, v. 292, n. 7, p. 92, Jun 2017. ISSN 1573-093X. Available from: <https://doi.org/10.1007/s11207-017-1113-4>. 19, 50, 69

ANDERSON, B. J. An overview of spacecraft observations of 10 s to 600 s period magnetic pulsations in the earth's magnetosphere. In: _____. **Solar wind sources of magnetospheric ultra-low-frequency waves**. American Geophysical Union (AGU), 1994. p. 25–43. ISBN 9781118663943. Available from: <https://agupubs.onlinelibrary.wiley.com/doi/abs/10.1029/GM081p0025>. 21, 22

AUSTER, H. U.; GLASSMEIER, K. H.; MAGNES, W.; AYDOGAR, O.; BAUMJOHANN, W.; CONSTANTINESCU, D.; FISCHER, D.; FORNACON, K. H.; GEORGESCU, E.; HARVEY, P.; HILLENMAIER, O.; KROTH, R.; LUDLAM, M.; NARITA, Y.; NAKAMURA, R.; OKRAFKA, K.; PLASCHKE, F.; RICHTER, I.; SCHWARZL, H.; STOLL, B.; VALAVANOGLOU, A.; WIEDEMANN, M. The themis fluxgate magnetometer. In: _____. **The THEMIS mission**. New York, NY: Springer, 2009. p. 235–264. ISBN 978-0-387-89820-9. Available from: <https://doi.org/10.1007/978-0-387-89820-9_11>. 37

BAKER, D. N.; ERICKSON, P.; FENNELL, J. F.; COSTER, J. C.; JAYNES, A. N.; VERRONEN, P. T. Space weather effects in the earth's radiation belts. **Space Science Reviews**, v. 214, n. 17, 2018. 12, 22, 31, 152

BAKER, D. N.; KANEKAL, S. G.; HOXIE, V. C.; BATISTE, S.; BOLTON, M.; LI, X.; ELKINGTON, S. R.; MONK, S.; REUKAUF, R.; STEG, S.; WESTFALL, J.; BELTING, C.; BOLTON, B.; BRAUN, D.; CERVELLI, B.; HUBBELL, K.; KIEN, M.; KNAPPMILLER, S.; WADE, S.; LAMPRECHT, B.; STEVENS, K.; WALLACE, J.; YEHLE, A.; SPENCE, H. E.; FRIEDEL, R. The relativistic electron-proton telescope (rept) instrument on board the radiation belt storm probes (rbsp) spacecraft: characterization of earth's radiation belt high-energy particle populations. **Space Science Reviews**, v. 179, n. 1, p. 337–381, Nov 2013. ISSN 1572-9672. Available from: <https://doi.org/10.1007/s11214-012-9950-9>. 40, 41

BAUMJOHANN, W.; TREUMANN, R. A. **Basic space plasma physics**. London: Imperial College Press, 1996. 8

BELCHER, J.; DAVIS, L. Large amplitude alfvén waves in the interplanetary medium. **Journal of Geophysical Research**, v. 76, p. 3534–3563, 1971. 38, 39

BITTENCOURT, J. A. **Fundamentals of plasma physics**. 3. ed. New York: Springer, 2004. 375 p. 16, 17

BLAKE, J. et al. The magnetic electron ion spectrometer (mageis) instruments aboard the radiation belt storm probes (rbsp) spacecraft. In: FOX, N.; BURCH, J. L. (Ed.). **The van allen probes mission**. [S.l.]: Springer, 2013. p. 383–421. 41

BONNELL, J.; MOZER, F.; DELORY, G.; HULL, A.; ERGUN, R.; CULLY, C.; ANGELOPOULOS, V.; HARVEY, P. The electric field instrument (efi) for themis. In: BURCH, J. L. (Ed.). **The THEMIS mission**. [S.l.: s.n.]. 37

BOSCHER, D.; BOURDARIE, S.; O'BRIEN, P.; GUILD, T. **IRBEM Library, version 4.4.0**. 2012. Available from: <http://sourceforge.net/projects/irbem/>. 46

BOYD, A.; REEVES, G.; SPENCE, H.; FUNSTEN, H.; LARSEN, B.; SKOUG, R.; BLAKE, J.; FENNELL, J.; CLAUDEPIERRE, S.; BAKER, D. et al. Rbsp-ect combined spin-averaged electron flux data product. **Journal of Geophysical Research: Space Physics**, v. 124, n. 11, p. 9124–9136, 2019. 41, 46

BOYD, A. J.; TURNER, D.; REEVES, G. D.; SPENCE, H.; BAKER, D.; BLAKE, J. What causes radiation belt enhancements: a survey of the van allen probes era. **Geophysical Research Letters**, v. 45, n. 11, p. 5253–5259, 2018. 30, 31, 152

BRAUTIGAM, D. H.; ALBERT, J. Radial diffusion analysis of outer radiation belt electrons during the october 9, 1990, magnetic storm. **Journal of Geophysical Research: Space Physics**, v. 105, n. A1, 2000. Available from: <https://doi.org/10.1029/1999JA900344>. xviii, 1, 3, 5, 25, 35, 55, 88, 91, 93, 105, 120, 121, 123, 139, 140, 141, 143, 148, 150, 154, 155, 159

CARPENTER, D. L.; ANDERSON, R. R. An isee/whistler model of equatorial electron density in the magnetosphere. **Journal of Geophysical Research: Space Physics**, v. 97, n. A2, p. 1097–1108, 1992. Available from: <https://agupubs.onlinelibrary.wiley.com/doi/abs/10.1029/91JA01548>. 12, 136

CASTILLO, A. M.; SHPRITS, Y. Y.; GANUSHKINA, N.; DROZDOV, A.; ASEEV, N.; WANG, D.; DUBYAGIN, S. Simulations of the inner magnetospheric energetic electrons using the imptam-verb coupled model. **Journal of Atmospheric and Solar-Terrestrial Physics**, v. 191, p. 105050, 2019. 42, 150

CHEN, Y.; FRIEDEL, R.; REEVES, G. Phase space density distributions of energetic electrons in the outer radiation belt during two geospace environment modeling inner magnetosphere/storms selected storms. **Journal of Geophysical Research: Space Physics**, v. 111, n. A11, 2006. 33

CHEN, Y.; FRIEDEL, R.; REEVES, G.; ONSAGER, T.; THOMSEN, M. Multisatellite determination of the relativistic electron phase space density at geosynchronous orbit: methodology and results during geomagnetically quiet times. **Journal of Geophysical Research: Space Physics**, v. 110, n. A10, 2005. 44

CLAUDEPIERRE, S. et al. A background correction algorithm for van allen probes mageis electron flux measurements. **Journal of Geophysical Research: Space Physics**, v. 120, n. 7, p. 5703–5727, 2015. 41

CRANK, J.; NICOLSON, P. A practical method for numerical evaluation of solutions of partial differential equations of the heat-conduction type. **Mathematical Proceedings of the Cambridge Philosophical Society**, v. 43, n. 1, p. 50–67, 1947. 53

CRUMLEY, J. P.; PALCZEWSKI, A. D.; KASTER, S. A. Examining the location of the magnetopause in an undergraduate lab. **arXiv preprint arXiv:0706.1985**, 2007. 72

DESSLER, A.; KARPLUS, R. Some effects of diamagnetic ring currents on van allen radiation. **Journal of Geophysical Research**, v. 66, n. 8, p. 2289–2295, 1961. 32

DIMITRAKOUDIS, S.; MANN, I. R.; BALASIS, G.; PAPADIMITRIOU, C.; ANASTASIADIS, A.; DAGLIS, I. A. Accurately specifying storm-time ulf wave radial diffusion in the radiation belts. **Geophysical Research Letters**, v. 42, n. 14, p. 5711–5718, 2015. Available from: <https://agupubs.onlinelibrary.wiley.com/doi/abs/10.1002/2015GL064707>. 35

DROZDOV, A. Y.; SHPRITS, Y. Y.; ORLOVA, K. G.; KELLERMAN, A. C.; SUBBOTIN, D. A.; BAKER, D. N.; SPENCE, H. E.; REEVES, G. D. Energetic, relativistic, and ultrarelativistic electrons: comparison of long-term verb code simulations with van allen probes measurements. **Journal of Geophysical Research: Space Physics**, v. 120, n. 5, p. 3574–3587, 2015. Available from: <https://agupubs.onlinelibrary.wiley.com/doi/abs/10.1002/2014JA020637>. 12

DUNGEY, J. W. Interplanetary magnetic field and the auroral zones. **Physical Review Letters**, v. 6, n. 2, p. 47, 1961. 10

_____. Hydromagnetic waves. In: MATSUSHITA, S.; CAMPBELL, W. H. (Ed.). **Physics of geomagnetic phenomena**. [S.l.]: Academic Press, 1967. 18, 51

EASTWOOD, J.; HIETALA, H.; TOTH, G.; PHAN, T.; FUJIMOTO, M. What controls the structure and dynamics of earth's magnetosphere? **Space Science Reviews**, v. 188, n. 1-4, p. 251–286, 2015. 9, 11

ELKINGTON, S. R. A review of ulf interactions with radiation belt electrons. In: **Magnetospheric ULF waves: synthesis and new directions**. [S.l.]: American Geophysical Union, 2006. Geophysical Monograph Series 169. 1, 20, 29, 30

ELKINGTON, S. R.; CHAN, A. A.; WILTBERGER, M. Global structure of ulf waves during the 24–26 september 1998 geomagnetic storm. In: _____. **Dynamics of the Earth's radiation belts and inner Magnetosphere**. American Geophysical Union (AGU), 2013. p. 127–138. ISBN 9781118704752. Available from: <https://agupubs.onlinelibrary.wiley.com/doi/abs/10.1029/2012GM001348>. 73

ELKINGTON, S. R.; HUDSON, M. K.; CHAN, A. A. Acceleration of relativistic electrons via drift-resonant interaction with toroidal-mode pc-5 ulf oscillations. **Geophysical Research Letters**, v. 26, n. 21, p. 3273–3276, 1999. 30

_____. Resonant acceleration and diffusion of outer zone electrons in an asymmetric geomagnetic field. **Journal of Geophysical Research: Space Physics**, v. 108, n. A3, 2003. 30

FALTHAMMAR, C.-G. Effects of time-dependent electric fields on geomagnetically trapped radiation. **Journal of Geophysical Research**, v. 70, n. 11, p. 2503–2516, 1965. 35, 49, 51

FEI, Y.; CHAN, A. A.; ELKINGTON, S. R.; WILTBERGER, M. J. Radial diffusion and mhd particle simulations of relativistic electron transport by ulf waves in the september 1998 storm. **Journal of Geophysical Research: Space Physics**, v. 111, n. A12, 2006. Available from: <https://agupubs.onlinelibrary.wiley.com/doi/abs/10.1029/2005JA011211>. 3, 4, 34, 35, 42, 49, 73, 76, 77, 79, 80, 150

FOK, M.-C. Current status of inner magnetosphere and radiation belt modeling. In: _____. **Dayside magnetosphere interactions**. American Geophysical Union (AGU), 2020. chapter 13, p. 231–242. ISBN 9781119509592. Available from: <https://agupubs.onlinelibrary.wiley.com/doi/abs/10.1002/9781119509592.ch13>. 25, 32, 69

FOK, M.-C.; BUZULUKOVA, N. Y.; CHEN, S.-H.; GLOCER, A.; NAGAI, T.; VALEK, P.; PEREZ, J. D. The comprehensive inner magnetosphere-ionosphere

model. **Journal of Geophysical Research: Space Physics**, v. 119, n. 9, p. 7522–7540, 2014. Available from: <https://agupubs.onlinelibrary.wiley.com/doi/abs/10.1002/2014JA020239>. 68

FUNSTEN, H.; SKOUG, R.; GUTHRIE, A.; MACDONALD, E.; BALDONADO, J.; HARPER, R.; HENDERSON, K.; KIHARA, K.; LAKE, J.; LARSEN, B. et al. Helium, oxygen, proton, and electron (hope) mass spectrometer for the radiation belt storm probes mission. **Space Science Reviews**, v. 179, n. 1-4, p. 423–484, 2013. 41

GANUSHKINA, N. Y.; LIEMOHN, M.; DUBYAGIN, S. Current systems in the earth's magnetosphere. **Reviews of Geophysics**, v. 56, n. 2, p. 309–332, 2018. 7, 8, 9, 14

GONZALEZ, W. D.; JOSELYN, J. A.; KAMIDE, Y.; KROEHL, H. W.; ROSTOKER, G.; TSURUTANI, B. T.; VASYLIUNAS, V. M. What is a geomagnetic storm? **Journal of Geophysical Research**, v. 99, n. A4, p. 5771–5792, 1994. 9, 10, 11, 109

GREEN, J. C.; KIVELSON, M. Relativistic electrons in the outer radiation belt: differentiating between acceleration mechanisms. **Journal of Geophysical Research: Space Physics**, v. 109, n. A3, 2004. 25, 30, 43

GREEN, J. C.; KIVELSON, M. G. A tale of two theories: How the adiabatic response and ulf waves affect relativistic electrons. **Journal of Geophysical Research: Space Physics**, v. 106, n. A11, p. 25777–25791, 2001. Available from: <https://agupubs.onlinelibrary.wiley.com/doi/abs/10.1029/2001JA000054>. 129

HANSER, F. A. **EPS/HEPAD calibration and data handbook**. [S.l.]: Assurance Technology Corporation. 42

HARTLEY, D.; DENTON, M. Solving the radiation belt riddle. **Astronomy & Geophysics**, v. 55, n. 6, p. 6–17, 2014. 43

HENDERSON, M.; MORLEY, S.; NIEHOF, J.; LARSEN, B. **LANLGeoMag: v1.5.16**. 2018. Available from: <drsteve/LanlGeoMagv1.5.16.https://doi.org/10.5281/zenodo.1195041>. 56

HUANG, C.-L.; SPENCE, H. E.; SINGER, H. J.; TSYGANENKO, N. A. A quantitative assessment of empirical magnetic field models at geosynchronous orbit

during magnetic storms. **Journal of Geophysical Research: Space Physics**, v. 113, n. A4, 2008. Available from: <https://agupubs.onlinelibrary.wiley.com/doi/abs/10.1029/2007JA012623>. 15

HUDSON, M. K.; BAKER, D. N.; GOLDSTEIN, J.; KRESS, B. T.; PARAL, J.; TOFFOLETTO, F. R.; WILTBERGER, M. Simulated magnetopause losses and van allen probe flux dropouts. **Geophysical Research Letters**, v. 41, n. 4, p. 1113–1118, 2014. Available from: <https://agupubs.onlinelibrary.wiley.com/doi/abs/10.1002/2014GL059222>. 1, 12, 33, 72

JACOBS, J.; KATO, Y.; MATSUSHITA, S.; TROITSKAYA, V. Classification of geomagnetic micropulsations. **Journal of Geophysical Research**, v. 69, n. 1, p. 180–181, 1964. 20

JAUER, P. R. et al. A global magnetohydrodynamic simulation study of ultra-low-frequency wave activity in the inner magnetosphere: corotating interaction region+ alfvénic fluctuations. **The Astrophysical Journal**, v. 886, n. 1, p. 59, 2019. 72

JAYNES, A.; LESSARD, M.; RODRIGUEZ, J.; DONOVAN, E.; LOTO'ANIU, T.; RYCHERT, K. Pulsating auroral electron flux modulations in the equatorial magnetosphere. **Journal of Geophysical Research: Space Physics**, v. 118, n. 8, p. 4884–4894, 2013. 42

JAYNES, A. N.; BAKER, D. N.; SINGER, H. J.; RODRIGUEZ, J. V.; LOTO'ANIU, T. M.; ALI, A. F.; ELKINGTON, S. R.; LI, X.; KANEKAL, S. G.; CLAUDEPIERRE, S. G.; FENNELL, J. F.; LI, W.; THORNE, R. M.; KLETZING, C. A.; SPENCE, H. E.; REEVES, G. D. Source and seed populations for relativistic electrons: their roles in radiation belt changes. **Journal of Geophysical Research: Space Physics**, v. 120, p. 7240–7254, 2015. 31

JORDANOVA, V. K.; ILIE, R.; CHEN, M. W. (Ed.). **Ring current investigations: the quest for space weather prediction**. Elsevier, 2020. ISBN 978-0-12-815571-4. Available from: <http://www.sciencedirect.com/science/article/pii/B978012815571400010X>. 11, 27

KAMIDE, Y.; CHIAN, A. C.-L. (Ed.). **Handbook of the solar-terrestrial environment**. [S.l.]: Springer Science & Business Media, 2007. 8, 9, 11, 12, 16, 18, 19, 20

KANEKAL, S. G.; BAKER, D. N. Radiation belts. In: KHAZANOV, G. V. (Ed.). **Space weather fundamentals**. [S.l.]: CRC Press, 2016. 25

KANG, S.-B.; FOK, M.-C.; KOMAR, C.; GLOCER, A.; LI, W.; BUZULUKOVA, N. An energetic electron flux dropout due to magnetopause shadowing on 1 june 2013. **Journal of Geophysical Research: Space Physics**, v. 123, n. 2, p. 1178–1190, 2018. 33

KIM, H.-J.; CHAN, A. A. Fully adiabatic changes in storm time relativistic electron fluxes. **Journal of Geophysical Research: Space Physics**, v. 102, n. A10, p. 22107–22116, 1997. 32

KIM, K. C.; LEE, D.-Y.; KIM, H.-J.; LEE, E.; CHOI, C. Numerical estimates of drift loss and dst effect for outer radiation belt relativistic electrons with arbitrary pitch angle. **Journal of Geophysical Research: Space Physics**, v. 115, n. A3, 2010. 61

KIVELSON, M. G.; RUSSELL, C. T. Geophysical coordinate transformations. In: **Introduction to space physics**. [S.l.]: Cambridge university press., 1995. p. 531–544. 9, 49

KLETZING, C. et al. The electric and magnetic field instrument suite and integrated science (emfisis) on rbsp. **Space Science Reviews**, v. 179, n. 1-4, p. 127–181, 2013. 37

LAVRAUD, B.; FOULLON, C.; FARRUGIA, C. J.; EASTWOOD, J. P. The magnetopause, its boundary layers and pathways to the magnetotail. In: **The dynamic magnetosphere**. [S.l.: s.n.], 2011. p. 3–28. 9

LEJOSNE, S.; KOLLMANN, P. Radiation belt radial diffusion at earth and beyond. **Space Science Reviews**, v. 216, n. 19, 2020. Available from: <https://doi.org/10.1007/s11214-020-0642-6>. 25, 26, 35

LI, L.-F.; TU, W.; DAI, L.; TANG, B.-B.; WANG, C.; BARANI, M.; ZENG, G.; WEI, C.; BURCH, J. Quantifying event-specific radial diffusion coefficients of radiation belt electrons with the ppmlr-mhd simulation. **Journal of Geophysical Research: Space Physics**, v. 125, n. 5, 2020. 4

LI, X.; BAKER, D.; TEMERIN, M.; CAYTON, T.; REEVES, E.; CHRISTENSEN, R.; BLAKE, J.; LOOPER, M.; NAKAMURA, R.; KANEKAL, S. Multisatellite observations of the outer zone electron variation during the

november 3–4, 1993, magnetic storm. **Journal of Geophysical Research: Space Physics**, v. 102, n. A7, p. 14123–14140, 1997. 32

LI, Z.; HUDSON, M.; CHEN, Y. Radial diffusion comparing a themis statistical model with geosynchronous measurements as input. **Journal of Geophysical Research: Space Physics**, v. 119, n. 3, p. 1863–1873, 2014. 156

LI, Z.; HUDSON, M.; JAYNES, A.; BOYD, A.; MALASPINA, D.; THALLER, S.; WYGANT, J.; HENDERSON, M. Modeling gradual diffusion changes in radiation belt electron phase space density for the march 2013 van allen probes case study. **Journal of Geophysical Research: Space Physics**, v. 119, n. 10, p. 8396–8403, 2014. 12, 30, 34, 136, 154

LI, Z.; HUDSON, M.; PATEL, M.; WILTBERGER, M.; BOYD, A.; TURNER, D. Ulf wave analysis and radial diffusion calculation using a global mhd model for the 17 march 2013 and 2015 storms. **Journal of Geophysical Research: Space Physics**, v. 122, n. 7, p. 7353–7363, 2017. 4

LIU, W.; TU, W.; LI, X.; SARRIS, T.; KHOTYAINTSEV, Y.; FU, H.; ZHANG, H.; SHI, Q. On the calculation of electric diffusion coefficient of radiation belt electrons with in situ electric field measurements by themis. **Geophysical Research Letters**, v. 43, n. 3, p. 1023–1030, 2016. Available from: <https://agupubs.onlinelibrary.wiley.com/doi/abs/10.1002/2015GL067398>. xviii, 5, 36, 55, 75, 88, 91, 92, 93, 94, 105, 121, 123, 139, 140, 143, 148, 150, 155, 159

LOTO'ANIU, T.; SINGER, H.; WATERS, C.; ANGELOPOULOS, V.; MANN, I.; ELKINGTON, S.; BONNELL, J. Relativistic electron loss due to ultralow frequency waves and enhanced outward radial diffusion. **Journal of Geophysical Research: Space Physics**, v. 115, n. A12, 2010. 1, 2, 4, 20

MANN, I. et al. The upgraded carisma magnetometer array in the themis era. **Space Science Reviews**, v. 141, n. 1-4, p. 413–451, 2008. 112

MANN, I. R. et al. Explaining the dynamics of the ultra-relativistic third van allen radiation belt. **Nature Physics**, v. 12, n. 10, p. 978–983, 2016. 34

McILWAIN, C. E. Coordinates for mapping the distribution of magnetically trapped particles. **Journal of Geophysical Research**, v. 66, n. 11, p. 3681–3691, 1961. 28, 61

MCILWAIN, C. E. Ring current effects on trapped particles. **Journal of Geophysical Research**, v. 71, n. 15, p. 3623–3628, 1966. 32

McPHERRON, L. R. Magnetic pulsations: their sources and relation to solar wind and geomagnetic activity. **Surveys in Geophysics**, v. 36, n. 5, 2005. 51

MCPHERRON, R.; BAKER, D.; CROOKER, N. Role of the russell–mcpherron effect in the acceleration of relativistic electrons. **Journal of Atmospheric and Solar-Terrestrial Physics**, v. 71, n. 10-11, p. 1032–1044, 2009. 2

MEDEIROS, C. et al. On the contribution of emic waves to the reconfiguration of the relativistic electron butterfly pitch angle distribution shape on 2014 september 12—a case study. **The Astrophysical Journal**, v. 872, n. 1, p. 36, 2019. 72

MORLEY, S.; HENDERSON, M.; REEVES, G.; FRIEDEL, R.; BAKER, D. Phase space density matching of relativistic electrons using the van allen probes: rept results. **Geophysical research letters**, v. 40, n. 18, p. 4798–4802, 2013. 47

MORLEY, S. K.; FRIEDEL, R. H. W.; SPANSWICK, E. L.; REEVES, G. D.; STEIBERG, J. T.; KOLLER, J.; CAYTON, T. E.; NOVEROSKE, E. Dropouts of the outer electron radiation belt in response to solar wind stream interfaces: Global positioning system observations. **Proceedings of the Royal Society A**, 2010. 2, 158

MURPHY, K. R.; MANN, I. R.; RAE, I. J.; SIBECK, D. G.; WATT, C. E. J. Accurately characterizing the importance of wave-particle interactions in radiation belt dynamics: the pitfalls of statistical wave representations. **Journal of Geophysical Research: Space Physics**, v. 121, n. 8, p. 7895–7899, 2016. Available from: <https://agupubs.onlinelibrary.wiley.com/doi/abs/10.1002/2016JA022618>. 105, 121, 124, 155, 156

MURPHY, K. R.; MANN, I. R.; SIBECK, D. G. On the dependence of storm time ulf wave power on magnetopause location: impacts for ulf wave radial diffusion. **Geophysical Research Letters**, v. 42, n. 22, p. 9676–9684, 2015. 79

NORTHROP, T. G.; TELLER, E. Stability of the adiabatic motion of charged particles in the earth's field. **Physics Reviews**, v. 117, p. 215–225, Jan 1960. 1

O'BRIEN, T. P.; MOLDWIN, M. B. Empirical plasmapause models from magnetic indices. **Geophysical Research Letters**, v. 30, n. 4, 2003. Available from: <https://agupubs.onlinelibrary.wiley.com/doi/abs/10.1029/2002GL016007>. 12, 13, 55, 136

OLIFER, L.; MANN, I. R.; MORLEY, S. K.; OZEKE, L. G.; CHOI, D. On the role of last closed drift shell dynamics in driving fast losses and van allen radiation belt extinction. **Journal of Geophysical Research: Space Physics**, v. 123, n. 5, p. 3692–3703, 2018. 23, 34, 149

OLIFER, L.; MANN, I. R.; OZEKE, L. G.; RAE, I. J.; MORLEY, S. K. On the relative strength of electric and magnetic ulf wave radial diffusion during the march 2015 geomagnetic storm. **Journal of Geophysical Research: Space Physics**, v. 124, n. 4, p. 2569–2587, 2019. Available from: <https://agupubs.onlinelibrary.wiley.com/doi/abs/10.1029/2018JA026348>. 4, 85, 88, 155

OLSON, W. P.; PFTIZER, K. A. **Magnetospheric magnetic field modeling**. [S.l.]: AFOSR, 1977. 61

ORLOVA, K.; SPASOJEVIC, M.; SHPRITS, Y. Activity-dependent global model of electron loss inside the plasmasphere. **Geophysical Research Letters**, v. 41, n. 11, p. 3744–3751, 2014. 33, 55, 57, 137

OZEKE, L. G.; MANN, I. R.; MURPHY, K. R.; RAE, I. J.; MILLING, D. K. Analytic expressions for ulf wave radiation belt radial diffusion coefficients. **Journal of Geophysical Research: Space Physics**, v. 119, n. 3, p. 1587–1605, March 2014a. Available from: <https://agupubs.onlinelibrary.wiley.com/doi/abs/10.1002/2013JA019204>. 35, 75, 105

OZEKE, L. G.; MANN, I. R.; MURPHY, K. R.; SIBECK, D. G.; BAKER, D. N. Ultra-relativistic radiation belt extinction and ulf wave radial diffusion: modeling the september 2014 extended dropout event. **Geophysical Research Letters**, v. 44, n. 6, p. 2624–2633, 2017. Available from: <https://agupubs.onlinelibrary.wiley.com/doi/abs/10.1002/2017GL072811>. 23

OZEKE, L. G.; MANN, I. R.; TURNER, D. L.; MURPHY, K. R.; DEGELING, A. W.; RAE, I. J.; MILLING, D. K. Modeling cross l shell impacts of magnetopause shadowing and ulf wave radial diffusion in the van allen belts. **Geophysical Research Letters**, v. 41, n. 19, p. 6556–6562, October 2014b. 1, 12, 30

PARKER, E. N. Dynamics of the geomagnetic storm. **Space Science Reviews**, v. 1, 1962. 62

PARKS, G. K. (Ed.). **Physics of space plasmas: an introduction**. [S.l.]: Westview Press, 2004. 7

PFITZER, K.; OLSON, W.; MOGSTAD, T. A time dependent source driven magnetospheric magnetic field model. **Eos Trans. AGU**, v. 69, n. 16, p. 426, 1988. 27

PRESS, W. H.; TEUKOLSKY, S. A.; VETTERLING, W. T.; FLANNERY, B. P. **Numerical recipes: the art of scientific computing**. [S.l.]: Cambridge University Press, 2007. 1043–1048 p. 53, 54

QIN, Z.; DENTON, R. E.; TSYGANENKO, N. A.; WOLF, S. Solar wind parameters for magnetospheric magnetic field modeling. **Space Weather**, v. 5, n. 11, 2007. Available from: <https://agupubs.onlinelibrary.wiley.com/doi/abs/10.1029/2006SW000296>. 15

REEVES, G.; SPENCE, H.; HENDERSON, M.; MORLEY, S.; FRIEDEL, R.; FUNSTEN, H.; BAKER, D. Electron acceleration in the heart of the van allen radiation belts. **Science**, v. 341, n. 6149, 2013. 30, 47, 48, 130

REEVES, G. D.; MCADAMS, K. L.; FRIEDEL, R. H. W. Acceleration and loss of relativistic electrons during geomagnetic storms. **Geophysical Research Letters**, v. 30, n. 10, 2003. 1, 23, 55

REGI, M.; CORPO, A. D.; LAURETIS, M. D. The use of the empirical mode decomposition for the identification of mean field aligned reference frames. **Annals of Geophysics**, v. 59, n. 6, 2016. 49, 50

RICHARDSON, I. G. Solar wind stream interaction regions throughout the heliosphere. **Living Reviews in Solar Physics**, v. 15, 2018. 2, 9, 38, 39

ROEDERER, J. G. **Dynamics of Geomagnetically Trapped Radiation**. Berlin: Springer-Verlag, 1970. 1, 3, 26, 28, 29, 33

ROEDERER, J. G.; LEJOSNE, S. Coordinates for representing radiation belt particle flux. **Journal of Geophysical Research: Space Physics**, v. 123, n. 2, p. 1381–1387, 2018. 25, 28, 43, 56

RUNOV, A.; ANGELOPOULOS, V.; ZHOU, X.-Z. Multipoint observations of dipolarization front formation by magnetotail reconnection. **Journal of Geophysical Research: Space Physics**, v. 117, n. A5, 2012. Available from: <https://agupubs.onlinelibrary.wiley.com/doi/abs/10.1029/2011JA017361>. 95

SAMSON, J. Geomagnetic pulsations and plasma waves in the earth's magnetosphere. **Geomagnetism**, v. 4, p. 481–592, 1991. 21

SAMSONOV, A. A.; BOGDANOVA, Y. V.; BRANDUARDI-RAYMONT, G.; SIBECK, D. G.; TOTH, G. Is the relation between the solar wind dynamic pressure and the magnetopause standoff distance so straightforward? **Geophysical Research Letters**, v. 47, n. 8, p. e2019GL086474, 2020. E2019GL086474 10.1029/2019GL086474. Available from: <https://agupubs.onlinelibrary.wiley.com/doi/abs/10.1029/2019GL086474>. 72

SHPRITS, Y.; THORNE, R.; FRIEDEL, R.; REEVES, G.; FENNELL, J.; BAKER, D.; KANEKAL, S. Outward radial diffusion driven by losses at magnetopause. **Journal of Geophysical Research: Space Physics**, v. 111, n. A11, 2006. 3, 5, 25, 30, 33, 154

SHPRITS, Y. Y.; ELKINGTON, S. R.; MEREDITH, N. P.; SUBBOTIN, D. A. Review of modeling of losses and sources of relativistic electrons in the outer radiation belt I: Radial transport. **Journal of Atmospheric and Solar-Terrestrial Physics**, v. 70, p. 1679–1693, 2008. 51

SHPRITS, Y. Y.; KELLERMAN, A.; ASEEV, N.; DROZDOV, A. Y.; MICHAELIS, I. Multi-mev electron loss in the heart of the radiation belts. **Geophysical Research Letters**, v. 44, n. 3, p. 1204–1209, 2017. 33, 34, 52, 155

SHPRITS, Y. Y.; MEREDITH, N. P.; THORNE, R. M. Parameterization of radiation belt electron loss timescales due to interactions with chorus waves. **Geophysical Research Letters**, v. 34, n. 11, 2007. 33, 55, 56, 137, 155

SHPRITS, Y. Y. et al. Wave-induced loss of ultra-relativistic electrons in the van allen radiation belts. **Nature Communications**, v. 7, n. 1, p. 1–7, 2016. 53

SHUE, J.-H.; CHAO, J.; FU, H.; RUSSELL, C.; SONG, P.; KHURANA, K.; SINGER, H. A new functional form to study the solar wind control of the magnetopause size and shape. **Journal of Geophysical Research: Space Physics**, v. 102, n. A5, p. 9497–9511, 1997. 13

SHUE, J. H. et al. Magnetopause location under extreme solar wind. **Journal of Geophysical Research**, v. 103, n. A8, p. 17,691–17,700, 1998. xi, xiii, xvi, 1, 2, 4, 12, 13, 14, 60, 62, 64, 71, 72, 109, 138, 149

SHULZ, M.; LANZEROTTI, L. J. **Particle Diffusion in the Radiation Belts**. New York: Springer-Verlag, 1974. 1, 29, 32, 33, 43, 52, 56

SOUZA, V. et al. Acceleration of radiation belt electrons and the role of the average interplanetary magnetic field bz component in high-speed streams. **Journal of Geophysical Research: Space Physics**, v. 122, n. 10, p. 10–084, 2017. 24

STRATTON, J. M.; HARVEY, R. J.; HEYLER, G. A. Mission overview for the radiation belt storm probes mission. **Space Science Reviews**, v. 179, n. 1, p. 29–57, Nov 2013. ISSN 1572-9672. Available from: <https://doi.org/10.1007/s11214-012-9933-x>. 40

SUMMERS, D.; THORNE, R. M.; XIAO, F. Relativistic theory of wave-particle resonant diffusion with application to electron acceleration in the magnetosphere. **Journal of Geophysical Research: Space Physics**, v. 103, n. A9, p. 20487–20500, 1998. 31

TAKAHASHI, K. Ulf waves in the inner magnetosphere. In: KEILING, A.; LEE, D.-H.; NAKARIAKOV, V. (Ed.). **Low-frequency waves in space plasmas**. [S.l.]: John Wiley & Sons, 2016. 20

THÉBAULT, E. et al. International geomagnetic reference field: the 12th generation. **Earth, Planets and Space**, v. 67, n. 1, p. 79, 2015. 77

THORNE, R. M. Radiation belt dynamics: the importance of wave-particle interactions. **Geophysical Research Letters**, v. 37, n. 22, 2010. 12, 20, 29, 33

TÓTH, G.; SOKOLOV, I. V.; GOMBOSI, T. I.; CHESNEY, D. R.; CLAUER, C. R.; ZEEUW, D. L. D.; HANSEN, K. C.; KANE, K. J.; MANCHESTER, W. B.; OEHMKE, R. C. et al. Space weather modeling framework: a new tool for the space science community. **Journal of Geophysical Research: Space Physics**, v. 110, n. A12, 2005. 68

TSURUTANI, B. T.; GONZALEZ, W. D.; GONZALEZ, A. L. C.; GUARNIERI, F. L.; GOPALSWAMY, N.; GRANDE, M.; KAMIDE, Y.; KASAHARA, Y.; LU, G.; MANN, I.; MCPHERRON, R.; SORAAS, F.; VASYLIUNAS, V. Corotating solar wind streams and recurrent geomagnetic activity: a review. **Journal of Geophysical Research**, v. 111, n. A07S01, 2006. 2

TSYGANENKO, N. Modeling the earth's magnetospheric magnetic field confined within a realistic magnetopause. **Journal of Geophysical Research: Space Physics**, v. 100, n. A4, p. 5599–5612, 1995. xv, 49

TSYGANENKO, N.; SITNOV, M. Modeling the dynamics of the inner magnetosphere during strong geomagnetic storms. **Journal of Geophysical Research: Space Physics**, v. 110, n. A3, 2005. 12, 14, 15, 63

TSYGANENKO, N. A. A model of the near magnetosphere with a dawn-dusk asymmetry 1. mathematical structure. **Journal of Geophysical Research: Space Physics**, v. 107, n. A8, p. SMP 12–1–SMP 12–15, 2002. Available from: <https://agupubs.onlinelibrary.wiley.com/doi/abs/10.1029/2001JA000219>. 14

TU, W. **Modeling Earth's outer radiation belt electron dynamics—radial diffusion, heating, and loss**. PhD Thesis (PhD) — University of Colorado at Boulder, 2011. 45, 54

TU, W.; CUNNINGHAM, G.; CHEN, Y.; HENDERSON, M.; CAMPOREALE, E.; REEVES, G. Modeling radiation belt electron dynamics during gem challenge intervals with the dream3d diffusion model. **Journal of Geophysical Research: Space Physics**, v. 118, n. 10, p. 6197–6211, 2013. 32

TU, W.; CUNNINGHAM, G.; CHEN, Y.; MORLEY, S.; REEVES, G.; BLAKE, J.; BAKER, D.; SPENCE, H. Event-specific chorus wave and electron seed population models in dream3d using the van allen probes. **Geophysical Research Letters**, v. 41, n. 5, p. 1359–1366, 2014. 32

TU, W.; ELKINGTON, S. R.; LI, X.; LIU, W.; BONNELL, J. Quantifying radial diffusion coefficients of radiation belt electrons based on global mhd simulation and spacecraft measurements. **Journal of Geophysical Research: Space Physics**, v. 117, n. A10, 2012. Available from: <https://agupubs.onlinelibrary.wiley.com/doi/abs/10.1029/2012JA017901>. 4, 34, 42, 73, 75, 155

TU, W.; LI, X.; CHEN, Y.; REEVES, G.; TEMERIN, M. Storm-dependent radiation belt electron dynamics. **Journal of Geophysical Research: Space Physics**, v. 114, n. A2, 2009. 12, 52, 136

TU, W.; XIANG, Z.; MORLEY, S. K. Modeling the magnetopause shadowing loss during the june 2015 dropout event. **Geophysical Research Letters**, v. 46, n. 16, p. 9388–9396, 2019. 3, 5, 33, 46, 52, 150

TURNER, D.; ANGELOPOULOS, V.; LI, W.; BORTNIK, J.; NI, B.; MA, Q.; THORNE, R.; MORLEY, S.; HENDERSON, M.; REEVES, G. et al. Competing

source and loss mechanisms due to wave-particle interactions in earth's outer radiation belt during the 30 september to 3 october 2012 geomagnetic storm. **Journal of Geophysical Research: Space Physics**, v. 119, n. 3, p. 1960–1979, 2014. 1, 33, 152

TURNER, D. L.; MORLEY, S. K.; MIYOSHI, Y.; NI, B.; HUANG, C.-L. Outer radiation belt flux dropouts: current understanding and unresolved questions. In: **Dynamics of the earth's radiation belts and inner magnetosphere**. [S.l.]: American Geophysical Union, 2012. Geophysical Monograph Series 99. 1, 23, 29, 32, 94

TURNER, D. L.; SHPRITS, Y.; HARTINGER, M.; ANGELOPOULOS, V. Explaining sudden losses of outer radiation belt electrons during geomagnetic storms. **Nature Physics**, v. 8, n. 3, p. 208–212, 2012. 1, 2, 30, 33, 71, 94, 157, 158

TÓTH, G.; HOLST, B. V. D.; SOKOLOV, I. V.; ZEEUW, D. L.; GOMBOSI, T. I.; FANG, F.; MANCHESTER, W. B.; MENG, X.; NAJIB, D.; POWELL, K. G.; STOUT, Q. F.; GLOCER, A.; MA, Y. J. Adaptive numerical algorithms in space weather modeling. **Journal of Computational Physics**, v. 231, n. 3, p. 870, 2011. 68

UKHORSKIY, A.; SITNOV, M.; MILLAN, R.; KRESS, B. The role of drift orbit bifurcations in energization and loss of electrons in the outer radiation belt. **Journal of Geophysical Research: Space Physics**, v. 116, n. A9, 2011. 56

UKHORSKIY, A.; SITNOV, M.; TAKAHASHI, K.; ANDERSON, B. Radial transport of radiation belt electrons due to stormtime pc5 waves. v. 27, n. 5, p. 2173–2181, 2009. 157

VAN ALLEN, J. The geomagnetically trapped corpuscular radiation. **Journal of Geophysical Research**, v. 64, n. 11, 1959. 22

VOLWERK, M. Ulf wave modes in the earth's magnetotail. In: KEILING, A.; LEE, D.-H.; NAKARIAKOV, V. (Ed.). **Low-frequency waves in space plasmas**. [S.l.]: John Wiley & Sons, 2016. 21

WALT, M. **Introduction to geomagnetically trapped radiation**. [S.l.]: Cambridge University Press, 2005. 41

WANLISS, J. A.; SHOWALTER, K. M. High-resolution global storm index: Dst versus sym-h. **Journal of Geophysical Research: Space Physics**, v. 111,

n. A2, 2006. Available from: <https://agupubs.onlinelibrary.wiley.com/doi/abs/10.1029/2005JA011034>. 11

WATERS, C. Ulf resonance structure in the magnetosphere. **Advances in Space Research**, v. 25, n. 7-8, p. 1541–1558, 2000. 51

WELLING, D.; KOLLER, J.; CAMPOREALE, E. Verification of spacepy's radial diffusion radiation belt model. **Geoscientific Model Development**, v. 5, n. 2, p. 277–287, 2012. 53, 54

WOO, R.; MARTIN, J. M. Source regions of the slow solar wind. **Geophysical research letters**, v. 24, n. 20, p. 2535–2538, 1997. 38

WYGANT, J. et al. The electric field and waves instruments on the radiation belt storm probes mission. **The Van Allen Probes Mission**, p. 183–220, 2013. 37

XIANG, Z.; NI, B.; ZHOU, C.; ZOU, Z.; GU, X.; ZHAO, Z.; ZHANG, X.; ZHANG, X.; ZHANG, S.; LI, X. et al. **Multi-satellite simultaneous observations of magnetopause and atmospheric losses of radiation belt electrons during an intense solar wind dynamic pressure pulse**. 2016. 493–509 p. 109

XIANG, Z.; TU, W.; LI, X.; NI, B.; MORLEY, S. K.; BAKER, D. N. Understanding the mechanisms of radiation belt dropouts observed by van allen probes. **Jornal of Geophysical Research**, v. 122, n. 10, p. 9858–9879, 2017. 33, 139

XIANG, Z.; TU, W.; NI, B.; HENDERSON, M.; CAO, X. A statistical survey of radiation belt dropouts observed by van allen probes. **Geophysical Research Letters**, v. 45, n. 16, p. 8035–8043, 2018. 30, 33, 149, 155

YU, Y.; KOLLER, J.; MORLEY, S. Quantifying the effect of magnetopause shadowing on electron radiation belt dropouts. In: COPERNICUS GMBH. **Annales Geophysicae**. [S.l.], 2013. v. 31, n. 11, p. 1929–1939. 52, 150

YUAN, C.-J.; ZONG, Q.-G.; WAN, W.-X.; ZHANG, H.; DU, A.-M. Relativistic electron flux dropouts in the outer radiation belt associated with corotating interaction regions. **Journal of Geophysical Research: Space Physics**, v. 120, n. 9, p. 7404–7415, 2015. 2

APPENDIX A - FIGURES

Figure A.1 - Case 1: D_{LL} from MHD simulation for $\mu = 700$ MeV/G.

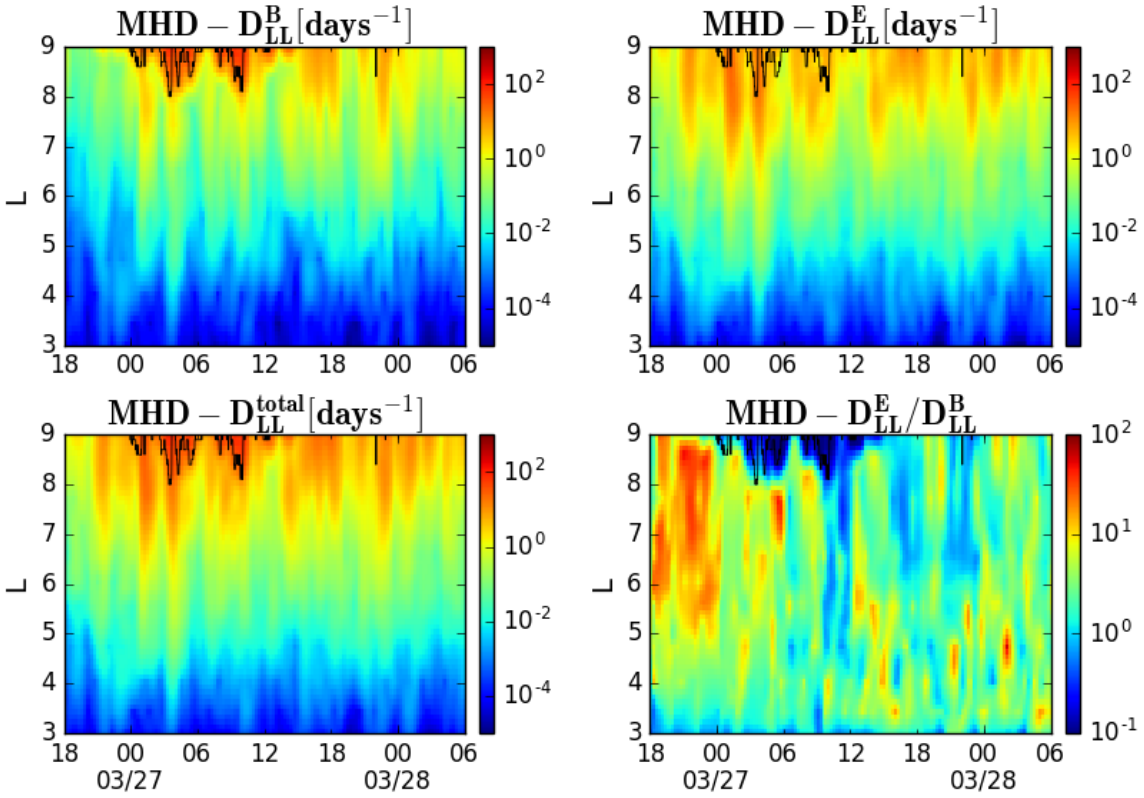

SOURCE: Produced by the author.

Figure A.2 - Case 1: D_{LL} from MHD simulation for $\mu = 2083$ MeV/G.

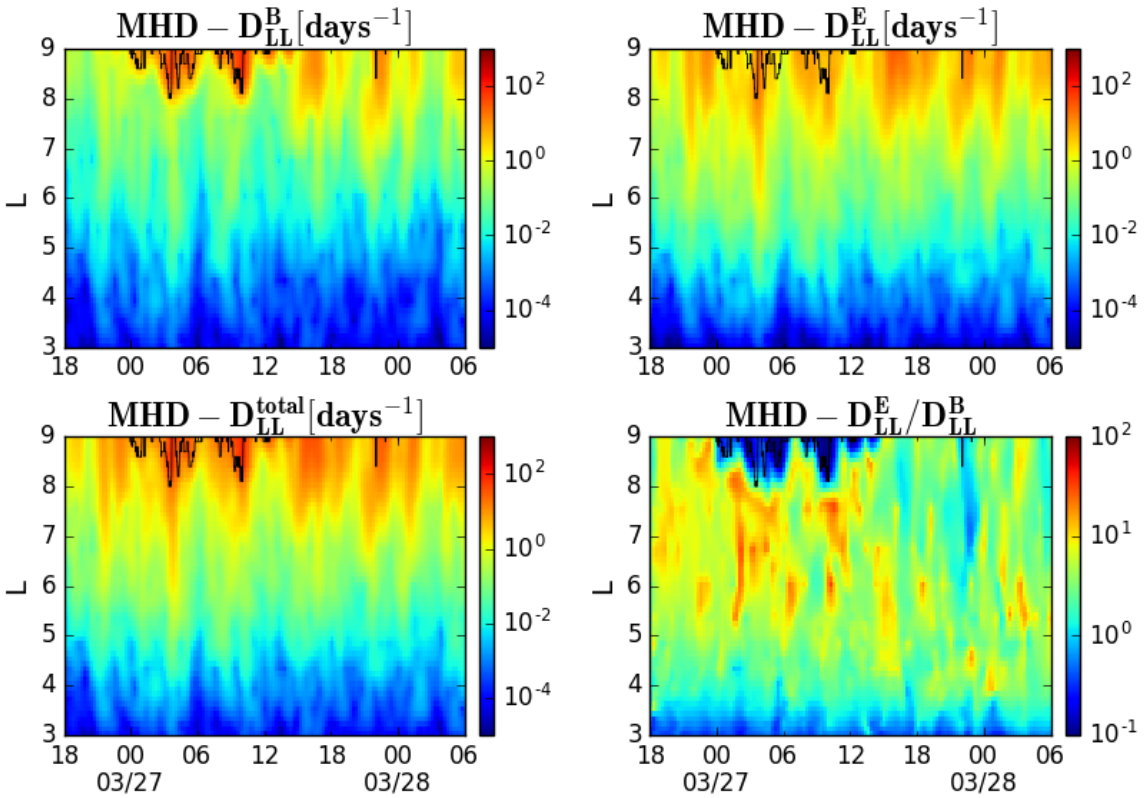

SOURCE: Produced by the author.

Figure A.3 - Case 2: D_{LL} from MHD simulation for $\mu = 700$ MeV/G.

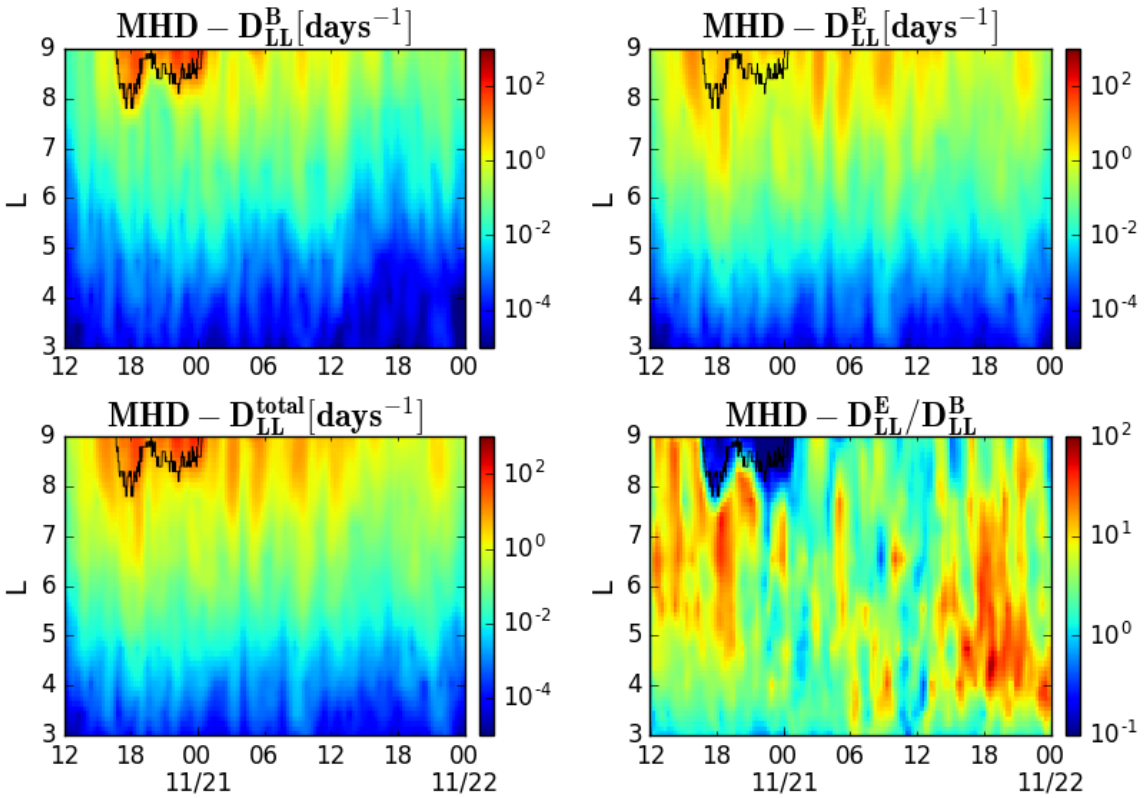

SOURCE: Produced by the author.

Figure A.4 - Case 2: D_{LL} from MHD simulation for $\mu = 2083$ MeV/G.

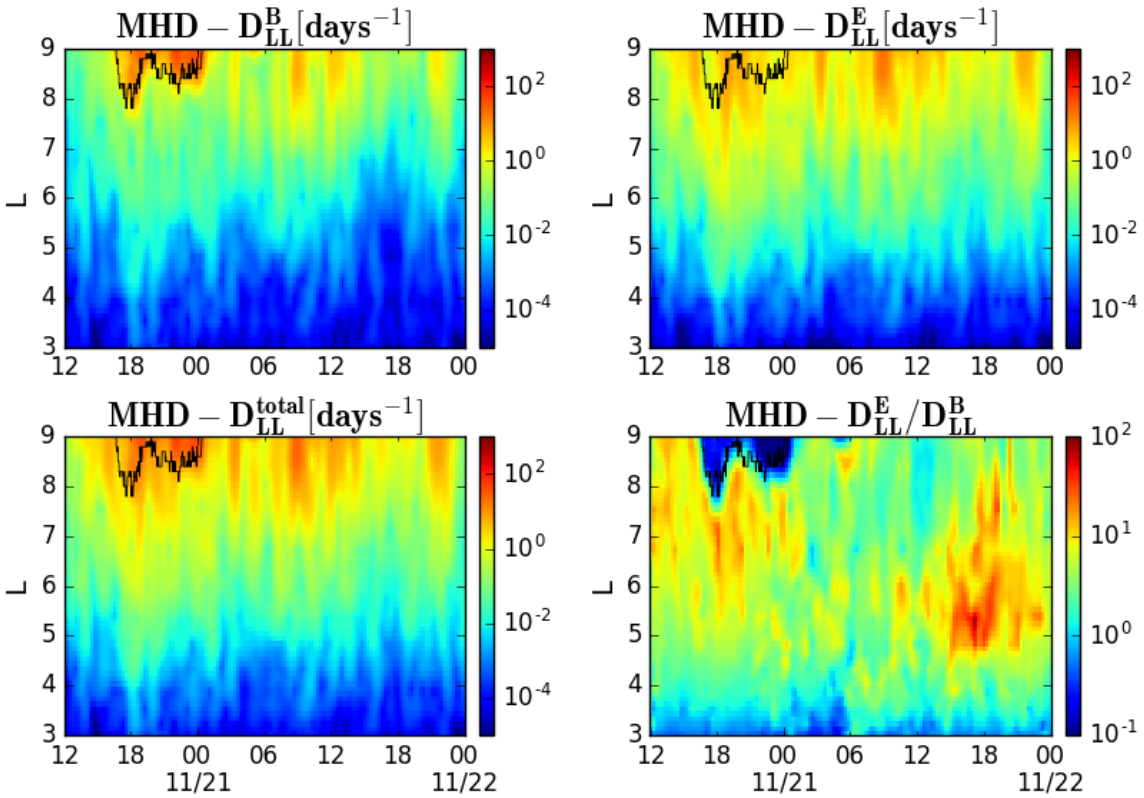

SOURCE: Produced by the author.

Figure A.5 - Case 1: Direct comparisons and respective ratios involving total D_{LL} rates interpolated from MHD simulation and taken from observations, computed for $\mu = 700$, 1318, and 2083 MeV/G.

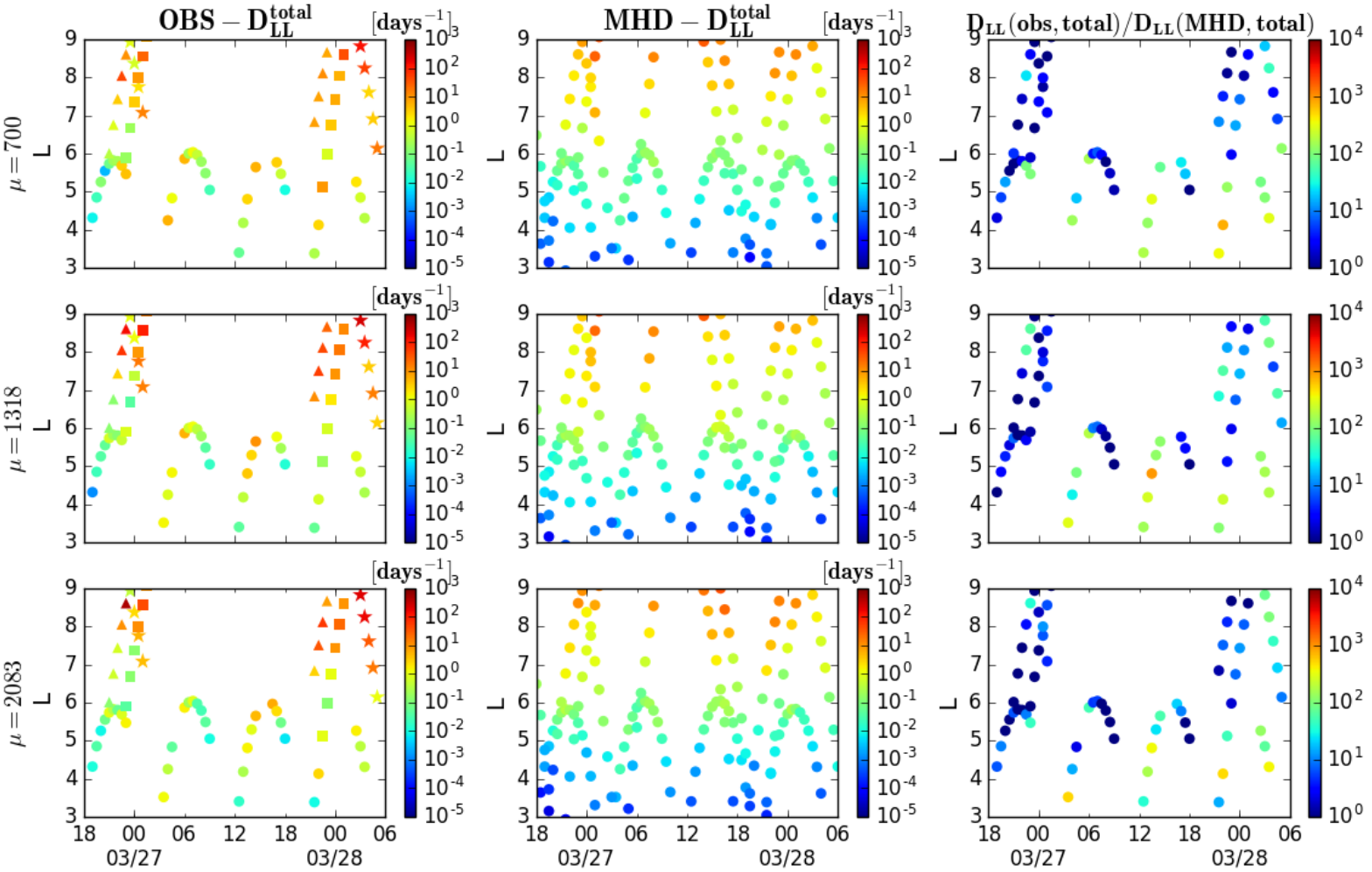

Panels from the same row in these subplots show, respectively, results of D_{LL}^{OBS}, D_{LL}^{MHD}, and ratios of $D_{LL}^{OBS}/D_{LL}^{MHD}$ at fixed μ.

SOURCE: Produced by the author.

Figure A.6 - Case 2: Direct comparisons and respective ratios involving total D_{LL} rates interpolated from MHD simulation and taken from observations, computed for $\mu = 700$, 1318, and 2083 MeV/G.

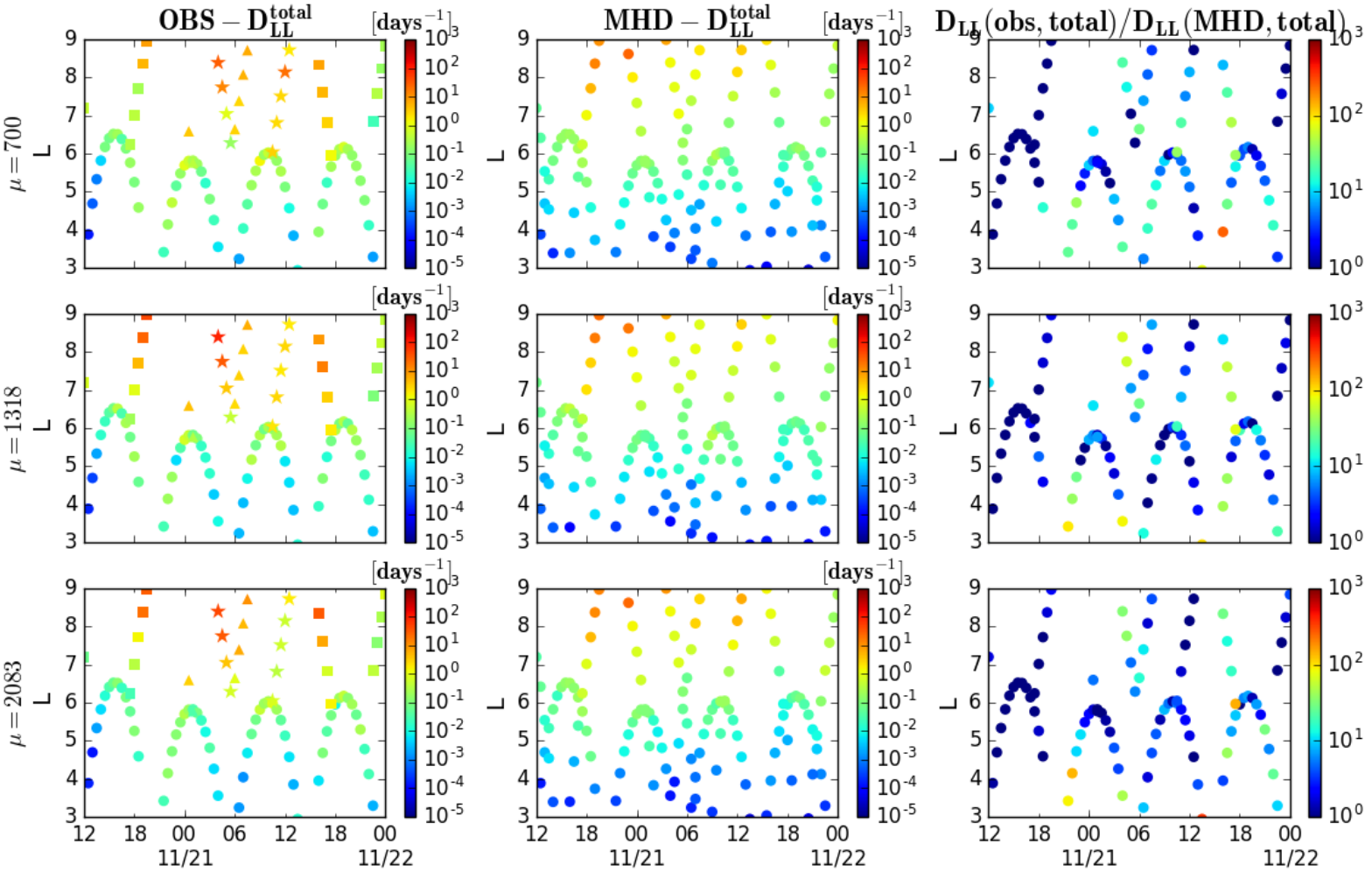

Panels from the same row in these subplots show, respectively, results of D_{LL}^{OBS}, D_{LL}^{MHD}, and ratios of $D_{LL}^{OBS}/D_{LL}^{MHD}$ at fixed μ.

SOURCE: Produced by the author.

Figure A.7 - Case study 4: Observations by Van Allen Probes (RBSP-A and RBSP-B), ACE and of the geomagnetic indices from December 4 through December 8, 2017.

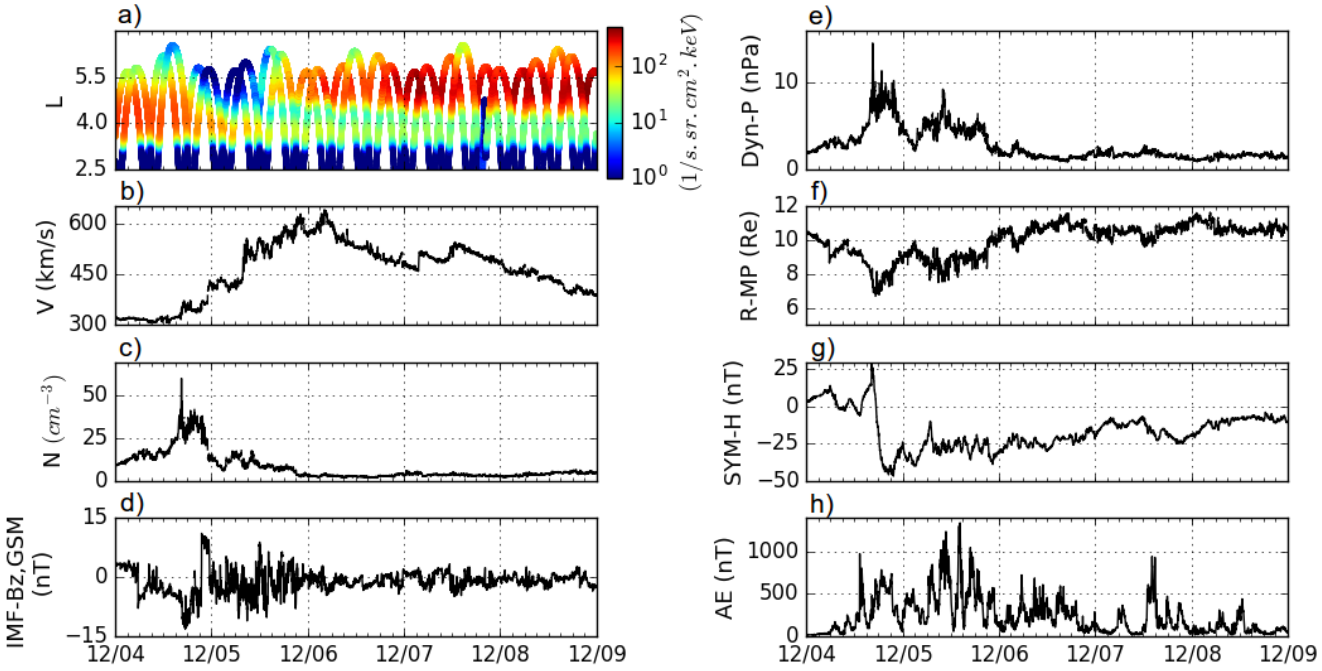

(a) Temporal and radial distribution of electron fluxes measured by the REPT instrument onboard the Van Allen Probes, at 1.8 MeV and 90° local pitch angle. (b-e) Solar wind velocity, density, IMF-B_z component and dynamic pressure, characterizing the full passing of the CIR and the HSS. (f-h) Changes in the magnetopause location (R_{MP}) and in the geomagnetic indices SYM-H and AE.

SOURCE: Produced by the author.

Figure A.8 - RBSP-A, RBSP-B, and GOES-15 observations of phase space density during case 2.

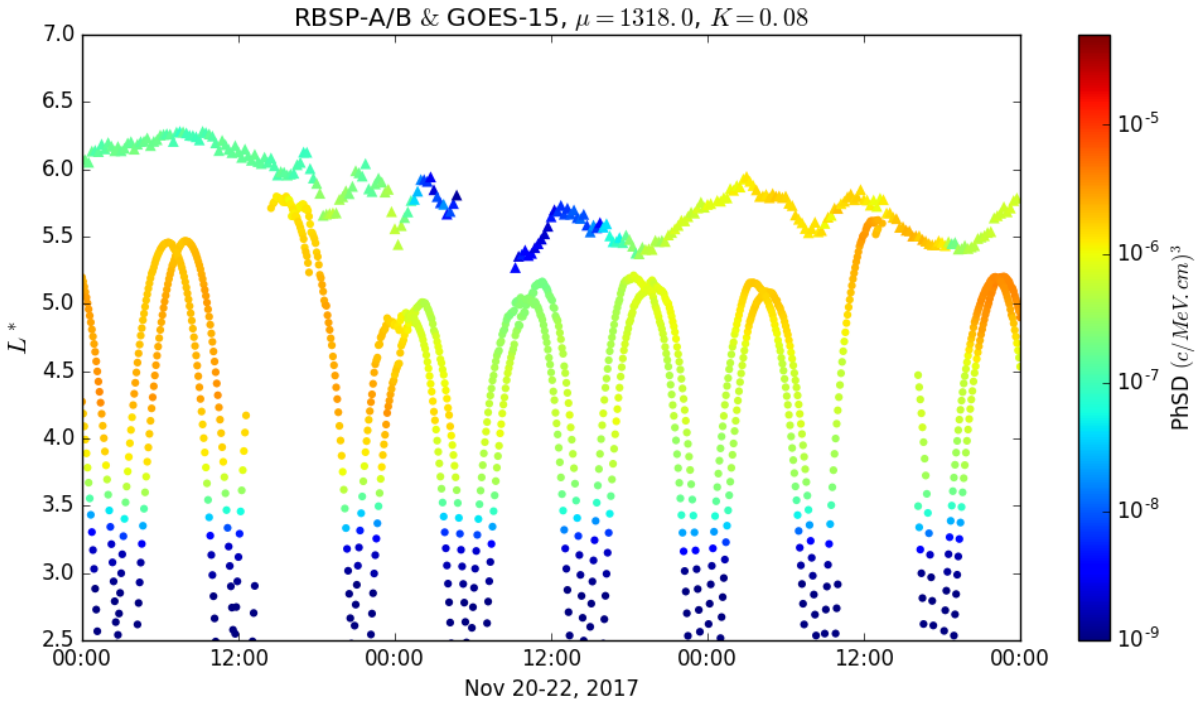

PhSD is plotted along the probes' L^* data calculated with the TS04 model. The PhSD data from GOES-15 shown is not calibrated. .

SOURCE: Produced by the author.

Figure A.9 - RBSP-A, RBSP-B, and GOES-15 observations of phase space density during case 4.

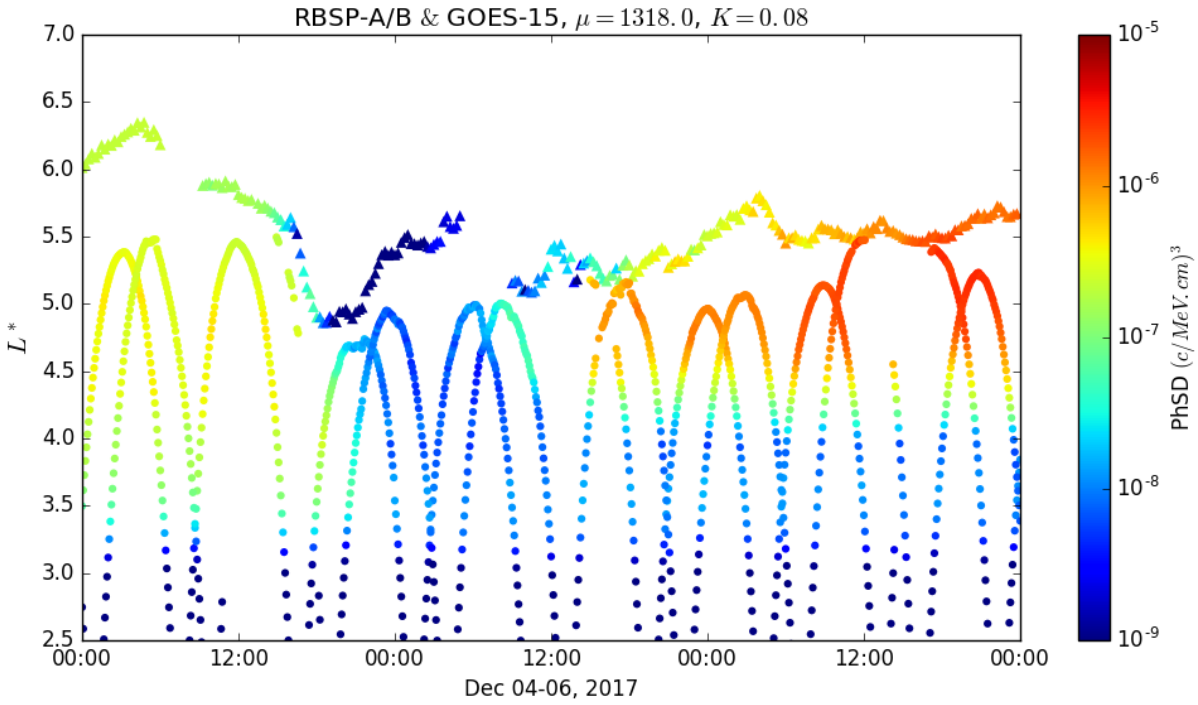

PhSD is plotted along the probes' L^* data calculated with the TS04 model. The PhSD data from GOES-15 shown is not calibrated. .

SOURCE: Produced by the author.

Figure A.10 - Case 1: Radial profiles of PhSD for $\mu = 700$ MeV/G, from an outbound pass of RBSP-A on 03/26 together with the calibrated estimate from GOES-15 at the conjunction ($L^* \sim 6$ and $\Delta L^* = 0.09$).

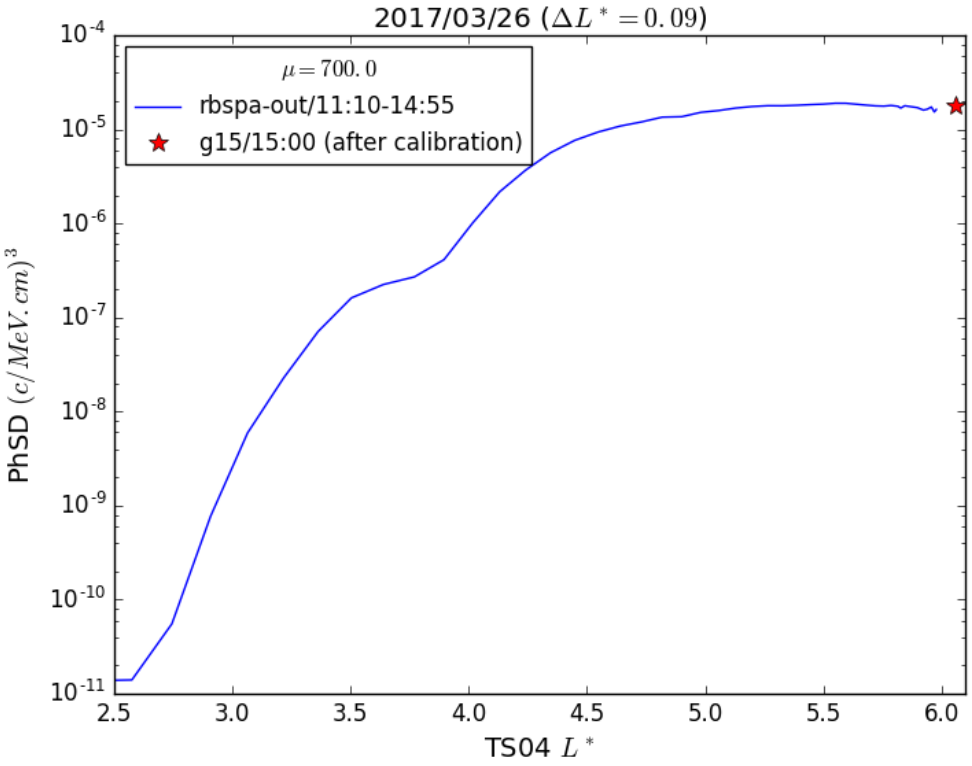

The L^*-conjunction occurred at $\sim$ 15 UT.

SOURCE: Produced by the author.

APPENDIX B - TABLE

Table B.1 - Catalog listing the recurrence periods of 11 CIRs identified through August 2016 to May 2018, and information on the associated HSS and coronal hole of origin.

CIRs	CH number	CH's Earth facing interval	HSS Passage
CIR1	838	28.11.2017 – 01.12.2017	30.11.2017
	843	20.12.2017 – 23.12.2017	24.12.2017
	848	16.01.2018 – 20.012018	21.01.2018
	851	12.02.2018 – 17.02.2018	16.02.2018
	857	10.03.2018 – 15.03.2018	14.03.2018
	860	06.04.2018 – 11.04.2018	09.04.2018
	863	02.05.2018 – 07.05.2018	05.05.2018
CIR2	824	10.09.2017 – 14.09.2017	14.09.2017
	828	07.10.2017 – 10.10.2017	10.10.2017
	834	03.11.2017 – 06.11.2017	07.11.2017
	839	01.12.2017 – 03.12.2017	04.12.2017
CIR3	818	31.07.2017 – 05.08.2017	04.08.2017
	822	28.08.2017 – 01.09.2017	31.08.2017
	826	23.09.2017 – 26.09.2017	27.09.2017
	831	20.10.2017 – 23.10.2017	24.10.2017
	837	16.11.2017 – 18.11.2017	20.11.2017
	842	13.12.2017 – 15.12.2017	16.12.2017
	847	09.01.2018 – 10.01.2018	13.01.2018
CIR4	825	20.09.2017 – 21.09.2017	24.09.2017
	830	17.10.2017 – 18.10.2017	21.10.2017
	836	13.11.2017 – 14.11.2017	15.11.2017
CIR5	827	01.10.2017 – 03.10.2017	04.10.2017
	833	29.10.2017 – 31.10.2017	02.11.2017
CIR6	804	16.05.2017 – 18.05.2017	19.05.2017
	808	14.06.2017 – 15.06.2017	16.06.2017
CIR7	756	20.08.2016 – 21.08.2016	22.08.2016
	777	05.12.2016 – 09.12.2016	07.12.2016
	782	01.01.2017 – 03.01.2017	03.01.2017
	788	28.01.2017 – 31.01.2017	30.01.2017
	792	25.02.2017 – 28.02.2017	01.03.2017

Table B.1 - continuation

CIRs	CH number	CH's Earth facing interval	HSS Passage
	798	24.03.2017 – 29.03.2017	27.03.2017
CIR8	781	27.12.2016 – 29.12.2016	31.12.2016
	787	23.01.2017 – 25.01.2017	26.01.2017
	791	19.02.2017 – 21.02.2017	23.02.2017
	797	18.03.2017 – 21.03.2017	21.03.2017
	801	13.04.2017 – 16.04.2017	18.04.2017
	803	12.05.2017 – 13.05.2017	15.05.2017
CIR9	769	23.10.2016 – 27.10.2016	25.10.2016
	774	20.11.2016 – 22.11.2016	24.11.2016
	780	17.12.2016 – 22.12.2016	21.12.2016
	786	16.01.2017 – 19.01.2017	18.01.2017
	790	12.02.2017 – 17.02.2017	16.02.2017
CIR10	746	04.07.2016 – 11.07.2016	12.07.2016
	753	30.07.2017 – 07.08.2016	09.08.2016
CIR11	757	26.08.2016 – 27.08.2016	01.09.2016
	763	22.09.2016 – 23.09.2016	26.09.2016

CH = Coronal hole; Date format = dd.mm.yyyy; CH number as given by Solen.info (http://www.solen.info/solar/coronal_holes.html) and HSS passage as cataloged by DONKI-NASA (https://kauai.ccmc.gsfc.nasa.gov/DONKI/search/). Signatures of each recurrence of the CIRs in solar wind data can be observed around the day indicated for the corresponding HSS passage. The recurrence dates of listed HSS/CIRs are shown from the start of notification of the long-lived CHs. **In blue are the events selected for investigation of dropouts with radial diffusion modeling.**

SOURCE: Produced by the author.